PORE STRUCTURES AND ADSORPTION CHARACTERISTICS OF ACTIVATED CARBON FIBERS HAVING BOTH MICRO- AND MESOPORES

Junichi Miyamoto, Hirofumi Kanoh, Katsumi Kaneko

Department of Chemistry, Chiba University
1-33 Yayoi, Inage, Chiba 263-8522 Japan

Introduction

The activated carbon fiber (ACF) is known as high specific surface area carbon material with about 1nm micro-pore diameter. ACF is widely applied in industry and consumer use such as the capacitor, gas separation material, vapor phase and/or liquid phase purification. Recently, the development of porous material which can adsorb the molecule of mesoporous size is desired. For example, we must develop an efficient adsorption for the effective canister in order to protect evaporative emission of gasoline from the fuel tank. Furthermore, we have an urgent issue to remove volatile organic compounds such as trihalomethane from drinking water. In this report, addition mesopores into activated carbon fiber was examined using chemical reagent impregnation and steam activation method.

Experimental

We used pitch-based activated carbon fiber A10 and A20 (AD'ALL co. Ltd.) as the precursor. The surface area and porosity parameters of A10 and A20 is summarized in Table1. Each of ACFs were pretreated at 383K in vacuum (under 1mPa) and then ACFs were vacuum impregnated in 0.3mol/L solution of Na_2HPO_4, $Ca(NO_3)_2 \cdot 4H_2O$ and K_2CO_3 at room temperature. Then they were filtrated and dried at 353K in a dry oven. The chemical reagent-impregnated ACF was activated with steam under the flow of steam containing Ar (100ml/min) at 1073-1173K for 1h. The porosity change was examined by N_2 adsorption at 77K with volumetric method (Quantachrome Autosorb-1). Micropore structural parameter was determined from α_s-plot using nitrogen adsorption isotherm[1,2], and mesopore size distributions were determined by Dollimore-Heal method.

Table 1 Micropore structure parameters of A10 and A20

| Sample	Total surface are (m^2/g)	Micropore volume(ml/g)	Mean micropore width(nm)
A10	1360	0.56	0.84
A20	1735	0.89	1.10

Results and Discussion

The nitrogen adsorption isotherms at 77K of original A10 and chemical reagent impregnated reactivation ACF are shown in **Fig.1a**. The ACFs reactivated with Na_2HPO_4, $Ca(NO_3)_2 \cdot 4H_2O$ and K_2CO_3 are denoted A10-P, A10-Ca, and A10-K, respectively. All isotherms show a sharp adsorption uptake in low relative pressure region, which indicates these reactivated ACFs are microporous materials. In addition, there is an explicit hysteresis loop in A10 reactivated with Na_2HPO_4; A10-P and $Ca(NO_3)_2$; A10-Ca. It indicates existence of mesopores in A10-P and A10-Ca. However, K_2CO_3 is not effective for mesopore formation. This result is similar to different pitch-based ACF A20 (**Fig.1b**). Accordingly, we can obtain the mesoporous ACF using disodium hydrogen phosphate and calcium nitrate.

Micropore size distribution from DFT method and mesopore size distribution from DH method for reactivated A20 are shown in **Figure 2**. From micropore size distribution, there is no difference
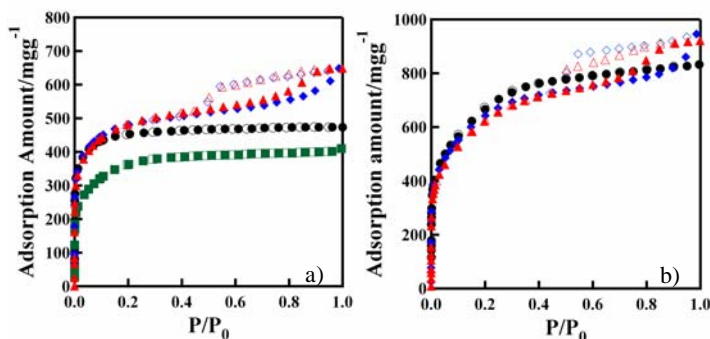
Figure 1. N_2 adsorption isotherm at 77K of reactivated ACF a)original A10 and reactivated at 1073K with Na_2HPO_4, $Ca(NO_3)_2 \cdot 4H_2O$ and K_2CO_3 b)original A20 and reactivated at 1073K with Na_2HPO_4, and $Ca(NO_3)_2 \cdot 4H_2O$

between A20-P and A20-Ca. On the contrary, mesopore size distribution is different from each other. Mesopore size of A20-P shows broad distribution from 10 to 70nm, while A20-Ca has a sharp distribution at 9nm. Accordingly, reactivation with $Ca(NO_3)_2$ is hopeful method to produce uniform mesopore.
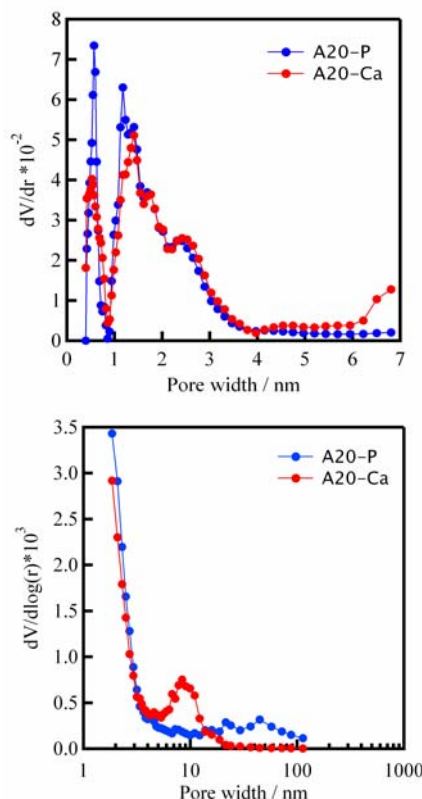
Figure 2. Micropore size distribution and Mesopore size distribution for A20-P and A20-Ca reactivated at 1073K

References

1 K. Kaneko, C. Ishii, M. Ruike, and H. Kuwabara, *Carbon*, **1992**, *30*, 1075.
2 K. Kaneko, C. Isihii, *Colloids and Surfaces*, **1992**, *67*, 203

ADSORPTION OF DIBENZOTHIOPHENE FROM LIQUID PHASE BY ACTIVATED CARBONS

Conchi O. Ania and Teresa J. Bandosz

Chemistry Department
City College of New York, City University of New York
138th Street at Convent Avenue
New York, NY 10031

Introduction

Nowadays, deep desulfurization of fuels (gasoline and diesel fuels) receives increasing attention in the research community worldwide due to strict environmental regulations and fuel specifications. Recently, U.S. Environmental Protection Agency has issued regulations that require the refineries to drastically reduce the sulfur content of gasoline from a current average of 300 to 30 parts per million by weight (ppmw) by 2006, and the sulfur content of highway diesel fuel from a current limit of 500 to 15 ppmw by 2006[1,2].

Conventional deep hydrodesulfurization (HDS) technology faces an important challenge to meet the new regulations due to the difficulty of removing the most refractory sulfur compounds (thiophene, bibenzothiophene and their alkyl derivatives). Besides, sulfur compounds exist in the presence of large excess of aromatic hydrocarbons. Their concentration exceeds 20% in comparison with less than 1% wt for sulfur compounds. Thus, a major challenge is to meet sulfur new specifications along with the requirements of aromatics contents of the fuels.

The objective of this research is to investigate the possibility of an application of activated carbon for the removal of refractarious sulfur-containing compounds from fuels (gasoline and diesels), as a promising alternative to overcome the current industrial procedures' technological problems. The difficulty settles on finding an adsorbent that selectively adsorbs the sulfur compounds, but does not adsorb (or only weakly adsorb) the co-existing aromatic hydrocarbons and olefins. The adsorption capacity of activated carbons obtained from different precursors has been investigated for the removal of sulfur-containing compounds from liquid hydrocarbon solutions. Dibenzothiophene (DBT) was used as the model for the refractarious sulfur-containing compounds present in the fuels.

Experimental

Adsorbents. Four activated carbons were chosen for this study. They are: BX (Westvaco, wood-based, H_3PO_4 activation), BP (Calgon, bituminous coal-based, physical activation); PC (PET-waste derived, CO_2 activation); PS (pyrolysis of polystyrene sulfonic acid-co-maleic acid salts-derived carbon). The procedures for the preparation of both PC and PS have been described elewhere[3,4]. In order to increase the surface heterogeneity, BX and BP carbons were oxidized with $(NH_4)_2S_2O_8$ as follows. The sample was treated with a saturated solution of ammonium persulfate in 4 N sulfuric acid [ratio 1:10] and left overnight. The oxidized samples were washed with distilled water and dried at 373 K. These samples are denoted as BXS and BPS. Before the experiments, carbons were washed in a Soxhlet apparatus with distilled water. The carbons were then dried and the tests for adsorption from liquid phase were carried out.

Adsorption experiments. Adsorption of DBT was carried out at room temperature in a stirred batch system. Previous kinetic studies were performed to determine the equilibration time of the system. Different amounts of carbons (from 25 mg to 1 g) were weighed and added to 15 bottles containing 40 ml of the sulfur-containing solution with an initial concentration of 1000 ppmw. All of the solutions were prepared in hexane. The covered bottles were placed in a shaking bath and allowed to shake for 72 h at a constant temperature. After equilibration the concentration in the liquid was determined using a UV spectrophotometer at the corresponding wavelength. The amount adsorbed was calculated from the formula $q_e=V(C_o-C_e)/m$, where q_e is the amount adsorbed, V is the volume of the liquid phase, C_0 is the concentration of solute in the bulk phase before it comes in contact with the adsorbent, C_e is the concentration of the solute in the bulk phase at equilibrium, and m is the amount of the adsorbent.

Characterization Methods. Nitrogen adsorption isotherms were measured using an ASAP 2010 (Micromeritics) at -196 ºC. Before the experiment the samples were heated at 120 ºC and outgassed at this temperature under high vacuum for 24 h. The BET specific surface area, total pore volume and pore size distributions were evaluated from the nitrogen adsorption data. The pore size distributions and total pore volumes, V_t were calculated using density functional theory (DFT)[5]. A subdivision of microporosity was made: narrow microporosity (pore diameter < 0.7 nm), and medium-sized microporosity (0.7<pore diameter<2 nm).

Thermal analysis of the as-received and the exhausted carbons was carried out using a TA Instrument thermal analyzer. The instrument settings were as follows: heating rate 10 ºC min⁻¹ and a nitrogen atmosphere with 100 mL min⁻¹ flow rate. For each measurement about 25 mg of a ground carbon sample was used. Potentiometric titration measurements were performed with a DMS Titrino 716 automatic titrator. Approximately 0.100 g samples were placed in a container with 50 mL of 0.01 M $NaNO_3$ and equilibrated overnight. The carbon suspension was continuously stirred and to eliminate CO_2 interference, the suspension was maintained under N_2 atmosphere. 0.1 M NaOH was used as a titrant. Experiments were carried out in the pH range of 3-10[6].

Results and Discussion

The adsorptive capacity of low-ash content activated carbons obtained from polymeric precursors (PC and PS) for the removal of DBT from liquid hydrocarbon solution was compared with that of commercial carbons.

The pore structure of the carbons might be expected to play an important role in the process of adsorption of DBT from liquid phase. From nitrogen adsorption isotherms, the textural characteristic of the studied activated carbons were evaluated and they are summarized in Table 1.

**Table 1. Structural Parameters of the Non-modified Activated Carbons (S -m²/g; V- cm³/g)**

	S_{BET}	V_t	V_{nmic}	V_{mic}	V_{mes}
PC	1049	0.470	0.092	0.245	0.051
PS	1737	1.021	0.146	0.368	0.288
BPL	1540	0.853	0.051	0.366	0.292
BX	2271	1.518	0.072	0.431	0.765

It should be pointed out that the carbons studied have remarkable differences in their textural properties. For instance, BX has the largest BET surface area; however, its relative microporosity defined as the ratio of micropore volume to total pore volume is the lowest, indicating a high degree of structural heterogeneity. Indeed, this carbon has a significant contribution of mesopores. In contrast, the PS and PC samples showed a pore size distribution more in favor of micropores. In fact, PS has the lowest BET surface area and the highest relative microporosity. After oxidation with ammonium

persulfate, the surface areas and pore volumes slightly decreased. Some changes in the pore sizes were also observed, due to the creation of functional groups on the carbon surfaces.

Figure 1 shows the DBT adsorption isotherms on the as-received and oxidized carbons. It should be pointed out that the lowest adsorption capacity is attained for BP carbon, despite its relatively large surface area and total pore volume. In contrast, the PC sample showed a higher uptake than that of BP, despite its lowest surface area and total pore volume. The results suggest that the adsorption capacity is rather related to the pore size distribution than to the surface area. Thus the capacity was correlated with the volume of narrow micropores and a linear relationship was found.

In addition, the mesoporosity was found to affect the kinetics of the adsorption process. The declining trend of sulfur removal was significantly much faster for the carbons with a well-developed mesoporosity. This indicates that mesoporosity increases the adsorption rate of DBT on activated carbons.
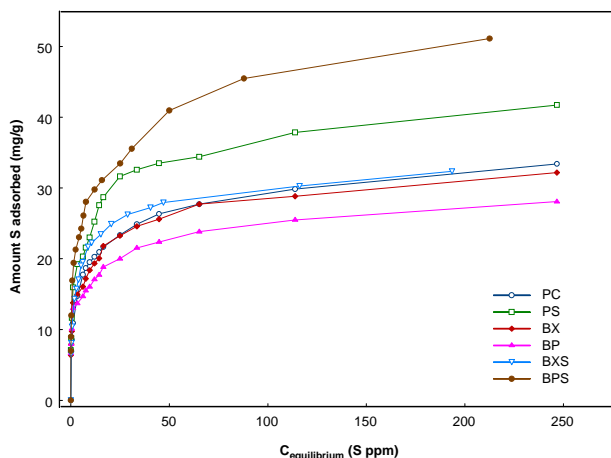
Figure 1. DBT adsorption isotherms from solution on the adsorbents studied.

The results show that the activated carbons chosen for this study are suitable for the removal of DBT from liquid solutions. Adsorptive capacities in the non-modified carbons are much larger than those reported in the literature for activated carbons and zeolites [7-11].

In addition, to exhibit a high adsorptive capacity and to be used in adsorption processes, the adsorbents have to satisfy the requirements concerning the selectivity in the removal of sulfur-containing compounds. Thus, the nature of the forces involved in the adsorption process of adsorption has to be clarified. To investigate these interactions, thermal analysis of the saturated activated carbons was carried out. The thermogravimetric profiles are shown in Figure 2. In all cases two peaks are observed. Since the first peak, centered at about 200 °C also appears for the equilibrated sample in the absence of DBT, it is assigned to the interaction of the solvent (hexane) with the carbons. The second peak appears at different temperatures for the carbons studied. In the case of PC and PS samples, this peak is centered at 515 °C. For BP and BX it is shifted to lower temperatures (i.e, 470 and 430 °C, respectively). These results suggested that the adsorption of DBT is most likely due to non-specific interactions between the adsorbate and the porous network of the carbons.
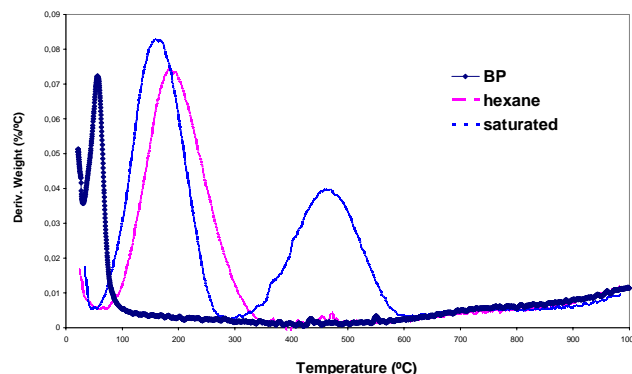
Figure 2. DTG profiles of the BP carbon before and after saturation with DBT in hexane solution.

The selectivity of the adsorption might be enhanced by increasing the surface heterogeneity of the carbons. For this purpose, BX and BP were oxidized with ammonium persulfate. This reagent is known to significantly increase the oxygen-containing functionalities of the activated carbon without altering noticeably its porous structure. The type and amount of surface functionalities created after oxidation was evaluated by potentiometric titration and Boehm method. The oxidation of the carbons resulted in a significant increase in the DBT adsorption capacity. This finding is linked to the increase in the number of acidic sites on the carbon surface. Introducing oxygen-containing groups increases the surface heterogeneity of the adsorbents and thus facilitates specific interactions between the adsorbent surface and the DBT molecule. These interactions were particularly enhanced in the case of BP carbon.

Conclusions

The results described above show the importance of activated carbon structural and chemical heterogeneity for the adsorption of DBT from liquid phase. While the volume of micropores governs the amount adsorbed, mesopores control the kinetics of the process. Introduction of surface functional groups enhances the amount adsorbed, likely as a result of specific oxygen-sulfur interactions.

References

1. US EPA, Control of Air Pollution from New Motor Vehicles Amendment to the Tier-2/Gasoline Sulfur Regulations, April, 2001.
2. US EPA, Reducing Non-road Diesel Emissions, April 2003.
3. Parra, J.B., Ania, C.O., Arenillas A., Pi.s, J.J., *J Stud. Surf. Sci. Catal.* **2002**, 144, 537.
4. Hines, D.H., Bagreev, A., Bandosz, T.J., *Langmuir*, **2004**, 20, 3388.
5. Olivier, J., *Carbon*, **1998**, 36, 1469.
6. Bandosz, T.J., Jagiello, J., Contescu, C., and Schwarz, J.A., *Carbon* **1993**, 31, 1193 (1993).
7. Jiang Z, Liu Y, Sun X, Tian F, Sun F, Liang C, You W, Han C, Li C., *Langmuir*, **2003**, 19 731.
8. Richardeau, D., Joly, G., Canaff, C., Magnoux, P., Guisnet, M., Thomas, M., Nicolaos, A., *Appl. Catal. A: General,* **2004**, 263, 49.
9. Hernandez-Maldonado, A.J., Yang, R.T., *Ind Eng Chem Res*., **2003**, 42, 3103.
10. Mikhail, S., Zaki, T., Khalil, L., *App. Catal. A: General*, **2002**, 227, 265.
11. Hernandez-Maldonado, A.J., Yang, R.T., *Ind Eng Chem Res.* **2003**, 42, 122.

ADSORPTION ISOTHERMS OF
AN IMIDAZOLINONE HERBICIDE
ON ACTIVATED CARBON

*Catherine Morlay[a], Michaela Pilshofer[a b], Etienne Quivet[b],
René Faure[b] and Jean-Pierre Joly[a]*

[a] Laboratoire d'Application de la Chimie à l'Environnement (UMR 5634), [b] Laboratoire des Sciences Analytiques (UMR 5180)
Université Claude Bernard Lyon 1
43 bd du 11 novembre 1918
69622 Villeurbanne Cedex, France

Introduction

According to the European Directive (CD 98/83/EC, dated on Nov 3, 1998)[1], the maximum concentration of individual pesticides in drinking water has to be lower than 0.1 µg l^{-1} and the total concentration for all pesticide species should not exceed 0.5 µg l^{-1}. These requirements could be achieved using activated carbon in the drinking water production process.

The studied pesticide is Imazamox {2-[4,5-dihydro-4-methyl-4-(1-methylethyl)-5-oxo-1$\underline{H}$-imidazol-2-yl]-5-(methoxymethyl)-3-pyridinecarboxylic acid ; $C_{15}H_{19}N_3O_4$; Mw = 305.3 g mol^{-1}}, an herbicide which belongs to the family of imidazolinones. This new class of pesticides is used to control a wide spectrum of broad-leaf weeds and grasses.

The activated carbon chosen for this study is Filtrasorb 400 (F400), a Chemviron Carbon product widely used for drinking water production and specially recommended to remove organic micropollutants, such as pesticides, from water.

Many factors may influence the adsorption phenomenon taking place in aqueous medium. Generally speaking, adsorption depends on both the speciation of the adsorbate (i.e. the distribution in its different chemical forms in aqueous solution) and the adsorbent characteristics (texture and surface chemistry)[2].

In this work, we determined the adsorption isotherms of Imazamox from aqueous solution onto F400 varying the pH and the ionic strength of the aqueous solution in order to get an insight into the mechanism of adsorption of this pesticide.

Experimental

Materials. Activated carbon F400 is produced from bituminous coal and is steam activated. Granular F400 was crushed and the particle size of the resulting powder (PAC) was lower than 50 µm. Powdered F400 was dried in an oven before weighting (130 °C ; 24 hours ; under air).

The technical product Imazamox (Technical RAPTOR®, purity ≥ 95.9 %) was purified by dissolution in ultra pure water, filtration and recrystallization. A final drying was carried out in an oven at 100 °C for 1 hour. The purified pesticide as well as its 250 mg l^{-1} (8.2 x 10^{-4} mol l^{-}) stock solution were kept in stopped flasks at 6 °C. The diluted solutions of purified Imazamox were prepared just before use.

Imazamox molecule contains four centers that can be protonated according to the pH of the solution. These centers are the three nitrogen atoms and the carboxylic acid function. **Figure 1** shows the structure of Imazamox (H$_2$L) and the acid-base equilibria leading to the cationic forms H$_3$L$^+$ and H$_4$L^{2+} or to the anionic forms HL$^-$ and L^{2-}. We propose the scheme shown in **Figure 1** for Imazamox by analogy with that given by Duda *et al.*[3] for Imazapyr, another herbicide belonging to the family of imidazolinones. The pK$_a$ values of Imazamox[4] are reported in **Figure 1**.
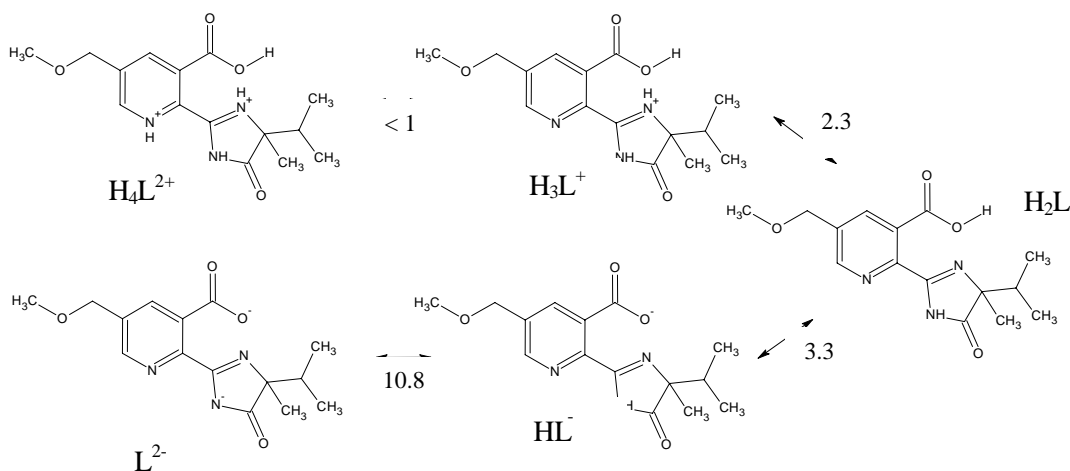
Figure 1. Imazamox successive protonation - deprotonation equilibria.

F400 textural characterisation. Nitrogen physisorption isotherm of F400 was determined at 77 K. Total surface area, external surface area, total pore volume (V_{tot}), microporous volume ($V_{\mu pores}$) and the mean pore size (L_0) were determined by means of BET theory, α_S method, the amount of N$_2$ adsorbed at P/P$_0$ = 0.995, DR method and Dubinin-Stoeckli formula, respectively.

Analyses of aqueous solutions. Imazamox concentrations were determined using liquid chromatography. A Chrompack Omnispher C 18 column preceded by a Chromosep pre-column was used in the isocratic elution mode with the mixture ultra pure water at pH = 3.0 ± 0.1 (H$_3$PO$_4$)/acetonitrile at 70/30 (v/v) as an eluent. UV detection wavelength was 250 nm.

Adsorption procedure. Experiments were carried out at 25 °C in static conditions. The suspensions of 10 mg of PAC in 25 ml of Imazamox solutions were stirred for 24 hours. We previously checked that this time was sufficient to reach equilibrium. The suspensions were membrane filtered before analysis.

Three types of experiments were performed : i) Imazamox solutions containing 0.05 or 0.25 mol l^{-1} NaNO$_3$ were used in order to study the influence of the ionic strength of the aqueous medium on adsorption at free pH (initial pH : 3.5-6.4), ii) Imazamox solutions containing 0.05 mol l^{-1} HNO$_3$ (ionic strength = 0.05 mol l^{-1}) were used in order to study the influence of the acidification of the aqueous medium on adsorption (equilibrium pH = 1.4), iii) starting from solutions having a constant initial concentration of

Imazamox (100 mg l^{-1}, i.e. 3.3 x 10^{-4} mol l^{-1}) and containing 0.05 mol l^{-1} NaNO$_3$, the equilibrium pH of the suspensions was imposed using microadditions of HNO$_3$ (the final ionic strength of the samples was always much lower than 0.25 mol l^{-1}).
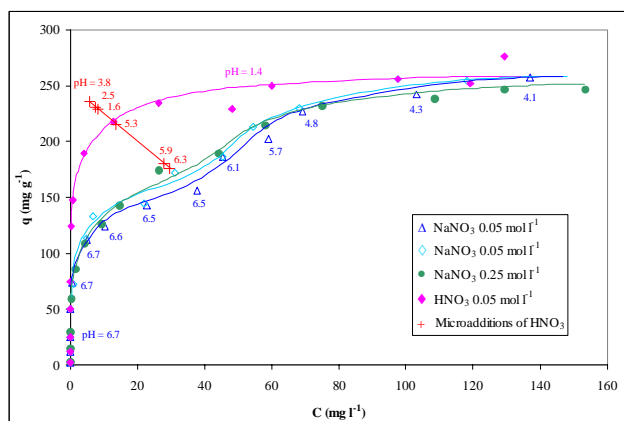
Results

F400 characterisation. Table 1 presents F400 textural characteristics. F400 pH of the point of zero charge (pH$_{PZC}$), determined by Noh and Schwarz's method[5], is equal to 10.3.

Table 1. Textural characteristics of F400.

BET surface area (m^2/g)	External surface area (m^2/g)	V$_{tot}$ (cm^3/g)	V$_{\mu pores}$ (cm^3/g)	L$_0$ (nm)
1010	112	0.57	0.37	1.0

Imazamox isotherms. Figure 2 gathers all the adsorption results obtained in the various experimental conditions described above. The isotherms obtained at free pH for different ionic strengths are close to each other in the whole concentration range considered ; we can thus conclude that varying the ionic strength of the solution in the range 0.05-0.25 mol l^{-1} has a negligible effect on Imazamox uptake by F400. During adsorption, an increase of the pH of the solutions was observed (equilibrium pH in the range 4.1-6.7). In contrast, imposing a very acidic pH with HNO$_3$ (pH = 1.4) lead to a much higher adsorption isotherm for the lower and intermediate Imazamox concentrations.

Figure 2. Adsorption isotherms of Imazamox on F400 and influence of equilibrium pH on Imazamox uptake (+).

Discussion

Generally speaking, the adsorption in liquid phase results from an interplay of electrostatic and non electrostatic interactions between species in solution and carbon surface[2]. However, the fact that adsorption do not depend on ionic strength of the solution suggests that the adsorption of Imazamox does not involve ionic species.

In addition, it must be kept in mind that, for all the experiments described above, the equilibrium pH we measured were lower than 7. Thus, the neat charge of the carbon surface was positive (solution equilibrium pH < pH$_{PZC}$ = 10.3).

Furthermore, for experiments carried out at free solution pH (Exp. Cond i)), this pH was in the range 4.1-6.7 and consequently, considering Imazamox speciation (**Figure 3**), the neutral (H$_2$L) and anionic (HL$^-$) forms coexisted in solution, the anionic form being the preponderant one (pK H$_2$L/HL$^-$ = 3.3). At this point, the possibility of an anionic adsorption of HL$^-$ on the positive surface of the carbon could be possibly considered. However we verified

that an imposed decrease of solution pH down to about 3 (Exp. Cond. iii)), which favours the neutral form H$_2$L, strongly increased Imazamox adsorption (**Figures 3** and **4**). Thus, an anionic adsorption is not likely.

On the other hand, when the pH of the solution was maintained constant and equal to 1.4 by means of nitric acid (Exp. Cond. ii)) the neutral (H$_2$L) and cationic (H$_3$L$^+$) forms of Imazamox coexisted in the solution, the cationic form being the preponderant one (pK H$_3$L$^+$/H$_2$L = 2.3). Nevertheless, the assumption of H$_3$L$^+$ species adsorption on the positive surface of the carbon should be discarded. Finally, we verified (Exp. Cond. iii)) that adsorption was maximum in the pH range 2.3-3.3, where the neutral form is preponderant in solution (**Figures 3** and **4**). All these observations confirm that the neutral form H$_2$L is responsible for Imazamox adsorption. A so-called $\pi-\pi$ mechanism[2] is likely in these circumstances.
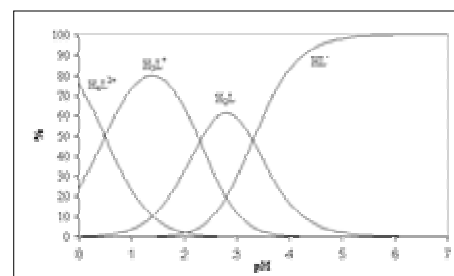
Figure 3. Distribution curves of the different forms of Imazamox in aqueous solution.
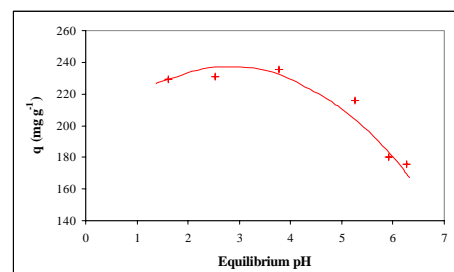
Figure 4. Imazamox uptake by F400 versus equilibrium pH (Imazamox initial concentration : 100 mg l^{-1}).

References
(1) Council Directive 98/83/EC. Directive on the quality of water intended for human consumption. Official Journal of the European Communities L 330/32. 3.11.**1998**.
(2) Radovic, L.R.; Moreno-Castilla, C.; Rivera-Utrilla, J., In: *Chemistry and Physics of Carbon*; Radovic, L.R. Ed.; Marcel Dekker: New York, 2000; pp. 227-405.
(3) Duda, A.M.; Dyba, M.; Kozlowski H.; Micera, G.; Pusino, A., *J. Agric. Food Chem.,* **1996**, *44*, 3698-702.
(4) United States Environmental Protection Agency, Office of Prevention, Pesticides and Toxic Substances, Pesticide Fact Sheet – Imazamox (Raptor herbicide) 22.05.**1997**.
(5) Noh, J.S.; Schwarz, J.A., *J. Colloid Interface Sci.*, **1989**, *130*, 157-64.

HIGH PERFORMANCE CARBON MONOLITHS

Krisztina László[a], György Onyestyák[b], Erik Geissler[c]

[a] Department of Physical Chemistry, Budapest University of Technology and Economics, Budapest, Hungary, H-1521
[b] Institute of Surface Chemistry and Catalysis, Chemical Research Center, Hungarian Academy of Sciences, H-1525 Budapest
[c] Laboratoire de Spectrométrie Physique UMR 5588 CNRS-Université J. Fourier de Grenoble, BP 87, 38402 St Martin d'Hères cedex, France

Introduction

Carbon adsorbent materials are of paramount importance in environmental technology, from gas purification and separation to gas storage or catalyst supports. These processes rely on specific pore size distributions that contribute to selective adsorption *via* size exclusion.

Recently a novel type of carbon adsorbent has appeared, the carbon molecular sieve (CMS). In these systems, a narrow distribution of pore sizes, several tenths of a nanometre in width, yields selective adsorption properties that depend on the close match between the pores and the probe gases to be adsorbed. A CMS is just like a kinetic adsorbent that separates, for example, nitrogen from air by distinguishing the minute size difference between O_2 and N_2 through faster sorption of oxygen. For dynamic processes where flow resistance must be minimized, special geometrical configurations must also be taken into account in addition to the nanoscale structure. This paper investigates one such superstructured carbon.

Lignocellulosic materials are well known carbon precursors[1,2], but few reports are concerned with their use in monolith form. The macro- and mesoporous texture of activated carbons of lignocellulosic origin conserves the features of the precursor, i.e. the skeleton of the plants used. Since both the nature of the starting material and the preparation process are crucial in determining the porous structure of the resulting monolith, it is possible by appropriate combination of raw material and processing to tailor porosities for specific applications. Clearly, for mass production of carbon adsorbents these technical considerations are also constrained by concerns of manufacturing costs.

The open channel structure, with a typical cross-section of several hundred μm^2 and wall thickness about 3 μm, offers the possibility of fast gas transport with low resistance to diffusion. Moreover, the channel walls can be converted to carbon of high adsorption capacity. The presence of this type of combined micro- and macroporosity makes these materials prime candidates for gas separation and/or catalyst supports.

We study wooden monolith samples prepared by a simple one-step physical method from *Pinus sylvestris*.

Experimental

Cubes of scotch fir (*Pinus sylvestris*) wood, of edge 10 mm, were carbonized in nitrogen flow at different temperatures between 600 °C and 1000 °C for 60 minutes. The samples are denoted PS600 through PS1000.
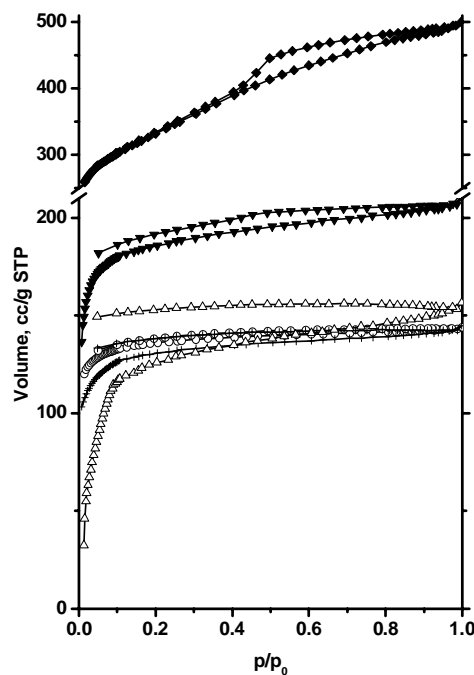
Nitrogen adsorption/desorption isotherms were measured at 77 K, using a Quantachrome Autosorb-1 computer controlled apparatus. The apparent surface area S_{BET} was derived according to the BET model. Micropore and mesopore analysis was performed by the Quantachrome software using the Horváth-Kawazoe (HK) and the Barrett, Joyner and Halenda (BJH) methods, respectively. The true density of the carbon samples (d_{He}) was determined by helium pycnometry using the AUTOSORB-1 instrument. The total pore volume (V_{tot}) was calculated from the amount of nitrogen vapour adsorbed at a relative pressure close to unity.

The transport dynamics of N_2 and O_2 were investigated by batch-type frequency response (FR) technique, as described in Ref. 3, at 195 K in the pressure range 60 – 600 Pa and in the frequency range 0.001 – 10 Hz.

Small angle X-ray scattering (SAXS) measurements were made at the BM2 beam line at the European Synchrotron Radiation Facility in Grenoble. Two incident energies were used, 8 keV and 18 keV, with sample‑detector distances between 23 cm and 1.85 m.

Results and Discussion

The low temperature nitrogen isotherms of the carbonized wooden cubes are shown in Fig. 1. PS600 and PS700 exhibit typical Type I microporous behaviour. PS900, in contrast, shows a slight slope, marking the appearance of mesoporosity. PS700, PS800 and PS900 display low pressure hysteresis (LPH), indicative of very narrow pores. In PS800 the LPH effect is strongest, revealing that this sample is in an intermediate state. The 1000°C treatment yields well developed micro- and mesoporosity, as can be concluded from the Type IV shape of the isotherm. The Type H2 hysteresis loop of PS1000 is commonly assigned to systems having ill-defined pore structure[4]. A sudden increase in specific surface area and pore volume associated with this sample can be attributed to a combined self-activation and chemical vapour deposition (CVD) process: in spite of the inert atmosphere, oxygen-containing degradation products operate as activating agents and contribute to the development of the porosity. Meanwhile, some of the degradation products may deposit on the pore walls, thus enhancing the microporosity of this carbon[5]. This complex effect resulted in a monotonic increase both of the slit width and surface area.

Figure 1. N_2 adsorption isotherms of the carbon samples (77 K). O: PS600, +: PS700, △: PS800, ▼: PS900, ◆: PS1000.

SAXS measurements were made with the samples oriented in two directions, with the incident beam respectively parallel and perpendicular to the channel axis in the specimen. Figure 2 shows a set of iso-intensity contours from the scattering patterns of PS700 at low and at high values of the wave vector q. At large values of q (Figure 2b & d), the iso-intensity contours become circular, i.e., the

scattering is isotropic at large angles. The other samples yielded qualitatively similar patterns.

a)   b)

c)   d)
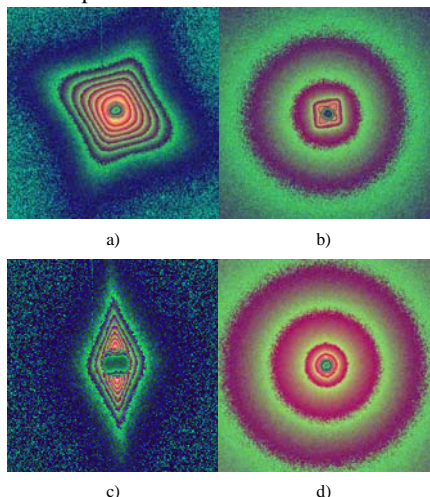
Figure 2. 2-dimensional SAXS patterns from sample PS700 with the channel axis parallel ($I_\parallel$) and perpendicular ($I_\perp$) to the incident X-ray beam; a: $I_\parallel$ at low q (1.85 m, 8keV), b: $I_\parallel$ at large q (0.23m, 18 keV), c: $I_\perp$ at low q (1.85 m, 8keV), d: $I_\perp$ at large q (0.23m, 18 keV).

Measurements of the Guinier radius of gyration R_G (Table 1) obtained from the azimuthally averaged scattering curves are found to be the same in the parallel and perpendicular directions, indicating that structural anisotropy at this length scale is small or nonexistent. The smallest characteristic size was found in PS700. The X-ray surface area S_X is estimated using the Porod procedure[6]. In all samples it was found that at high q the X-ray response can be approximated by $I(q) = Kq^{-4} + b$, where K is the final slope of the intensity and b describes scattering from atomic disorder. The intensity measured in the parallel and perpendicular directions $I_\parallel(q)$ and $I_\perp(q)$ is not identical. Since the scattering from atomic disorder is isotropic, the integrated intensities $Q = \int_0^\infty (I(q)-b)q^2 dq$ in the two directions can be normalized by the corresponding values $b_{\parallel}$ and $b_\perp$. The specific surface areas in the two directions are

$$S_{\parallel X} = \frac{\pi V_{tot}}{1+V_{tot}d_{He}}\left[\frac{3K_\parallel}{Q_\parallel + 2b_\parallel Q_\perp / b_\perp}\right], S_{\perp X} = \frac{\pi V_{tot}}{1+V_{tot}d_{He}}\left[\frac{3K_\perp}{b_\perp Q_\parallel / b_\parallel + 2Q_\perp}\right]$$

Table 1. Selected data from adsorption and X-ray measurements

Sample	S_{BET} (m²/g)	V_{tot} (cm³/g)	$R_{G\parallel}$ (nm)	$R_{G\perp}$ (nm)	$S_{\parallel X}$ (m²/g)	$S_{\perp X}$ (m²/g)	w_X (nm)
PS700	468	0.224	0.41	0.40	1380	1320	0.33
PS800	496	0.242	0.45	0.44	1310	1190	0.39
PS900	660	0.325	0.48	0.47	1270	1310	0.50
PS1000	1152	0.774	0.48	0.48	2380	2300	0.66

The results show that the specific surface area increases significantly with increasing temperature of treatment. Analogous differences between S_{BET} and S_X have been observed previously on activated carbons[7] and were attributed on the one hand to the simplifying assumptions of the BET model, which requires a smooth surface and single layer coverage, and on the other hand to the kinetic hindrance of the low temperature nitrogen molecules in narrow pores. The ratio S_{BET}/S_X tends to a constant value at high temperature, indicating that the population of pores that are inaccessible to nitrogen

diminishes with increasing temperature of treatment. This result is in agreement with the increasing pore size $w_X = V_{tot}/S_X$ listed in Table 1.

Table 2. Relaxation rates deduced from the FR measurements

Sample	$1/\tau$ (s⁻¹)	
	O_2	N_2
PS600	0.076	0.027
PS700	0.019	0.004
PS800	not detectable	
PS900	not detectable	
PS1000	0.095	0.080

Table 2 shows the FR results on three samples, PS600, PS700 and PS1000, in the presence of nitrogen and oxygen gas[8]. The selectivity, i.e., the ratio of oxygen/nitrogen adsorption rates, in favour of oxygen is most pronounced for the sample prepared at 700°C. In PS1000 the oxygen adsorption rate increases by a factor of 5 but selectivity with respect to nitrogen is practically lost. (For the intermediate temperatures the response rates lay outside the observable frequency range.) These findings are consistent with the SAXS and gas adsorption results, which show an increase in the pore size with increasing temperature of treatment.

As commercially available CMSs show selectivity ratios varying between 1.2 and 24, the *Pinus sylvestris* monolith PS700 emerges as a highly promising candidate for air separation[9].

Conclusions

Carbon monoliths, prepared by heating wood from *Pinus sylvestris* in a nitrogen atmosphere to temperatures T from 600°C to 1000°C, display a surface area that increases with increasing T. Below 900°C the system is essentially microporous, but at 1000 °C, pronounced micro- and mesoporosity are observed. S_X is isotropic, while the ratio S_{BET}/S_X increases from about 1/3 in the 700 °C treatment to about 1/2 at the two highest temperatures, 900°C and 1000°C, as a result of the increase in pore size with increasing T, while the ratio of microporosity diminishes by about 30%. The FR measurements show that strongly selective properties for oxygen/nitrogen mixtures are achieved with the PS700 sample.

References
(1) Hoinkis, E. In *Chemistry and Physics of Carbon;* vol 25, Thrower, P.A., Ed.; Dekker: New York, 1997; pp. 71-241.
(2) Calo, J.M.; Baker, F.S.; Hall, P.J. *Carbon 2004*, Providence (RI USA) July 2004, G032.
(3) Rees, L.V.C.; Shen, D. *Gas Sep. Purif.* **1993**,*7*,83.
(4) Gregg, S.J.; Sing, K.S. *Adsorption, Surface Area and Porosity*; Academic Press: London, 1982.
(5) Howard, H.; Hulett, G.J. *Chem. Phys.* **1924**,*28*,1082.
(6) Porod, G. In *Small Angle X-ray Scattering*;. Kratky, O.; Glatter, O. Eds.; Academic Press, 1983.
(7) László, K.; Marthi, K.; Rochas, C.; Ehrburger-Dolle, F.; Livet, F.; Geissler, E. Langmuir **2004**,*20*,1321.
(8) Onyestyák, G.; László, K.; Rees, L.V.C. *Helv. Chim. Acta* **2004**,*87*,1888.
(9) Shen, D.; Bülow, M.; Lemcoff, N.O. *Adsorption* **2003**,*9*,295.

CONTROLLING THE HIERARCHICAL PORE STRUCTURE OF RESORCINOL-FORMALDEHYDE CARBON CRYOGEL MICROHONEYCOMBS

Shin R. Mukai, Hirotomo Nishihara, Takashi Yoshida,
Ken-ichi Taniguchi, and Hajime Tamon

Department of Chemical Engineering
Kyoto University
Katsura, Nishikyo-ku
Kyoto, 615-8510, Japan

Introduction

Carbon gels[1] are unique porous carbons with high surface areas and large mesopore volumes. They can be synthesized through the carbonization of precursor organic gels. Carbon gels derived from resorcinol-formaldehyde are called RF carbon gels and their micro/mesoporosity is known to be controllable by changing the composition of their precursor sols, especially the concentration of the catalyst.[2-4] From their unique properties, RF carbon gels are expected to be used for various purposes such as gas filters, electrodes for capacitors, catalyst supports, and stationary phases for HPLC.

Recently, we developed a new processing method, ice-templating method, for the preparation of ordered macroporous materials using sol-gel transformation.[5,6] When precursor hydrogels are unidirectionally frozen at a fairly constant rate under a fairly constant thermal gradient, pseudosteady state growth of ice crystals occurs inside their matrices. The ice crystals are micro-rods with polygonal cross-sections and constant diameters throughout their length. Such micro-rods are regularly aligned parallel to the freezing direction, and play the role of a template. Therefore, a microhoneycomb morphology is formed at this freezing stage. After removal of the ice crystals by thawing and drying, organic/inorganic gel microhoneycombs with micro/mesopores inside their honeycomb walls can be obtained. We have succeeded in preparing carbon cryogel microhoneycombs (CMHs) by applying this new method to RF hydrogels.[6]

In this work, we show the relationship between the preparation conditions and the morphology of the resulting RF cryogels, and describe how to prepare fine CMHs. We also describe how to control the macroporosity of CMHs along with the micro/mesoporosity inside their honeycomb walls.

Experimental

Sample Preparation. RF hydrogels were prepared by the sol-gel polymerization of resorcinol (R) with formaldehyde (F) using sodium carbonate (C) as a basic catalyst and distilled water (W) as a diluent. The ratios of resorcinol to water (g/cm^3; R/W) and resorcinol to formaldehyde (mol/mol; R/F) were fixed to 0.2 and 0.5, respectively. The ratio of resorcinol to catalyst (mol/mol; R/C) was varied in order to change the catalyst concentration, which mainly determines the rates of sol-gel polymerization and the micro/mesoporosity of the RF carbon cryogels.

Mixtures of these reagents were stirred to obtain homogeneous solutions, and were cast into glass molds (i.d.: 4.0 mm, L: 100 mm). They were cured at 25 ℃, and after sol-gel transformation occurred, the gelled samples were further cured at the same temperature. Note that the curing time before sol-gel transformation is defined as gelation time, t_{gel}, and that after sol-gel transformation at 25 ℃ is denoted as t_{age}, hereafter. The resulting transparent RF hydrogels were washed five times with distilled water and placed into polypropylene tubes, which were filled with distilled water. Then they were unidirectionally frozen by dipping the tubes perpendicularly into a cold bath maintained at a constant temperature of T_f at a constant rate of v_f. After the samples were completely frozen, they were thawed at 50 ℃. Then the samples were washed with *t*-butanol and freeze-dried, yielding RF cryogel microhoneycombs (RFMHs).

In the preparation of RF gels, curing is usually conducted at high temperatures for a sufficient time in order to develop mesopores inside them. However, in the ice-templating method, short curing periods are required to obtain a microhoneycomb morphology. Therefore, hydrothermal treatments of the thawed samples were conducted in order to develop mesopores inside the samples. The thawed samples were immersed into deionized and distilled water for a designated period of t_{hyd} at 90 ℃. RFMHs were converted to CMHs through carbonization at 1000 ℃ for 4 h in a N_2 flow.

Characterization Methods. The morphology of the obtained samples was directly observed using a scanning electron microscope (JEOL Japan Inc.; JSM-6340FS), and the average macropore sizes (d_{mac}) of CMHs were estimated from the obtained images.

The micro/mesoporosity of CMHs was examined through nitrogen adsorption-desorption measurements conducted at -196 ℃. BET surface areas, S_{BET}, were calculated through the Brunauer-Emmett-Teller (BET) method. Mesopore size distributions and mesopore volumes, V_{mes}, were calculated by applying the Dollimore-Heal method to the obtained desorption isotherms.

Results and Discussion

The morphology, which is formed at the ice-templating stage, changed from microhoneycomb to polygonal fiber depending on the degree in sol-gel polymerization of the precursor RF hydrogel. When t_{age} was short and the precursor RF hydrogel had a relatively soft structure, a fine microhoneycomb morphology was formed (Fig. 1 a, b). On the other hand, when t_{age} was long and the precursor RF hydrogel became firm by thorough aging, independent polygonal fibers were formed (Fig. 2 a, b). The same dependency of morphology on precursor firmness was also observed in SiO_2 systems[5].
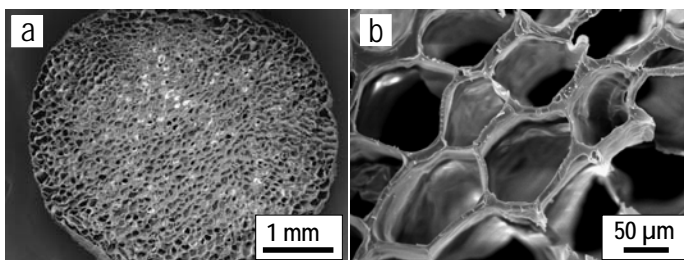

Figure 1. SEM micrographs of a typical CMH obtained in this work

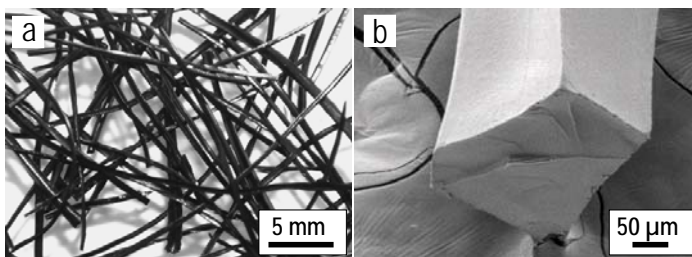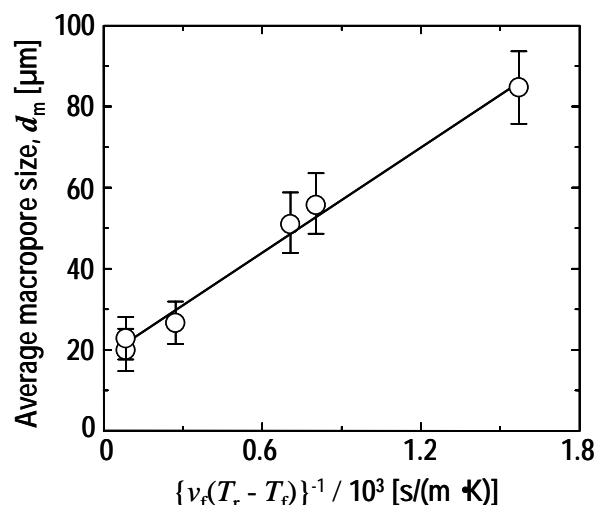**Figure 2.** Photograph (a) and SEM micrograph (b) of typical carbon cryogel fibers obtained in this work

**Figure 3.** Relationship between macropore size and freezing parameter, $\{v_f(T_r - T_f)\}^{-1}$

Figure 4. N_2 adsorption-desorption isotherms of typical CMHs with and without hydrothermal treatment(C/W = 3.6)

It was observed that the macropore sizes (cell sizes) of the CMHs changes when freezing conditions, such as the dipping rate, v_f, and the freezing temperature, T_f, were varied. The macropore size, which reflects the diameter of the template ice-rods, became smaller with the increase in v_f and with the decrease in T_f. In the case of fiber production using unidirectional freezing, the diameters of fibers (d_f) can be related to the freezing rate and the thermal gradient (G) by the equation $d_f = a\{v_f G\}^{-1} + b$, where a and b are constants[7]. By assuming that fiber production and microhoneycomb production are analogous, we plotted the average macropore sizes (d_m) of CMHs against $\{v_f(T_r - T_f)\}^{-1}$ (T_r: room temperature) as shown in Fig. 3. It can be seen that d_m can be related to $\{v_f(T_r - T_f)\}^{-1}$ by the equation $d_m = a\{v_f(T_r - T_f)\}^{-1} + b$. Interestingly, CMHs which were prepared from the same parent gel under different freezing conditions showed identical nitrogen adsorption-desorption isotherms. Therefore, it can be said that these CMHs have different macroporosity and the same micro/mesoporosity. This indicates that it is possible to control the macroporosity of CMHs independently of their micro/mesoporosity by changing the freezing parameter, $\{v_f(T_r - T_f)\}^{-1}$.

CMHs have controllable macropores and walls formed by RF carbon cryogels, which contain developed micro/mesopores. Therefore, CMHs are expected to be used as a porous carbon with a hierarchical pore system of controllable micro-, meso-, and macropores. In order to control the micro/mesoporosity of CMHs, we used hydrothermal treatment after thawing, which is an effective method to develop the mesoporosity of CMHs. It was found that by applying hydrothermal treatment after thawing, the microporosity decreased and mesoporosity increased. The nitrogen adsorption-desorption isotherms and mesopore size distributions of CMHs prepared at C/W = 3.6 are compared in Fig. 4 and Fig. 5, respectively. It can be seen that after sufficiently long hydrothermal treatment, the isotherm becomes a typical type IV isotherm, which shows the developed mesoporosity of the sample. As this hydrothermal treatment was conducted after thawing, the macropore size of the CMH has already been fixed. Therefore, this indicates that it is possible to control the micro/mesoporosity of CMHs independently of their macroporosity by hydrothermal treatment.
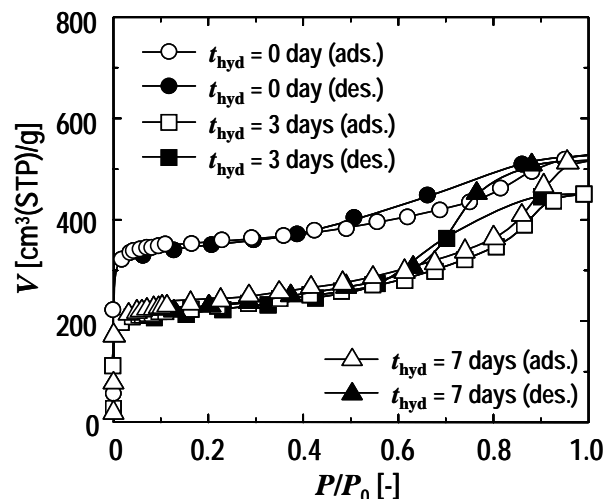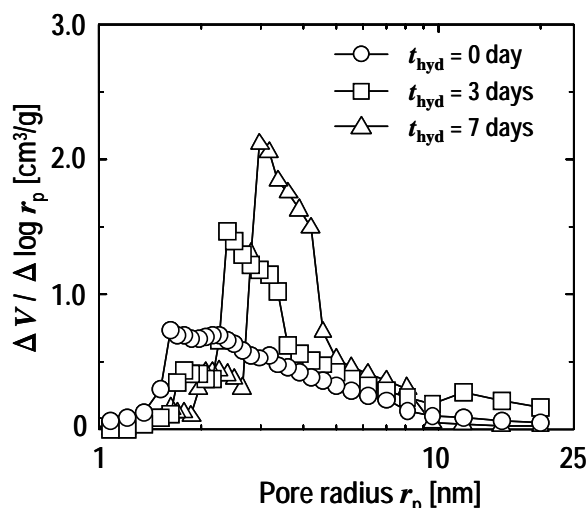
Figure 5. Mesopore size distributions of typical CMHs with and without hydrothermal treatment (C/W = 3.6)

References
(1) Al-Muhtaseb, S. A,; Ritter, J. A.. *Adv. Mater.* **2003**, 15, 101.
(2) Pekala, R. W.; Schaefer, D. W. *Macromolecules* **1993**, 26, 5487.
(3) Tamon, H.; Ishizaka, H.; Mikami, M.; Okazaki, M. *Carbon* **1997**, 35, 791.
(4) Yamamoto, T.; Nishimura, T.; Suzuki, T.; Tamon, H. *J. Non-Cryst. Sol.* **2001**, 288, 46.
(5) Mukai, S. R.; Nishihara, H.; Tamon, H. *Chem. Commun.* **2004**, 7, 874.
(6) Nishihara, H.; Mukai, S. R.; Tamon, H. *Carbon* **2004**, 42, 899.
(7) Maki, T.; Teranishi, Y.; Kokubo, T.; Sakka, S. *Yogho-kyokai-shi* **1985**, 93, 387.

ADSORPTION OF BTX ON MSC5A IN SUPERCRITICAL CO2, EXPERIMENT WITH MOLECULAR SIMULATION

Kazuyuki Chihara, Ryota Suzuki, Naoki Omi, Yusuke Inoue

Department of Industrial Chemistry,
Meiji University,
1-1-1 Higashi-mita, Tama-ku, Kawasaki, 214-8571, JAPAN

Introduction

Supercritical CO_2 fluid is attractive solvent whose solubility of organics can be changed with changes of pressure and temperature. New process of adsorptive separation using supercritical fluid might be possible since removal of adsorbate from adsorbent can be performed efficiently. On the other hand molecular simulation is now attracting much attention as a powerful means of understanding and estimating adsorption phenomena, i.e., adsorption equilibria and adsorption dynamics in microporous adsorbents.

In this study, chromatographic measurements were made for the adsorption of benzene, toluene and m-xylene on molecular sieving carbon (MSC) in supercritical fluid CO_2. Supercritical chromatograph packed with MSC was used to detect pulse responses of organics. Adsorption equilibria and adsorption dynamics for organics were obtained by moment analysis of the response peaks. Dependences of adsorption equilibrium constants, K*, and micropore diffusivity, D, on the amount adsorbed were examined. And, molecular simulation of multicomponent adsorption equilibria was performed, and potential parameters were determined by comparing the simulation with experimental results.

Experimental

The experimental apparatus (Super 200-type 3; Japan Spectroscopic Co., LTD) was supercritical chromatograph. The carrier fluid of the chromatograph was supercritical CO_2 (critical temperature 304K, critical pressure 7.3 MPa) and it's mixture with the above-stated organics (benzene, toluene or m-xylene) respectively. The adsorbates used in the form of pulse were the same of or the different from organics mixed with supercritical CO_2. For example, in the case of CO_2 mixed with benzene, the organic used in the form of pulse was benzene or, toluene or m-xylene. The volumes of the pulse were fixed to be $8 \times 10^{-9} m^3$ as liquid. MSC 5A (Takeda chemicals Co., HGK882.) was crushed and screened to obtain particle size between 1.49×10^{-4} - $1.77 \times 10^{-4} m$ (an average particle radius of 8.12×10^{-5} m). $4.82 \times 10^{-4} kg$ of these particles were packed into the chromatographic column of 5×10^{-2} m long and 4.6×10^{-3} m in diameter. The void fraction, ε, of the bed was determined to be 0.355. The properties of MSC5A are shown in Table 1 in reference (Chihara et al. 1978). Flow rate of supercritical CO_2 was $1.33 \times 10^{-7} m^3/s$ at 268K and at 15.0, 20.0 and 25.0MPa respectively and flow rate of adsorbate (benzene, toluene or m-xylene) was $1.67 \times 10^{-10} m^3/s$, 5.00×10^{-10} m^3/s and 1.00×10^{-9} m^3/s as liquid at room temperature (298K). The column pressure was kept at 15.0, 20.0 and 25.0 MPa respectively. The pressure drop across the adsorbent bed was estimated to be about 0.1Mpa and was assumed to be negligible. The experimental column temperature was kept at 313, 333 and 353 K respectively. Before experimental runs started, the adsorbent particles were regenerated and stabilized by feeding pure CO_2 for 2 hours at the experimental pressure and temperature. Pulse responses were detected using a multi-wave length UV detector (Multi-340; Japan Spectroscopic Co., LTD.) (195-350 nm). Response data were processed by a personal computer.Moment analysis of supercritical fluid chromatogram was tried, and the apparent adsorption equilibrium constant, K* and time constant of micropore diffusivity, D/a^2 obtained from first and second moment of response peak, as in references (Chihara et al. 1978; Chihara et al. 1993; Chihara et al. 1995).

Results and Discussion

Figure 1 shows adsorption isotherm of benzene at 313K. According to Fig.1, the amount adsorbed increased with increases of molarity of benzene, and reached to saturation. The amounts adsorbed became larger with decreases of column pressure. It was considered that the situation is competitive adsorption and amount adsorbed of toluene decreases as CO_2 adsorption increase with increases of column pressure.

Figure 2 shows dependency of adsorption equilibrium constants, K*, for benzene, toluene, and m-xylene on amount adsorbed of benzene at 20Mpa. This is reasonably decreasing, which corresponds to Fig.1.
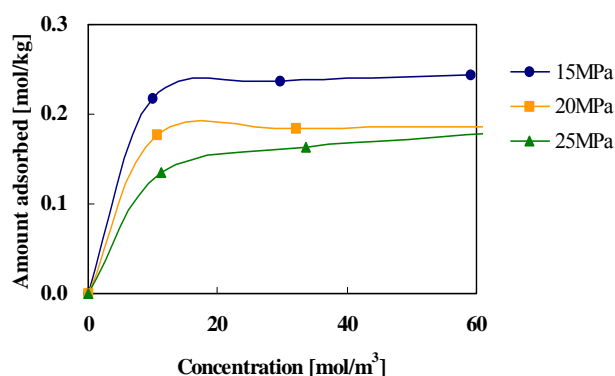

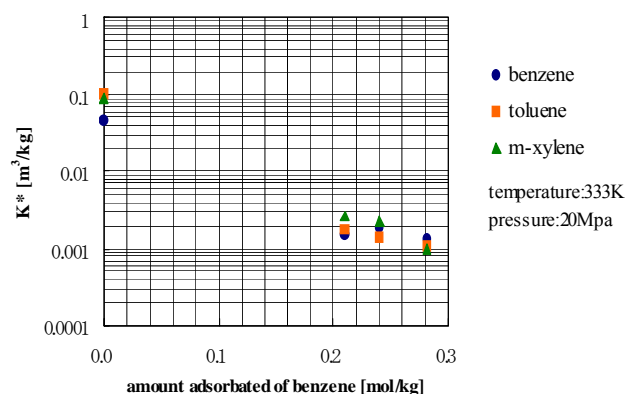**Figure 1**. Adsorption isotherm : benzene at 313K

Figure 2. Dependencies of K* on the amount adsorbed of benzene

Figure 3 shows dependency of micropore diffusivity, $D/\bar{a}^2 \exp(\sigma^2)$, for benzene, toluene, and m-xylene on amount adsorbed of benzene at 20MPa. The increase of $D/\bar{a}^2 \exp(\sigma^2)$ for benzene could be reasonably explained by chemical potential driving force. However, as for dependency of $D/\bar{a}^2 \exp(\sigma^2)$ of toluene and m-xylene on amount adsorbed of benzene, further discussion would be necessary.
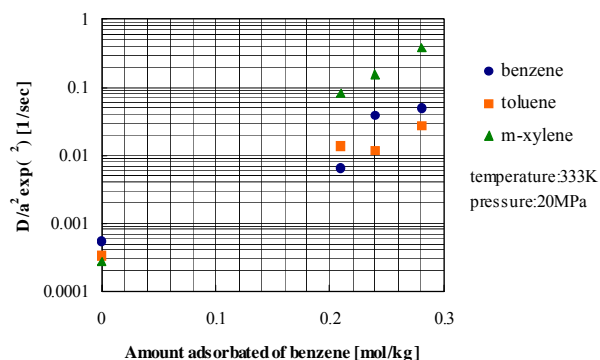
Figure 3. Dependencies of $D/a^2\exp(\sigma 2)$ on the amount adsorbed of benzene

In these calculations, contribution of four mass transfer steps in pulse response (μ'_2, as width) were accounted for, such as axial dispersion in te bed, film mass transfer, macro pore diffusion and micro pore diffusion. The effect of micropore diffusion is dominant in all the conditions examined.


MSC68RC1 model

MSC84RC1 model
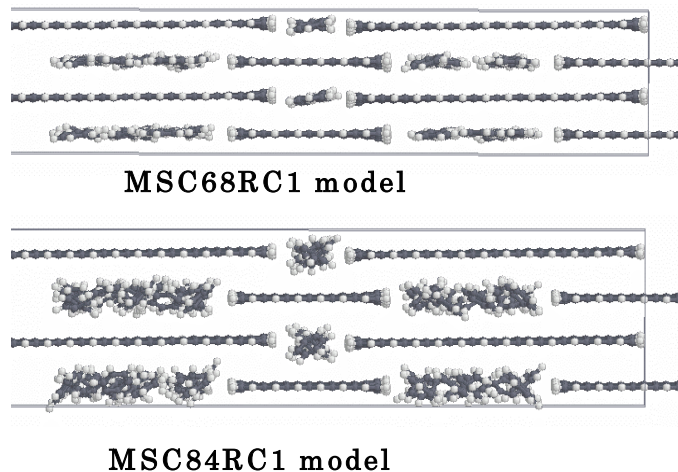
Figure 4. Adsorption state of benzene

Molecular simulation. Cerius2 (MSI Inc.) was used throughout the simulations. Three kinds of force field parameters in the Cerius2 library were used. The Grand Caronical Monte Carlo method (under constant chemical potential (μ), volume (V), temperature (T)) was used to get the equilibrium amount adsorbed. The purpose of performing simulation is to elucidate an adsorption mechanism on the molecule level. The simulation was performed on the same conditions as an experiment in order to compare with experiments. MSC68-RC1 and MSC84-RC1 model were used as adsorbent. Each model has 6.8 A or 8.4 A of distance between the centers of two graphitic carbon layers, respectively.

Adsorption state. First, we examined how molecules of adsorbate is located. Benzene was used for the adsorbate here. The results are shown in **Figure 4**. We see from Fig. 4 that benzene adsorbs into the adsorption space, which simulates micro pore. Here, benzene adsorbed in parallel to layer in MSC68 model. On the other hand, it is adsorbed aslant in MSC84 model.

Adsorption isotherm. The simulation was carried out for the binary component. Benzene and CO_2 were used for adsorbate. Conditions are 313 K and 15 MPa. The amount of adsorption increased with increases of molarity of benzene. **Figure 5** shows comparison of adsorption isotherm for a molecular simulation different force field and an experiment. UNIVERSAL1.02, London, and DREIDING2.11 were used for the force field, respectively. An experiment value approaches MSC68-RC1 model in force field UNIVERSAL1.02 and London, and is close to MSC84-RC1 model in DREIDING2.11. Since pore size of the adsorbent used in the experiment is 5 A, it is in agreement with the adsorption space of MSC84-RC1 model. Therefore, it can be said that DREIDING2.11 is most suitable.
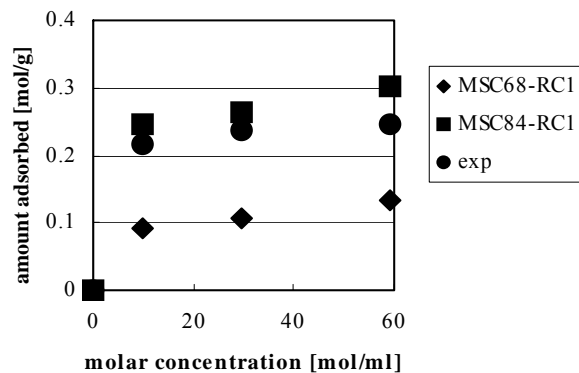
Figure 5. Comparison with experiment and molecular simulation : Adsorption isotherm

Conclusions

Adsorption equilibrium and adsorption dynamics on MSC were evaluated for each organics in supercritical CO_2 fluid mixed with adsorbate by chromatographic measurement. The dependencies of adsorption equilibrium constants, K*, and micropore diffusivity, D, of toluene, benzene and m-xylene, on molarity of benzene, toluene or m-xylene with each parameters of temperature or pressure were obtained, respectively. It was found that the values of K* and D for an organic substance depended on the amount adsorbed of other organics strongly. The usefulness of a simulation was able to be seen by one of the features of the molecule simulation that a molecule can be visuallized, about the adsorption state. The experimental amount adsorbed could be simulated partly.

References
1. Chihara, K., Kawazoe, K., Suzuki, M., AIChE J, 1978, 24: p. 237
2. Chihara, K., Aoki, K., AIChE Annual Meeting, 1993.
3. Chihara, K., Oomori, K., Kaneko, R., Takeuchi, Y., AIChE Annual Meeting, 1995.

ADSORPTION BEHAVIOR OF WATER VAPOR ON VARIOUS CARBONS

Yan Song, Wenming Qiao, Seong-Ho Yoon, Isao Mochida

Institute for Materials Chemistry and Engineering,

Kyushu University,

6-1 Kasugakoen, Kasuga, Fukuoka 816, Japan

Introduction

The behavior of water molecules in nanopores has attracted much attention from biology, geology and chemistry [1]. Although the adsorption of water on activated carbons has been studied for many years, the adsorption mechanism is not clearly elucidated. Water molecules are slightly adsorbed at low relative pressure, indicting that carbon surface is hydrophobic. At the middle range of relative pressure, the predominant water adsorption begins. The steep adsorption uptake has been believed to be associated with the cluster formation. In order to understand water adsorption mechanism better, we investigated water adsorption behavior on ACFs with different structure and carbon nanofibers through by using microbalance.

Experimental

Pitch-based ACFs (supplied by Osaka Gas Co.), PAN-based ACF (FE300), herringbone-type carbon nanofiber (CNF) and its activated form were used in the experimental. Among of them, OG15A and FE300 were heat-treated under different temperature respectively. Water adsorption was investigated by using CAHN1000. The sample (ca.100mg) was placed in quartz basket, and the water vapor was induced by bubbling method. The weight change of the sample was recorded continuously. Before measurement, the sample was heated at 150^oC to remove the adsorbed water. BET surface area and total pore volume were calculated by nitrogen adsorption at 77K using a Sorptomatic 1990 instrument. Before adsorption the samples were outgassed at 200^oC for 12hr until constant weight. Average pore size of the samples was calculated by 129Xe-NMR measurement. Samples were degassed at 150^oC under vacuum overnight before 129Xe-NMR measurement. Average pore size of ACF was obtained by comparing its chemical shift in Xe-NMR on the master curve.

Results and discussion

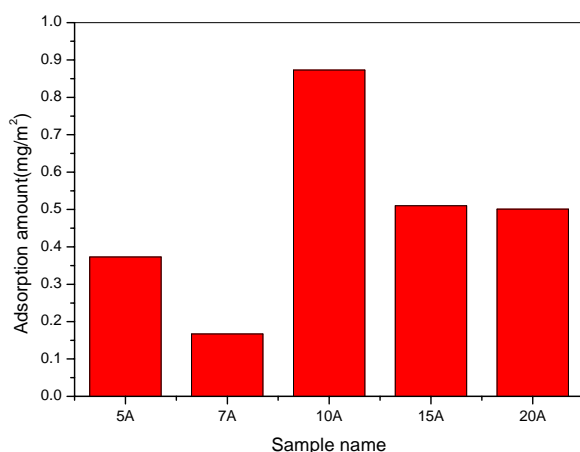**Influence of pore structure on the adsorption behavior.** The pore structure of OG series ACFs and CNFs was listed in **Table 1**. The sequence of surface area and pore volume of ACFs were as followed: OG5A<OG7A<OG10A<OG15A<OG20A, while the order of average pore size of ACFs was following: OG7A<OG5A<OG15A<OG20A<OG10A. The water adsorption curves of these samples were shown in **Figure 1**. It can be seen that the order of water adsorption rate of ACFs is following: OG7A≈ OG5A>OG20A>OG10A>OG15A, and the water adsorption amount is as followed: OG7A<OG5A<OG15A<OG10A<OG20A. Combined with **Table1** and **Figure 1**, it can be found that the water adsorption amount of OG series ACFs increased with the increase of surface area, and at the same time, the sample with small pore size had the fast water adsorption rate. By comparing the water adsorption amount per surface area of the ACFs (see **Figure 2**), it can be seen that excluding the factor of surface area, OG10A has the largest water adsorption capacity. That is to say, ACF with bigger pore size shows larger water adsorption amount. At the same time, the water adsorption rate of CNF is very slow for it mainly contains mesopores. After activation the water adsorption rate increased greatly for activation introduce some micropores. The increase of adsorption amount of CNF after activation should ascribe to the enhancement of surface area.

Table 1.   Pore structure of ACFs, CNF and its activated form

Sample	S_{BET} (m^2/g)	V_{total} (cm^3/g)	Average pore size(nm)
OG5A	573	0.31	0.9
OG7A	690	0.36	0.8
OG10A	953	0.52	1.5
OG15A	1390	0.75	1.2
OG20A	1862	1.00	1.3
CNF	300	0.45	---
ACNF	866	0.77	---
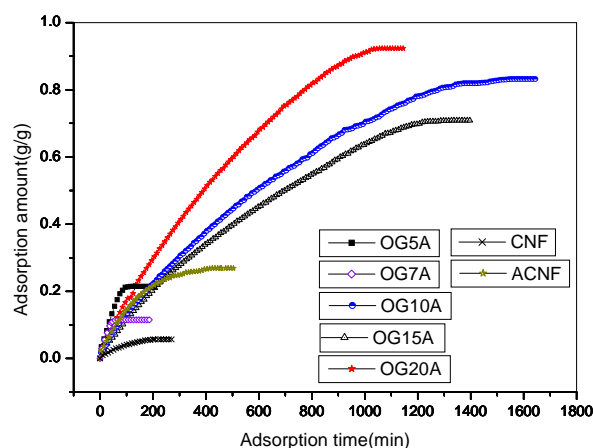
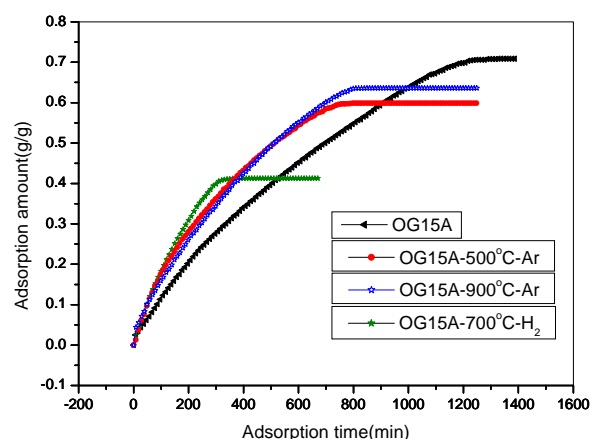**Figure 1.** Water adsorption behavior of samples

Figure 2. Water adsorption amount per surface area

Influence of element content on the adsorption behavior. **Table 2** listed the pore and surface structures of OG15A, FE300 and their heat-treated samples. After heat-treatment under high temperature, the surface area and oxygen content of the samples decreased to some extent. **Figure 3** showed the water adsorption curves of these samples. Water adsorption rate increased and the adsorption amount decreased after heat-treatment for OG15A series. Generally speaking, pore size will become smaller for the shrinkage at heat-treatment. So the adsorption rate increased. After remove more oxygen groups at heat-treatment, the hydrophobic of ACF increased, so the water adsorption capacity decreased. At the same time, FE300-800°C-Ar and OG7A has the similar surface area, but the former has the higher water adsorption capacity, which may be ascribed to its higher nitrogen content.

Table 2. Structure and elemental analysis of various samples

Sample	S_{BET}	V_{total}	O/C	N/C
OG15A	1390	0.75	0.047	---
OG15A-500°C-Ar	1126	0.60	0.037	---
OG15A-900°C-Ar	1225	0.69	0.025	---
OG15A-700°C-H$_2$	1068	0.58	0.024	---
FE300	793	0.43	0.076	0.037
FE300-800°C-Ar	702	0.40	0.028	0.041

Figure 3. Water adsorption behavior of OG15A with heat-treatment

Mechanism of water adsorption on ACF. The diameter of water molecules is about 0.31nm [2], so the pore with diameter about 0.62-0.93nm (2-3 ratio of the water molecular) is most suitable for water adsorption. After the water molecule is adsorbed in the micropore, it will form dimer or even pentamer [3]. Then the bigger pore has the larger adsorption capacity of water. Of course, the surface element content of carbon will also affect the water adsorption amount. In specific, higher oxygen and nitrogen content will reinforce the water adsorption behavior.

Summary

Water adsorption behavior of various kinds of carbons was investigated using CAHN. The results showed that carbon with smaller pore size has the fast water adsorption rate, and the carbon with bigger pore size shows larger water adsorption capacity. At the same time, the oxygen and nitrogen groups will enhance the water adsorption capacity of carbon.

References

(1) T. Iiyama, M. Ruike, K. Kaneko, Chemical physics letters 2000, 331, 359

(2) Muller, E A., L.F.Rull, L.F.Vega, and K.E.Gubbins, J. Phys. Chem., 1996, 100, 1189

(3) K. Kaneko, Y. Hanzawa, T. Iiyama, T. Kanda and T. Syzuki, Adsorption, 1999, 5, 7

ACTIVATED CARBON AS CATALYST FOR REMOVING HYDROGEN SULFIDE: ON THE FORMATION OF BY-PRODUCTS

Xianxian Wu, Andrew K. Kercher, Viviane Schwartz,
Steven H. Overbury and Timothy R. Armstrong

Oak Ridge National Laboratory (ORNL), Oak Ridge, TN 37831

Introduction

The use of activated carbon as a catalyst for selective partial oxidation of hydrogen sulfide (H_2S) could be a preferred approach for the removal of H_2S from gas streams.[1] A key advantage of H_2S selective oxidation is that the gas is cleaned and the sulfur recovered (as elemental sulfur, S) in a single step process. Formation of gaseous sulfur compounds, such as sulfur dioxide (SO_2) and carbonyl sulfide (COS), is one of the main challenges. Experimental investigations showed that different activated carbons have different activity and selectivity (to S) for desulfurization of hydrogen-rich gas streams.[2,3] A series of activated carbons produced at ORNL displayed excellent catalytic activity and selectivity.[4] As part of the effort to understand these differences and why ORNL carbons display exceptional catalytic performance, a comparative study was carried out using different gas streams. The results obtained for two typical samples are reported here, and the by-product formation is discussed.

Experimental

A commercial activated carbon, Centaur 20×50 (Calgon Carbon) and a typical laboratory-made activated carbon (sample W-5) were selected for this study. The precursor and procedures for synthesizing sample W-5 were the same as those reported earlier,[3] except a longer hold time at the activation temperature was used. Nitrogen isotherms on the samples were measured at 77K using an AUTOSORB-1. Characteristic data derived from the isotherms and the ash content of the samples (determined by TGA) are listed in Table 1.

Table 1. Properties of Activated Carbon Samples

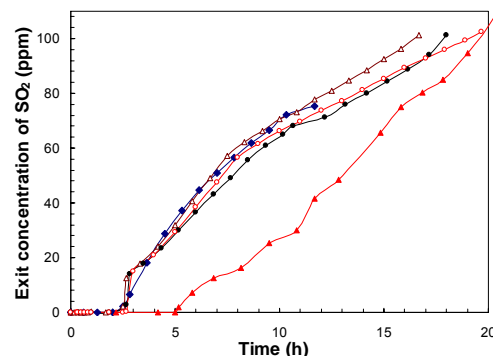| Sample	Centaur	W-5
Particle size (mesh)	20×50	20×30
BET surface area (m^2/g)	815	1055
Total pore volume (cm^3/g)	0.40	0.52
Micropore volume (cm^3/g)	0.33	0.39
Ash content (%)	4.78	2.62

Catalytic experiments were conducted in a laboratory-scale, fixed-bed reactor system.[3] The concentrations of the exhaust gases from the reactor were monitored by gas chromatography with a detection limit of 200 ppb for sulfur compounds. The experiments were conducted at 150°C at atmospheric pressure with a space velocity of 3100 h^{-1} (GHSV). The volume of carbon catalyst was approximately 10 cm^3 and the input concentration of H_2S was 1000 ppm. Air was introduced through the inlet at an O_2:H_2S ratio of 2:1. Five gas streams with different components were used as carriers (Table 2). The water vapor contained in the reformate stream was produced by heating water injected by a syringe pump through the inlet tubing (stainless steel). Gas A was used as a comparison with the reformate, and gas B and gas C were chosen to explore the contribution of CO or CO_2 to the formation of COS.

Table 2. Gas compositions of the gas streams

| Gas stream	Gas composition (vol%)				
	H_2	H_2O	CO	CO_2	CH_4
H_2	99	-	-	-	-
Reformate	50	23	15	9	2
Gas A	73	-	15	9	2
Gas B	80	-	-	16	3
Gas C	80	-	16	-	3

Results and discussion

The catalytic behavior of the Centaur sample was tested in all five gas streams. This catalyst showed a strong catalytic activity for H_2S oxidation.[2,5] During all tests, no emission of H_2S was detected (after almost 20 hours) which indicated 100% conversion of H_2S. The measured SO_2 emissions at the reactor exit as a function of reaction time are shown in Figure 1. It is apparent from Figure 1 that the over-oxidation of sulfur to SO_2 in all dry gas streams started at about 2 hours and that there was no significant difference in SO_2 emission for these gas streams. For the reformate, however, the emission of SO_2 was observed after 5 hours, and at a lower concentration than the other gas streams.
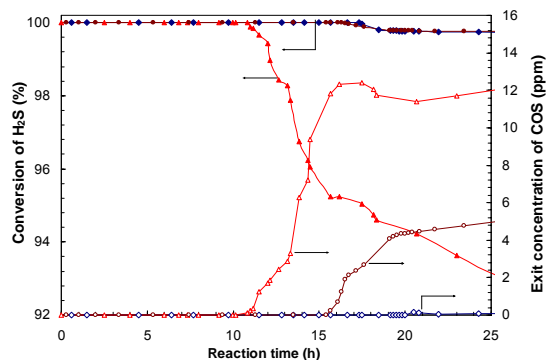

Figure 1. Exit concentration of SO_2 in the presence of the Centaur sample: ♦ in H_2 stream, ▲ in reformate, △ in gas A, ● in gas B, ○ in gas C.
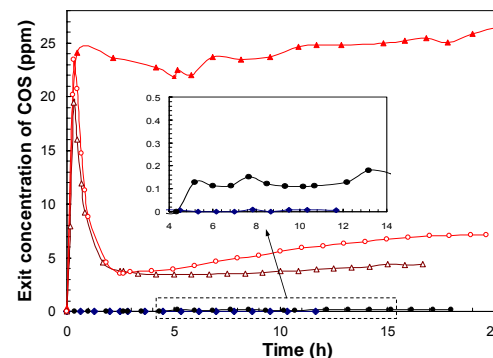
Figure 2. Exit concentration of COS in the presence of the Centaur sample: ♦ in H_2 stream, ▲ in reformate, △ in gas A, ● in gas B, ○ in gas C.

Figure 2 shows the COS emissions in the presence of the Centaur carbon. The emission of COS was detected immediately after the introduction of H_2S and air when CO-containing gas streams (reformate, gas A, and gas C) were used. In contrast, only an amount close to the detection limit (200 ppb) of COS was measured for gas B after about 5 h. As shown in Figure 2, the level of COS emissions was about 25 ppm in the reformate, about 6 ppm in gas C, and about 5 ppm in gas A. When the gas carrier was H_2, no COS was detected.

The conversion of H_2S and the by-product emissions when carbon W-5 was used in the H_2 stream, reformate and gas A are shown in Figures 3 and 4. No H_2S, SO_2 or COS was detected after more than 10 hours, indicating a combination of good activity and selectivity of this lab-produced carbon in different gas streams. In the case of reformate, sulfur compounds were measured earlier and at higher levels than in the other two gas streams. Concentration of H_2S, SO_2 and COS reached about 70, 60 and 12 ppm, respectively, after 25 hours in the reformate, while only about 2 ppm H_2S and 20 ppm SO_2 were measured after the same reaction period in H_2 and gas A. In addition, after about 15 hours, about 5 ppm COS was measured in gas A and occasional traces of COS were detected in H_2 after about 20

Figure 3. Conversion of H_2S and COS emissions in the presence of sample W-5: ♦◇ in H_2 stream, ▲△ in reformate, ●○ in gas A.
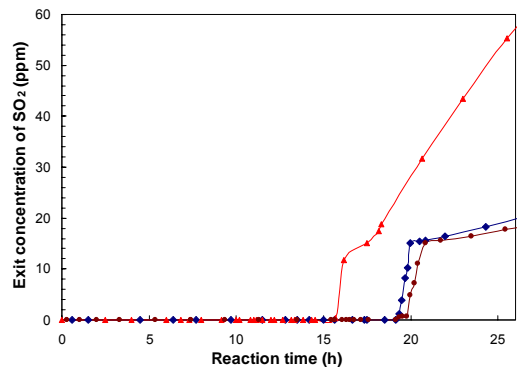
Figure 4. Exit concentration of SO_2 in the presence of sample W-5: ♦ in H_2 stream, ▲ in reformate, ● in gas A.

It has been suggested that sulfur vapor is the source of SO_2 and COS by reacting with surface bound O or CO via the reactions:[2]

$$\tfrac{1}{n} S_n(g) + 2O \rightarrow SO_2 \qquad (1)$$

$$\tfrac{1}{n} S_n(g) + CO \rightarrow COS \qquad (2)$$

In all dry gas streams, reaction (1) may be the main pathway for SO_2 formation, even though the direct oxidation of H_2S or COS to SO_2 is possible at 150^oC.[6,7] Emission of SO_2 was only detected after certain reaction times, which suggested that the vapor pressure of the sulfur product may reach a certain level only after filling of the smaller pores. The superior selectivity of the sample W-5 compared to the Centaur product may, then, be partially explained by the micro-structure of W-5, *i.e.*, a larger volume of small pores. Reaction (2) is responsible for COS formation, but other pathways are possible, such as a reverse reaction of COS hydrolysis and a reaction between S and surface oxygen complexes formed by chemisorption of O_2 on carbon sites:

$$CO_2 + H_2S \leftrightarrow COS + H_2O \qquad (3)$$

$$C(surface) + \tfrac{1}{2} O_2 \rightarrow CO^*(surface)$$
$$CO^*(surface) + \tfrac{1}{n} S_n \rightarrow COS \qquad (4)$$
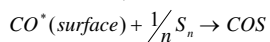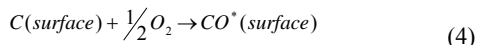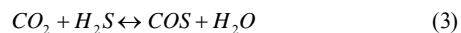
Reaction (3) is responsible for the COS formation in the case of gas B, whereas reaction (4) is responsible for occasional COS emission in H_2. As shown in Figures 2 and 3, the amount of COS formed by such pathways is very small in the dry gas carriers. In gas A and gas C, the reason for the appearance of a maximum COS emission at the beginning of the tests (Figure 2) is not clear. Almost the same trends in COS emissions were observed in the first 2 hours of reaction. This may be because reaction (2) is controlled by S vapor pressure in that period, whereas after it is shifted to the control region of CO partial pressure. This shift is coincident with the appearance of SO_2 (Figure 1), which supports the above speculation.

In the reformate stream, emissions of SO_2 and COS were different from those in gas A for both catalysts. This difference could be related to the supply of water va   th

concentration of COS involved the contribution from reaction (3) occurring in the inlet tubing because COS hydrolysis is reversible and can be catalyzed by many substances and ions.[8] A blank experiment in which the simulated reformate was flowed through an empty reactor (no catalyst) showed that both COS and SO_2 were detected after the stainless steel inlet tubing. The reason why SO_2 was only detected after certain reaction time in the presence of activated carbon, then, may be due to the reaction:

$$2H_2S + SO_2 \rightarrow H_2O + \tfrac{3}{n} S_n \qquad (5)$$
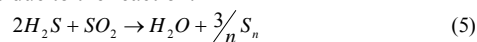
As sulfur accumulates, the catalyst was deactivated and SO_2 was detected.

The availability of sulfur vapor and reaction (5) may be a plausible argument accounting for the emissions of SO_2 which appear after more than 15 hour reaction when sample W-5 was used in different gas streams. This is not, however, enough to explain why there is no COS emission after this sample was in the reformate stream for more than 10 hours. As discussed earlier, the formation of COS in the inlet tubing is a main contributor to the emission of COS in that case. The reason why there was no COS measured, then, may be due to the ability of the sample W-5 to catalyze the partial oxidation of COS via the reaction:[9]

$$COS + \tfrac{1}{2} O_2 \rightarrow CO_2 + \tfrac{1}{n} S_n \qquad (6)$$
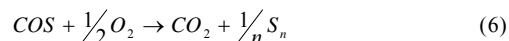
Most likely, the carbon W-5 had the ability to catalyze reaction (6), but the Centaur product did not. Deactivation of carbon W-5 resulted in the loss of catalytic activity and subsequent emission of COS after certain reaction times. Of course, these arguments do not rule out other plausible explanations.

Conclusions

The comparative study using different gas mixtures on two activated carbons provided useful information about the formation of by-products and why the laboratory-made carbon had a better selectivity than the Centaur product. The microstructure of carbon W-5 and its capacity to catalyze partial oxidation of COS are among the likely reasons which accounted for its unique performance.

References
(1) Kohl, A. L.; Nielsen, R. *Gas Purification*, 5th ed.; Gulf Professional Publishing Company: Houston, 1997.
(2) Gardner, T. H.; Berry, D. A.; Lyons, K. D.; Beer, S. K.; Freed, A. D. *Fuel* **2002**, *81*, 2157.
(3) Wu, X.; Kercher, A. K.; Schwartz, V.; Overbury, S. H.; Armstrong, T. R. "Removing hydrogen sulfide from hydrogen-rich gas streams by selective catalytic oxidation"; 228th ACS National Meeting, August 22-26, 2004, Philadelphia, PA, USA. 49 (2): 893.
(4) Wu, X.; Kercher, A. K.; Schwartz, V.; Overbury, S. H; Armstrong, T. R. *Carbon* **2004**, *Submitted*.
(5) Wu, X.; Kercher, A. K.; Schwartz, V.; Gallego, N. C.; Overbury, S. H.; Armstrong, T. R. "Activated carbons as catalyst for selective partial oxidation of hydrogen sulfide"; Carbon2004, July 11-16, 2004, Providence, RI, USA.
(6) Steijns, M.; Derks, F.; Verloop, A.; Mars, P. *Journal of Catalysis* **1976**, *42*, 87.
(7) Griffith, R. H.; Hill, S. G. *Journal of the Chemical Society* **1938**, 2037.
(8) Ferm, R. J. *Chemical Reviews* **1957**, *57*, 621.
(9) Bawn, C. E. H. *Journal of the Chemical Society* **1933**, 145.

IMPORTANCE OF INORGANIC-ORGANIC PHASES ARRANGEMENTS FOR GAS PHASE DESULFURIZATION ON CATALYTIC CARBONACEOUS ADSORBENTS

Adil Ansari, Teresa J. Bandosz

Department of Chemistry, The City College of New York

Introduction

One of the reasons for removal of hydrogen sulfide from air is increasing concerns about the acid rain pollution (1). In the atmosphere H_2S is easily oxidized to SO_2 and SO_3 which is followed by formation of H_2SO_4 when scavenging by rain droplets occurs. The precipitation of acid rain causes environmental damage in ecosystems (soil, water) and in infrastructure (detoriation of concrete and corrosion of steal). The Acid Rain Program of Clean Air Act of 1990 requires reduction and continuous monitoring of sulfur containing gases emission (2).

One of the ways to efficiently remove hydrogen sulfide is its adsorption on activated carbons. The adsorbents, owing to their large surface area, high pore volume, and catalytic surface properties (3) are able to retain significant amount of hydrogen sulfide (4). Via various paths of surface reactions governed mainly by surface pH (5, 6), the pollutant is oxidized either to elemental sulfur or sulfuric acid. When the former is desirable, sulfuric acid deposition may create problems of hazardous waste disposal when the recovery of the reaction products is not applied. Some carbons, as for instance Calgon's Centaur®, are able to converts significant amount of H_2S to H_2SO_4. Moreover, after this process the surface is regenerated just using simple water washing.

Based on the results obtained in earlier work (7-9) the objective of this paper is to investigate the effect of almost nonporous carbonaceous phase on the performance of sewage sludge- waste paper based adsorbents. In spate of the fact that this carbonaceous phase is basic in its chemical nature, to check if addition of well-dispersed H_2S dissociation promoting catalyst can influence the performance, various amounts of calcium were added to the precursor before carbonization. The results are discussed in terms of the content of carbonaceous phase, the porosity and the presence of calcium.

Experimental
Materials

Adsorbents were prepared from dewatered sludge (from Wards Island Water Pollution Control Plant, NYC DEP), waste paper and mixtures of both precursors and calcium hydroxide with following weight percentage of waste paper/dewatered sludge/calcium hydroxide: 22/72/6; 24.5/74.5/1, 45/45/5, 58/38/4, and 75/25/0. Waste paper was first ground to a fine powder then mixed with powdered dried sludge and homogenized using the small amount of water with an appropriate content of calcium hydroxide. Prepared pulp was extruded into 4 mm granules and dried. In all cases the pyrolysis was done in a horizontal furnace at nitrogen atmosphere with heating rate 10 deg/min. The final pyrolysis temperature was 950 °C with holding time one hour. The composite adsorbents are referred to as C, which is followed by numbers representing an increasing ratio of the waste paper to sludge and percentage of calcium hydroxide added to the precursor mixture. The adsorbent obtained from dewatered sludge is referred to as CS and carbon obtained from waste paper – CC. The names of adsorbents, and their yields are collected in Table 1.

Table 1. Names of Samples, Yields, Bulk Density and Ash Content

Sample	Composition	Yield [%]	Density [g/cm^3]	Ash Content [%]
CS	sludge	40	0.63	75
CC	Waste paper	22	0.19	31
C-1Ca6	22/72/6	40	0.52	70
C-2Ca1	24.5/74.5/1	30	0.59	65
C-3Ca5	42.5/42.5/5	34	0.48	64
C-4Ca4	58/38/4	33	0.34	60
C-5	75/25/0	27	0.24	50

Methods

The dynamic tests were carried out at room temperature to evaluate the capacity of the adsorbents for H_2S, removal (7-9) Moist air (relative humidity 80% at 25°C) containing 3000 ppm of H_2S, CH_3SH or SO_2 was passed through a column with 6 ml of adsorbent at 500 ml/min. The outlet concentrations of gases were monitored with electrochemical sensors. The tests were stopped at the breakthrough concentrations of 350 ppm. The adsorption capacities of each carbon were calculated by integration of the area above the breakthrough curve (from the inlet concentration of gas, flow rate, breakthrough time), and carbon weight.

Sorption of nitrogen was used to characterize the porosity of adsorbents. Nitrogen isotherms were measured using an ASAP 2010 (Micromeritics) at -196 °C. Before experiments the samples were outgassed overnight at 120°C under the vacuum of 10^{-5} Torr to a constant pressure. The isotherms were used to calculate the total specific surface areas (S_t), micropore volumes (V_{mic}), total pore volumes (V_t), and pore size distributions using Density Functional Theory (DFT).

pH of carbon surface for initial and exhausted samples was estimated by placing 0.4g of carbon powder in 20 ml of water. The suspension was equilibrated during night and then its pH was measured.

In order to evaluate either the species present on the initial carbon surface or surface reaction products, thermal analysis was carried out using TA Instruments Thermal Analyzer. The instrument settings were: a heating rate of 10°C/min in a nitrogen atmosphere, 100 ml/min flow rate.

X-Ray Fluorescence analysis was applied to study the calcium content in the samples. The SPECTRO model 300T Benchtop Analyzer from ASOMA Instruments, Inc was used. The instrument has a titanium target X-ray tube and a high-resolution detector. The samples were studied in a solid phase after grounding and sieving in order to use the matrices with similar physical properties

Results and Discussion

The yields of materials collected in Table 1 show the dependence on the content of waste paper (cellulose). More paper in the composition leads to smaller yield, which is in fact expected knowing the low efficiency of the cellulose carbonization in term of the mass of the final product. Nevertheless, the yields of materials obtained in this research are much higher than those for sludge-organic polymer mixtures where washing was a necessary step to remove the deposited metals and to develop the porosity (7).

The density also decreases with an increase in the content of paper. This is related either to a decrease in the content of ash with increasing amount of waste paper (higher carbon content) or caused by an increase in the total porosity, which may have its origin in carbonaceous phase. This is going to be discussed later in this paper.

The performance of materials as hydrogen sulfide adsorbents is presented in Table 2. It is worth to mention that H_2S removal capacity on of these materials is better than that on virgin activated

carbon (20 mg/cm^3) and comparable to catalytic carbon Centaur® (60 mg/ cm^3) and caustic impregnated carbons (114 g/cm^3) determined using standard ASTM test. Also, taking into account their smaller density than that of the majority of coal derived activated carbon the capacity per unit mass is exceptionally high.

Table 2. H$_2$S Breakthrough Capacity Results

Sample	H$_2$S brth. Cap.[mg/cm^3]	H$_2$S brth. Cap.[mg/g]	pHin	pHE
CS	72	115	10.6	9.6
CC	17	90	12.6	12.2
C-1Ca6	64	124	12	10.7
C-2Ca1	50	85	11.5	10.9
C-3Ca5	105	211	12.0	11.5
C-4Ca4	120	351	12.0	11.2
C-5	57	237	12.3	9.8

It is interesting that there is only a slight increase in the capacity per unit volume with a noticeable increase in the content of calcium for two samples having similar sludge content, C-1 and C-2. On the other hand, a increase in the content of waste paper with the calcium added resulted in a huge capacity, comparable to that on caustic impregnated activated carbons, for C-3C5 and C4-Ca4 samples with over 30 % of sulfur adsorbed on the surface of the C-4Ca4 sample. Since these two samples have similar addition of calcium, higher capacity of the C-4Ca4 is clearly linked to the higher content of carbon from waste paper. Nevertheless, when no calcium is added the capacity of the adsorbent is still over twice higher than that of virgin activated carbon and over 22 % of sulfur is deposited in its pore system. To interpret these finding, the detailed analysis of surface porosity and chemistry is needed.

Calcium is added to our samples to compensate for smaller contents of the catalytic phase having its origin in a sewage sludge precursor (8-10). As shown elsewhere, CS contains 6 % of calcium oxide. Calcium provides basicity of the surface needed for efficient hydrogen sulfide dissociation and can react with H$_2$S forming sulfides. When well dispersed, it contributes to the specific function of microreactors formed in the pore systems of catalysts where hydrogen sulfide is oxidized to elemental sulfur (10). The high capacity of C-5 sample suggests that basicity of the matrix without calcium catalyst might be sufficient for feasible H$_2$S removal. The previous studied showed that the high capacity can be achieved with pH as high as 10 (5).

It is important to mention here that adding waste paper to sludge does not necessary decrease the total content of active calcium in the adsorbents. It is well known that calcium carbonate and minerals containing calcium are added to paper to improve its quantity and interactions with the ink. In fact 30% of ash in CC sample must have its origin in the paper production process.

The dependence of the H$_2$S capacity on the intensity of calcium XRF peaks for samples containing total calcium originated form cellulose, sludge and that added as hydroxide to the precursor is presented in Figure 1. The results for CC and CS are not included due to the apparent differences in the physical features of the matrices. The linear trend clearly shows the importance of calcium containing components of the wastes to the process of desulfurization from the gas phase.

The presence of calcium in the waste paper precursor is also reflected by the high pH of the CC carbon. All samples containing waste paper, either with calcium addition or without, have the pH greater than 12, which is even higher that that for the sewage sludge derived sample. That high pH enables dissociation of adsorbed H$_2$S in the film of water and provides buffer capacity for the adsorbents for reaction with hydrogen sulfide. After H$_2$S adsorption the

materials are still basic which suggests formation of either salts or elemental sulfur. In fact, based on the adsorbent composition, two reaction products are expected. Sewage sludge component and addition of calcium oxide should contribute to formation of sulfur (8). Some calcium and metal oxides present in sludge will react with H$_2$S forming sulfide and sulfates. The biggest decrease in the pH is found for the sample, which has the highest content of the carbonaceous phase, C-5 (69 % of carbon). As described previously, the carbonaceous phase, when small micropores are present preferably oxidizes H$_2$S to H$_2$SO$_4$ (4). Formation of small amount of sulfuric acid (depending on the porosity of carbonaceous phase) may contribute to 3 pH unit increase in the surface acidity.
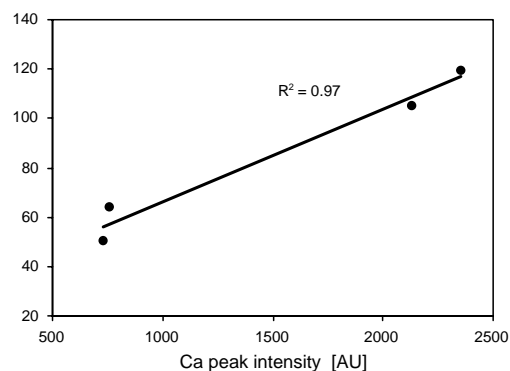
Figure 1. Dependence of the H$_2$S breakthrough capacity on the intensity of XRF calcium peak,

**Table 3. Structural Parameters of Adsorbents Studied**

Sample	S$_{N2}$ [m^2/g]	V$_{mic}$ [cm^3/g]	V$_t$ [cm^3/g]
CC	66	0.017	0.128
CCE	15.7	0	0.074
CS	75	0.011	0.111
CSE	20	0.0	0.088
C-1Ca1	91	0.016	0.108
C-1Ca1E	29	0	0.115
C-2Ca6	108	0.024	0.112
C-2Ca6E	20	0	0.085
C-3Ca5	72	0.012	0.097
C-3Ca5E	20	0.	0.077
C-4Ca4	67	0.012	0.102
C-4-Ca4E	14	0	0.052
C-5	73	0.018	0.119
C-5E	16	0	0.064

Information about the changes in the porosity is provided in Table 3. At the first glance, the specific surface areas and volumes of pores are similar to those obtained from the pure precursors. These findings indicate that carbon phase does not contribute to the development of microporosity. The opposite was found to be true when adsorbents were obtained from the mixture of sludge with an organic polymer (7).

It is very interesting that for adsorbents with a small content of papers derived phase a significant, about 30%, increase in the surface area is observed. Moreover, the surface is higher when the content of calcium increases. The latter can be explained by contribution of calcium for development of porosity as a gasification catalyst. When the waste paper component of the precursor riches about 50 % the trend in the surface area follows the expected one for the physical

mixture of the components and its is independent on the addition of calcium. It is likely that the small content of carbon form waste paper (in fact, after recalculation of yields, it contributes to only about 15 % of total mass of the C-1 and C-2 adsorbents) is able to create a thin deposit between the bulky granules of sewage and on that interface additional pores exist for penetration by nitrogen molecules. Moreover, addition of calcium also contributes to development of porosity in the thin layer. With higher content of waste paper, the aggregates of carbonaceous phase are bigger, their level of dispersion significantly decreases, calcium is not able to promote the gasification and the surface area is a summary of the surfaces of both coexisting, next to each other, phases. That carbon phase from waste paper is almost nonporous and can be considered as a char since no activation was used. Its location results in a decrease in the bulk density of adsorbent with an increase in the content of waste paper. The presence of these bulky low density "inserts" between the sludge-derived phase can increase the accessibility of its catalytic phase for H_2S oxidation.

It is noteworthy that after H_2S adsorption the volume of micropores disappears completely making the removal process even more efficient than in the case of sewage sludge based materials. since the pore volume here is utilized in 100 %. It is obvious that about 30% of sulfur cannot be stored in so small volume of micropores. Assuming the density of sulfur equal to 2 g/cm^3 only about 10 % of total sulfur can be located there. Thus other pores, meso- and big macropores between the particles must be active in retaining the oxidation products.
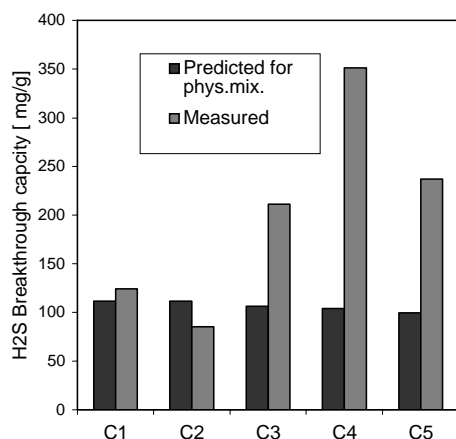
Figure 2. Comparison of H_2S breakthrough capacity predicted for physical mixtures of the components and measured.

All the features listed above contribute to the measured exceptional H_2S breakthrough capacity of our adsorbents. In order to see synergetic/catalytic effect of samples composition the capacities expected for the physical mixtures of the components were calculated (without the contribution of calcium as H_2S adsorbent/oxidant). They are plotted in Figure 2 in comparison with the measured values. Contrary to the trend found for development of porosity for adsorbents with low content of waste paper, regardless the amount of calcium, the measured capacities more or less match the expected ones. The difference arises for the samples with the content of waste paper in the precursor is about 50 % or higher. However the performance of adsorbents has been already link to the content of calcium (Figure 1) based on the results present in Figure 2, chemistry cannot be the only one governing factor. The C4-Ca4

and C3-Ca5 samples have similar added content of calcium. Although the contribution of calcium from the waste paper derived phase is higher for the former sample than for the latter, that difference cannot account for such significant differences in H_2S breakthrough capacity. The plausible explanation is that those bulky "inserts" of light density char mentioned above in the discussion of porosity enhance the capacity. Although they do not provide the high volume of micropores, inside them the space for sulfur deposition exist. They are in close contact with catalytic phase of sludge origin and this enable the migration of sulfur. Support for this is the very high capacity of the C-5 sample where no calcium was added. The apparent effect of lack of calcium and thus lower "buffer capacity" of the adsorbent is in the fact that a small fraction of hydrogen sulfide is oxidized to sulfuric acid.
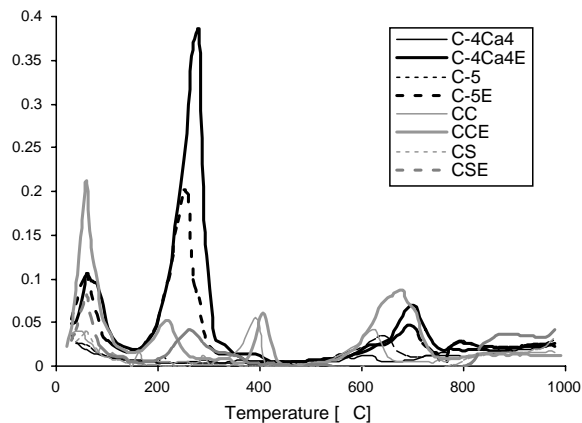
Figure 3. DTG curves in nitrogen for selected samples.

Some information about the speciation of H_2S surface reaction products can be obtained from the analysis of the pH values and their changes after H_2S adsorption. As indicated above, based on the values collected in Table 2 we expect mainly sulfur in the surface with some contribution of salts such as sulfides or sulfates and carbonates. Figure 3 shows DTG curves in nitrogen for the selected initial and exhausted samples. The peaks represent the removal of sulfur containing species and their surface areas reflect the weight loss at a certain temperature range. For all exhausted samples an increase in intensity of peaks located at temperature smaller than 200 ^oC, between 200 and 400 ^oC and between 600 and 800 ^oC is observed. The first peak may represent the removal of adsorbed water and weakly adsorbed H_2S or SO_2 from oxidation of hydrogen sulfide. The second weight loss peak is likely linked to the removal of elemental sulfur (8). Its intensity increases with an increase in the performance of materials in the process of hydrogen sulfide removal. The lower temperature of that peak than that found previously for activated carbon (4) is related to deposition of sulfur in big pores, which are in large volume in these materials as shown from the analysis of pore size distributions. For the samples whose volume of micropores is the highest, the shoulder exists at about 400 ^oC, which represents removal of sulfur from very small pores. The large peak between 600 and 800 ^oC present for samples with cellulose and calcium is linked to decomposition of calcium sulfate (10) formed as a result of the reaction of sulfuric acid with calcium oxide. That peak is much smaller for sewage sludge derived sample. For the CC sample and its exhausted counterpart there is a sharp weight loss at 400 ^oC. Lack of differences in intensity of that DTG peak for these two samples suggests its origin in dehydroxylation of clay, likely kaolinite, used as a paper filler . It is interesting that this peak is not

present for other samples containing waste paper. The reason can be in the solid state reactions of clay at high temperature in the presence of various inorganic components of the sewage sludge.

Conclusions

The results described above demonstrate the importance of the composition and arrangement of inorganic/organic phases for the removal of hydrogen sulfide. By mixing sewage sludge and waste paper the exceptionally good adsorbents were obtained. Their capacity is comparable to those of the best activated carbons existing on the market. The interesting finding is that however some microporosity is necessary to increase the storage area for oxidation products, the carbonaceous phase does not need to be highly microporous. Its is important that it provides space for deposition of sulfur which is formed on the inorganic phase catalyst. That space can be in meso and macropores as shown in the case of char derived from the waste paper.

References
(1) Manahan S.E. Environmental Chemistry, 6th ed.; CRC Press: Boca Raton, FL, 1994
(2) http://www.epa.gov/air/caaac/dieselreview.pdf
(3) Bansal, R. C., Donnet, J. B., and Stoeckli, F. *Active Carbon*: :Marcel Dekker: New York, 1988.
(4) Bandosz, T.J.; *J. Colloid. Interface Sci.*, **2002**,*246*,1
(5) Adib .;, Bagreev A.; Bandosz T.J. *J Coll Interface Sci* **1999**, *216*, 360.
(6) Adib F.; Bagreev A.; Bandosz T.J.. *Environ Sci Technol* **2000**, *34(4),* 686.
(7) Ansari, A.; Bagreev A.; Bandosz T.J. *Carbon*, in press.
(8) Bagreev A.; Bashkova S,; Locke D.C,; Bandosz T.J. *Environ Sci Technol* **2001**, *35(7),* 1537.
(9) Bagreev A,; Bandosz T.J. *Environ Sci Technol* **2004,** *38,* 345.
(10) Bagreev A,; Bandosz T.J. *Ind. Eng. Chem. Res.*, submitted.
(11) Leon y Leon, C. A., and Radovic, L. R. In *Chemistry and Physics of Carbon*; P.A. Thrower, Ed.; M. Dekker: New York, 1992; Vol. 24, pp. 213-310
(12) Handbook of Chemistry and Physics; Weast RC, ED., 67th edition, CRC Press, Boca Roton, FL 1986.

ANTIBACTERIAL ABILITY OF ACTIVATED CARBON CONTAINING ZNO PARTICLES

Osamu Yamamoto

Research Institute of Materials and Resources, Faculty of
Engineering and Resource Science, Akita University,
1-1 Tegata Gakuen-machi, Akita 010-8502, Japan

Introduction

The occurrence of antibacterial activity by using ceramic powders, CaO MgO and ZnO, has been pointed out with much attention as a novel technique that can substitute for conventional ones using organic agents. ZnO powders have been found to show a marked antibacterial activity without the presence of light (1). The occurrence of the activity of ZnO has been assumed to be due to the generation of active oxygen, hydrogen peroxide, from its surface. However, it was known that the active oxygen contributed to the antibacterial activity weakens with lengthening the diffusion distance of active oxygen until it reaches bacteria. Yamamoto et al. (2) reported that the large amount of bacteria absorbed on the surface of activated carbon. Therefore, activated carbon containing ZnO particles may be a stronger antibacterial activity than ZnO itself, because of the short diffusion distance of active oxygen that reaches bacteria.

In present work, spherical activated carbons containing ZnO particles were prepared through the carbonization of the resins ion-exchanged by Zn ions. The antibacterial activity of as-prepared carbon samples was evaluated.

Experimental

An ion-exchanged resin having carboxyl group as exchangeable function group was used a starting material, which was treated for 24h by Zn complex solution. The treated resin was carbonized for 10 min in a nitrogen gas at the temperature ranging from 500 to 900℃, to prepare the activated carbons containing ZnO particles. The carbon samples thus obtained were suspended with a physiological saline. They were used in antibacterial tests. The formation of ZnO in carbon samples was examined by XRD. The amount of ZnO in the samples was determined by oxidizing at 1000℃ in air. The specific surface area of the samples was estimated by analyzing the adsorption isotherms of nitrogen at -196℃.

Escherichia coli (*E. coli*) and *Staphylococcus aureus* (*S. aureus*) were used as test bacteria. These bacteria were cultured in brain heat infusion broth (BHI) at 37℃ for 24h. The bacterial culture was suspended in a sterile physiological saline at a final concentration of 10^2 CFU/cm^3 (CFU: Colony Forming Unit). The antibacterial activity of carbon samples was evaluated by measuring the changes in electrical conductivity with bacterial growth. The conductivity changes were monitored during the incubation at 37℃ for 30h without the presence of light. The hydrogen peroxide (H_2O_2) generated from carbon samples was measured by oxygen electrode. In the detail, the following reaction occurs; H_2O_2 + catalase $\rightarrow$ H_2O + $1/2O_2$. The concentration of H_2O_2 generated can be calculated from the concentration of O_2 detected by the oxygen electrode.

Results and Discussion

The diffraction peaks corresponding to ZnO of hexagonal type were detected in all carbon samples. The ZnO content, the specific surface area and the pH value of carbon samples prepared in this work are summarized in Table 1. The amount of ZnO in carbon samples when ion-exchanged resins were carbonized at 500℃ was about 65 mass%, and decreased with increasing carbonization temperature. The mass loss of ZnO is assumed to be due to the vaporization of zinc during the carbonization. The specific surface area of carbon samples increased with increasing carbonization temperature. Nakagawa et al. (3) prepared the activated carbon by carbonizing the ion-exchange resin having different cations, such as zinc, nickel and copper ions. They also clarified that the formation of micro pores in the carbons was due to the pillars that were formed in the molecular structure of an ion-exchanged resin, i.e., pillar effect. Therefore, the increase in the specific surface area is assumed to be due to the pillar effect.

Table 1. Characterization of activated carbon containing ZnO

Carbonization temperature (℃)	ZnO content (mass %)	Surface area (m²/g)	pH (-)
500	65	201	5.7
700	63	242	5.6
900	52	523	5.6

The comparison in antibacterial activity of three carbon samples carbonized at 500, 700 and 900℃ was performed, based on the results of the changes in electrical conductivity with bacterial growth (Fig. 1). In this figure, If the values of DT/DT$_{control}$ are changed with a steep rise at the lower powder concentration, it ca be evaluated to show the stronger antibacterial activity. Antibacterial activity was found to be a strong at higher powder concentration of carbon samples. Also, the antibacterial activity of carbon samples decreased with increasing carbonization temperature. The behavior in antibacterial activity toward *E. coli* was comparable with that toward *S. aureus*. In the comparison of same powder concentration, however, the antibacterial activity of carbon samples toward *E. coli* was found to be weaker than that toward *S. aureus*.
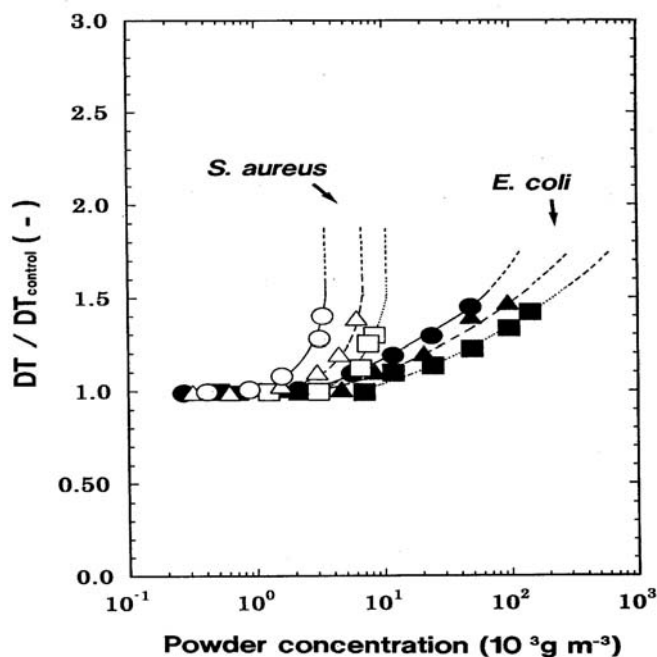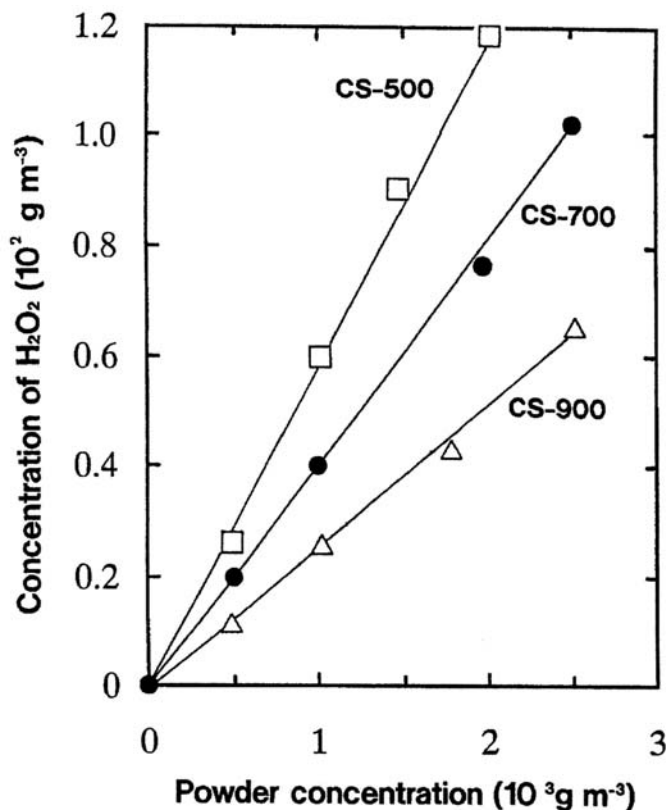

Figure 1. The comparison in antibacterial activity toward S. aureus and E. coli. The symbols of circles, triangle and squares show the carbon samples carbonized at 500, 700 and 900℃.

The concentration of H_2O_2 generated from carbon samples increased linearly with increasing powder concentration and decreasing carbonization temperature (Fig. 2).

References
(1) Yamamoto, O.; *Inter. J. Inorg. Mater.* **2001**, 3, 643.
(2) Yamamoto, O. Nakakoshi, K. Sasamoto, T. Nakagawa, H. Miura, K.; *Carbon*, **2001**, 39, 1643.
(3) Nakagawa, H. Watanabe, K. Harada, Y. Miura, K.; *Carbon*, **1999**, 37, 1455.
(4) Yamamoto, O. Sawai, J.; *Bull. Chem. Soc. Japan* **2001**, 74, 1761.

Figure 2. The changes in concentration of H_2O_2 with amount of carbon samples

The following two factors may affect the antibacterial activity; that is, they are pH value in medium and H_2O_2 generated from ZnO. However, the pH values measured in this work, pH=5.6-5.7, generally do not affect the antibacterial activity (4). By the oxygen electrode analysis, H_2O_2 was detected, which may contribute to the occurrence of antibacterial activity, because H_2O_2 is well known to be effective for the antibacterial activity. Therefore, the increase in antibacterial activity is supposed to be due to the increase of ZnO content in carbon samples, i.e., the increase of the concentration of generated H_2O_2. The reason that the carbon samples showed the stronger antibacterial activity toward *S. aureus* than that toward *E. coli* is assumed to be due to the difference of the sensitivity for H_2O_2.

Conclusions

The specific surface area of activated carbon containing ZnO particles increased with increasing carbonization temperature and the amount of ZnO in activated carbon decreased. From the comparison in antibacterial activity, it was found that the activity toward *S. aureus* was stronger than that toward *E. coli*. The occurrence in antibacterial activity was assumed to be a H_2O_2 generated from ZnO particles in activated carbon.

OXIDATION KINETICS OF MERCURY IN FLUE GAS

Edwin S. Olson, Blaise A. Mibeck

Energy & Environmental Research Center
15 North 23rd Street
Grand Forks, ND 58203

Abstract

Understanding the details of the interactions between mercury and flue gas components on the activated carbon surface is crucial to designing carbons with faster kinetics and greater capacities for mercury sorption in utility flue gas streams. A series of experiments were conducted with a thin bed of activated carbon in a flow-through reactor with synthetic flue gas compositions including elemental mercury. Since oxidation continues unimpeded after capacity breakthrough, the oxidation can be decoupled from the binding step for Hg(II) by measuring unreacted Hg^0 and total Hg in the effluent from the bed. NO_2 had a moderate effect on the kinetics, and HCl had a small effect. SO_2 had very little effect. These data are consistent with the model presented earlier involving conversion of carbene basic sites to carbenium ions that can oxidize the Hg^0.

Introduction

Over the last decade, the Energy & Environmental Research Center (EERC) has intensively investigated methods for control of mercury emissions from coal-burning power plants. Injection of fine-powdered activated carbon into the hot flue gas stream of a utility power plant has been successful in removing a large portion of the mercury in the flue gas, even when the mercury is mainly elemental. But the amounts of carbon injected are still relatively large and, therefore, costly. High heterogeneous reaction rates of the gas-phase elemental mercury on the carbon sorbent surface may be needed to capture the mercury in the short contact time demanded when the sorbent is quickly removed from the gas stream, such as with an electrostatic precipitation of ash and carbon particulates. Understanding the details of the interactions between mercury and flue gas components on the activated carbon surface is crucial to design of carbons with faster kinetics and greater capacities.

Pioneering studies were conducted at the EERC that provided needed information on the flue gas mercury interactions. These studies included a large factorial series of tests using powdered activated carbons that were conducted in a bench-scale system consisting of a thin fixed-bed reactor in gas streams (100° to 150°C) containing 11 to 15 $\mu g/m^3$ of Hg^0 in various simulated flue gas compositions consisting of acidic SO_2, NO_2, and HCl gases plus a base mixture of N_2, O_2, NO, CO_2, and H_2O (1, 2). As a result of these experiments and two series of tests where carbon samples were exposed to various flue gas compositions and analyzed by x-ray photoelectron spectroscopy (3, 4), a number facts emerged that were important to understanding the activating and poisoning effects exhibited by flue gas. Conclusions based on these facts are summarized as follows (5):

(1)   The sorption of Hg^0 in flue gas is entirely chemisorption to form Hg(II).
(2)   Hg(II) competes for the basic binding sites on the carbon with other acids in flue gas and the sulfuric acid formed from SO_2 oxidation on the carbon.
(3)   The main poisoning effect on the carbon basic sites results from accumulation of sulfur(VI).
(4) NO_2 in the flue gas is the major oxidant for both Hg^0 and SO_2 on the catalytic carbon surface.
(5) H_2O is also required for sulfur(VI) accumulation.
(6)   Most of the Hg emitted after breakthrough is (oxidized) Hg(II).
(7)   Previously bound Hg(II) is emitted after breakthrough.

Based on these capacity data, an initial model was presented (5) that described the chemisorption of Hg^0 in flue gas. Fact 6 is very important for at least two reasons. Although the binding sites cannot effectively bind Hg(II) at breakthrough, the oxidation reaction is unaffected, since nearly 100% oxidation occurs even after complete breakthrough. This fact argues against any explanation for loss of capacity based on pore plugging by species resulting from acid gases, since this would inhibit both reactions. This fact also shows that the binding and oxidation steps can be decoupled. The Hg(II) species that forms or is released after breakthrough is volatilized as $HgCl_2$ or $Hg(NO_3)_2$ (6).

A refinement of the binding site model was proposed (7) that offers more detail on the nature of the carbon site and its interaction with flue gases and Hg (Figure 1). This model uses the concept of zigzag carbene structures recently proposed for states at the edges of the carbon graphene layers (8) rather than oxygen functional groups suggested by other authors. In the carbene model, the zigzag carbon atom positioned between aromatic rings is hypothesized to be the Lewis base site. The zigzag Lewis basic carbene reacts with the Hg(II) species, as shown in Figure 1, to form an organomercury carbenium ion and also with HCl, H_2SO_4, and SO_2 to form carbenium ions with associated chloride and sulfate that can combine to form the observed organochlorine and, possibly, also ester moieties.

In tests conducted at relatively high HCl concentrations (50 ppm), the capture of mercury at the start was always very high (less than 5% of inlet concentration), but in very low HCl concentrations such as those obtained when low-Cl coals are burned (1 ppm), an initial breakthrough was observed at about 50%–60% of inlet (9), followed by an increase in capture efficiency to the 5%–10% level. The higher HCl concentration thus eliminated this induction period where poor capture is obtained. It is clear that HCl is not an oxidizing reagent, since it already in the most reduced state. This is, therefore, a promotional effect of the HCl on the activity of the carbon in catalyzing the oxidation of mercury. A similar promotional effect of adding aqueous HCl to the sorbent was reported recently by Ghorishi et al. (10). As shown in Figure 1, the Hg^0 is oxidized at the carbenium site. Thus oxidation and binding occur at different forms of the same carbon site (11). A primary oxidant (for example NO_2) completes the cycle so that Hg(II) can be released from the site after breakthrough.
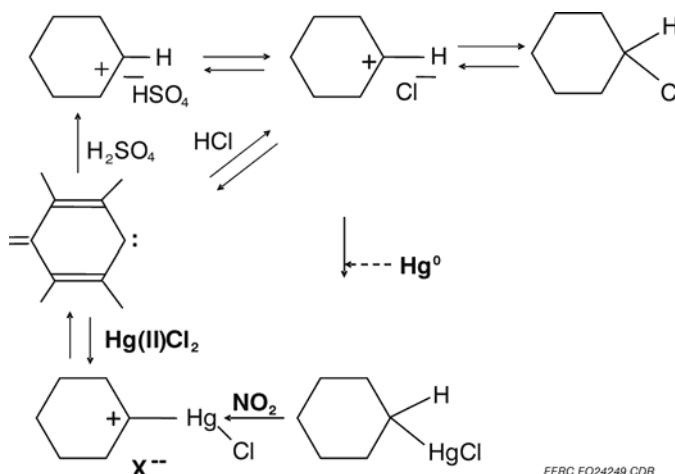

Figure 1. Oxidation mechanism – carbenium ion oxidant

A series of experiments was conducted to determine the effects of acid gas components on the kinetics of oxidation of Hg^0. These experiments use the effect described above that the oxidation of Hg continues long after the capacity of the carbon has been exceeded. Thus the oxidation is uncoupled from binding and can be studied independently of binding by measuring the concentration of Hg^0 in the effluent from the carbon bed where the influent gas composition and temperature are varied.

Experimental

The experimental procedure used a thin bed of the sorbent placed in a synthetic mixture of flue gas compositions, exactly as described previously (1, 2). Total and elemental mercury were continuously analyzed by online detection. The initial breakthrough as well as the oxidation experiments were conducted with high acid gas conditions, except when components (HCl, SO_2, and NO_2) were turned off sequentially to determine effects on the oxidation. In Set A, the gases were turned off after breakthrough, and the spent carbon was stored overnight. All gases were turned on the next day to initiate the set of experiments. In Set B, the set of experiments was initiated immediately after breakthrough.

Results
Set A (Single gas omitted)
Exp. 1. All gases on.
Hg^0 was at 0%. There was no increase of Hg^0 with time, indicating that SO_2 was not poisoning the oxidation sites. The total Hg was at 100% of inlet. Thus all Hg was emitted as oxidized mercury, consistent with earlier observations.

Exp. 2. HCl off.
Hg^0 increased slightly (to 2% of inlet) ($\mu g/m^3$) indicating that the HCl is not a requirement for oxidation and has only a small promotion effect on the oxidation rate when all the sites are already acid-promoted. Total Hg decreased significantly over 45 min (to 55%) ($\mu g/m^3$) This indicates that there is less conversion of bound Hg(II) to volatile products when HCl is absent.

Exp. 2A. HCl turned back on (original condition).
Hg^0 decreased to 1%. Since it did not return to 0%, it suggests that the oxidation became slightly poisoned. Total Hg jumped back up to 150% then leveled at 100% (somewhat erratic). This indicates that HCl is available for conversion to volatile products, giving an initial spike of $HgCl_2$ from Hg(II) that had been accumulating.

Exp. 3. NO_2 off.
Hg^0 increased significantly (up to 10% and leveled out), indicating that oxidation of Hg is less effective without NO_2, but still occurs. Total Hg increased significantly, then came back down to 90%. Explanation is that less H_2SO_4 formed, so more HCl binds and frees Hg as $HgCl_2$. Then the loss of H_2SO_4 by evaporation results in the capacity being not entirely filled.

Exp. 3A. NO_2 back on (original condition).
Hg^0 dropped back down to 2%, indicating effective oxidation returned. Total Hg was at about 100%.

Exp. 4. SO_2 off.
Hg^0 increased very slightly from 2.0% to 2.4% over 2.3 hr, indicating that SO_2 has little effect on oxidation of Hg^0. Total Hg increased significantly, then came back down to 90%, for the same reason as Exp. 3.

Set B (one, two, and three gases omitted)
Exp. 1. All gases on.
Hg^0 increased from 0% to 5% over 2 hr, then leveled out at 5%.

Exp. 2. NO_2 off.
Hg^0 increased from 5% to 12.5% and leveled out, consistent with the NO_2 oxidation effect (Set A).

Exp. 3. HCl and NO_2 both off.
Hg^0 increased from 12.5% to 14.5% and leveled off. The effects of turning off these is exactly additive. Total Hg decreased to 50%, consistent with the decrease in emission seen in Set A when HCl was off.

Exp. 4. HCl, NO_2, and SO_2 all off.
Hg^0 decreased to 11%, indicating a small negative effect on oxidation for SO_2, but only with the HCl off. Total Hg decreased further to 30%, indicating some restoration of binding sites.

Exp. 5. HCl turned on, NO_2 and SO_2 off.
Hg^0 stayed level at 11%, consistent with the small HCl oxidation effect when carbon is acid-promoted. Total Hg increased to 80%, consistent with HCl liberation of bound Hg(II).

Exp. 6. NO_2 turned on, HCl on, SO_2 still off.
Hg^0 dropped to 5% baseline, consistent with positive NO_2 effect on oxidation and negligible SO_2 effect on oxidation.

Exp. 7. NO_2 on, HCl turned off, SO_2 off.
Hg^0 increased slightly to 5.5%, consistent with small rate increase for HCl. Total Hg decreased to 70%, consistent with HCl effect on volatilization of bound Hg(II).

Conclusions

By decoupling the oxidation of Hg^0 from the binding of Hg(II) by using beds of spent sorbent that emit mostly Hg(II), we demonstrated that the effects of acid gases on the oxidation rate are in agreement with the oxidation-binding model. The flow throughout the experiments showed that SO_2 exerts very little poisoning effect on oxidation. NO_2 at 6 ppm is highly beneficial for the oxidation kinetics and, therefore, plays a major role in oxidation. HCl exhibits a much smaller effect. These experiments allow us to calculate space velocities for mercury oxidation. The oxidation rates were faster at higher temperatures, in contrast to the negative effects of temperature on capacity. The negative effect is, however, due to the increase in sulfur oxidation at higher temperature, which poisons the carbon more quickly. Further experiments with other gas components showed that oxygen and NO also are able to oxidize Hg^0 on the carbon surface, but require much higher concentrations.

References
(1) Miller, S.J.; Dunham, G.E.; Olson, E.S.; Brown, T.D. *Fuel Process. Technol.* **2000**, *65–66*, 343–363.
(2) Olson, E.S.; Miller, S.J.; Sharma, R.K.; Dunham, G.E.; Benson, S.A. *J. Hazard. Mater.* **2000**, *74*, 61–79.
(3) Laumb, J.D.; Benson, S.A.; Olson, E.S. *Fuel Process. Technol.* **2004**, *85* (6–7), 577–585.

(4) Olson, E.S.; Crocker, C.R.; Benson, S.A.; Pavlish, J.H.;
     Holmes, M.J. *J. Air Waste Manage*. **2004**.
(5) Olson, E.S.; Laumb, J.D.; Benson, S.A.; Dunham, G.E.;
     Sharma, R.K.; Miller, S.J. Pavlish J.H. Prepr. Pap*.—Am.
     Chem. Soc., Div. Fuel Chem.* **2002**, *47* (24), 481.
(6) Olson, E.S.; Thompson, J.S.; Pavlish, J.H. *Anal. Bioanal.
     Chem.* **2002**, *374*, 1045.
(7) Olson, E.S.; Laumb, J.D.; Benson, S.A.; Dunham, G.E.;
     Sharma, R.K.; Miller, S.J.; Pavlish, J.P. *Prepr. Pap.—Am.
     Chem. Soc., Div. Fuel Chem.* **2003**, *48* (1), 30–31.
(8) Radovic, L.R.; Bockrath, B. *Prepr. Pap.—Am. Chem. Soc.,
     Div. Fuel Chem.* **2002**, *47* (2), 428.
(9) Pavlish, J.H.; Holmes, M.J.; Benson, S.A.; Crocker, C.R.;
     Galbreath, K.C. In *Proceedings of the Air Quality III:
     Mercury, Trace Elements, and Particulate Matter Conference*;
     Arlington, VA, Sept 9–12, 2002; Paper A4-4.
(10) Ghorishi, S.B.; Keeney, R.M.; Serre, S.D.; Gullet, B.K.;
     Jozewicz, W.S. *Environ. Sci. Technol.* **2002**, *36*, 4454–4459.
(11) Olson, E.S.; Laumb, J.D.; Benson, S.A.; Dunham, G.E.;
     Sharma, R.K.; Mibeck, B.A.; Miller, S.J.; Holmes, M.J.;
     Pavlish, J.H. *J. Phys. IV France* **2003**, *107*, 979–982.

SURFACE CHEMISTRY AND REACTIVITY OF AMORPHOUS CARBON NITRIDE (a-CN$_X$) FILMS

A. Lagrini [a], H. Cachet [a], C. Debiemme-Chouvy [a],
C. Deslouis [a], V. Vivier [a], M. Benlahsen [b], S. Charvet [b]

[a]UPR 15 CNRS "LISE", Univ. P. et M. Curie, 4 place Jussieu, 75252, Paris Cedex 05, France
[b]LPMC UPRES-EA 2081, Université de Picardie, 33 rue Saint Leu, 80039 Amiens Cedex 1, France

Introduction

Diamond Like Carbon (DLC) or Boron or Nitrogen Doped Diamond (BDD or NDD) materials are extensively studied due to their large potential window in water solvent together with a relatively high surface reactivity. This makes them appropriate for a wide range of applications to electroanalytical chemistry or water treatment.

However, several factors may affect this reactivity: mode of synthesis, pre-treatment, dopant content… In particular, different values of the apparent rate constant for fast outer-sphere electrochemical reactions have been measured on BDD ($k_0 \leq 10^{-2}$ cm.s^{-1}) depending on the boron content [1-4]. Significant values ($k_0 \sim 10^{-2}$ cm.s^{-1}) have been also found for NDD [5]. For DLC materials like a-CN$_x$H$_y$ or a-CN$_x$ similar values have been obtained: lower values ($k_0 \sim 10^{-4}$ cm.s^{-1}) for the former [6] and presumably higher ones for the latter [7] because the potential difference between the oxidation and reduction peaks was found around 70 mV, a value ascribable to a quasi-reversible system. These rate constant values strongly depend on the surface state of the materials and it has been early observed that pre-treatments, either electrochemical or by plasma, have a crucial influence [8-12].

Several investigations tried to correlate the electrochemical reactivity with the electrochemical, chemical or plasma-assisted pre-treatments of the material surface and the nature of the terminations, –O or –H, was invoked to explain the observed effects. Latto *et al.* [8] showed for the ferri-ferrocyanide couple that an oxidizing pre-treatment on BDD films enhances the electron transfer rate. In most cases however, cathodic pre-treatments resulted in improved electron transfer [9-12]. Anodic pre-treatment is likely to form carbonyl or carboxyl groups which are nucleophilic and therefore slow down the electron transfer for outer-sphere redox reactions. Conversely, electrophilic terminations resulting from a cathodic pre-treatment favour the electron transfer rate.

In this work, electrochemical techniques (Cyclic Voltammetry (CV), Electrochemical Impedance Spectroscopy (EIS), Scanning Electrochemical Microscopy (SECM)) and X-Ray Photoelectron Spectroscopy (XPS) were combined to characterize the surface state and the effect on the outer-sphere reaction (ferri-ferrocyanide system) between as-prepared and cathodically pre-treated a-CN$_x$ samples.

Experimental

Films synthesis. The a-CN$_x$ films were elaborated using a radiofrequency (13.56 MHz) magnetron sputtering technique of a graphite target by a plasma of argon diluted with nitrogen. This mixture plays the role of sputtering and reacting gas and its pressure was kept constant at 1 Pa. All other details can be found in [13]. An optimum of both the electrochemical reactivity for ferri-ferrocyanide system and bulk electrical conductivity was found for an atomic nitrogen percentage in the film of 13% corresponding to a partial pressure of nitrogen in the gas of 0.03 Pa [13]. This content was

chosen here. The substrates were highly doped Si (100) wafers. The thickness of the deposited films was about 200 nm.

Electrochemical characterization methods. The electrochemical reactivity was assessed using CV and EIS. A three-electrode cell arrangement was used with a saturated calomel electrode (SCE) as reference electrode, a large area platinum mesh as counter electrode and the carbon film on Si wafer as working electrode. The electrolytes consisted of a H$_2$SO$_4$ solution for electrode activation, of a LiClO$_4$ solution to determine the potential window and finally of a KCl solution containing an equimolar concentration of ferri-ferrocyanide species (10^{-2} M) to study the electrode reactivity. The temperature was maintained at 25°C. The electrolyte was quiescent. An AUTOLAB 30 (METROHM) interface was used for electrochemical measurements.

The SECM apparatus allowing to check the surface reactivity in the micrometer range was a home-made device already described in [14]. The electrochemical tip was a 10 μm in diameter platinum microelectrode.

The nitrogen amount at the film surface was evaluated by XPS. The analysis was performed using an ESCALAB 250i-XL apparatus equipped with a monochromated Al K$_\alpha$ X-ray source and a hemispherical analyzer. In this system, binding energy was referenced to the Au$_{4f7/2}$ peak (at 83.8 eV). The C1s peak on Au was observed at 285.0 eV.

Results and Discussion

The sample was tested first as-prepared and then after a cathodic treatment by cycling the potential between -1.5 and -0.5 V/SCE for 10 minutes in 0.5 M H$_2$SO$_4$. The CV curves in the absence of redox couple confirm that this material provides a wide potential window (see Figure 1). In the presence of the redox couple (see figure 2), the pre-treatment markedly increases the surface reactivity. It is noteworthy that the pre-treatment also improves the potential window which is increased by about 0.5 V with respect to the as-prepared sample.
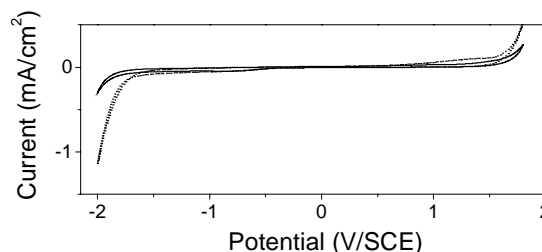
Figure 1. CV curves for the a-CN$_x$ sample in a 0.5M LiClO$_4$ solution. (….), as-prepared sample; (——), cathodically pre-treated sample. Scan rate : 50 mV/s.
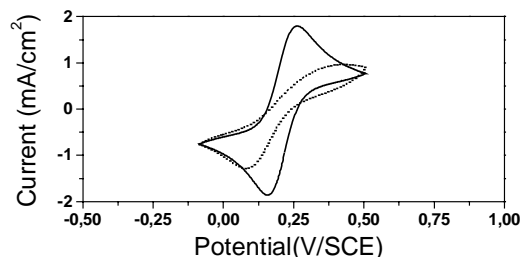

Figure 2. CV curves for the a-CN$_x$ sample in a 10^{-2} M Ferri-ferrocyanide + 0.5M KCl solution. (….), as-prepared sample; (——), cathodically pre-treated sample. Scan rate : 50 mV/s.

From EIS data, the apparent rate constant k_0 was determined for the two types of samples. This parameter can be obtained by measuring the charge transfer resistance R_t which represents the electron transfer at the solution/a-CN$_x$ interface:

$$k_0 = RT/(F^2 A R_t C)$$

R is the molar gas constant (8.32 J.mol^{-1}K^{-1}), T the temperature (°K), F the Faraday constant (96485 Coulombs), A the electrode area (6×10^{-5} m^2) and C the ferri-ferrocyanide concentration (10 mol.m^{-3}). k_0 increases from 2.9×10^{-4} cm/s for the as-prepared sample to 1.8×10^{-3} cm/s for the pre-treated one.
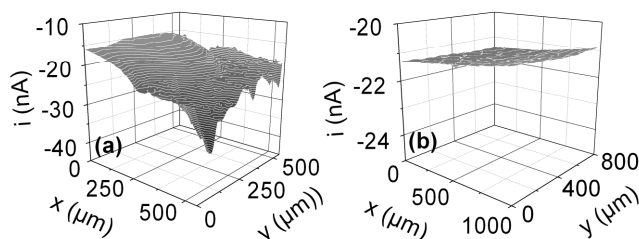
Figure 3. SECM mapping of the local current density over the same samples as in figure 2. (a) as-prepared sample ; (b) cathodically pre-treated sample. Electrolyte : 10^{-2}M [Fe(CN)$_6$]$^{3-}$, 0.5 M KCl.

Simultaneous SECM measurements were carried out in the same interface conditions. The tip was always polarized at a potential corresponding to the reduction of ferricyanide ($E = - 0.2$ V/SCE). Conversely, the substrate was polarized at a potential corresponding to the oxidation of ferrocyanide. The system operated in the so-called positive feedback conditions. The approach curves at any point are well fitted and the adjustable parameter is the apparent standard rate constant k_0 of the oxidation reaction ferro- to ferricyanide. The result is an image which contains the reaction rate as parameter and the surface can be mapped *vs*. local current and therefore *vs*. local reaction rate. The curves in figure 3a have been obtained for the as-prepared sample and show that the reaction rate and therefore reactivity is not uniform. After cathodic treatment, the reaction rate becomes perfectly uniform (see the figure 3b) and the overall variations do not exceed 2.5%.

Table 1. Superficial Atomic Contents in C and N elements and ratios of =N / N$_{total}$ % and −N / N$_{total}$% for the as-prepared and cathodically pre-treated sample determined by XPS.

a-CN$_x$ Sample	C / at.%	N / at.%	=N / N$_{total}$%	−N / N$_{total}$%
As-prepared	87	13	42	58
After cathodic pre-treatment	91	9	54	46

XPS measurements have been carried out to characterize the surface modifications associated with the cathodic treatment. It was showed by XPS [13] that the microstructure of a-CN$_x$ films is explained by the substitution of carbon atoms in the graphitic clusters by nitrogen atoms, which break the long-range order of the graphitic structure and promote the clustering of sp^2 sites. The N-Csp^3, N=Csp^2 and C=Csp^2 bonds have been characterized *vs*. the increasing amount of nitrogen. It has thus been shown that the amount of N-Csp^3 and

N=Csp^2 bonds increases while that of C=Csp^2 bonds decrease, suggesting the dissociation of the C=Csp^2 bonds and the recombination in N-Csp^3 and N=Csp^2 bonds. The main effect of nitrogen is thus to increase sp^2 fraction and the clustering of sp^2 phase. The resulting structures were assumed to be mainly bonded at the edges of Csp^2 graphitic clusters in planar position as well as in out-of-planar positions. The XPS spectra recorded before and after electrochemical treatment display two main results (see Table 1): The atomic surface contents of carbon and nitrogen are 87 and 13% respectively before treatment. After treatment, they become respectively 91 and 9%. When one looks more specifically how these changes have occurred, it appears that C-N bonds which were dominant for the as-prepared samples have decreased due to the electrochemical treatment.

This brings another contribution to the fact that electron transfer occurs through the sp^2 sites as already proposed for BDD for which it was shown that graphitic sites were the preferred sites for electron exchange. Due to the overall decrease of the atomic nitrogen content, it appears that there is no exchange between the two types of sites but rather a removal of the C-N bonds, possibly by reduction of those sites and NH$_3$ evolution.

Conclusion

Combining the results of the different techniques, it can be inferred that before treatment the situation is rather that of a partition of the interface between active and insulating sites, the former being sp^3 C=N sites and the latter sp^3 C-N sites. Such a distribution of sites has been invoked in the case of BDD by Becker and Jüttner [4] who postulated that the centre parts of the microcrystalline domains were inactive, while the grain boundary domains full of graphitic zones behaved as active sites.

References
(1) R. Ramesham, *Thin Solid Films*, **1999**, 339.
(2) M.C. Granger and G.M. Swain, *J. Electrochem. Soc.*, **1999,** 146, 4551.
(3) C. Lévy-Clément, F. Zenia, N.A. Ndao, A. Deneuville, *New Diamond and Frontier Carbon Technology*, 1999, 9(3), 189.
(4) D. Becker and K. Jüttner, *Electrochimica Acta*, 2003, 49, 29.
(5) Q. Chen, D.M. Gruen, A.R. Krauss, T.D. Corrigan, M. Witek, G.M. Swain, *J. Electrochem. Soc.*, **2001,** 148, E44.
(6) H. Cachet, C. Deslouis, M. Chouiki, B. Saidani, N.M.J. Conway, C. Godet, *J. Electrochem. Soc.*, **2002**, 149, E233.
(7) A. Lagrini, C. Deslouis, H. Cachet, M; Benlahsen, S. Charvet, *Electrochem. Comm.*, **2004**, 6, 245.
(8) M.N. Latto, D. Jason Riley, P.W. May, *Diamond Relat. Mater.*, **2000**, 9, 1181.
(9) S.Ferro, A. De Battisti, *Electrochimica Acta*, **2002**, 47, 1641.
(10) T. Kondo, K. Honda, D.A. Tryk, A. Fujishima, *Electrochimica Acta*, **2003**, 48, 2739.
(11) I. Yagi, H. Notsu, T. Kondo, D.A. Tryk, A. Fujishima, *J. Electroanal. Chem.*, **1999**, 473, 173.
(12) H.B. Suffredini, V.A. Pedrosa, L. Codognoto, S.A.S. Machado, R.C. Rocha-Filho, L.A. Avaca, *Electrochimica Acta*, **2004**, 49, 4021.
(13) A. Lagrini, S. Charvet, M. Benlahsen, C. Debiemme-Chouvy, C. Deslouis, H. Cachet, *Thin Solid Films*, in press.
(14) C. Gabrielli, F. Huet, M. Keddam, Ph. Rousseau, V. Vivier, *J. Phys. Chem. B*, **2004**, 108, 11620.

CONTROLLED RADICAL POLYMERIZATION OF POLYACRYLONITRILE INITIATED FROM SURFACE OF NANOPOROUS SILICA AND SYNTHESIS OF POROUS CARBON FROM POLYACRYLONITRILE GRAFT

Michal Kruk,[§] Bruno Dufour,[§] Ewa B. Celer,[‡] Tomasz Kowalewski,[§] Mietek Jaroniec[‡] and Krzysztof Matyjaszewski[§]

[§] Department of Chemistry, Carnegie Mellon University, 4400 Fifth Avenue, Pittsburgh, PA 15213, USA; [‡] Department of Chemistry, Kent State University, Kent, OH 44242, USA

Introduction

Ordered mesoporous carbons (OMCs) [1,2] are a new family of materials that are synthesized using ordered mesoporous silicas as templates.[3,4] It should be noted here that mesopores are defined as pores of diameter from 2 to 50 nm. Due to their high surface area and large mesopore volume, these carbons are attractive as adsorbents for large, hydrophobic molecules, chromatographic packings, catalyst supports, and components of electrochemical double-layer capacitors, fuel cells and Li-ion batteries.[5,6] At present, there is much interest in the ordered mesoporous carbons with semi-graphitic or graphitic pore walls,[7] which are attractive from the point of view of applications in chromatography and applications requiring good electrical conductivity. Several different carbon precursors were used for the synthesis of such OMCs, including aromatic hydrocarbons,[7,8] mesophase pitch,[9] and petroleum pitch.[10] Polyacrylonitrile (PAN) is another attractive carbon precursor, which is commonly used in the synthesis of carbon fibers. Recently, the synthesis of nanostructured carbon films and carbon nanoobjects from PAN-containing block copolymers was reported.[11,12] Herein, the synthesis of OMCs from PAN is presented. A detailed account of this work will be reported elsewhere.[13] PAN was introduced into the pores of the silica templates using surface-initiated atom transfer radical polymerization,[14,15] which is one of the living polymerization methods. We are aware of only one prior report on the synthesis of OMCs from PAN,[16] and our carbons have much higher adsorption capacities and mesopore diameters, which can be attributed to our unique synthesis method.

Experimental

Materials. Ordered mesoporous silica templates with 2-dimensional hexagonal structure (SBA-15)[4] and with predominantly cubic close-packed structure (FDU-1)[17,18] were synthesized using block copolymer templates (Pluronic P123, $EO_{20}PO_{70}EO_{20}$, BASF; B50-6600, $EO_{39}BO_{47}EO_{39}$, Dow) using literature procedures with appropriate modification of the synthesis time and temperature.[13] The ATRP initiator sites were introduced on the silica surface through a reaction with 1-(chlorodimethylsilyl)propyl 2-bromoisobutyrate. The surface was further reacted with trimethylchlorosilane. The acrylonitrile polymerization was carried out in N,N-dimethylformamide at 55°C using CuCl and 2,2'-dipyridyl as catalyst. In some cases, $CuCl_2$ was added to improve the control over initial stages of the polymerization process. The polymerization time ranged from one hour to seven days. PAN was converted to carbon through the stabilization by heating under air to 300°C and carbonization at 800°C for three hours. The silica template was dissolved in NaOH solution to isolate the carbon material.

Measurements. N_2 adsorption measurements were performed on Micromeritics ASAP 2010 and 2020 volumetric adsorption analyzers. Transmission electron microscopy (TEM) images were recorded using a JEOL 200EX instrument operated at 200 kV. Raman spectra were collected on a Jobin Yvon T64000 Raman system (ISA, Edison, NJ) with microprobe sampling optics. The excitation was at 514.5 nm (Ar^+ laser, Model 95, Lexel Laser, Fremont, CA).
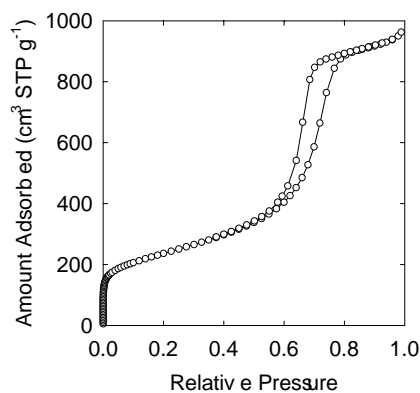
Results and Discussion

SBA-15 and FDU-1 silica templates exhibited the total pore volumes of 0.9-1.25 cm^3 g^{-1} and pore diameters of 11-14 nm. After reaction with chlorosilane containing 2-bromoisobutyrate groups, and subsequent reaction with trimethylchlorosilane, the total pore volume decreased to 0.6-0.7 cm^3 g^{-1}, and pore diameter decreased by 1.5-2 nm. After acrylonitrile polymerization for 1-2 days, the pores were not accessible to nitrogen. In the case of SBA-15 template, the polymerization of AN for one day was sufficient to attain PAN content that would approximately correspond to the essentially complete filling of the ordered mesopores with PAN. The stabilization of PAN under air and its carbonization under nitrogen afforded silica/PAN composites in which the content of the carbonaceous material was about 30 wt.%. Nitrogen adsorption isotherms for the silica/carbon composites with the aforementioned carbon content typically did not feature capillary condensation steps at relative pressures similar to those for the capillary condensation pressure in the mesopores of the silica template, which suggests that the mesopores of the template were uniformly filled with the carbonaceous material.

Shown in Figure 1 are TEM images of OMC synthesized using SBA-15 silica as a template, which was reported earlier to be suitable for the synthesis of OMCs from sucrose,[19] PAN[16] and other carbon precursors. As expected on the basis of cylindrical pore shape of the template, the carbon consisted of nanorods of uniform diameter, which were arranged in a 2-D hexagonal structure. A side projection of this structure produced a series of parallel stripes, whereas the projection along the rods gave rise to a honeycomb pattern, as seen in Figure 1.
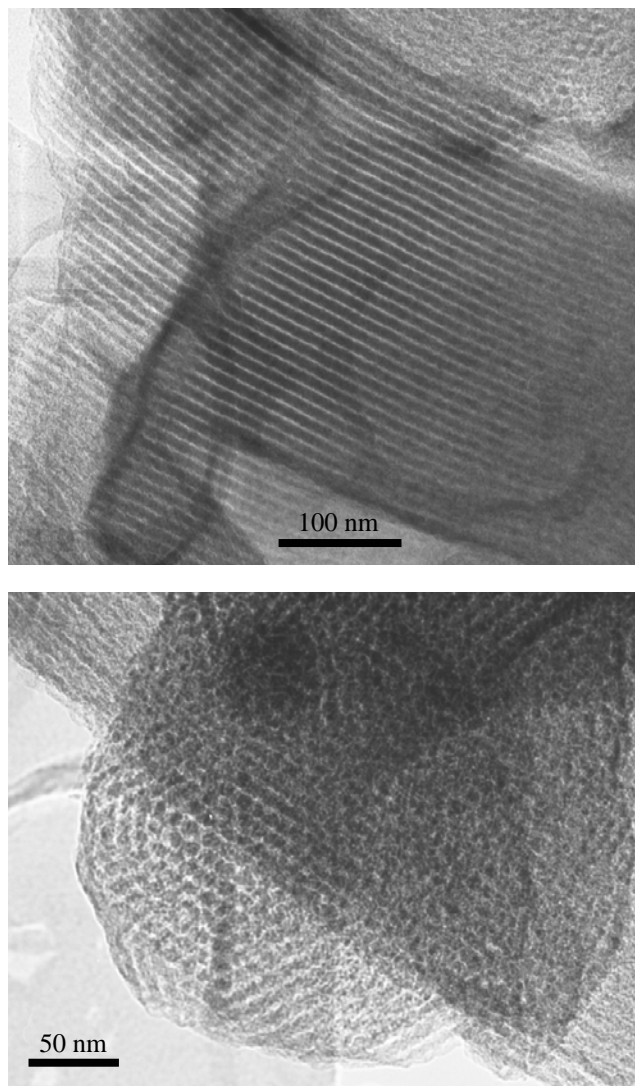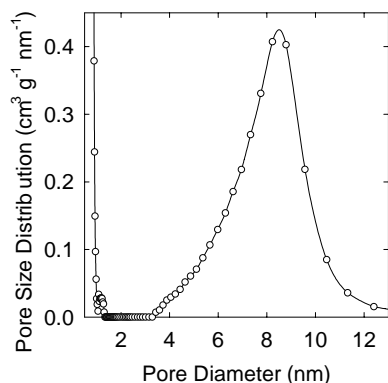
Figure 1. TEM images of an ordered mesoporous carbon synthesized from PAN using SBA-15 silica as a template.
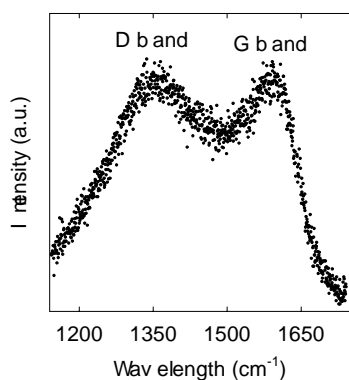

Figure 2. Nitrogen adsorption isotherm for an ordered mesoporous carbon synthesized from PAN using SBA-15 silica as a template.

Figure 3. Pore size distribution for an ordered mesoporous carbon synthesized from PAN using SBA-15 silica as a template.

The nitrogen adsorption isotherm for the carbon inverse replica of SBA-15 featured a prominent capillary condensation step at a relative pressure of 0.7-0.8 (see Figure 2), which is characteristic of mesoporous materials with narrow pore size distribution. The adsorption data allowed us to evaluate the BET specific surface area of 840 m^2 g^{-1}, the pore diameter of 8.5 nm and the total pore volume of 1.49 cm^3 g^{-1} (with a primary contribution from the volume of ordered mesopores). The adsorption data were also used to evaluate the micropore volume, which was typically below 0.1 cm^3 g^{-1} for carbons from PAN carbonized at 800°C. OMCs reported earlier exhibited either low microporosity and low mesopore volume, or appreciable microporosity and high mesopore volume. So, our carbons are unique examples of OMCs with high adsorption capacity and low microporosity. The pore diameter of 8.5 nm is very large as for an OMC, which is likely to be advantageous in some important prospective applications of OMCs, such as adsorption of large molecules and chromatography.

The ordering of the carbon frameworks on atomic scale was investigated using XRD and Raman spectroscopy. The XRD patterns for the carbons from PAN featured a peak at ~24°, and a weaker peak at 44°. These peaks can be indexed as (002) and (10) peaks of the graphitic carbon structure. The corresponding spacing between graphene sheets is ~0.37 nm, which is about 10% higher than that of graphite. Raman spectra (see Figure 4) featured G bands, which are characteristic of sp^2 carbons, and D bands, which are related to defective sites in the sp^2 carbon structure. On the basis of these results, one can conclude that our OMCs exhibit some extent of graphitic ordering, but the degree of perfection of the semi-graphitic structure is still quite low. Anyway, in comparison to mesoporous carbons prepared from other carbon precursors and carbonized at about 800°C,[10,20] the atomic scale ordering of these carbons is appreciable.

We also synthesized a well-ordered inverse replica of FDU-1 silica. Projections characteristic of face-centered cubic structure were clearly seen in TEM images for this OMC. The total pore volume was as high as 1.8 cm^3 g^{-1}. The carbon had a narrow pore size distribution centered at about 12 nm, which is the highest pore diameter for any OMC synthesized so far using ordered mesoporous silica templates. The carbon inverse replica of FDU-1 appears to be an array of three-dimensionally connected spheres. Only a few examples of similar OMC structures have been reported before.[21]

Figure 4. Raman spectra of an ordered mesoporous carbon synthesized from PAN using SBA-15 silica as a template.

Conclusions

PAN is an excellent precursor for the templated synthesis of ordered mesoporous carbons. The volume of ordered mesopores of the carbons from PAN tends to be higher than those of ordered mesoporous carbons prepared from other carbon precursors, with exception of some carbons with hollow (tubular) structures.[22] The carbons from PAN have low microporosity and some degree of ordering of graphene sheets in their frameworks. The surface-initiated atom transfer radical polymerization is a convenient way to uniformly infiltrate the silica template with carbon precursor.

References

(1) Ryoo, R.; Joo, S. H.; Jun, S. *J. Phys. Chem. B* **1999**, *103*, 7743.

(2) Lee, J.; Yoon, S.; Hyeon, T.; Oh, S. M.; Kim, K. B. *Chem. Commun.* **1999**, 2177.

(3) Kresge, C. T.; Leonowicz, M. E.; Roth, W. J.; Vartuli, J. C.; Beck, J. S. *Nature* **1992**, *359*, 710.

(4) Zhao, D.; Feng, J.; Huo, Q.; Melosh, N.; Frederickson, G. H.; Chmelka, B. F.; Stucky, G. D. *Science* **1998**, *279*, 548.

(5) Ryoo, R.; Joo, S. H.; Kruk, M.; Jaroniec, M. *Adv. Mater.* **2001**, *13*, 677.

(6) Lee, J.; Han, S.; Hyeon, T. *J. Mater. Chem.* **2004**, *14*, 478.

(7) Kim, T.-W.; Park, I.-S.; Ryoo, R. *Angew. Chem. Int. Ed.* **2003**, *42*, 4375.

(8) Kim, C. H.; Lee, D.-K.; Pinnavaia, T. J. *Langmuir* **2004**, *20*, 5157.

(9) Li, Z.; Jaroniec, M. *J. Phys. Chem. B* **2004**, *108*, 824.

(10) Vix-Guterl, C.; Saadallah, S.; Vidal, L.; Reda, M.; Parmentier, J.; Patarin, J. *J. Mater. Chem.* **2003**, *13*, 2535.

(11) Kowalewski, T.; Tsarevsky, N. V.; Matyjaszewski, K. *J. Am. Chem. Soc.* **2002**, *124*, 10632.

(12) Tang, C.; Qi, K.; Wooley, K. L.; Matyjaszewski, K.; Kowalewski, T. *Angew. Chem. Int. Ed.* **2004**, *43*, 2783.

(13) Kruk, M.; Dufour, B.; Celer, E. B.; Kowalewski, T.; Jaroniec, M.; Matyjaszewski, K. *J. Phys. Chem. B*, submitted for publication.

(14) Matyjaszewski, K.; Xia, J. *Chem. Rev.* **2001**, *101*, 2921.

(15) Wang, J.-S.; Matyjaszewski, K. *J. Am. Chem. Soc.* **1995**, *117*, 5614.

(16) Lu, A.; Kiefer, A.; Schmidt, W.; Schueth, F. *Chem. Mater.* **2004**, *16*, 100.

(17) Yu, C.; Yu, Y.; Zhao, D. *Chem. Commun.* **2000**, 575.

(18) Matos, J. R.; Kruk, M.; Mercuri, L. P.; Jaroniec, M.; Zhao, L.; Kamiyama, T.; Terasaki, O.; Pinnavaia, T. J.; Liu, Y. *J. Am. Chem. Soc.* **2003**, *125*, 821.

(19) Jun, S.; Joo, S. H.; Ryoo, R.; Kruk, M.; Jaroniec, M.; Liu, Z.; Ohsuna, T.; Terasaki, O. *J. Am. Chem. Soc.* **2000**, *122*, 10712.

(20) Kim, S.-S.; Shah, J.; Pinnavaia, T. J. *Chem. Mater.* **2003**, *15*, 1664.

(21) Fan, J.; Yu, C.; Gao, F.; Lei, J.; Tian, B.; Wang, L.; Luo, Q.; Tu, B.; Zhou, W.; Zhao, D. *Angew. Chem. Int. Ed.* **2003**, *42*, 3146.

(22) Joo, S. H.; Choi, S. J.; Oh, I.; Kwak, J.; Liu, Z.; Terasaki, O.; Ryoo, R. *Nature* **2001**, *412*, 169.

DESIGN OF EFFICIENT PHOTOCATALYSTS USING SIC-TIC NANO PARTICLES FOR DEGRADATION OF ORGANIC POLLUTANTS DILUTED IN WATER

Hiromi YAMASHITA[1], Yoshikatsu NISHIDA[1],
Osamu CHIYODA[1], Iwao KATAYAMA[1], Masaki NARISAWA[2]*

*[1]Department of Materials Science and Processing,
Graduate School of Engineering, Osaka University
2-1, Yamada-oka, Suita, Osaka 565-0871, Japan.
E-Mail: yamashita@mat.eng.osaka-u.ac.jp
TEL & FAX: +81-6-6879-7457

[2]Department of Materials Engineering,
Graduate School of Engineering, Osaka Prefecture University
1-1, Gakuen-cho, Sakai, Osaka 599-8531, Japan.

Introduction

Several kinds of application of photocatalyst system had been of vital interest. The design of highly efficient photocatalytic systems which work for the reduction of global atmospheric pollution and the purification of polluted water is attractive and one of the most desirable yet challenging goals in the research of environmentally-friendly catalysts [1-10]. TiO_2 semiconductor photocatalysts are known as one of the most stable and highly reactive catalysts. Also the utilization of extremely small TiO_2 particles as photocatalysts has recently attracted a great deal of attention, especially for such environmental applications. On the other hand, SiC has high mechanical strength and is easy to be molded into a filter. Although it may be a useful support for photocatalysts used in liquid phase, there have been no reports on the properties of TiO_2 photocatalysts deposited on SiC.

In the present study, we deal with the preparation and characterization of TiO_2 photocatalysts deposited on SiC using the precursor of SiC-TiC powders [11] and carried out its successful utilization for the photocatalytic degradation of 2-propanol diluted in water. Moreover, the advantages of SiC-TiC powders as the precursor of the efficient TiO_2 photocatalysts have been clarified.

Experimental

On the basis of the process reported in the previous study [11], the liquid mixtures of tetraethyl orthosilicate, titanium tetraisopropoxide and phenolic resin were prepared. After the continuous stirring of the mixtures, the acid catalyst (30 wt% of toluenesolfonic acid solution in water) was added and stirred up to the gelation. The obtained gels were dried in vacuum, crushed and pyrolyzed at 1273 K (heating rate: 5 K/min, holding time: 1 h) in a nitrogen atmosphere (heating rate: 1 L/min). The precursor pyrolyzed at 1273 K was put into the graphite furnace preheated at 1873 K under Ar flow rate of 1 *l*/min to yield the SiC-TiC powders by carbothermic reduction. The obtained SiC-TiC powders were then calcined in air at 773 K and 1073 K for 5 h to synthesize TiO_2 deposited on SiC powder (TiO_2-SiC). The XANES spectra were obtained in the fluorescence mode at the BL-9A facility of the Photon Factory at the National Laboratory for High Energy Physics, Tsukuba.

The photocatalyst (50 mg) was transferred to a quartz cell with an aqueous solution of 2-propanol (2.6×10^{-3} mol dm^{-3}, 25 ml). Prior to UV irradiation, the suspension was stirred for 1 h under dark conditions. The sample was then irradiated at 295 K using UV light ($\lambda > 250$ nm) from a 100 W high-pressure Hg lamp with continuous stirring under O_2 atmosphere in the system. The products were analyzed by gas chromatography.

Results and Discussion

Figure 1 shows the XRD patterns of untreated SiC-TiC and TiO_2-SiC photocatalysts prepared by the oxidation of SiC-TiC at 773 K and 1073K, respectively. In the SiC-TiC sample, the formation of SiC and TiC crystalline phases were observed. After the oxidation of SiC-TiC sample at 773 K and 1023 K, the formation of the mixture of anatase and rutile phase of TiO_2 crystalline was observed clearly. On the other hand, TiO_2/SiO_2 photocatalysts prepared by the sol-gel method and calcined at 773 K exhibited no XRD peak due to the crystallized phases, indicating that the TiO_2 species exist in an amorphous phase or as ultrafine particles.
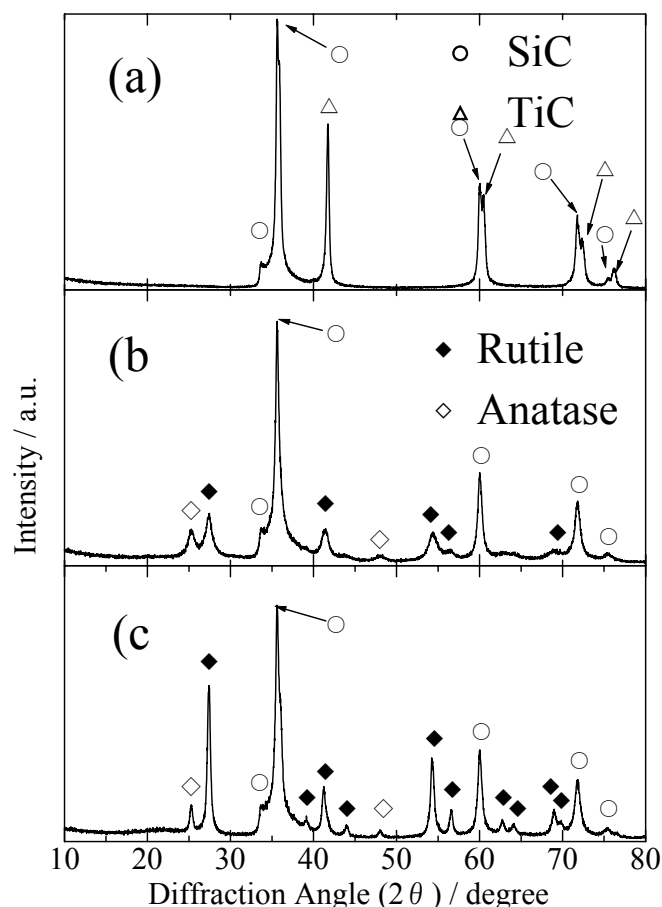

Figure 1. XRD patterns of untreated SiC-TiC (a) and TiO_2-SiC photocatalysts prepared by the oxidation at 773 K (b) and 1073K (c), respectively.

The XANES spectra at the Ti K-edge showed several well-defined preedge peaks which are related to the local structure surrounding the Ti atom. The relative intensities of these preedge peaks provide useful information on the coordination number of the Ti atom [5-10]. TiO_2-SiC prepared by the oxidation at 773 K and 1073 K exhibited three small well-defined preedge peaks which can be assigned to the presence of the mixture of anatase and rutile TiO_2 species (octahedral coordination) with high crystallinity. On the other hand, TiO_2/SiO_2 exhibited only one intense peak, indicating the presence of amorphous TiO_2 species or tetrahedral coordinated titanium oxide species. These results indicate that the titanium oxide species can be crystallized easily to form the mixture of anatase and rutile TiO_2 ultrafine particles on the support of hydrophobic SiC.

The Ti2p and Si2p XPS spectra were measured with untreated SiC-TiC and TiO_2-SiC photocatalysts prepared by the oxidation at 773 K and 1073 K, respectively. The changes in the spectra with samples indicated that by the oxidation treatment not only TiC was oxidized into TiO_2 but also partial of surface SiC was also oxidized into SiO_2.

Figure 2 shows the reaction time profiles of the liquid-phase photocatalytic reaction on the SiC-TiC sample and TiO_2-SiC photocatalyst. In the initial stage of the reaction under dark conditions, the adsorption of 2-propanol onto the photocatalysts can be observed. When UV light is turned on, 2-propanol is decomposed into acetone, CO_2 and H_2O, and finally, acetone is also decomposed into CO_2 and H_2O. TiO_2-SiC photocatalyst exhibited the higher photocatalytic reactivity than a commercial TiO_2 powder (P-25) and TiO_2 loaded on SiO_2 (TiO_2-SiO_2) prepared by the sol-gel method. The amount of H_2O adsorption on TiO_2-SiC is much smaller than TiO_2-SiO_2, suggesting that the hydrophobic property of TiO_2-SiC is one of the important determining factors in the efficient photocatalytic reactivity for the liquid phase reaction [6]. Furthermore, the high conductivity of SiC is preferable for the efficient charge separation on the irradiated TiO_2 photocatalyst. These results indicate that TiO_2-SiC photocatalyst is more effective for the degradation of organic compounds diluted in water than the commercial TiO_2 powder and TiO_2-SiO_2 photocatalyst.
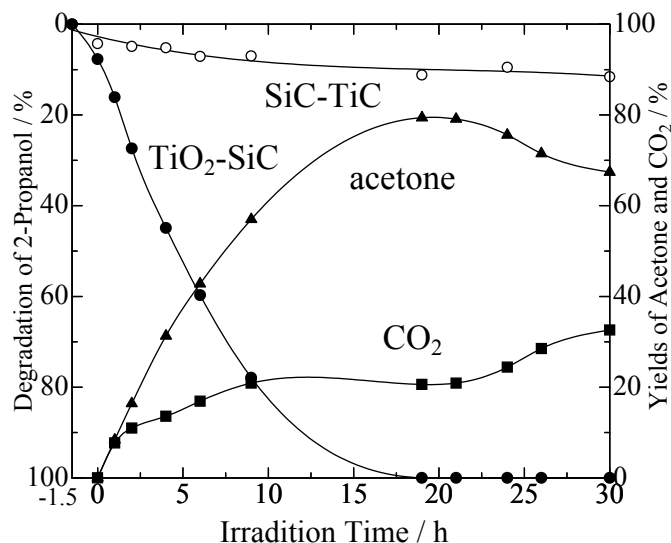
Figure 2. Photocatalytic degradation of 2-PrOH diluted in water on untreated SiC-TiC and TiO_2-SiC photocatalyst prepared by the oxidation at 1073 K.

Conclusions

It has been found that TiO_2 photocatalysts deposited on SiC (TiO_2-SiC) prepared by an oxidation of the precursor SiC-TiC nano-powders showed higher photocatalytic reactivity for the degradation of 2-propanol diluted in water than commercial TiO_2 powder in comparing their relative reactivities per weight of TiO_2. The formation of well-crystallized TiO_2 on SiC and the unique properties of SiC such as hydrophobic surface property and high conductivity were found to be related to the efficient photocatalytic reactivity of TiO_2-SiC. Since SiC is mechanically strong enough to be used as a filter for water purification, SiC-TiC is a good candidate for the precursor for TiO_2 supported photocatalysts used in liquid phase reactions.

References
(1) Minero, C.; Mariella, G.; Maurino, V.; Pelizzetti, E. *Langmuir* **2000**, *168*, 964.
(2) Takeda, N.; Torimoto, T.; Sampath, S.; Kuwabata, S.; Yoneyama, H.; *J. Phys. Chem.*, **1995**, *99*, 9986.
(3) Horikoshi, S.; Hidaka, H.; Serpone, N. *Env. Sci. Tech.* **2002**, *36*, 1357.
(4) Yamashita, H.; Takeuchi, M.; Anpo, M. In *Encyclopedia of Nanoscience and Nanotechnology Vol. 10*; Nalwa, H. S., Ed.; American Scientific Publishers: Stevenson Ranch, **2004**; pp. 639-654.
(5) Yamashita, H.; Anpo, M. *Current Opinion in Solid State & Materials Science*, **2004**, *7*, 471.
(6) Yamashita, H.; Maekawa, K.; Nakatani, Y.; Park, J.-J..; Anpo, M. *Chem. Lett.*, **2003**, 930.
(7) Yamashita, H.; Harada, M.; Tanii, A.; Misaka, J.; Nakao, H.; Anpo, M. *Mol. Crys. Liq. Crys.*, **2002**, *388*, 39.
(8) Yamashita, H.; Honda, M.; Harada, M.; Ichihashi, Y.; Anpo, M.; Hatano, Y. *J. Phys. Chem. B*, **1998**, *102*, 10707.
(9) Yamashita, H.; Kawasaki, S.; Ichihashi, Y.; Harada, M.; Anpo, M.; Stewart, G.; Fox, M. A.; Louis, C.; Che, M.; *J. Phys. Chem. B*, **1998**, *102*, 5870.
(10) Yamashita, H.; Ichihashi, Y.; Harada, M.; Stewart, G.; Fox, M. A.; Anpo, M. *J. Catal.*, **1996**, *158*, 97.
(11) Narisawa, M.; Ukon, H.; Okamura, K.; Shimada S.; Kamiyama, T. *J. Ceram. Soc. Jpn.*, **2002**, *110*, 518.

ADHESION BEHAVIOR BETWEEN CARBON FIBERS AND MODEL POLYMER MATRICES

Frank Thielmann[1], Daniel Burnett[2], and Alexander Bismarck[3]

1) Surface Measurement Systems Ltd., 3 Warple Mews, Warple Way, London W3 0RF, United Kingdom
2) Surface Measurement Systems Ltd., 2222 South 12th Street, Suite D, Allentown, PA 18103, USA
3) Department of Chemical Engineering and Chemical Technology, Imperial College London, South Kensington Campus, London, SW7 2 AZ, United Kingdom

Introduction

The ultimate quality and performance of carbon fiber composites depends strongly on the interfacial interaction between the two components. These interactions are typically described as adhesion or cohesion phenomena, which depend on the materials' surface energy. Surface energies have been traditionally measured by contact angle methods. The main downfall of this technique is the limited sensitivity. Therefore contact angle or other wettability techniques are unsuitable for measuring subtle differences between materials. In recent years, Inverse Gas Chromatography (IGC) has become an attractive alternate due to its high sensitivity and reproducibility.

IGC is a well-established technique for the characterization of particulates (1), fibers (2), and films (3). IGC involves the sorption of a known adsorbate (probe molecule) onto an adsorbent stationary phase (solid sample), thus inverting the traditional relationship between stationary and mobile phase found in analytical chromatography.

When IGC experiments are carried out in pulse mode, a certain amount of vapor or gaseous probe molecule is injected into an inert carrier gas mobile phase. The probe molecule is transported to the stationary adsorbent and for ideal conditions equilibrium is reached. The adsorbed probe molecule will then be eluted by the carrier gas and is detected as a peak by conventional chromatographic detectors. The retention time can be obtained from the peak maximum and the net retention time, V_N, is calculated from Equation 1.

$$V_N = j / m \cdot w \cdot (t_R - t_0) \frac{T}{T_{Ref}} \qquad (1),$$

where T is the column temperature, T_{Ref} is the reference temperature for the flow rate measurement, m is the sample mass, w is the exit flow rate, t_R the retention time for the adsorbing probe and t_0 is the mobile phase hold-up time (dead time). "j" is the James-Martin correction, which corrects the retention time for the pressure drop in the column bed.

A material's surface energy can readily be determined using IGC. The surface energy is defined as the energy required to form a unit surface under reversible conditions and is the analogue to the surface tension of a liquid. In practical terms, the higher the surface energy the more reactive the surface. This parameter can be divided into a dispersive and a specific component. The dispersive surface energy can be obtained from a plot of the logarithm of the retention volume of a series of alkane probe molecules (multiplied by the column temperature and the gas constant) versus the product of (square root of the) liquid tension and molecular area (4). The result is a straight line and the dispersive surface energy γ_S^D is calculated from the slope according to Equation 2.

$$RT \ln V_N = 2 N_A \left(\gamma_S^D\right)^{1/2} a_m \left(\gamma_L^D\right)^{1/2} + C \qquad (2)$$

In this equation γ_L^D is the liquid tension of the probe molecule, a_m its cross sectional area, and C is a constant. The other parameters have the same meaning as described above.

The specific contribution of the surface energy is obtained indirectly by the specific free energy for a range of polar probe molecules. Points representing a polar probe are located above the alkane straight line. The difference is equal to the specific component of the free energy of desorption ΔG_{SP} (Equation 3).

$$\Delta G_{SP} = RT \ln V_N - RT \ln V_N^{ref} \qquad (3)$$

From the specific free energy acid-base numbers can be calculated if an appropriate concept is applied.

The study of acid-base properties by IGC has the benefit that changes in the orientation of surface groups can be studied. Those changes are not necessarily related to variations in composition. For this reason spectroscopic methods are less appropriate for the study of these effects (5).

The van Oss concept (6) provides acid and base numbers in the same unit as the surface energy.

$$\Delta G_{sp} = N_A * a_m * 2 * ((\gamma_L^+ * \gamma_S^-)^{1/2} + (\gamma_L^- * \gamma_S^+)^{1/2}) \qquad (4)$$

In this equation γ_S^+ and γ_S^- are the electron acceptor and donor parameters of the surface and γ_L^+ and γ_L^- are the are electron acceptor and donor parameters of the probe molecule.

Unfortunately, in its original form this equation can only be used for relative comparison due to inaccurate starting parameters leading to an overestimation of the basicity [7].

Once the individual surface energetics are determined the work of adhesion between the individual solids can be calculated according to Equation 5.

$$W_{total}^A = 2(\gamma_1^d * \gamma_2^d)^{1/2} + 2((\gamma_1^+ * \gamma_2^-)^{1/2} + (\gamma_1^- * \gamma_2^+)^{1/2}) \quad (5)$$
with: $\gamma_S^{SP} = 2 \cdot \sqrt{\gamma_S^+ \cdot \gamma_S^-}$.

The scope of this study is the investigation of the impact of a sizing agent on the adhesion and mechanical strength of single fiber polymer matrices.

Experimental

Materials. Unsized (AS4) and sized (AS4-GP) PAN based carbon fibers were obtained from Hexcel and used as received. The epoxy-based sizing agent used in the AS4-GP sample is intended to improve handling and processing of the fiber during the weaving process. Polysulfone, Polycarbonate, and Polyetherimide were all obtained from Sigma-Aldrich and were used as model thermoplastic matrices.

IGC Experiments. The samples were packed into silanized glass columns (30 cm long, 4 mm ID). Prior to measurement the sample was pre-treated at 303 K for 2 hours in situ.

IGC measurements were carried out using the SMS-IGC 2000 system. The samples were measured at 303 K with a carrier gas flow rate of 10 ml/min. Probe molecules were decane, nonane, octane, heptane, dichloromethane, and ethyl acetate. The probe molecules were injected from the head-space via a loop with 250 µl volume. The injection concentration was 0.03 p/p₀ to obtain infinite dilution conditions. The deadtime was determined by a methane injection.

Mechanical Adhesion. Mechanical strength results (practical adhesion), based on single fiber pull-out tests to obtain the apparent shear strength, τIFSS, were taken from [8].

Results and Discussion

The dispersive, specific, and total surface energy values as measured via IGC as described in the Introduction section are listed in Table 1. The unsized (AS4) sample has much higher total surface energy than the sized (AS4-GP) sample. For the polymers, the total surface energy trends are as follows: polycarbonate > polysulfone > polyetherimide.

Table 1. Dispersive, specific and total surface energy values for the two carbon fibers and three polymer matrices measured by IGC.

Sample	Dispersive Surface Energy (mJ.m^{-2})	Specific Surface Energy (mJ.m^{-2})	Total Surface Energy (mJ.m^{-2})
AS4	77.88	205.60	283.48
AS4-GP	34.82	175.13	209.95
Polysulfone	33.09	130.03	163.12
Polycarbonate	36.15	150.59	186.74
Polyetherimide	39.96	109.91	149.87

From the surface energy values in Table 1, the total work of adhesion for each carbon fiber-polymer pair was calculated using equation 5. This work of adhesion is a thermodynamically derived measure of the interfacial bonding strength between the carbon fiber and polymer matrix. As a measure of practical or mechanical adhesion, the interfacial sheer stress was also measured for each carbon fiber-polymer pair. These two measures of adhesion (thermodynamic and mechanical) are compared in Figure 1.
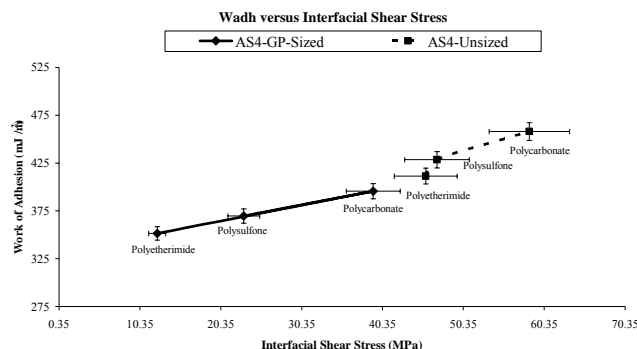
Figure 1. Total work of adhesion plotted versus interfacial sheer stress for the AS4 (unsized; dashed trace) and AS4-GP (sized; solid trace) carbon fibers with each polymer.

As Figure 1 clearly indicates, there is a direct correlation between the work of adhesion measured via IGC and interfacial sheer stress. A higher interfacial sheer stress correlates to a higher work of adhesion and a stronger fiber-polymer bond. Also, both the work of adhesion and interfacial sheer stress are larger for the unsized, AS4 sample compared to the sized, AS4-GP sample. These results indicate that the sizing agent used in the AS4-GP sample is not compatible with the thermoplastic matrices used in this study. Finally, both the interfacial sheer stress and work of adhesion values show the same trend between polymers for both carbon fibers: polycarbonate > polysulfone > polyetherimide.

Conclusions

Work of adhesion calculations based on the individual components correlated directly to practical adhesion measurements on the carbon fiber-polymer composites. Therefore, IGC can be used as a predictive tool in formulating the carbon fiber-polymer system yielding the strongest interfacial bond. Similar procedures could be extended to a wide range of composites and blends where adhesion is a critical parameter.

References
 (1) Thielmann, F., review paper accepted for publication in *Journal of Chromatography* **2004**.
 (2) Van Astem, A. et al.,. *J. Chrom. A.* **2000**, *888*, 175.
 (3) Pawlish, C., Macris, A., and Laurence, R., *Macromolecules.* **1987**, *20*, 1564.
 (4) Schultz, J. et al., *J. Adhesion.* **1987**, *23*, 45.
 (5) Buckton, G. et al., *Intern. J. Pharm.* **1991,** *72,* 157.
 (6) Oss, C., Good, R., and Chaudhury, M., *Langmuir*, **1988**, *4*, 884.
 (7) Della Volpe, C., Sibioni, S., *J. Coll. Interf, Sci.* **1997**, *195*, 121.
 (8) Bismarck, A. and Schulz, E., *J. Material Sci.* **2003**, *38*, 4965.

UPTAKE OF HYDROGEN SULFIDE BY CARBONACEOUS SORBENTS AT HIGH TEMPERATURES

Wenguo Feng and Radisav Vidic

Department of Civil and Environmental Engineering, University of Pittsburgh, Pittsburgh, PA 15261

Introduction

Carbon-based sorbents have been evaluated for the removal of hydrogen sulfide due to the need to control odorous gases generated in sewer systems and wastewater treatment plants. In addition, the ability of carbon-based sorbents to remove hydrogen sulfide from a variety of waste streams was evaluated at near-ambient temperatures. However, removal of hydrogen sulfide at elevated temperatures (300-700 °C) and pressures (300-1000 psi) could be advantageous for Integrated Gasification Combined Cycle (IGCC) process in order to maintain overall efficiency of the process. Previous studies reported that significant amount of sulfur was incorporated into the carbon surface at high temperatures and in the absence of oxygen and both HNO_3 oxidation and Zn impregnation improved the H_2S adsorption capacity [1, 2]. Blayden and Patrick [3] suggested that the bonding in C-S complexes was akin to that of thioethers or disulfides. Puri and Hazra [4] observed that amount of sulfur fixed on the carbon surface correlates well with the oxygen content present as "CO-Complex" (the oxygen containing complex that releases CO upon heat treatment). It has been suggested that oxygen and hydrogen content, extent of surface heterogeneity, and pore structure were more important parameters than surface area. Sugawara et al. [5] studied the effect of hydrogen sulfide on the behavior of organic sulfur in coal and char during heat treatment up to 1073 K. They concluded that a considerable amount of hydrogen sulfide was absorbed during heat treatment, forming organic sulfur forms, such as thiophenes and sulfides. Recently, Ozaki et al. [6] suggested that the surface iron species on thermally stable turbostratic carbons were responsible for the decomposition of H_2S around 350 °C, while decomposition of H_2S above 600 °C might be due to the Lewis sites. This study is designed to study the mechanism and products of H_2S uptake by carbon surfaces at high temperatures.

Experimental

Activated carbon fibers (ACFs) produced from the novolac resin (American Kynol, Inc., Pleasantville, NY) have carbon content of over 95%. ACF10, ACF15, ACF20, and ACF25 were produced using increasing activation time that leads to higher surface area and larger pores, with nominal surface areas of 1000, 1500, 2000, and 2500 m^2/g, respectively. Commercially available activated carbon produced from bituminous coal (BPL, Calgon Carbon Corporation, Pittsburgh, PA) was sieved to 16×50 U.S. mesh size, which was used in this study.

A fixed bed reactor system was used for H_2S uptake test. Influent H_2S stream were generated by diluting 5% H_2S standard gas in nitrogen (Praxair, certified) with nitrogen (Praxair, UHP). Mixed gas with a total flow rate of 150 ml/min was fed through a quartz reactor (38cm long with 1cm OD), which was positioned in the middle of a vertical tubular furnace (Lindberg Heavi-Duty, Watertown, WI). 500 mg of carbon sample was loaded in the reactor. After drying at 120 °C for 2 hours, adsorption of H_2S at high temperatures was carried out at set temperatures for 6 hours. After adsorption, the reactor was cooled down to room temperature in UHP nitrogen. Sulfur loading was determined from H_2S breakthrough curve and was measured using the sulfur analyzer (SC-132, Leco Sulfur Analyzer, St. Joseph, MI).

Results and Discussion

Effect of Temperature. Figure 1 shows the effect of temperature on sulfur uptake by ACF-25 and BPL carbon. Sulfur loading on these carbonaceous sorbents increased with an increase in temperature. The exact mechanism of the uptake of sulfur in this temperature range is not yet clear and is the subject of the ongoing studies. It is reasonable to assume that high temperatures can provide more energy to overcome chemisorption energy barrier.
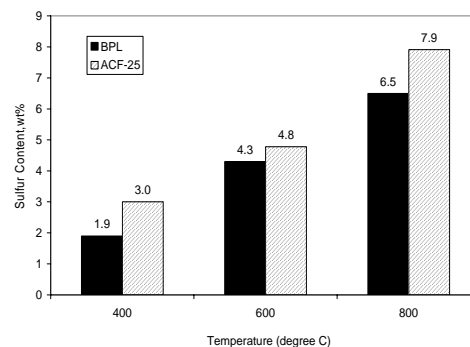
Figure 1. Effect of temperature on sulfurization of ACF25 and BPL at 400-800 °C

EDAX was used to determine elemental composition on the carbon surface. The S, O, and C content on the surface was determined after sulfurization at different temperatures and the surface sulfur content is compared with that from the bulk sulfur analysis in Table 1. Table 1 shows that the increase in temperature lead to a decrease in oxygen content and increase in the sulfur content. Such behavior indicates that possible substitution of the oxygen by sulfur and/or carbon [1,7] may be an important mechanism for H_2S uptake at high temperatures by ACFs. Another observation is that sulfur content on the surface is higher than that in the bulk. With the increase in temperature, the ratio of these two is increasing, which suggests higher temperature promotes better diffusion through the carbon structure and enabled sulfur to be deeper embedded into the carbon matrix.

Table 1. Sulfur content in the bulk (sulfur analysis) and on the surface (EDAX)

| Sample	Bulk Sulfur Content [wt.%]	Surface Content [wt.%]		
		S	O	C
ACF25-Raw	0.2	0.2	4.38	95.41
ACF25-400C	3.0	6.04	2.13	91.83
ACF25-600C	4.8	6.95	1.61	91.44
ACF25-800C	7.9	11.52	1.31	87.17

Effect of Sorbent Characteristics. As discussed before, the starting materials, especially the oxygen and hydrogen content, exhibited important impact on the ultimate sulfur content resulting from high-temperature adsorption of H_2S by carbonaceous sorbents. Four different carbon materials (i.e., three ACFs and BPL carbon) were tested for H_2S uptake at 600 °C. The results shown in Table 2 clearly indicate that the sulfur content on the sorbent increased with the increase in ACFs serial number. EDAX analysis showed that the oxygen content also increases with the increase in ACF serial number (data not shown). Therefore, it is possible that substitution of oxygen

is an important pathway for the uptake of H₂S at this temperature. Sulfurized BPL carbon exhibited consistently lower sulfur content than ACF-25 at all the temperatures tested (Figure 1) but it has higher sulfur content than ACF-20 at 600 °C. Since BPL is a carbon of different origin, it is hard to tell the exact difference without complete examination of the properties of both carbon materials.

**Table 2. Effect of different starting carbon materials on H₂S uptake at 600 °C**

Sample	S%, wt%
ACF10-600C	2.1
ACF20-600C	3.1
ACF25-600C	4.8
BPL-600C	4.3

XPS Analysis of the Reaction Products. XPS analysis was conducted to identify the produced sulfur species and the typical spectrum is shown in Figure 2. Standard library spectra provide the following information about the peaks related to sulfur species: free elemental sulfur has a peak around 164.05eV; chemisorbed sulfur has a peak at 161.8-162.6eV; organic sulfur has a peak between 163-164.1 eV; and oxidized sulfur shows a peak above 167eV. Unfortunately, there is an overlap between the region of elemental sulfur and that of organic sulfur. The results depicted on Figure 2 suggest that either organic sulfur or elemental sulfur were the dominant sulfur forms on ACF surface. Because the boiling point of elemental sulfur at atmospheric pressure is 444 °C, it is hard to imagine that a substantial quantity of elemental sulfur would remain on the carbon surface after exposure to 600 °C and 800 °C for 6 hours. According to Sugawara et al. [5], thiophene may be the possible structure of organic sulfur products.
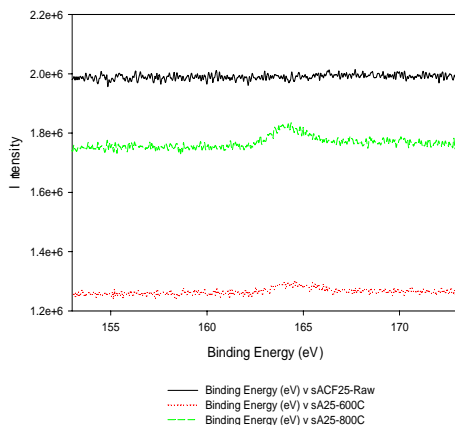
Figure 2. XPS analysis of ACF25 before and after sulfurization

The pore size distribution for BPL before and after hydrogen sulfide uptake is shown in Figure 3. Slight increase in the pore volume in the 1-2 nm range can be observed from this figure. However, the change in pore size distribution as a result of hydrogen sulfide uptake is not significant. Such observation leads to the conclusion that the sulfurized compounds retained by the carbon surface are extremely well distributed on the surface of the sorbent. Furthermore, it is more likely that the organic sulfur is the dominant sulfur form since the elemental sulfur would tend to agglomerate into isolated islands on the carbon surface and significantly alter the pore size distribution of the sorbent.
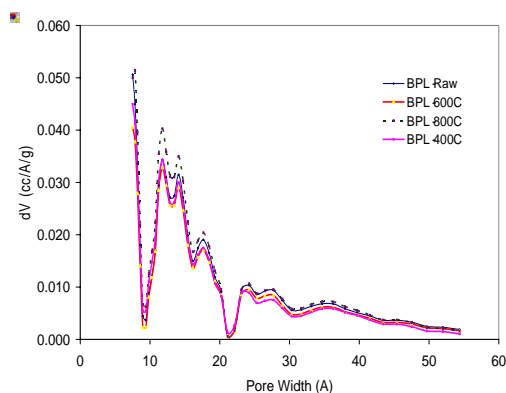
Figure 3. Pore size distributions of BPL before and after H₂S uptake at high temperatures

Conclusions

In summary, sulfurization at higher temperatures resulted in higher sulfur content than that under relatively lower temperatures. Sulfur content was higher on the surface than in the bulk. The increase in sulfur content and the decrease in oxygen/carbon content with the increase in temperature suggest substitution of oxygen/carbon by sulfur. The produced sulfur is either organic sulfur or very strongly bonded elemental sulfur. There is no significant change in the pore size distribution after H₂S uptake.

References
(1) Cal, M.P., Strickler, B.W., and Lizzio, A.A.. *Carbon*, **2000**. 38(13), 1767-1774.
(2) Cal, M.P., Strickler, B.W., and Lizzio, A.A. *Carbon*, **2000**. 38(13), 1757-1765.
(3) Blayden, H.E., Patrick, J. W. *Carbon*, **1967**, 5, 533-544.
(4) Puri, B.R., R. S. Hazra, *Carbon,* **1971**, 9, 123-134.
(5) Sugawara, K.,Enda, Y., Kato, Sugawara, T., Shirai, M., *Energy & Fuels*, **2003**, 17(1), 204-209.
(6) Ozaki, J., Yoshimoto, Y., Oya, A., Takarada, T., Kuzunetsov, V.V., and Ismagilov, Z.R. *Carbon*, **2001**, 39(10), 1611-1612.
(7) Puri, B.R., *in Physics and Chemistry of Carbon,* ed. P.L. Walker. Vol. 6. 1970, New York: Marcel Dekker, Inc. 191-282.

ELECTRIC DOUBLE LAYER CAPACITANCE OF B-DOPED MULTI-WALLED CARBON NANOTUBES

Soshi Shiraishi, Masaaki Kibe, and Asao Oya

Department of Nano-Material Systems,
Graduate School of Engineering, Gunma University,
Tenjin-cho 1-5-1 Kiryu, Gunma 376-8515, Japan

Introduction

Recently, double layer capacitance of nanocarbons such as carbon nanotubes or carbon nanofibers has attracted a great deal of attention on both of electrochemistry of carbon and development of new electric double layer capacitor. Multi walled carbon nanotubes (MWCNTs) or single walled carbon nanotubes (SWCNTs) are composed of tubular graphene layers, so can be considered as ideal cylinder-like nanoporous materals.

The essence of the interfacial capacitance of microporous carbon electrode in electrolytes has been investigated at the viewpoint of dielectric nature of ions or solvent molecules adsorbed at the interface. However, it was also discussed that the interfacial capacitance of carbon electrode depends on the space charge layer, which influences the apparent double layer capacitance of carbon electrode as well as semiconductor pn junction. The apparent double layer capacitance (= interfacial capacitance, C_a) is expressed by using the series combined capacitance of Helmholz layer capacitance (C_H) and the space charge layer capacitance (C_{SC}) of carbon electrode as $1/C_a = 1/C_H + 1/C_{SC}$. The tubular graphene sheet at the SWCNT might enhance the space charge layer capacitance of carbon to realize the high specific capacitance [1].

The discussion about C_{SC} contribution strongly suggests the positive effect of hetero-atom doping to carbon electrode [2]. The substituted hetero-atom in porous carbon materials can enhance the space charge layer capacitance, which is well known to be correlated with carrier concentration as well as Si semiconductor. In this paper, the double layer capacitance properties of highly pure MWCNT are correlated with the nanostructure such as morphology, pore structure, and carbon crystallinity. Additionally, we demonstrate the effect of hetero-atom doping on the capacitance by using B-doped MWCNT prepared with the diffusion method at high temperature.

Experimental

MWCNT prepared by CVD process (commercial name: cvdMWCNT95) was purchased from ILJIN Nanotech Co., Ltd. as start material for this work. This original MWCNT sample contains a small amount (~ 1wt%) of metallic Fe catalyst. The catalyst-removal & the tube-end opening of the MWCNT were conducted by the thermal oxidation in air at 600°C for 30 min and the following acid-washing with HCl aqueous solution. After the acid-washing, the samples was heat-treated at 800°C for 1h in N_2 to reduce excess surface functionalities formed by the thermal oxidation. The resulting product (yield: 50wt%) was referred to as "oxHCl-800". And furthermore, the heat-treatment at 3000°C in Ar for 1h was performed for the ox-HCl-800 sample to improve the carbon crystallinity and recover the defects induced by the thermal oxidation. The resulting product was referred to as "oxHCl-3000".

The oxHCl-3000 sample was heat-treated at 2200°C for 30 min with graphite crucible containing 10wt% boron to obtain the boron-doped sample "B-2200".

The double layer capacitance measurement was conducted in the same way as our previous paper [1]. The propylene carbonate solution containing 0.5 moldm^{-3} $(C_2H_5)_4NBF_4$ was used as electrolyte (0.5 M TEABF$_4$/PC). The capacitance was measured by typical three-electrode system at galvanostatic condition to calculate the gravimetric capacitance per carbon weight in test electrode.

Results and Discussion

Nanostructure of MWCNTs. The TEM images of the MWCNTs indicated that the outer diameter of the MWCNT is 10~20 nm and the inner is ~5 nm. Comparison with **Fig.1(a)** and **Fig.1(b)** shows that the morphology of the B-doped MWCNT is almost the same as that before the B-doping. The B-doping with the diffusion method cannot affect the nano-structure of the MWCNT.

The XRD patterns revealed that d_{002} or L_c is 0.344nm or 4nm for the original MWCNT, respectively. The thermal oxidation and heat-treatment caused only small structural change. The XRD pattern of B2200 exhibited the formation a small part of graphitic part, but the 002 diffraction angle was the same as oxHCl3000. Therefore, the B-doping of this work almost never influences the accumulated graphene structure of the MWCNTs.

The Raman spectra of **Fig.2** give us some additional information of the carbon nano-structure of the MWCNTs. All samples showed the two band of ~1570 cm^{-1} (G-band) and ~1340 cm^{-1} (D-band), assigned to hexagonal carbon plane and its crystal defect / imperfection, respectively. The intensity ratio of G and D bands (I_D / I_G) of ox-HCl-800 was larger than the original. It means the introduction of crystal defects and imperfection by the thermal oxidation, corresponding to the destruction of the tube-ends. The ox-HCl-3000 showed the small I_D / I_G, which can be derived from the crystal restoration through the heat-treatment at 3000°C. Interestingly, the B-2200 had the larger I_D / I_G. The literatures state that atomically local disorder in graphene layers is induced by B-doping, but does not deteriorate the ordering structure of hexagonal carbon planes [3]. The Raman spectra about the induced local disorder were observed anywhere, suggesting the uniform distribution of the doped boron atoms in the MWCNTs.

Pore Structure of MWCNTs. The BET specific surface area (S_{BET}), the mesopore volume (V_{meso}), and the specific surface area of mesopores (S_{meso}) were summarized in **Table1**. S_{BET} and S_{meso} of the original MWCNT were around 200 m^{2}g^{-1} and the both of the surface areas were comparable. The agreement of S_{BET} with S_{meso} indicates no micropores. The SEM and TEM showed the original MWCNT contained a few opened tubes, so the mesopore volume and surface area can be attributed to the inter-space between tubes working as mesopore (2nm~50nm). The surface area of S_{BET} and S_{meso} of oxHCl-800 were around 400 m^{2}g^{-1}. These surface areas correspond to the double of the original, which comes from the tube-end opening to access the interior tube wall. The reductions in S_{BET} and S_{meso} for the oxHCl-3000 suggest that the heat-treatment at 3000°C shut the gate to the tube interior and cover the surface defects to decrease the surface area. The B-2200 had the comparable pore structure to the oxHCl-3000. This result also confirms that the B-doping does not influence the tube structure of the MWCNT. Consequently, the total surface area of the original, oxHCl-3000, and B-2200 corresponds to the external surface area of tubes, while that of the oxHCl-800 includes the interior surface area of the tubes in addition to the external one.

Capacitance of MWCNTs. The parameter of S_{BET}, the gravimetric capacitance (C_g), and the specific capacitance per BET surface area (C_S) were also summarized in **Table 1**. These results reveal that the gravimetric capacitances of the MWCNTs are much smaller than those of the ACFs. The very small C_g of the MWCNTs can be mainly owing to their small surface area accessible to ion adsorption, which is no more than 10~20 % of S_{BET} for conventional activated carbon fibers (ACFs). The C_g order for the original, the oxHCl-800, and the oxHCl-3000 are related to the S_{BET} one, but this

tendency cannot be applied to the B-2200, because the oxHCl-3000 with smaller C_g had larger S_{BET} compared to the B-2200.

The specific capacitances (C_S) of the MWCNTs are from 5 to 7 μFcm^{-2}, comparable to those of ACFs. It can be seen that the tubular graphene layers of the MWCNTs used in this work are not effective in the enhancement of C_S although the relative higher C_S was observed for the HiPcoTM-SWCNTs. These results suggest that the C_S of carbon nanotubes depends on the numbers of accumulated graphene layers or layer curvature. In the comparison with the original MWCNT, the C_S reduction for the oxHCl-800 might be suggestive of the C_s difference bet ween the outer surface and the inner surface of MWCNT. The oxHCl-3000 showed the smaller C_S than the oxHCl-800. Considering that surface defects such as exposed edge-plane have relatively high specific capacitance for highly oriented pyrolytic graphite (HOPG), it can be seen that the heat-treatment at 3000°C recovers the surface defects to reduce the specific capacitance of the MWCNTs.

The B-2200 had 6.5 μFcm^{-2} of C_S, indicating the C_S increment of more 10% than before the B-doping. The morphology changes by the B-doping were not observed as discussed at the previous section, the higher C_S after the B-doping can originate in the physicochemical change for the surface of MWCNT. The B1s XPS spectrum of the B-2200 shows that the boron atoms in the MWCNT samples had various chemical states. The presence of the substituted B suggests the possibility of the enhancement of the space charge layer capacitance through increasing the number of hole as charge carrier or the DOS change at the Fermi level[2]. All of the contained B atoms are not in the substituted position in the hexagonal carbon plane. Furthermore, the ICP-AES and XPS analyses revealed that the total of atomic concentration of B was only around 0.2 at% and 0.7 at%, respectively. The concentration and chemical state control for induced B will lead to more enhancement of C_S.

References
(1) Shiraishi, S.; Kurihara, H.; Okabe, K.; Hulicova, D.; Oya, A. *Electrochem. Commun.* **2002**, *4*, 593.
(2) Randin, J. P.; Yeager, E. *J. Electronal. Chem.* **1974**, 54, 93.
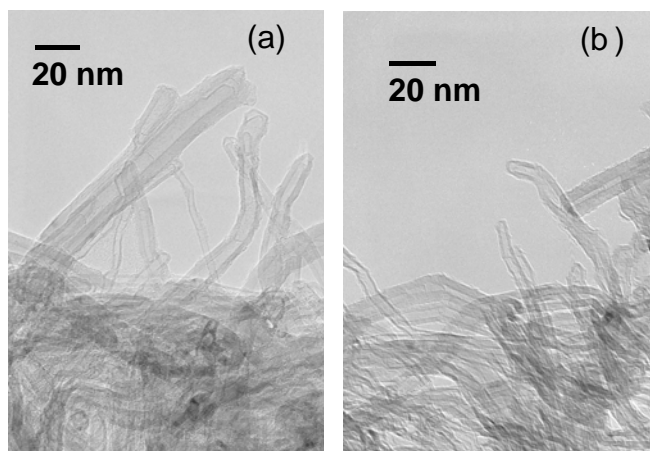(3) Hishiyama, Y.; Irumano, I.; Kaburagi, Y.; Soneda. Y. *Phys. Rev. B.* **2001**, 63, 245406.

Figure 1. TEM images of the MWCNTs, (a) oxHCl3000 and (b) boron-doped MWCNT (B-2200).
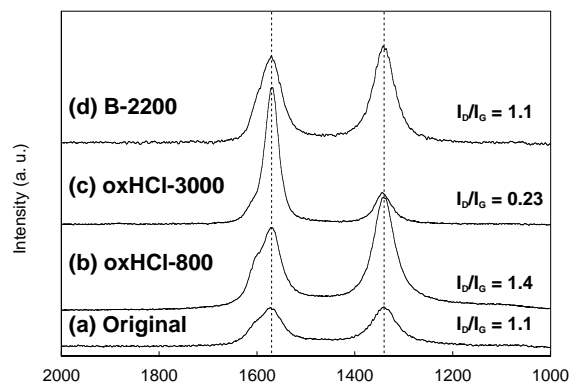
Figure 2. Raman spectra (532 nm, 5 mW, spot-size: 2μm) of MWCNTs, (a) original, (b) oxHCl-800, (c) oxHCl-3000, and (d) B-2200.

Table 1. BET Specific Surface Area and Double Layer Capacitance of MWCNTs and ACFs

Sample	S_{BET}	S_{meso}	V_{meso}	C_g	C_S
	$[m^2g^{-1}]$	$[m^2g^{-1}]$	$[mlg^{-1}]$	$[Fg^{-1}]$	$[\mu Fcm^{-2}]$
Original	222	232	0.47	14.5	6.5
OxHCl800	382	391	0.70	23.5	6.2
OxHCl3000	191	213	0.56	10.7	5.7
B-2200	185	219	0.60	12.1	6.5
ACF1	930	-	-	40	4.1
ACF2	1150	-	-	69	6.0
ACF3	1480	-	-	96	6.5
ACF4	1780	-	-	102	5.7

C_g; gravimetric capacitance measured for 2~4Vvs.Li/Li$^+$
C_S ; specific capacitance per surface are = C_g / S_{BET}

Activated Glassy Carbon for Energy Storage

Artur Braun [1,2], Vasudevan Mahalingam[3]

[1]Dept. of Chemical & Materials Engineering, Consortium for Fossil Fuel Sciences, University of Kentucky, Lexington KY 40506, USA
[2]General Energy Research Department, Paul Scherrer Institute CH-5232 Villigen PSI, Switzerland
[3]Department of Computer Engineering, University of Kentucky, Lexington KY 40506, USA

Introduction

Glassy carbon is a solid and monolithic form of a hard carbon with a high number density of nano-sized voids [1-2]. Oxidative treatment [3] opens and connects these voids and creates an active carbon film with a sponge-like structure and open porosity on the surface of the monolith, with internal surface areas as large as 1000 m^2/g and more [4-8]. The open pores in the active film are as small as one nanometer and can be soaked with electrolyte [4-5]. The superposition of film growth and film burn-off yields a unique growth law of a sandwich-like structure, which can be exactly described by the Generalized Lambert W function [9,10]. The unreacted glassy carbon core between the surface films can be used as a diffusion barrier, allowing the design of bipolar electrode cell assemblies for supercapacitors with the highest power densities ever reported [4,11]. One additional potential application of activated glassy carbon is its use for a monolithic assembly for hydrogen storage. The current paper addresses some issues of the film growth for flat and spherical sample geometry.

Experimental

Sigradur K glassy carbon plates of 55 micron thickness were thermochemically activated in an air floated muffle furnace for several hours at 450°C [5-7]. Also, GC powder with 10 micron sphere diameter was activated in the same way [8]. Film thicknesses on plates were determined with electron microscopy. Electrochemical capacities were determined with electrochemical methods like cyclic voltametry, and impedance spectroscopy. Hydrogen and methane storage was carried out according to the protocol published recently [14]. Pore sizes of activated and unactivated GC were obtained with small angle X-ray scattering [5,13].

Results and Discussion

Film Growth on Flat Plates. One direct visual observation during GC activation is the shrinking sample thickness. Additional techniques such as electron microscopy are necessary to observe the active film. Sample shrinking and film growth are superimposed processes, as schematically illustrated in Figure 1. The active film is drawn in gray color and envelopes the non-activated (black) bulk. The experimental observation is that the shrinking is a process linear in time, unlike the film growth. Instead, film growth follows more a sigmoidal, square-root like type of growth. Shown here, the initial GC thickness is about 60 micron. After about 165 minutes, the non-reacted core vanishes and the entire sample is active film. After about 200 minutes of activation, the entire sample thickness is around 45 micron.
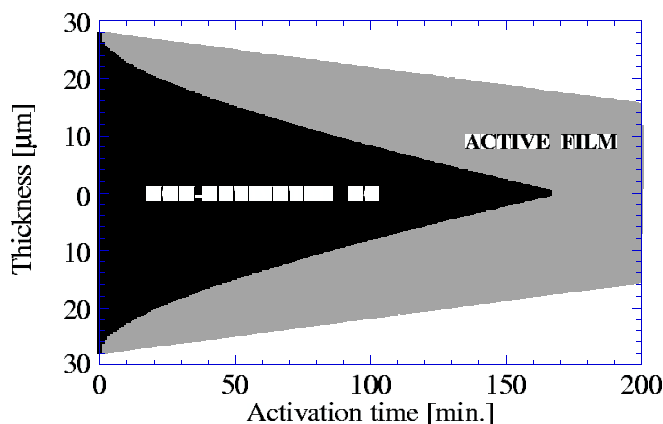
Figure 1. Schematic illustration of a flat shrinking GC sample, and relative growth of active film (gray). The black material is the non-activated GC.

Readily available theory on the gas phase conversion and combustion of coal (progressive conversion model) and on the oxidation of metal catalysts (unreacted shrinking core model) is combined and extended, and then applied to the activation of glassy carbon [9,10]. We introduce abbreviations for the constants governing the reaction controlled burn-off of the film, α, and the diffusion controlled growth of the film, β. The temperature dependant reaction constant is k(T), and D is the effective diffusion coefficient. C, b, and ρ are the concentrations, stoichiometry coefficients, and densities, respectively.

$$\alpha = \frac{b^* \cdot k^* \cdot C^*_{AS}}{\rho_{film}} \ , \ \beta = \frac{b \cdot D_{eff} C_{AS}}{\rho_{bulk}}$$

For the film thickness L(t) on a flat sample we find following ordinary first order differential equation:

$$L \cdot \left(\alpha + \frac{dL}{dt} \right) - \beta = 0$$

There exists an exact analytical solution for this flat sample problem, involving the Lambert W function W, or, more directly, the Generalized Lambert W function: G.

$$L(t) = \frac{\beta}{\alpha} \left(1 + W \left(\exp \left(-1 - \frac{\alpha^2 t}{\beta} \right) \right) \right) = \frac{\beta}{\alpha} G \left(-\frac{\alpha^2 \cdot t}{\beta} \right)$$

This analytical formulation allows easy interpretation of the processes taking place during activation. Most noteworthy, the film thickness for very long activation times is a constant, given by β/α. Altering the oxygen concentration has impact on the speed of the activation, but not on the film thickness.

Film Growth on Spheres. Importance of film growth on flat samples is proven because supercapacitors have been built already, based on flat monolithic electrodes [11]. Activation of spheres is important as well because powders are usually made from sphere-like particles, and it is mostly powders that are used in industrial applications, such as electrode materials. Figure 2 shows cyclic voltamograms of activated GC powder, bonded on a titanium plate. This assembly is intended for electrochemical applications [Schüler, Kötz, Swiss Patent]. The area enclosed by this CV is several orders of magnitude larger than the CV from non-activated GC powder, in

analogy to the GC plates. Shown is also that activated GC has a slightly higher capacitance after electrochemical reduction.
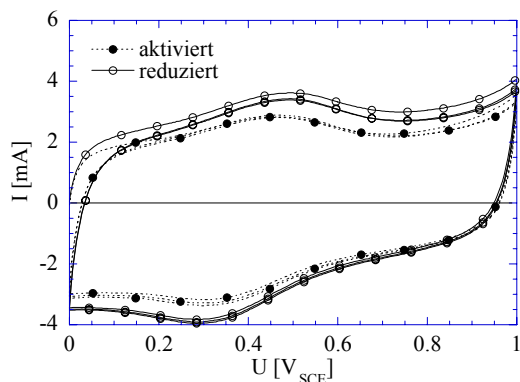
Figure 2. Cyclic voltamogram (CV) of thermally activated GC powder, bonded to a titanium plate. Open symbols denote GC after electrochemical reduction.

The particular geometry of spheres, in contrast to plates, imposes additional complications both experimentally and theoretically.
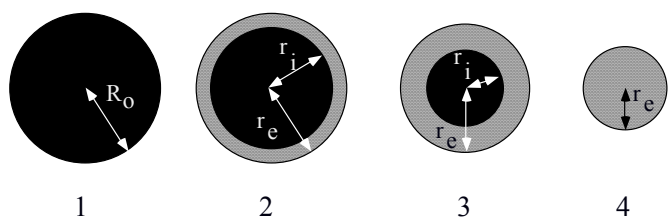

Figure 3. Schematic illustration of four stages of shrinking GC samples (black), and relative growth of active film (gray). Stages 1 and 4 show the extreme cases of non-activated GC (1), and totally activated GC (4). Intermediate stages 2 and 3 contain both activated and non-activated GC.

The equation for the spherical case is given below and involves an additional quantity, the initial sphere radius R_0:

$$\frac{(r_e - L)}{r_e} \cdot L \cdot (\alpha + \acute{L}) - \beta = 0 \text{ , and } r_e = R_0 - \alpha \cdot t$$

No analytical solution is known yet. However, it is obvious that for very thin films ($L/r_e \approx 0$), the plate solution is a good approximation for the sphere problem.

Numerical solutions for the sphere problem are illustrated in the plot below, for $\alpha = 0.008$, and values for β from 10 to 140.
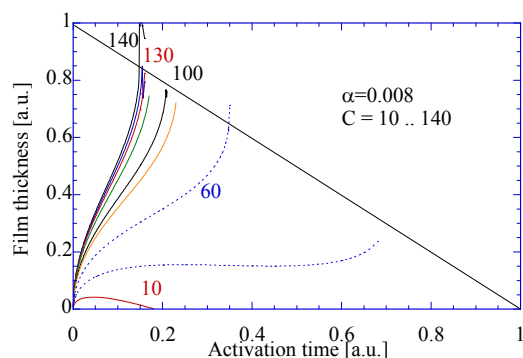
Figure 4. Numerical solutions for the differential equation of the sphere geometry for one particular α, and for a set of different diffusion coefficients in β.

The straight line with slope −1 represents the overall diameter of the spherical GC particle during the course of activation, and burn-off. The film growth can be approximated by a $t^{1/2}$ law in the very beginning of activation, by a linear function $\sim t$ in the middle range, and by a $t^{3/2}$ for large t at the very end of the activation. Note, that there is one particular time, at which the unreacted core in the spheres vanish, and the entire material is activated. This is the desired state for GC powder in technical applications, because unreacted GC as a diffusion barrier is not necessary, but it would contribute to the weight and be of no further use. It is thus important to have a very monodisperse GC powder for activation, and to know the exact process parameters to find the time at which the activation can be stopped. Another important issue for industrial GC powder activation is that the powder must be fluidizable. In the present case, it was necessary to distribute the powder as a thin layer on a surface for successful activation.

The mathematical models do not take into account a possible inhomogeneity in the active film. Direct experimental evidence for such inhomogeneity comes from Raman microscopy data, for instance.
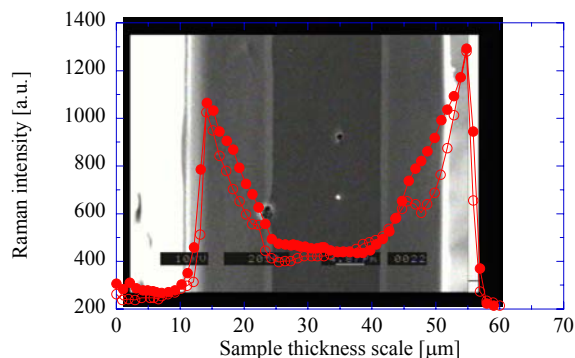
Figure 5. Cross section of a broken GC platelet with active film to the left and right. Overlayed is the Raman scattered intensity, showing inhomogeneous Raman optical density in the active film.

Figure 5 shows a cross section of a partially activated GC sheet, and overlayed to that the scattered Raman intensity of the G band, obtained from such sample by scanning across the cross section in micron-sized steps. The non-activated part of the GC shows a flat response along the cross section. This holds, too, for GC, which has not been activated at all (not shown here). But the active GC film shows a steep increase of the carbon Raman G band starting from the active/non-active interface of GC, towards the sample surface.

This means that the active GC film is more graphitic than GC bulk. This finding confirms earlier X-ray diffraction results [5].

Another correction that has to be made is that the overall sample thickness expands from 55 micron before activation to around 58 micron in the very first few minutes after activation. Oxygenation of the GC maybe causes the graphene sheets to expand their distance to each other, similar to an intercalation, which is probably confined to the outer boundary of the graphene sheets. This picture would also explain the drastic increase of surface roughness, as evidenced by the small angle scattering of GC samples that were activated for 5 minutes or less [Braun A, Saliger R., unpublished].

The mathematical model presented here also overlooks that the electrochemical double-layer capacitance at very early stages of activation increases exponentially, which is not surprising when we assume that the internal surface growth during activation is basically the process of normal reproduction.

Conclusions

Glassy carbon is relatively unknown as electrode material for energy storage and conversion purposes. This is probably because only few research groups have seen the potential of this interesting material, and possess the know how to reveal and optimize its performance. It is an excellent material for supercapacitors with ultrahigh power density. Also, powder can be activated and used for high-surface area electrode materials. Use of glassy (vitreous) carbon for hydrogen storage has been reported only once, to the best of the author's knowledge. But that group did not activate the vitreous carbon powder before hydrogen loading, and hence basically failed [15]. We have used activated GC plates for hydrogen storage experiments, with very promising results.

References
1. Lewis J.C., Redfern B., Cowlard F.C. Vitreous Carbon as a Crucible Material for Semiconductors. Solid-State Electronics 6 (3), 251-254 (1963).
2. Jenkins G. M., Kawamura K., Polymeric Carbons - Carbon Fiber, Glass and Char, 1st ed., *Cambridge University Press, Cambridge UK*, 1976.
3. Lewis J.C., Floyd I.J., Cowlard F.C. A comparative study of gaseous oxidation of vitreous carbon and various graphites at 1500-3000 degrees K Carbon 6 (2): 223 pp. (1968).
4. Miklos J., Mund K., Naschwitz W., Patent DE 30 11 701 A1. Siemens AG and German Patent Office (1980).
5. Braun A., Bärtsch M., Schnyder B., Kötz R., Haas O., Haubold H.-G., Goerigk G. X-ray Scattering and Adsorption Studies of Thermally Oxidized Glassy Carbon. J. Non-cryst. Sol. **260** (1-2), 1-14 (1999).
6. Braun A., Bärtsch M., Geiger F., Haas O., Kötz R., Schnyder B., Carlen M., Christen T., Ohler Ch., Unternährer P., Desilvestro H., Krause E. *A Study on Oxidized Glassy Carbon Sheets for Bipolar Supercapacitor Electrodes*in: New Materials for Batteries and Fuel Cells (Symposium CC). Proceedings of the MRS 1999, Vol. **575**, CC7.3. (1999) pp. 369-380. Editors: D.H. Doughty, H-P. Brack, K. Naoi, L.F. Nazar, ISBN: 1-55899-482-3 Code: 575-A9.
7. Braun A., Bärtsch M, Merlo O., Schaffner B., Schnyder B., Kötz R., Haas O., Wokaun A. Evolution of Electrochemical Double Layer Capacitance in Glassy Carbon during Thermal Oxidation - Crossover from Exponential to Logistic Growth. Carbon **41** (4) 759-765 (2003).
8. Braun A., Bärtsch M., Schnyder B., Kötz R., Haas O., Wokaun A. Evolution of BET Internal Surface Area in Glassy Carbon Powder during Thermal Oxidation. Carbon **40** (3) 375-382 (2002).
9. Braun A., Bärtsch M., Schnyder B., Kötz R. A Model for the film growth in samples with two moving boundaries- An Application and Extension of the Unreacted-Core Model. Chem. Eng. Sci. **55** (22), 5245-5254 (2000).
10. Braun A., Wokaun A., Hermanns H.-G. Analytical Solution to a Growth Problem with Two Moving Boundaries. Appl. Math. Model. **27** (1) 47-52 (2003).
11. Bärtsch M., Braun A., Schnyder B., Kötz R., Haas O. Bipolar Glassy Carbon Electrochemical Double-Layer Capacitor: 100,000 Cycles Demonstrated. Journal of New Materials for Electrochemical Systems **2**, 273-277 (1999).
12. Gille W. and Braun A. SAXS chord length distribution analysis and porosity estimation of activated and non-activated glassy carbon. J. Non-cryst. Sol. **321** (2003) 89-95.
13. Braun A., Kohlbrecher J., Bärtsch M., Schnyder B., Kötz R., Haas O., Wokaun A. Small angle neutron scattering and cyclic voltammetry study on electrochemically oxidized and reduced pyrolytic carbon. Electrochimica Acta **49** (7) 1105-1112 (2004).
14. Smith, M. R., Jr., Bittner, E. W., Shi, W., Johnson, J. K., Bockrath, B. C. Chemical Activation of Single-Walled Carbon Nanotubes for Hydrogen Adsorption. J. Phys. Chem. B. **107**(16); 3752-3760 (2003).
15. Kajiura H, Tsutsui S, Kadono K, Kakuta M, Ata M, Murakami Y. Appl.Phys.Lett. (2003) 82 (7) 1105-1107.

HYPERCROSSLINKED RESINS AS PRECURSORS TO CARBON ELECTRODES IN ELECTROCHEMICAL CAPACITORS: PORE STRUCTURE CHARACTERIZATION OF RESINS AND PYROLYTIC CARBONS

Euan J. Bain[i], Peter J. Hall[i], David C. Sherrington[ii], Richard K. Heenan[iii] and Dennis Wozniak[iv]

i) Department of Chemical and Process Engineering
University of Strathclyde
James Weir Building
75 Montrose Street
Glasgow, G1 1XJ, UK

ii) Department of Pure and Applied Chemistry
University of Strathclyde
Thomas Graham Building
295 Cathedral Street
Glasgow, G1 1XL, UK

iii) Rutherford Appleton laboratory
ISIS Division
Chilton, Didcot
Oxfordshire, OX11 0QX, UK

iv) Intense Pulsed Neutron Source Division
Argonne National Laboratory
9700 South Cass Ave.
Argonne, IL 60439

Introduction

Electrochemical capacitors are a relatively new electrostatic energy storage technology.[1] Storing charge in the double-layer that exists between an electrode and electrolyte, they are able to offer energy and power densities which bridge the gap between batteries and capacitors and thus allow the development of new energy storage and supply systems. Activated carbon currently represents by far the most common electrode material being used and researched for application in electrochemical capacitors.[2]

Hypercroslinked resins, derived from gel-type divinylbenzene-chloromethyl styrene (DVB-VBC) resins, exhibit surface areas in excess of $1500 m^2.g^{-1}$ and possess pore networks which are dependent on their synthesis route and parent resin.[3] Although such materials have been widely applied and investigated as adsorbents and catalyst supports[4,5], their high surface area, controllable pore structure and the possibility of synthesis as monoliths have highlighted them as promising carbon precursors for application as electrochemical capacitor electrodes.

The successful development of activated carbon electrochemical capacitor electrodes from hypercrosslinked resin networks is dependent on gaining a detailed understanding of how synthesis conditions, from gel-type resin to hypercrosslinked resin to pyrolytic carbon to activated carbon, affect the pore structure of the final material.

Presented here are the results of the characterization of the pore networks of a gel-type resin, hypercrosslinked resin and a subsequent series of pyrolytic carbons.

Experimental

Hypercrosslinked resin synthesis. 2% nominal crosslink ratio (NCR) microbeads were synthesized via the radical suspension polymerization of a comonomer solution of divinylbenzene (DVB) and chloromethyl styrene (CMS). The gel-type beads were washed using water, extracted in boiling acetone for 24 hours and dried in a vacuum oven at 60°C for 24 hours. 3.5g of dry beads were then swollen in 20ml of 1,2-dichloroethane (DCE) for 45 minutes then hypercrosslinked at 80°C in 80ml of DCE in the presence of $FeCl_3$. $FeCl_3$ was present in the mass ratio of resin/catalyst 5/4. The hypercrosslinked resin was washed thoroughly in acetone and methanol, extracted in boiling acetone for 24 hours then dried in a vacuum oven at 60°C for 24 hours. The effect on the resin structure of varying the swelling time between 0 minutes & 30 minutes and varying the CMS solution between 90% *p*-CMS and 97% *m,p*-CMS was investigated.

Pyrolytic carbons. Carbon samples were prepared by applying a two-tier heating strategy, using a tube-furnace under flowing argon, to hypercrosslinked resin samples. Samples were heated from room temperature to isotherm T_1 at 20 K/min and held for 30 minutes. The temperature was then raised to isotherm T_2 at 20 K/min and held for 30 minutes before being decreased at 20 K/min to room temperature. The results of varying T_1 between 600°C & 700°C and T_2 between 900°C & 1200°C are discussed in this paper.

Characterisation Methods. The pore networks of all samples were characterized using Nitrogen adsorption at 77K. Hypercrosslinked resins and pyrolytic carbons were also characterized using small angle neutron scattering (SANS). Contrast Matching SANS (CM-SANS) was also undertaken on the pyrolytic samples. Nitrogen adsorption was carried out using a Micromeritics ASAP 2000 instrument. SANS was undertaken at the Small Angle Neutron Diffractometer (SAND) at the Intense Pulsed Neutron Source and also at the LOQ instrument at the Rutherford Appleton Laboratory.

Results and Discussion

The gel-type resin is devoid of any internal pore structure in the dry state. The only porosity present is that which exists in the interstices between the gel spheres. The surface area of the dry gel-type resin is generally around $1 m^2.g^{-1}$.
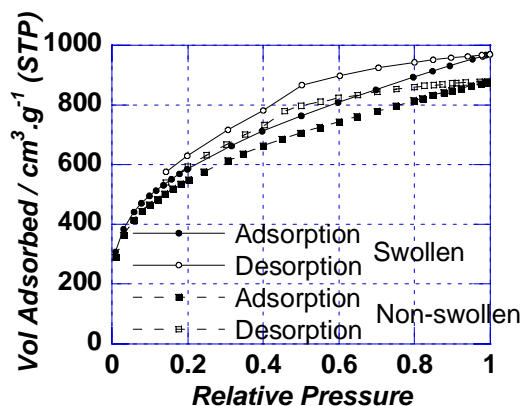

Figure 1. Nitrogen adsorption isotherms for hypercrosslinked resins synthesized with no preswelling and 30 minutes preswelling

A hypercrosslinked resin sample which was synthesized with no swelling time prior the introduction of heat and $FeCl_3$ displayed a BET (Brunauer-Emmett-Teller) surface area of $1990 m^2.g^{-1}$. Analysis of the SANS data showed that the scattering at low *q* was proportional to a negative power of the scattering vector *q*. The data was fitted to a mass-fractal model[6] which yielded a fractal dimension of 2.63. A hypercrosslinked resin sample which was synthesized by allowing the gel-type resin to swell for 30 minutes prior to the introduction of $FeCl_3$ and heat exhibited a surface area of 2131 $m^2.g^{-1}$

and a fractal dimension of 2.07. **Figure 1** shows the isotherms attained for the swollen and 'non-swollen' resin. Inspection of the isotherms for the two samples combined with the BJH (Barrett-Joyner-Halenda) and neutron scattering analyses suggest that the 'non-swollen' sample possesses a highly convoluted 3D surface with surface area largely present in micropores. Similar analyses of the swollen sample suggest that the swelling has the effect of smoothing the surface somewhat and propagating surface area held within mesopores.

A hypercrosslinked sample which was synthesized using 97% m,p-CMS exhibited a surface area of 1811 m^2.g^{-1} with around 1675 m^2.g^{-1} of this being located in meso/macro porosity. BJH analysis further yielded a total pore volume of 1.40 cm^3.g^{-1} and a mean pore diameter of 31.1 Å. A sample synthesized using 90% p-CMS returned a surface area of 1279 m^2.g^{-1}; 715 m^2.g^{-1} of this was located in meso/macro porosity. This sample exhibited a total pore volume of 0.81 cm^3.g^{-1} and a mean pore diameter of 28.1 Å. The results show that the use of 90% p-CMS yields a resin with a lower surface area and a more microporous nature (both qualitatively and quantitatively). This is attributed to a combination of the DCE having less of a swelling effect on the gel-type resin and the steric hindrance to hypercrosslinking resulting from there being only one CMS stereoisomer present.
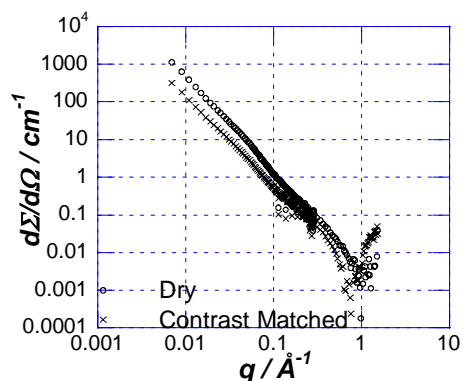
Figure 2. SANS & CM-SANS results for a pyrolytic carbon prepared using a T_1 of 600°C

Figure 2 shows the results from the dry and contrast matched SANS carried out on a pyrolytic carbon prepared using a T_1 of 600°C. The pyrolytic carbon synthesized using a T_1 of 600°C exhibited a BET surface area of 82 m^2.g^{-1} and a total pore volume of 0.109 cm^3.g^{-1}. The dry and contrast matched surface areas from SANS and CM-SANS were 658 m^2.g^{-1} and 189 m^2.g^{-1} respectively. The sample prepared with a T_1 of 700°C yielded a BET surface area of 65 m^2.g^{-1} and a total pore volume of 0.089 cm^2.g^{-1}. The dry and contrast matched surface areas from SANS and CM-SANS were 453 m^2.g^{-1} and 259 m^2.g^{-1} respectively. Both samples have mean pore diameters of 50 Å and exhibit scattering from a mass fractal of dimension 2.38-2.66 with T_1 of 600°C consistently being of lower dimension.

The investigation into the influence of the second isotherm temperature showed that the sample prepared at 900°C exhibited a BET surface area of 233 m^2.g^{-1} and SANS surface areas of 268 m^2.g^{-1} and 22 m^2.g^{-1} dry and contrast matched respectively. BJH desorption analysis yielded a mean pore diameter of 31 Å for this sample. Increasing T_2 to 1200°C resulted in a decrease in BET surface area to 115 m^2.g^{-1}. Dry and contrast matched SANS yielded surface areas of 263 m^2.g^{-1} and 137 m^2.g^{-1} respectively. This sample's mean pore

diameter was found to be 50 Å. These results suggest that increasing the value of T_2 results in an increase in the abundance of closed porosity within the sample yet little change in the overall surface area. Scattering from mass fractal structures was observed for both samples with dimensions between 2.6 and 2.8. The sample prepared at a lower temperature consistently displayed a higher dimension in overall and contrast matched data. This suggests, along with the data on mean pore diameter, the presence of a more convoluted structure.

Conclusions

The pore structures of hypercrosslinked resin networks are highly dependent on synthesis conditions. It has been shown that allowing gel-type resins to swell for 30 minutes prior to the introduction of FeCl$_3$ and heat has the effect of increasing the surface area of the sample. Furthermore this swelling serves to deconvolute the structure and propagate mesoporosity whilst reducing the abundance of microporosity.

Hypercrosslinked resins synthesized using 97% m,p-CMS generally possess higher surface areas, less microporosity and higher total pore volumes than resins synthesized using 90% p-CMS. This has been attributed to steric hindrance in the hypercrosslinking process due to the reduction in abundance of stereoisomers and DCE having a lesser swelling effect on gel-type resins synthesized from 90% p-CMS.

Lowering the first isotherm temperature in a two-tier pyrolysis strategy yields a carbon with a higher surface area and pore volume, mainly in open/accessible porosity yet still possessing significant areas of closed/inaccessible porosity.

The use of a lower second isotherm temperature tends to yield a more microporous carbon with less closed/inaccessible porosity.

References
(1) Becker, H. I., U.S. Patent 2,800,616
(2) Frackowiak, E., Beguin, F., *Carbon* **2001**, *39*, 937-950.
(3) Davankov, V. A., Tsyurupa, M. P., *React. Polym.*, **1990**, 13, 27-42
(4) Davankov, V. A., Tsyurupa, M. P., *Pure & Appl. Chem.*, **1989**, 61, 1881-1888
(5) Sherrington, D. C., *Chem. Commun.*, **1998**, 2275-2286
(6) Schmidt, P. W., *J. Appl. Cryst.*, **1991**, 24, 414

SURFACE TREATMENT OF SILICON COATED SYNTHETIC FLAKE GRAPHITE AS A NEGATIVE ELECTRODE OF LITHIUM SECONDARY BATTERIES

MyiungroLee, Dongjin Byun, ,Bup-Ju Jeon, Joong Kee Lee*

Eco-Nano Research Center
Korea Institute of Science and Technology
P.O.Box 131, Cheongryang.
Seoul 130-650, Korea

Introduction

Commercial rechargeable lithium batteries are employed as power supplies for cellar phones and portable computers. Usually carbonaceous materials have been used as the negative electrode because of their better cycling performance and dimensional stability compared to lithium alloys However, theoretical maximum storage capacity of graphite is 372 mAh/g [1].

In order to increase the specific capacity of the lithium secondary batteries, silicon is considered as one of the promising alternative anode materials. According to the electrochemical reactions between silicon and lithium, silicon can alloy with lithium up to 4.4 Lithium per silicon at high temperature. Theoretical capacity of silicon, therefore, is about 4,000 mAh/g. However, silicon is difficult to applied due to the problems as follows: the first one is poor cyclability caused by severe volume expansion and the second one is the high irreversible capacity at first cycle [2]. For the carbon-silicon composite system, therefore, we expect synergy effect of silicon-carbon composite system. In this system, silicon acts lithium alloying reactants during charge-discharge process and also carbon matrix play a role as the lithium intercalation sites and conducting medium between silicon particles as well.

Here, the purpose of this study is to find the relationship between electrochemical properties of silicon coated graphite and the heat treatment condition in hydrogen atmosphere. The employed temperature range is from 200 to 800°C.

Experimental

Commercial synthetic flake graphite with average particle diameter of about 6μm (Sfg6, Lonza Chem., Japan) was used as raw material. Coating solutions were prepared by mixing of non-polar solutions such as hexane and benzene were used as a dispersive agent. Spray coating was carried out with fluidized-bed process: fluidized graphite powder were coated and dried simultaneously inside the Wurster column, and then calcined in the furnace under H_2 or N_2 atmosphere. Electrostatic sprayer was employed to increase the dispersion of coating solution. The values of specific charge capacities, discharge capacities and initial efficiencies were dependent on combination of metal species and Si coated. In this study, the employed coating technique for the preparation of silicon-graphite composite is a gas-suspension spray coating method. All the graphite particles consists bed are all just suspended in upwarding flow gas. For spray coating, the atomized liquid droplet from the spray nozzle which was placed at the bottom of the bed contact the suspending graphite particles and spread over on the surface of the particles. The wetted particles are extensively dried through solvent evaporation. The repeated motion of the particles through the spray zone allows a continuous coating of material to build up and, finally uniform coating particle can be prepared. The precursor containing silicon was employed as a coating solute and ethanol mixture used for the solvent. After particles were coated, they were calcined in a furnace in the range of 200~800°C under an hydrogen atmosphere. Electrode for half-cells of lithium ion batteries were manufactured with the samples prepared under different conditions and their electrochemical properties were compared. Negative electrodes were fabricated by mixing a slurry containing 6 wt.% polyvinylidiene fluoride (PVDF) binder, 3 wt.% acetylene black as the conductor, and 91 wt.% active materials. The metals-coated carbon electrode does not contain acetylene black. The graphite, in the presence of some acetone was mixed in a vortex mixer at 5000 rpm. A slurry containing carbonaceous material was spread to form a 100 μm thick sheet on a copper foil by dipping. The sheet was allowed to dry at ambient temperature for a day, followed by drying in an oven at 80°C. The composite was then pressed at 110~120°C in a roll press. The pressed composite was cut into 2×2 cm pieces and dried in a vacuum at 110°C for 24 hours. All cells were assembled in a dry-room (max. moisture < 5%). The counter electrodes were lithium metal foils of 75 μm thickness, while the separator was a polypropylene film. The electrolyte employed in this study was 1M $LiPF_6$ dissolved in a mixture of ethylene carbonate (EC), diethyl carbonate (DEC), propylene carbonate (PC) and dimethyl carbonate (DMC)..

Results and Discussion

Scanning electron microscopy was employed to investigate the difference in surface morphology between the raw graphite and the silicon coated graphite. Figure 1(a) is the surface morphology of raw sfg6. Rather smooth surface with very few pores can be observed. Figure 1(b) shows that silicon films of about 50nm are covered throughout the specimen.
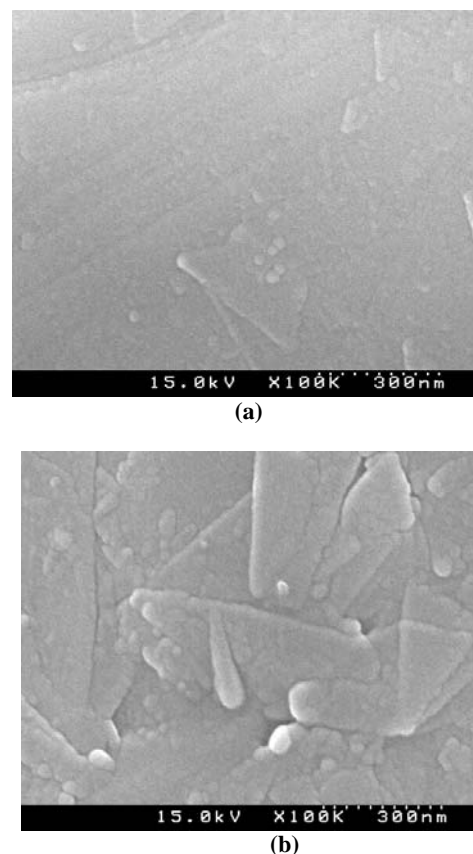

(a)

(b)

**Figure 1**. SEM images of raw sfg6(a) and silicon-coated sfg6(b).

Figure 2 shows the specific charge capacities and discharge capacities of bare synthetic flake graphite and silicon-coated graphites. For reversible capacity of bare synthetic graphite showed about 280 mAh/g, and the reversible capacity of the silicon-coated graphite increases with silicon coating The enhancement of specific capacity attributed by alloying formation between silicon and lithium during cycles However reversible capacity of silicon coated graphite decreases with increase of HTT.

XPS analysis of the silicon coated samples was performed using PHI5800 surface analysis system with mono-chromatic AlKα(aluminium Kei alpha) radiation. Figure3 shows Si2P spectra on the natural surface of silicon coated graphite. This spectrum can be resolved into two components. The first one located at 101.7eV seems to be due to SiOx.(0<x<2) And the third one at 102.5eV is due to SiO$_2$.

As can be seen Figure 3 (a), (b) and (c), the SiOx peak decreases with increase of HTT. Comparing the Figure 2 and 3, the reversible capacities of silicon coated graphite is closely related the amount of SiOx in Figure3 . SiOx reacts reversibly with lithium. A decrease in SiOx content decreases the reversible capacity even though SiO2 content increases.
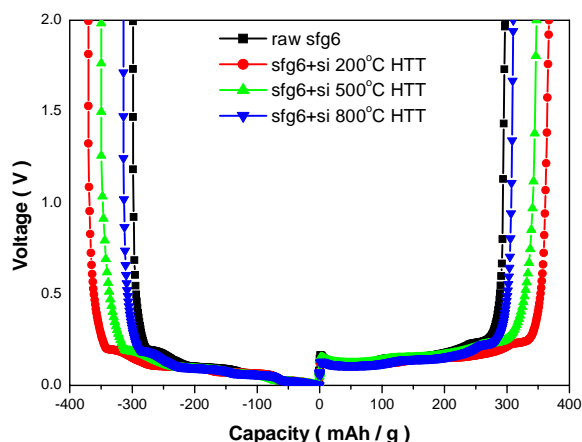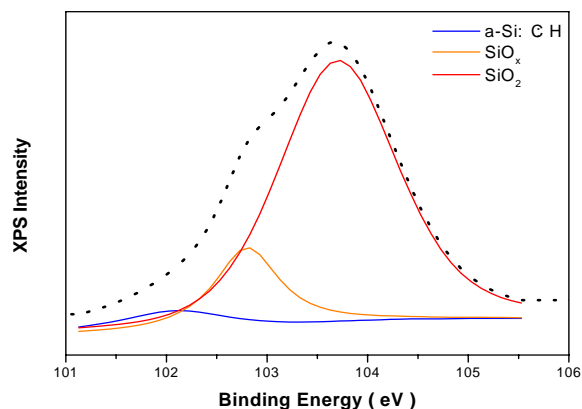

Figure 2. Charge-discharge curves for bare and silicon coated synthetic flake graphite at 2nd cycle   with 0.1 mA/cm^2 current density.

(a) 200°C

(b)500 ^{o}C
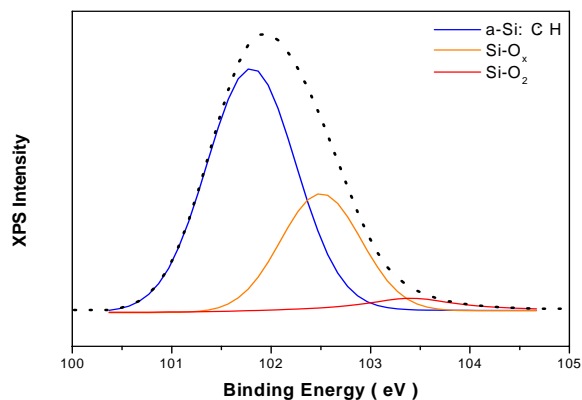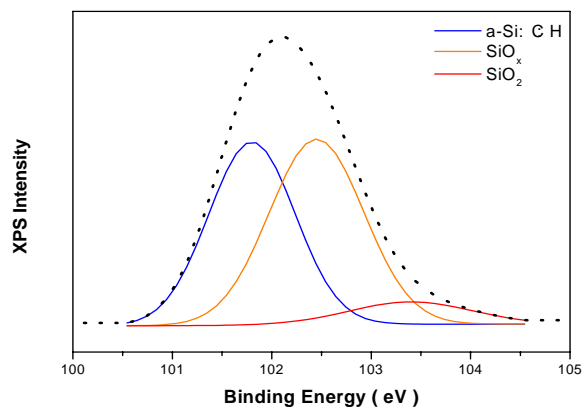
(c)800 ^{o}C

Figure 3. Experimental XPS spectra of Si 2p core-level spectra of silicon films on graphte with different HTT: (a) 200°C; (b) 500°C; 800°C.

References
1. Simon B, Flandrois S, Guerin K, Fevrier-Bouvier A, Teulat I, Biensan P. On the choice of graphite for lithium ion batteries. Journal of Power Sources1999;81/82:312-316.
2. Bourderau S, Brousse T, Schleich DM. Amorphous silicon as a possible anode material for Li-ion batteries. Journal of Power Sources 1999;81/82:233-236.

PREPARATION OF ELECTROCATALYST CARBONS FOR PEMFC FROM BLACK LIQUOR – A BIOMASS FROM PAPER MILLS.

Jun-ichi Ozaki[1], Takayuki Kogure[2], Kayoko Morishita[2], Asao Oya[1], and Takayuki Takarada[2]

[1]Graduate School of Engineering, Gunma University
[2]Faculty of Engineering Gunma University
1-5-1, Tenjin-cho, Kiryu, Gunma 376-8515, Japan.

Introduction

Proton exchange membrane fuel cell (PEMFC) is recognized as a promising option of power supply for domestic, automobile and small electronic devices. The high cost for the production of PEMFC is one of the obstacles preventing its implementation. The fact that a plenty amount of platinum is needed for promoting the oxygen reduction reaction (ORR) is a serious problem. Finding high performance electrocatalysts for ORR is an urgent issue. We have shown that the carbons prepared in the presence of metal complexes in carbonization could give improved electrocatalytic activities. [1]

Black liquor is a biomass emitted from paper mills. It is composed with lignin and alkaline metals. The utilization of the material as energy source is now extensively studied in Japan. We consider this can be a less expensive source of electrocatalyst carbons, if our carbonization technique, i.e. altering carbonization process by adding metal complexes, is effective even for this material

In the present study, we investigated the possibility of the preparation of electrocatalyst carbon for ORR from black liquor by modifying its carbonization by cobalt phthalocyanine (CoPc). We present the results how the introduction of CoPc affected the carbonization of black liquor and the electrocatalytic activity of the carbonized black liquors.

Experimental

Black liquor (C: 43.1% daf, ash: 55.1%) were treated with 6M HCl aqueous solution in order to remove the alkaline metal included in it as ash components. The acid-washed sample is referred to as BL. Cobalt phthalocyanine (CoPc) was added to BL by using a planetary ball mill (Fritsch, P-7, 800 rpm, 3 h). This is called as CoPc-BL.

Heat treatment was performed on BL and CoPc-BL, in a nitrogen stream up to a predetermined temperature (230-1000°C) at a rate of 10°Cmin^{-1}. After reaching the temperature, the sample was kept at the temperature for 1 h. The carbonization behavior was studied by using TG analyzer (TG-8120, Rigaku) and FTIR spectrometer (Avatar 360, Thermo Nicolet). X-ray diffraction was also applied to the samples to study the crystallographic changes (RINT2100, Rigaku).

ORR activity of the obtained samples was measured by rotating disk electrode method. The prepared carbons were pasted on a glass-like carbon disk electrode with 6 mm diameter by using Nafion as a binder. Voltammograms were recorded by sweeping the electrode potential from the open circuit potential (OCP) to -0.1 V vs. Ag/AgCl in an O_2-saturated 1M H_2SO_4 aqueous solution.

Results and Discussion

Carbonization Behaviors. Table 1 shows the elemental composition of the acid-washed sample, BL.

Table 1. Elemental Composition of BL (in wt%)

| C	H	N	O(diff.)
56.5	5.4	0	38.1

TG-DTG diagrams are presented in Figure 1. BL showed a maximum weight loss at 355°C and it gave 41% of carbonization yield at 1000°C. CoPc-BL showed an additional weight loss at 587°C and resulted in the yield of 45% at 1000°C.
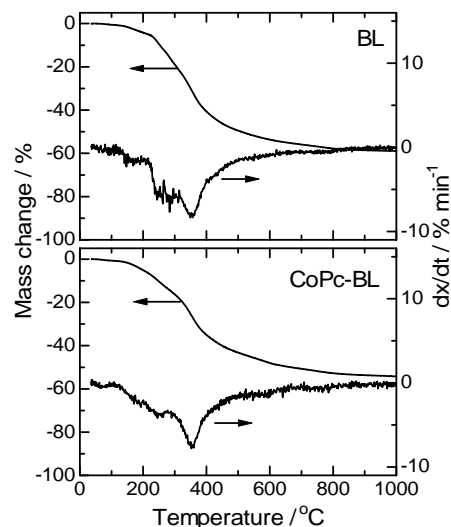
**Figure 1.** TG-DTG diagrams of black liquor (BL) and CoPc-doped BL (CoPc-BL).

Figure 2 shows the FTIR spectra obtained for the samples heat treated at different temperatures. BL included the following absorptions; aromatic δ(C-H) at <920 cm^{-1}, ether ν(C-O) at 1050-1250 cm^{-1}, alkyl δ(C-H) at 1420-1460 cm^{-1}, aromatic ν(C=C) at 1600 cm^{-1}, carbonyl or carboxyl ν(C=O) at 1720 cm^{-1}.

Decreases of ether and alkyl groups and of carbonyl and hydroxyl groups were found at >370°C and >550°C, respectively. In the case of CoPc-BL, the developments of the band at 1600 cm^{-1} and 3400 cm^{-1}. The former was considered to be a superposition of ν(C=C) and pyridinic skeleton vibrations, and it remained even after the heat treatment at 1000°C. The latter was assigned to as ν(N-H), and it vanished at 1000°C. The above observations suggested the incorporation of nitrogen atom into the carbon structure during carbonization.
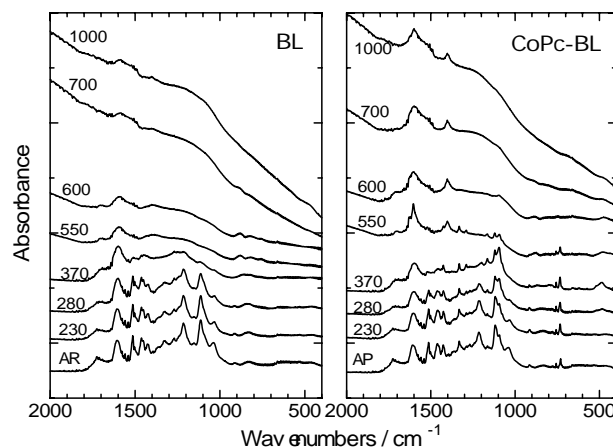
Figure 2. Changes in FTIR spectra of BL and CoPc-BL with heat treatment.

ORR Activity of the Carbonized Samples. The samples heat treated above 600°C were subjected to the ORR activity tests. The voltammogrames are presented in Figure 3. Since ORR is the cathode reaction of PEMFC, the carbons that show reduction currents at higher potentials are catalytically active for ORR. With the increase in the heat treatment temperature, the traces shifted to the higher potentials. We represented the activity of a carbon by the potential, E_{O2}, where the reduction current density of 10 μAcm^{-2} was obtained.
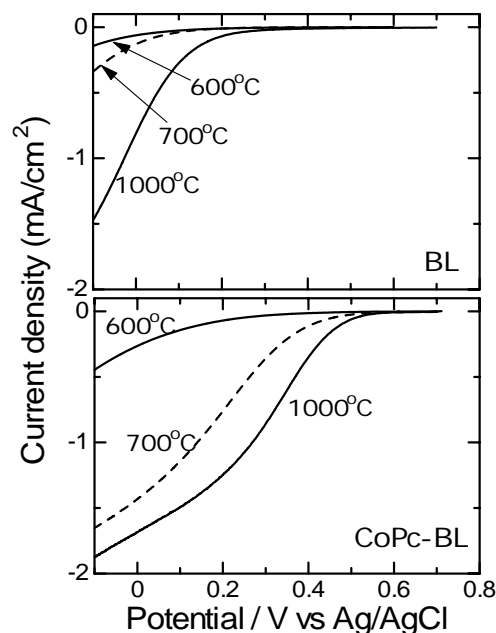
Figure 3. Hydrodynamic voltammograms of BL and CoPc-BL for oxygen reduction reaction (ORR).

The values of E_{O2} are listed in Table 2. Commonly CoPc-BLs showed higher E_{O2}, when the BLs and the CoPc-BLs with the same heat treatment temperatures were compared. We also found that the obtained the E_{O2} obtained for CoPc-BL1000 was higher than the carbons derived from the CoPc-poly(furfuryl alcohol) mixtures.[1]

Table 2. ORR Activities of BLs and CoPc-BLs in Terms of E_{O2} (V vs. Ag/AgCl).

HTT (°C)	BL	CoPc
600	0.20	0.44
700	0.20	0.56
1000	0.40	0.58

The surface areas of the 1000°C-treated BL and CoPc-BL showed similar values, i.e. 135 m^2g^{-1} and 128 m^2g^{-1}, respectively. These results indicated that the ORR activity is not caused by the differences in the surface areas, but by the differences in the chemical natures of the carbons. We are now conducting studies from the viewpoint of the crystallinity and the composition of the surfaces of the carbons.

Conclusions

We could show the possibility of black liquor as a starting material for the preparation of carbon materials for the electrocatalysts in PEMFC, if we properly control its preparation processes.

References

(1) Ozaki, J;Furuichi, A; andOya, A. Carbon2004, E038, 2004, Providence, USA.

METHANOL OXIDATION PROPERTY OF PTRU ANODE CATALYST SUPPORTED ON THE NANO-TUNNELED CARBON NANOFIBER FOR DIRECT METHANOL FUEL CELL

S-H Hong, S-H Yoon, M.-S. Jun, S-Y Lim, and I. Mochida

Institute of Materials for Chemistry and Engineering,
Kyushu University, Japan

Introduction

The methanol oxidation property of catalyst supported on the Nano-tunneled carbon nanofiber (CNF) was examined to improve the activity of Pt-Ru/CNF catalyst for the performance of the Direct Methanol Fuel Cell (DMFC). The effect of Nano-tunnel on the CNF was evaluated using a Cyclic Voltammetry (CV) method, SEM, TEM, and so on. The CNF was prepared from thermal CVD method using metal catalyst in our laboratory. Carbon nanofiber and their adequate modifications can afford various defined structures, surfaces, and nano-spaces for Pt-Ru metal particles. We developed a new material composed of carbon nanofibers which are highly porous and have a very narrow distribution of nanopores distributed radially within the fiber. These new porous fibers contain very few micropores, which distinguishes them from other high surface area carbons. The present authors examined the Pt-Ru catalytic performances of defined parts of carbons, such as nano-pores, edge and basal planes, oxygen functional groups and Ru contents. Measurements of methanol oxidation property were carried out using 60 wt% Pt-Ru (1:1 mol/mol) supported on the Nano-tunneled CNF using 3-electrode half cell connected CV system. The anodic performance of catalyst supported on the Nano-tunneled CNF was compared to that of the commercial E-TEK catalyst.

Experimental

The carbon paper (Toray co., SHF-806B) was used in this experiment as the electrode diffusion layer and catalyst supporting material which was treated for giving the hydrophobicity as Teflon dispersion solution (Mitsui・Dupont Fluorochemical Inc., FEP120-J). The PtRu/CNFs catalyst was prepared after mixing the CNFs with distilled water, and added $RuCl_3 \cdot nH_2O$ (Wako Co.) and $H_2PtCl_6 \cdot 6 H_2O$ (Wako Co.) with stirring. The slurry was reduced using 0.5M $NaBH_4$. and the filtering, washing and drying were subsequently done. The catalyst slurry was prepared through the mixing with 20 wt% of Nafion solution (Wako Co, 5% Nafion dispersion solution) compared to Pt weight and catalyst. The slurry was brushed on the carbon paper. The weight of Pt-Ru/C catalyst was controlled to 2±0.5mg and subsequently dried at room temperature for 12hr. The Cyclic Voltammogram was measured at the room temperature for the scan speed of 20mV/sec using an equipment of Hokudo Denko Inc., HZ-3000.

Results and Discussion

Figure 1 show SEM and TEM photographs of as-prepared herringbone CNF, and those of the Nano-tunneled CNF were shown in figure 2. The porous surface was observed in the SEM photograph and the nano-pore perpendicular to the fiber axis was also observed in the TEM photograph of figure 2.
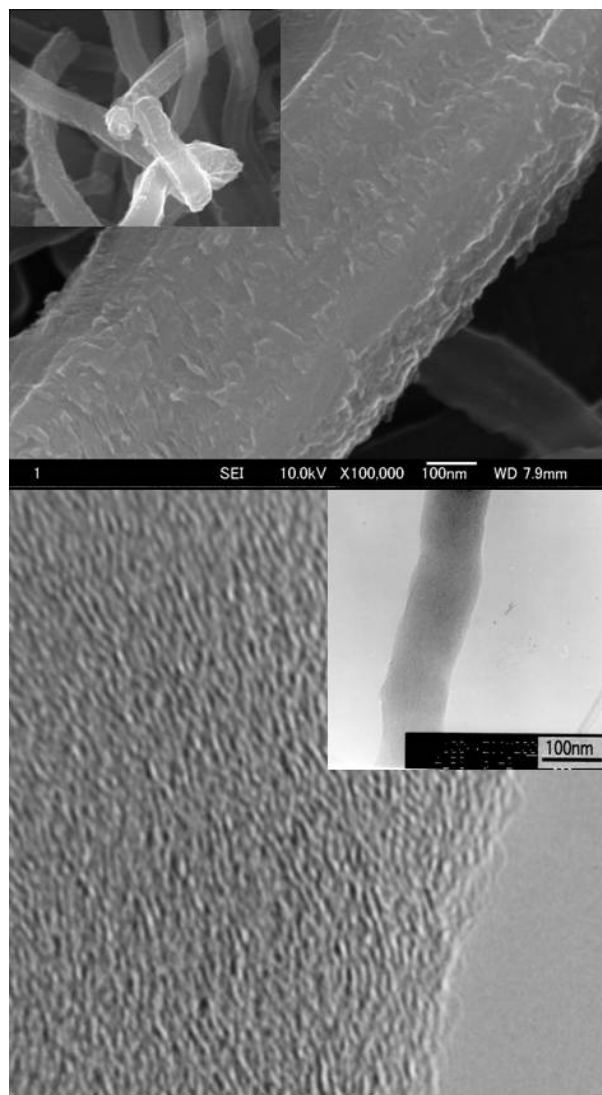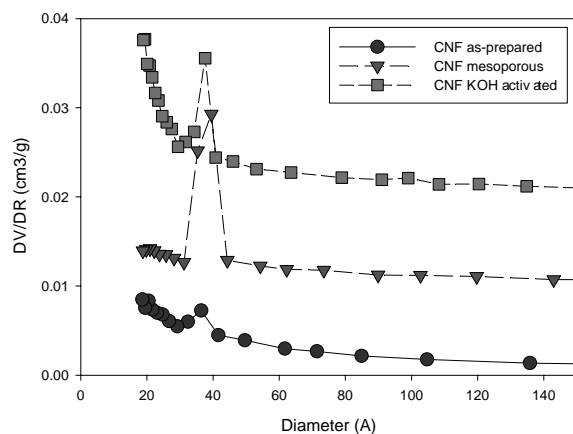

**Figure 1.** SEM and TEM photographs of as-prepared herringbone CNF.
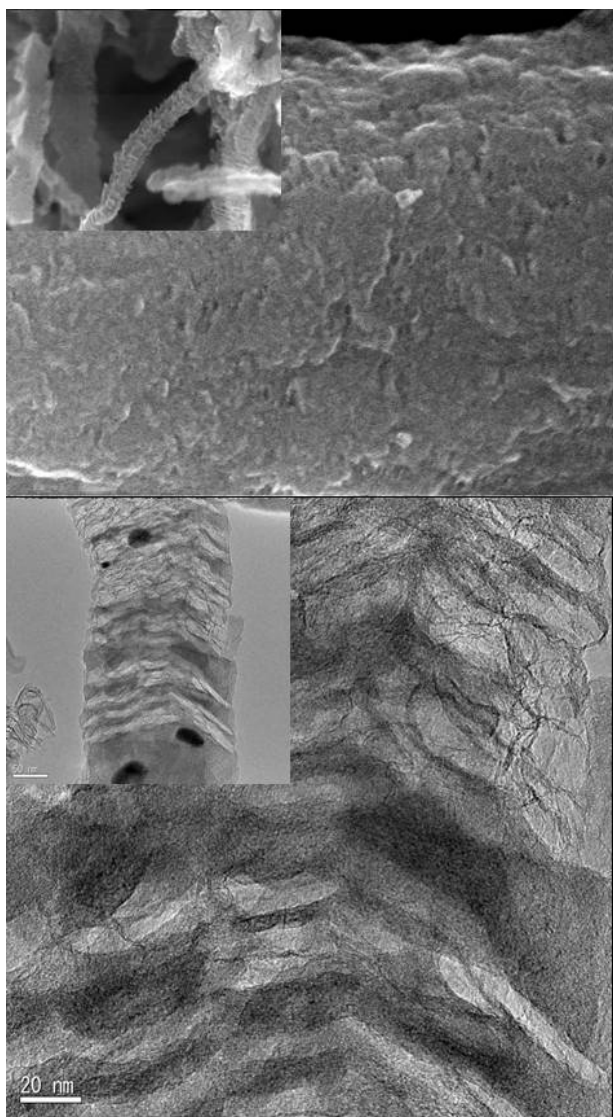
Figure 2. SEM and TEM photographs of Nano-tunneled herringbone CNF.

Figure 3 shows the pore size distribution from the BET method. The average diameter was calculated to be 3-4 nm.


Figure 3. The pore size distribution from the BET method.

Figure 4 shows the cyclic voltammograms of catalysts supported on the as-prepared and nano-tunneled CNFs compared to the E-TEK catalyst. The methanol oxidation properties of H-CNF and E-TEK catalysts showed almost the same about 120mA. However, it was improved in the PtRu 60w%/CNF catalyst supported on the nano-tunneled CNF to be 280 mA.
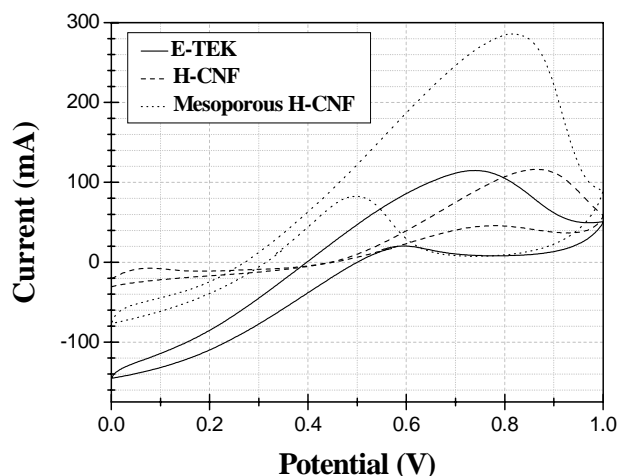

Figure 4. Cyclic voltammograms of PtRu 60 wt% catalysts supported on the as-prepared and nano-tunneled CNFs compared to the E-TEK catalyst.

Figure 5 show the methanol oxidation properties of various contents of PtRu catalysts supported on the nano-tunneled CNF and E-TEK catalysts.
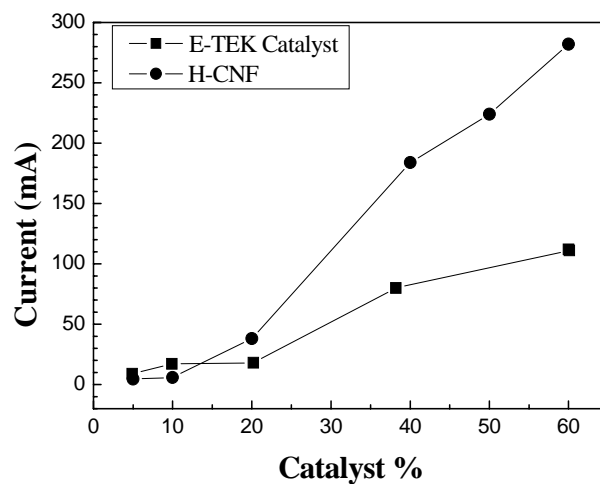
Figure 5. Methanol oxidation properties of PtRu catalysts supported on the nano-tunneled CNF and E-TEK catalysts.

Figure 6 show TEM photographs of PtRu 60 wt% catalyst supported on the nano-tunneled CNF. We concluded that the improvement of the methanol oxidation capability should be from the increase of the effective surface area of supporting material, contact among the catalyst, proton conducting material and methanol, and decrease of the internal resistance from the micropore.
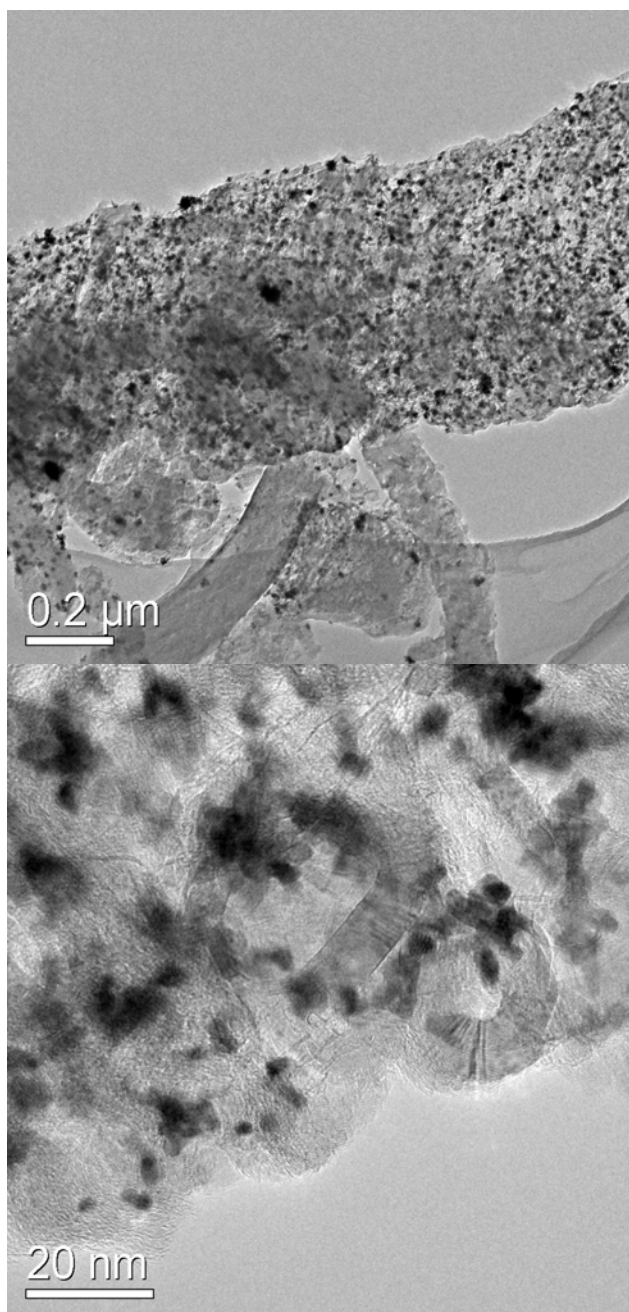
Figure 6. TEM photographs of PtRu 60wt% catalyst supported on the nano-tunneled CNF.

CARBON NANOTUBES FOR MICRO FUEL CELL APPLICATIONS

G. Girishkumar[1], Matthew Rettker[2] K. Vinodgopal[1, 2], and Prashant V. Kamat[1]

Radiation Laboratory and Dept. of Chemical Engineering,
University of Notre Dame, Notre Dame, IN 46556
and
Department of Chemistry,
Indiana University Northwest, Gary, IN 46408

Introduction

Unique electrical and electronic properties, high mechanical strength and wide electrochemical stability window makes carbon nanotubes a promising carbon support for the development of fuel cell electrodes[1,2]. A membrane electrode assembly (MEA) for the H_2/O_2 fuel cells has now been fabricated using single walled carbon nanotubes (SWCNT). Electrophoretic deposition technique[3,4] has been employed to obtain 3-D assembly of single wall carbon nanotubes as thin film on electrode surfaces. Under the influence of a dc electric field (80 V/cm) the SWCNTs become asymmetrically charged and get deposited on the electrode surface (carbon paper or carbon cloth). The same method is extended to deposit commercial platinum black on the SWCNT films and develop catalytically active electrodes.

The paper will focus on electrophoretic deposition of the SWCNT on the electrode surface, surface characterization of the nanotube assemblies and their electrocatalytic performance for reductive and oxidative processes. The Pt modified SWCNT electrodes have been evaluated for methanol oxidation, hydrogen evolution and oxygen reduction reactions.

Figure 1 shows the Tafel plots for the hydrogen evolution reactions at SWCNT/Pt electrode and Carbon Black/Pt electrode. Depending upon the overpotential window regime, a Tafel slope between 30 and 130 mV /decade was obtained for the hydrogen evolution reaction for the Carbon Black/Pt electrode and a platinum black electrode. For all three electrodes, we obtain similar values between 25 and 33 mV/decade, indicating that similar mechanisms are operating on all three electrodes in the lower potential regime. At higher overpotential regime we see a difference on Tafel slope values for SWCNT/Pt electrodes indicating a different mechanism is operative, in this region. The exchange current density for a SWCNT-Pt electrode ($-log(I_0/Acm^{-2})$) is 1.84 when compared with that of commercial Pt black 3.20 and also comparison of the overpotential at a useful value of current density shows that the overpotential value for a SWCNT electrode is low and hence a better electrocatalyst. In addition, we have also conducted electrochemical impedance spectroscopy (EIS) measurements. These experiments reveal a lower charge transfer reaction resistance (R_{ct}) for SWCNT/Pt based electrodes compared with commercial black/Pt based electrodes for hydrogen evolution reaction.
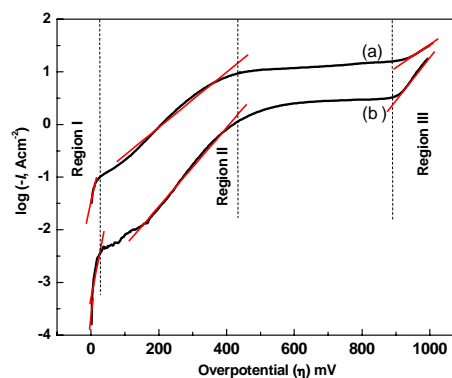
Figure 1. Tafel polarization curves for the HER at (a) SWCNT/Pt electrode and (b) CB/Pt electrode in 1M H_2SO_4. The scan rate was 20 mV/sec and the area of the electrode is 1.4 cm^2.

The electrophoretic deposition technique employed in the present study is simple and convenient to fabricate carbon fuel cell electrode assembly with Pt-modified single wall carbon nanotubes (SWCNT) catalyst loading. The galvanostatic polarization of SWCNT/Pt based fuel cell is shown in Figure 2. Details on the performance of hydrogen fuel cell will be discussed.
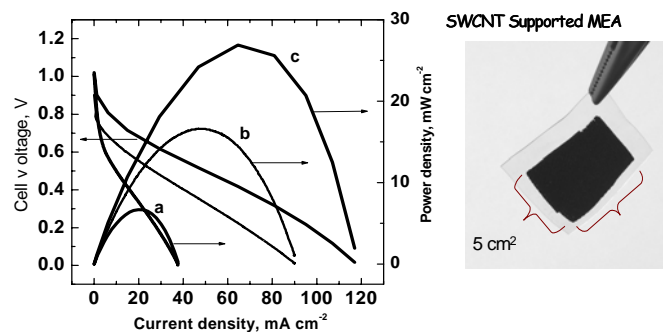
Figure 2. Galvanostatic polarization data of a MEA prepared by electrophoretic deposition of Pt black on varying amount of SWCNTs . Trace (a) corresponds to a loading of 0.25, (b) 0.7 and (c) 1 mg/cm^2 of SWCNT. The loading of Pt on all electrodes was kept constant at 1mg/cm^2. The electrolyte was Nafion 117 and the cell operating temperature was 25°C, electrode area 5 cm^2 and anode back pressure of 15 psi. The digital photograph of the MEA that is used for the present study is shown adjacent to the polarization curve.

References

(1) Wang, C.; Waje, M.; Wang, X.; Tang, J. M.; Haddon, R. C.; Yan, Y. S. *Nano Lett* 2004, *4*, 345-348.
(2) hoi, W.-B.; Chu, J.-U.; Pak, C.-H.; Chang, H. In *U.S. Pat. Appl. Publ*; Samsung SDI Co., Ltd.: S. Korea, 2004; Vol. 01, pp A1-A10.
(3) Kamat, P. V.; George Thomas, K.; barazzouk, S.; Girish kumar, G.; Vinodgopal, K.; Meisel, D. *Journal of the American Chemical Society* 2004, *126*, 10757-10762.
(4) Morikawa, H.; Tsuihiji, N.; Mitsui, T.; Kanamura, K. *J Electrochem Soc* 2004, *151*, A1733-A1737.

CARBON NANOFIBERS AS CATHODE CATALYST SUPPORTS FOR DIRECT METHANOL FUEL CELLS

Wu Mei, Yoshihiko Nakano, Seiichi Suenaga, Maki Yonetzu, Yoshihiro Akasaka, Hideyuki Oozu, Yashuhiro Goto

Advanced Functional Materials Laboratory
Corporate Research & Development Center
Toshiba Corporation.
Kawasaki, Japan 212-8582

Introduction

Direct methanol fuel cells (DMFCs) have recently attracted great attention for their potential as clean portable power sources. Since the compactness of DMFCs is important to their commercialization, high cell performance at low air feeding rates is desired to downsize the DMFCs. This usually requires a good cathode electrode which has enough gas-catalyst-electrolyte triple phase boundaries, high diffusion of O_2 and low water flooding. One solution is to explore novel nanocarbon materials as supports for cathode catalysts. Recently, various nanocarbon materials have been found, such as C60, carbon nanotubes (CNTs) and carbon nanofibers (CNFs). Here CNTs are referred as the one with a tube like graphite sheet structure, while CNFs are those with flat graphite sheets, which, according to the orientation angel (θ) between graphite closest-packing plane and fiber axis, can be further divided to ribbon-type ($\theta = 0°$), platelet-type ($\theta = 90°$), and Herringbone-type ($0° < \theta < 90°$), respectively. Previous studies indicate that CNTs supported cathode catalysts (Pt/CNT) [1~4] and CNF supported anode catalysts [5,6] may be good candidates for DMFCs catalysts. However, less has been studied on the cell performance at low air feeding rates. The possibility of CNFs as cathode catalyst supports and the origin of the nanocarbon effects are not clear.

In this reports, the potential of carbon nanofibers as the cathode catalyst supports of DMFCs was explored to achieve a high DMFCs performance at low air feeding rates. Herringbone-type carbon nanofibers (HCNFs) were used owing to their geometric potential for high density metal supporting.

Experimental

Polycrystalline Herringbone CNFs were used. Their average diameter is of 300 nm, BET surface area is about 200 m^2/g. Supported catalysts (Pt/HCNF) were synthesized with precipitaion method, where the supports was mixed with aqueous H_2PtCl_6 solution and then titrated with aqueous NaOH solution. The resultant was dried and finally reduced at 200~900 °C. According to the desired Pt supporting density (weight ratio of Pt/(Pt + Carbon)) process parameters were optimized to provide homogeneous fine Pt particles. For comparison, VulcanXC 72 carbon black supported catalyst (Pt/VulcanXC72) was also prepared with the same method.

Composition analysis, powder X-ray diffraction (XRD), transmission electron microscopy (TEM) and rotating disk electrode cyclic voltammetry (CV) were performed to characterize the supported catalysts. Cathode electrodes (typical metal loading: 1.5 Pt mg/cm^2) were prepared by mixing appropriate amounts of supported catalysts (supporting density: 50 wt. %), distilled water with Nafion^{TM} solution, and then printing the mixture (ink) on Toray carbon papers. Similarly, anode catalysts (PtRu/VulcanXC72) and anode electrodes (typical metal loading: 4 mg PtRu/cm^2) were prepared and 10 cm^2 membrane electrode assemblies (MEAs) were then fabricated by hot pressing the anode electrodes, cathode electrodes onto opposite faces of Nafion^{TM} 117 films.

The voltage vs current density curves and the voltage at 150 mA/cm^2 of the above MEAs were measured in DMFCs at 70 °C, with 1M methanol aqueous solution fed into anode at a rate of 0.6 ml/min. and air into cathode at a rate of 50~500 ml/min. under near ambient pressure. The pore distribution of the cathode electrodes was determined using mercury porosimetry method.

Results and Discussion
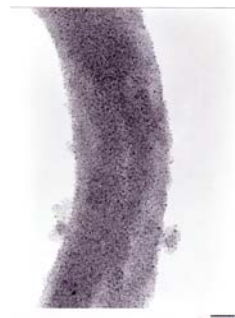
Figure 1. Typical TEM photo of Pt/HCNF supported catalysts (supporting density: 50 wt.%). Scale length: 50nm.

Figure 1 shows a typical TEM photo of the supported catalysts of Pt/HCNF. The supporting density is 50 wt.%. Homogeneous fine Pt particles were obtained, with an average diameter of 3 nm revealed by XRD and TEM analysis. This is quite different from the CNT supported catalysts [3], where many Pt particles with a diameter larger than 5 nm exist even though the supporting density is just about 15 wt.%. The answer may be found in Figure 2, a typical TEM photo showing the cross section of the Pt/HCNF. It is clear that, most of the Pt particles exist inside the fibers, different from the CNT supported one, for which Pt particles nearly stay on the CNT surface and special treatment is usually necessary for retain them on the surface. For the Herringbone fibers, probably, the edge opening among the graphite sheets and the boundaries among the different carbon grains supply a large amount of supporting sites for the Pt particles. It should be mentioned that agglomeration of the Pt particles was observed for the one with a supporting density exceeding 60 wt.%.


Figure 2. Typical TEM photo of the cross section of the Pt/HCNF supported catalysts (supporting density: 50 wt.%). Scale length: 50nm.
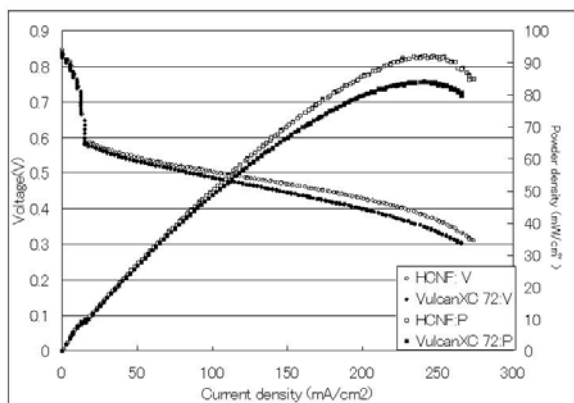
Figure 3. Current density vs voltage curves of DMFCs. 70 °C, MeOH: 1M, 0.6 ml/min.; Air: 100 ml/min..

Figure 3 shows current density vs voltage curves of DMFCs using Pt/HCNF and Pt/VulcanXC72 as cathode catalysts (cathode catalyst loading: 1.5 mg/cm²). The HCNF one gives high performance than the Vulcan72 one, exhibiting about 25 mV higher voltage at 150 mA/cm². The maximum power density of the HCNF one is about 94 mW/cm², while the Vulcan one only shows 86 mW/cm². The performance increase may arise from improvement of (1) catalyst activity via catalysts-supports interaction or/and (2) mass transportation resulted from electrode structure modification.
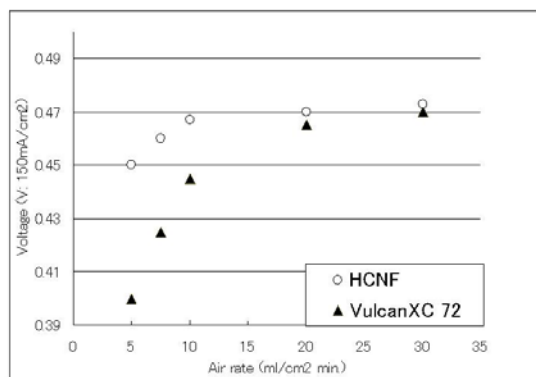

Figure 4. Air rate dependences of the cell voltage at 150 mA/cm².

Figure 4 shows the air rate dependences of the cell voltage at 150 mA/cm² of the above two kinds of DMFCs. At higher air feeding rates, the voltage gap between the two curves is small. This suggests that no obvious catalyst activity difference between the two kinds of supported catalysts, considering almost the same MEA resistivity of the two cells. However, as air rate decreases, the voltage gap becomes bigger. This indicates that the performance difference at low air rates, also as shown in the Figure 3, is caused mainly by the change of mass transportation rather than the catalyst activity or/and conductivity. Probably, in the catalyst layers using HCNF supported catalysts, the diffusion of O_2 and/or H_2O is easier, and thus can produce more triple phase boundaries of gas-catalyst-electrolyte and exhibit higher properties than the Vulcan one. This is also supported by our CV determination, where no obvious difference in O_2 reduction potential and current density was confirmed for the above two kinds of catalysts with diffusion effect carefully removed.

The transportation of O_2 and H_2O through catalyst layer is mainly affected by the diffusion distance, pore distribution and

wettability. Previously, Li et al attributed the higher performance in Pt/CNT PEMFC to the thinner catalyst layer of Pt/CNT electrode compared to a Vulcan black one [4]. However, in our experiments, the Pt/HCNF layer is thicker than the Pt/VulcanXC72 one. This implies that, neglecting the effects of wettability, the diffusion improvement should arise from the pore distribution. From the thickness and the load amounts of carbon and Nafion™, the porosity of the Pt/HCNF and Pt/VulcanXC72 layers could be roughly estimated as 70 vol.% and 35 vol.% respectively. This confirms a large amount of pores existing in the Pt/HCNF catalyst layers. Figure 5 shows the pore distribution of the two kinds of catalyst layers. The Pt/HCNF one shows a strong broad peak around a pore diameter of about 600 nm, while the Pt/VulcanXC72 one possesses a weak sharp peak with a peak diameter of about 50 nm. It is likely that the higher porosity and such a pore structure caused the higher low air rate performance in the Pt/HCNF one, by improving the O_2 diffusion and/or suppressing the water flooding in the cathode electrodes.
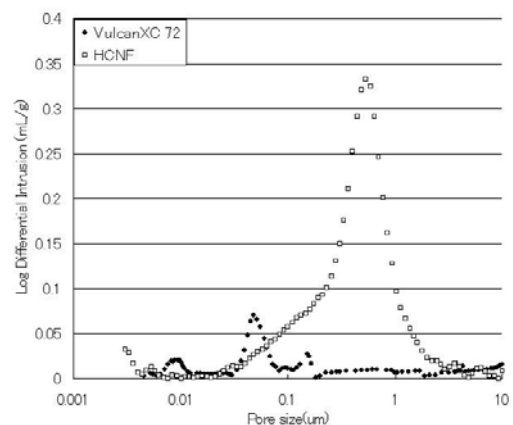
Figure 5. Pore distribution of the electrode (1.5mg Pt/cm²).

Conclusions

Herringbone carbon nanofiber supported catalysts (Pt/HCNF) with high Pt supporting density of 40 wt.% and homogeneous fine Pt particles were synthesized. Higher DMFCs performance at low air feeding rates was obtained using Pt/HCNF as cathode catalysts than Pt/VulcanXC72. This can be mainly attributed to catalyst layer structure modification more than catalyst activity improvement.

References
1. Che Guanli, Brinda B. Lakshmi, Ellen R. Fisher & Charles R. Martin, *Nature*, **1998**, *393*, 346.
2. Matsumoto, T.; Komatsu, T.; Nakano, H.; Arai, K.; Nagashima, Y.; Yoo, E.; Yamazaki, T.; Kijima, M.; Shimizu, H.; Takasawa, Y.; Nakamura, J.; *Catalysis Today*, **2004**, *90(3-4)*, 277-281
3. Chen, J.; Xu, C.; Mao, Z.; Chen, C.; Wei, B.; Ling, J.; Wu, D.; *Science in China, series A; Mathematics, Physics, Astronomy*, **2002**, *45(1),* 82-86.
4. Li, W.; Liang, C.; Qiu, J.; Zhou, W.; Han, H.; Wei, Z.; Sun, G.; Xin, Q.; *Carbon*, **2002**, *40(5),* 791-794.
5. Bessel, C. A.; Laubernds, K.; Rodriguez, N. M.; Baker, R.T.K.; *J. of Phys. Chem. B*, **2001**,*105(6)*, 1115
6. Steigerwalt, E.S.; Gregg, A.D.; Lukehart, C.M.; *J. of Phys. Chem. B*, **2002**,*106*, 760.

ELECTROCHEMICAL PROPERTIES OF GRAPHITIZED CARBON NANO-BEADS

Takeshi Abe, Wang Hongyu, Yasutoshi Iriyama, Zempachi Ogumi, and Kazuo Yoshikawa*

Graduate School of Engineering, Kyoto University, Nishikyo-ku, Kyoto 615-8510, Japan
* Fuji Research Laboratory, Tokai Carbon Co. Ltd., Oyama, Shizuoka 410-1431, Japan

Introduction

Recently, our group has developed graphitized carbon nano-beads (GCNB) as a promising anode material for lithium-ion batteries. In addition to the virtue of low and flat working voltage characteristic of common graphitized carbon anode materials, GNCB demonstrates superior tolerance towards propylene carbonate (PC)-based electrolytes, even the solvent of sole PC. This advantage was tentatively attributed to its special onion-like texture, in which mainly the inert basal-plane surface exposes outside. Moreover, GNCB possesses high rate performance, which benefit might come from its small particle size. To shed more light on nano-carbon beads (NCB) as anode materials, we have carried out systematic studies on series of NCB samples. We found there are two vital factors could be tailored to control the physical and electrochemical properties of NCB, particle size and heating temperature. In this study, we will focus on the effect of heat treatment.

Experimental

Samples (radius, 100 nm - 200 nm, NCB28, 24, 20, 16) were prepared in Tokai Carbon. Each sample was mixed with the solution of PVDF/NMP(N-methyl pyrrolidinone) (KF#1120, Kureha) to make a slurry with suitable viscosity. The weight ratio of GNCB to PVDF was adjusted to 9:1. Then the slurry was spread onto a copper foil thinly and evenly to fabricate electrode. Let the electrode stand in the draft overnight to sublime most of the NMP solvent, and then vacuum dried at 80 °C for one day. The electrolytes used in the test contained 1M LiClO$_4$/PC and 1M LiClO$_4$/EC:DEC (1:1 by volume).

Results and Discussion

Figure 1 compares the cyclic voltammograms (CVs) of NCB samples in the electrolyte of 1M LiClO$_4$-PC. All these CVs show quite satisfactory cycle performance since there is little decline of current against cycles. Specially in the case of highly graphitized sample NCB28, the big irreversible peak in the first cycle due to graphite exfoliation accompanied by drastic PC decomposition could hardly been observed. The rough trend is, the higher the heating temperature, the narrow distribution of redox peaks towards low potential. In the CV of NCB16, there are two couples of broad redox peaks could be identified in the low and high potential range, respectively.

We have performed suite of impedance investigations on these samples at different open circuit voltage (OCV). For example, for NCB16 in 1M LiClO$_4$/PC, at potentials lower than 1 V vs. Li/Li$^+$, at least two arcs could be found in the spectra in the higher and lower frequency range, respectively. The former is ascribed to SEI film, whereas the latter to charge transfer across the interface between the electrode and the electrolyte. The charge-transfer resistance for NCB are compared and correlated with the rate performance in combination with the Li$^+$ diffusivity in NCB. The detailed information will be present in the meeting.
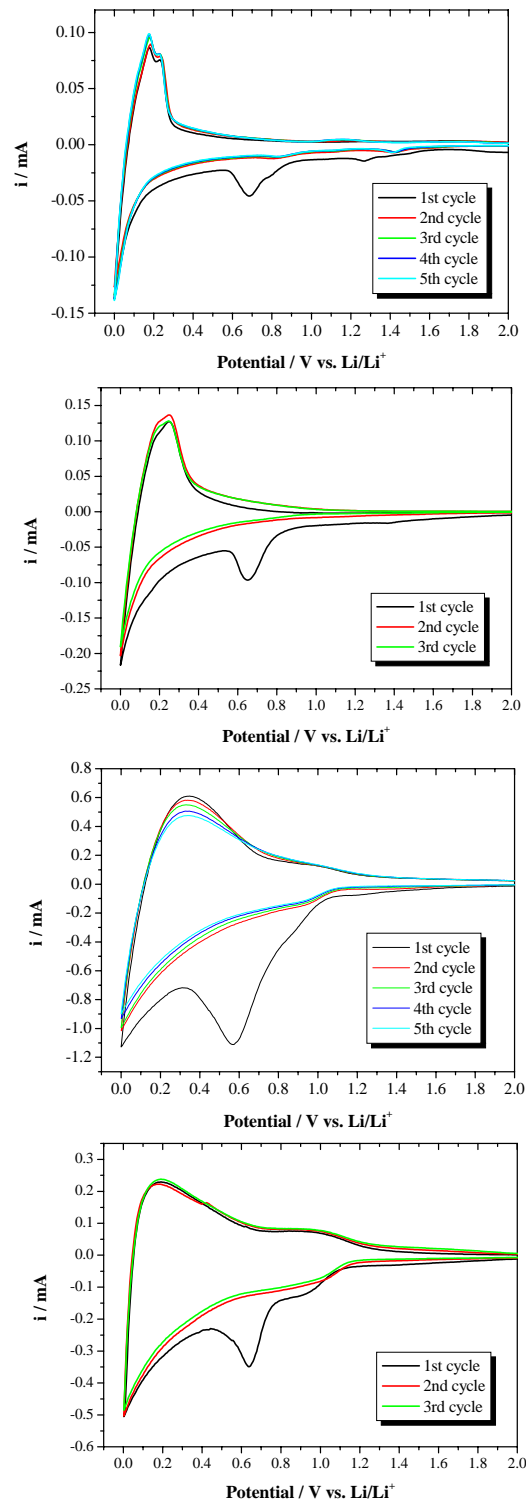
Figure 1. Cyclic voltammograms of NCB samples in the electrolyte of 1M LiClO$_4$-PC, scan rate: 0.1 mV/sec.

SONOCHEMICALLY PREPARED PLATINUM NANOPARTICLES FOR FUEL CELL APPLICATIONS

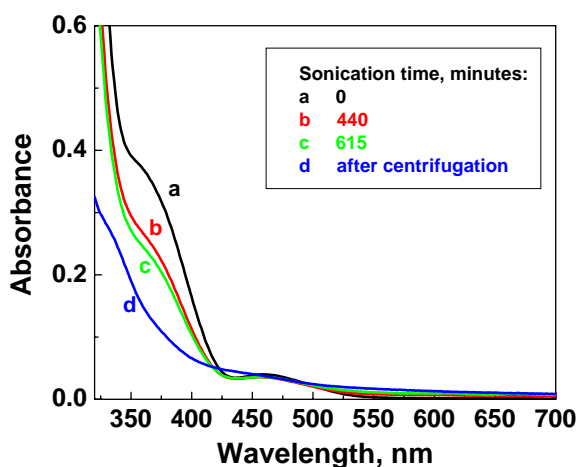*K. Vinodgopal[1], G. Girishkumar[2], Robert Underhile[1], and Prashant V. Kamat[2]*

Department of Chemistry,
Indiana University Northwest, Gary, IN 46408
and
Radiation Laboratory and Dept. of Chemical Engineering,
University of Notre Dame, Notre Dame, IN 46556

Introduction

The primary process that dictates the operation of the fuel cell is the oxidation of the fuel, hydrogen or methanol at the anode and the reduction of oxygen at the cathode. Both reactions require a precious metal catalyst usually platinum. It is widely believed that size control of the metal catalyst will lead to higher surface areas and thereby enhance oxidation. Synthesis of metal nanoparticles using a variety of methods has been widely reported in the literature[1,2]. A number of groups, have shown that ultrasound irradiation of aqueous solutions containing noble metal salts produce the corresponding colloids of the noble metal.[3]

We achieve optimum reduction of the hexachloroplatinate, when we use a 80:20 mixture of ethanol and water as the solvent. Figure 1 shows the absorption spectrum of a 10^{-3} M solution of hexachloroplatinic acid as a function of sonication time. The absorption bands arising from the Pt (IV) disappears with increasing sonication time. The sonication time is a function of the water content. The fairly long sonication times that are required to achieve complete reduction of the Pt (IV) is due to the limited water content in the solution. What remains is a featureless absorbance extending into the visible and is characteristic of colloidal platinum. The solution is centrifuged (1000 rpm) at this point to isolate the small Pt particles that still remain in the suspension. The Pt suspension of 2 nm diameter particles is a pale yellow solution and was used for electrophoretic deposition. This solution is stable up to a week, after this the solution gets progressively turbid as the colloidal particles begin to agglomerate and settle down.

The high resolution TEM image of the sonochemically prepared colloidal solution is shown in Figure 2. The image reveals well dispersed ultra-small particles of platinum. A close up shown in Figure 2 reveals that the individual particles are ~2 nm in diameter. We can obtain films of nano-sized Pt colloids, on an electrode surface using an electrophoretic deposition method. We have used these Pt electrodes subsequent as an anode catalyst in a H_2/O_2 fuel cell. The fuel cell performance of nano-sized Pt based catalyst will be presented.
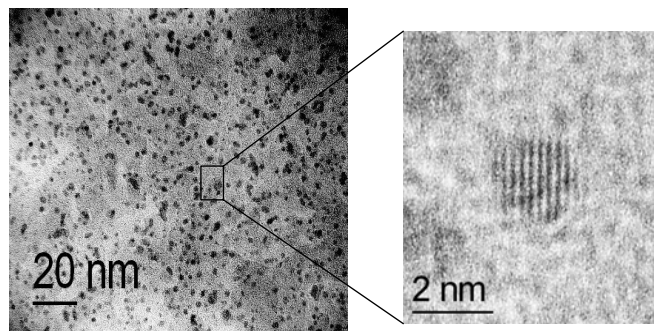
Figure 2. HRTEM image of a sonochemically synthesized colloidal Pt showing defined lattice fringes.

References
(1) Dalmia, A.; Lineken, C. L.; Savinell, R. F. *Journal of Colloid and Interface Science* **1998**, *205*, 535-537.
(2) Schmidt, T. J.; Noeske, M.; Gasteiger, H. A.; Behm, R. J.; Britz, P.; Bonnemann, H. *Journal of the Electrochemical Society* **1998**, *145*, 925-931.
(3) Caruso, R. A.; Ashokkumar, M.; Grieser, F. *Colloids and Surfaces a-Physicochemical and Engineering Aspects* **2000**, *169*, 219-225.

Figure 1. Shows the absorption spectrum of a 10^{-3} M solution of hexachloroplatinic acid as a function of sonication time. Trace a-d corresponds to the sonication time in minutes.

NEW, DIRECT ROUTE TO MESOPOROUS CARBONS BASED ON PYROLYSIS OF BLOCK COPOLYMERS WITH POLYACRYLONITRILE BLOCKS

Chuanbing Tang[§], Michal Kruk[§], Ewa B. Celer[‡], Abigail Laurent[†], Mietek Jaroniec[‡], Krzysztof Matyjaszewski[§], Tomasz Kowalewski[§]*

[§] Department of Chemistry, Carnegie Mellon University, 4400 Fifth Avenue, Pittsburgh, Pennsylvania 15213; [‡] Department of Chemistry, Kent State University, Kent, Ohio 44242; [†] Department of Chemical Engineering, Carnegie Mellon University, Pittsburgh, Pennsylvania 15213

Introduction

Porous carbons and activated carbons in particular, are widely used as adsorbents, owing to their well-developed microporous structures of high adsorption capacity (micropores are pores of width below 2 nm). Porous carbons include other applications of chromatographic packings, catalyst supports, and components of electrochemical double-layer capacitors, and electrochemical batteries.[1-6] However, from the point of view of these applications, micropores of activated carbons are typically too narrow. Therefore, there is currently much interest in the synthesis of high-surface-area carbons with wider pores, primarily in the mesopore range (2-50 nm).[2,7-11] The mesoporous carbons are often prepared using mesoporous silicas as hard templates,[1,2,8,12] which usually involves the preparation of a template, followed by the infiltration of its pores with a carbon precursor, the carbonization of the precursor, and the removal of the template. Although this approach provides a variety of opportunities in the fabrication of mesoporous carbons with tailored structures and some degree of tunability of the pore size, it involves multiple steps, including the use of HF or NaOH to dissolve the template. Moreover, these mesoporous carbons are difficult to obtain in the form of thin films, which is a serious disadvantage in the development of numerous devices. Herein, we report a convenient route to mesoporous carbons using block copolymers composed of polyacrylonitrile (PAN) and the so-called sacrificial block(s) of lower stability. In this direct procedure, PAN serves as a carbon precursor, whereas the sacrificial block (e.g., poly(n-butyl acrylate), PBA) facilitates the formation of nanoscale domains of PAN through the nanoscale phase separation, and is eliminated during the conversion of PAN to carbon. Block copolymers can be easily fabricated in the form of films, and therefore our route provides an excellent way to prepare mesoporous carbons for the use in thin-film-based devices. This new approach to the mesoporous carbon synthesis is based on our recent discovery that block copolymers with PAN domains can be thermally treated to convert them into partially graphitic carbon thin films and individual carbon nanoobjects with concomitant volatilization of the sacrificial block.[13-15]

Experimental

Materials. PBA-*b*-PAN diblock copolymers with varying PAN content were synthesized using atom transfer radical polymerization (ATRP), as reported earlier.[14] PAN content was varied through the range assuring formation of PAN domains with morphologies ranging from spheres, to cylinders and lamellae, as conformed by atomic force microscopy (AFM). Copolymer compositions, contents of PAN (in weight %, which is approximately equivalent to volume %) and observed morphologies are listed in Table 1. For the mesoporous carbon synthesis, bulk PBA-*b*-PAN samples were thermally treated under air at 280°C to stabilize PAN and then heated to 800°C under nitrogen to yield shiny black carbon powders.

Characterization. Tapping Mode Atomic Force Microscopy studies were performed using a NanoScope III-M system (Digital Instruments, Santa Barbara, CA), equipped with a J-type vertical engage scanner. The AFM observations were performed at room temperature under air using silicon cantilevers with nominal spring constant of 50 N/m and nominal resonance frequency of 300 kHz (standard silicon TESP probes). Morphologies of carbons were imaged with the aid of transmission electron microscope (TEM) (JEOL JEM-2000 EX II with acceleration voltage 200KV). Nitrogen adsorption isotherms were measured at -196°C on a Micrometritics ASAP 2010 adsorption analyzer. X-ray diffraction (XRD) scans were performed on a Rigaku Geigerflex equipped with a theta/theta goniometer. It employed a copper target x-ray tube with a power setting of 35kV and 25mA. 1.0 degree divergence and scatter slits were used along with 0.3 mm receiving slits. A curved graphite monochromator was used on the diffracted beam. Raman spectra were collected on a Jobin Yvon T64000 triple Raman system (ISA, Edison, NJ) in subtractive mode with microprobe sampling optics. The excitation was at 514.5 nm (Ar^{+} laser, Model 95, Lexel Laser, Fremont, CA).

Table 1. PBA-*b*-PAN Diblock Copolymer Precursors for Mesoporous Carbons

| Sample	DP_{BA}/DP_{AN}	wt.% PAN	Morphology of PAN domains
P1	202/54	10.0%	Spherical
P2	202/106	17.8%	Cylindrical
P3	141/126	27.0%	Cylindrical or Lamellar
P4	78/114	37.7%	Branched
P5	40/116	54.6%	Continuous

Results and Discussion

AFM imaging revealed a strong dependence of the nanoscale morphology on the composition of diblock copolymers, consistent with trends typically observed in block copolymer structures. For instance, an AFM image of P2 precursor (Figure 1(a)) shows short, cylindrical, rigid domains, which can be identified as PAN dispersed in PBA matrix. The PBA-*b*-PAN precursors were then subjected to the thermal treatment to convert them to nanostructured carbons. The carbon nanostructure had a morphology similar to that of the PAN domains. Carbons prepared from precursors with a lower content of PAN tended to preserve the nanoscale structure better than those from precursors with a higher PAN content. As evident in Figure 1(b), the carbon material displayed short cylinders similar to the cylinders of PAN observed for the precursor P2.
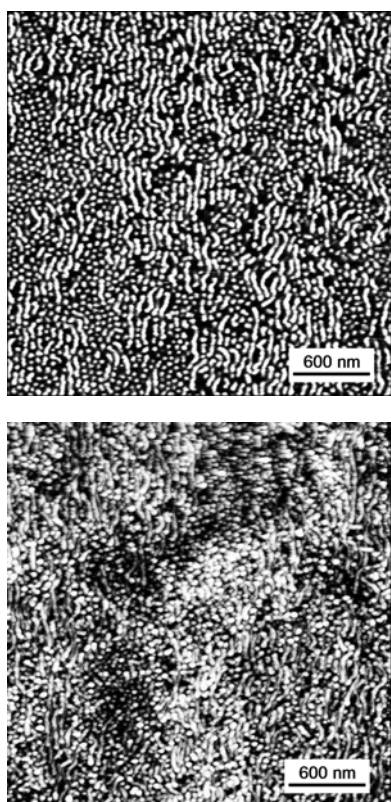
Figure 1. AFM phase image of precursor P2 (a) and height image of the derived carbon (b).

As seen from TEM (Figure 2), the morphologies of carbon powders prepared from bulk copolymer precursors resembled the morphologies of PAN domains of the precursor films and the resulting carbon films. The carbon from P2 precursor was composed of short cylinders, which were separated from one another, thus creating an accessible porous structure. The carbon from P4 precursor was composed of connected short filaments, resembling the branched morphology of its precursor observed by AFM.

Figure 3 shows nitrogen adsorption isotherms at -196°C for the carbons derived from P2-P5 PBA-b-PAN copolymers. The isotherms featured capillary condensation steps at high relative pressures (p/p_0=0.8–0.99), and hysteresis loops characteristic of mesoporous materials, consistent with the TEM images. The adsorption data pointed to the presence of a certain amount of micropores, which are presumably in the framework of the nanostructured carbon. Further studies will be needed to determine the micropore content and to verify whether the micropores can be eliminated through a heat treatment at higher temperatures. The carbon derived from P1 copolymer exhibited a very low adsorption capacity. Apparently, the isolated PAN spheres merged into a structure, which could not be accessed by nitrogen gas at -196°C.
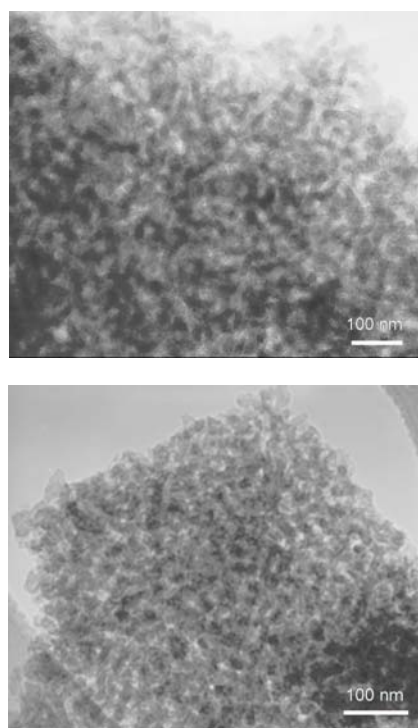

Figure 2. TEM images of carbons obtained from precursor P2 (a) and P4 (b).

The BET specific surface areas of the carbons were in the range from 100 to 300 m^2 g^{-1}. The carbon derived from P4 copolymer with PAN content of 38 wt.% exhibited the highest specific surface area (~300 m^2 g^{-1}) and pore volume (~0.40 cm^3 g^{-1}). The pore size distributions (PSDs) showed the presence of mesopores, whose size monotonously increased with the increase of the molecular weight of the sacrificial block. The sizes of the pores in our carbons were primarily above 10 nm, and thus larger than those for ordered mesoporous carbons.[2,5,8] The large pore diameter is beneficial from the point of view of a number of applications, including those requiring the accessibility of pores to large molecules. Although the adsorption capacity of these carbons is moderate or low, when compared to that of many other types of mesoporous carbons, it is expected that it can be improved through the optimization of carbon precursors and synthesis conditions. Moreover, the adsorption capacity currently achieved is sufficient from the point of view of many prospective applications, including those where thin-film morphology, which can be readily achieved in the present case, is of primary importance.
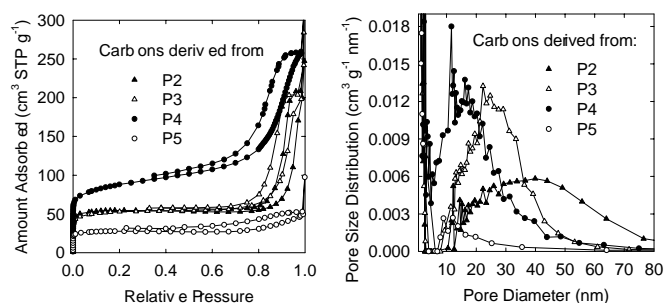
Figure 3. (a) N_2 adsorption isotherms (left) and (b) PSDs for carbons (right).

The partially graphitic nature of obtained carbons was confirmed by wide-angle XRD and by Raman spectroscopy. As seen in Figure 4(a), XRD peaks at *2θ* of ~25°, 45° and 80°, which correspond to the (002), (101), and (110) reflections of the graphitic structure, were observed. The position of the (002) peak indicates that the spacing between graphene sheets in the carbon framework is equal to ~0.358 nm. Multi-wall carbon nanotubes and some of the most graphitic ordered mesoporous carbons reported so far show intense, narrow (002) peaks.[16] In our case, the (002) peak was intense, but somewhat broader. On the other hand, many mesoporous carbons, including those synthesized from sucrose, exhibit much weaker and/or broader (002) peaks. This comparison suggests that our carbons exhibit an appreciable degree of ordering on atomic scale, and yet are not fully graphitic. This is also evident from Raman scattering spectra, which featured G and D bands characteristic of graphitic carbon (sp^2) and less well-defined carbon structures carbon (Fig. 4 (b)).
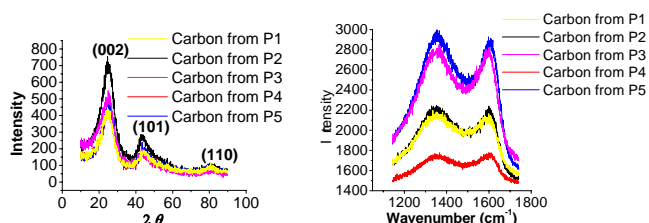
Figure 4. (a) XRD patterns (left) and (b) Raman scattering spectra (right) of mesoporous carbons.

Conclusions

In conclusion, a convenient strategy was developed for the synthesis of mesoporous carbons with tailorable structures through pyrolysis of PAN-containing block copolymers. The structure of the mesoporous carbon usually closely resembled the structure of PAN domains of the block copolymer precursors, which opens an opportunity of design of carbon nanostructures through the choice of block copolymer precursors with suitable nanostructures. Furthermore, this route opens an easy way to fabricate mesoporous carbons in the form of thin films. The carbons exhibited XRD patters and Raman scattering spectra typical for partially graphitic materials.

References
(1) Knox, J. H.; Kaur, B.; Millward, G. R. *J. Chromatogr.* **1986**, *352*, 3.
(2) Ryoo, R.; Joo, S. H.; Jun, S. *J. Phys. Chem. B* **1999**, *103*, 7743.
(3) Yoon, S.; Lee, J. W.; Hyeon, T.; Oh, S. M. *J. Electrochem. Soc.* **2000**, *147*, 2507.
(4) Joo, S. H.; Choi, S. J.; Oh, I.; Kwak, J.; Liu, Z.; Terasaki, O.; Ryoo, R. *Nature* **2001**, *412*, 169.
(5) Ryoo, R.; Joo, S. H.; Kruk, M.; Jaroniec, M. *Adv. Mater.* **2001**, *13*, 677.
(6) Choi, M.; Ryoo, R. *Nature Mater.* **2003**, *2*, 473.
(7) Pekala, R. W.; Alviso, C. T.; Kong, F. M.; Hulsey, S. S. *J. Non-Cryst. Solids* **1992**, *145*, 90.
(8) Lee, J.; Yoon, S.; Hyeon, T.; Oh, S. M.; Kim, K. B. *Chem. Commun.* **1999**, 2177.
(9) Han, S.; Hyeon, T. *Carbon* **1999**, *37*, 1645.
(10) Tamon, H.; Ishizaka, H.; Yamamoto, T.; Suzuki, T. *Carbon* **2000**, *38*, 1099.
(11) Li, Z.; Jaroniec, M. *J. Am. Chem. Soc.* **2001**, *123*, 9208.
(12) Yu, C. Z.; Fan, J.; Tian, B. Z.; Zhao, D. Y.; Stucky, G. D. *Adv. Mater.* **2002**, *14*, 1742.
(13) Kowalewski, T.; Tsarevsky, N. V.; Matyjaszewski, K. *J. Am. Chem. Soc.* **2002**, *124*, 10632.
(14) Tang, C.; Kowalewski, T.; Matyjaszewski, K. *Macromolecules* **2003**, *36*, 1465.
(15) Tang, C.; Qi, K.; Wooley, K.; Matyjaszewski, K.; Kowalewski, T. *Angew. Chem. Int. Ed.* **2004**, *43*, 2783.
(16) Kim, T. W.; Park, I. S.; Ryoo, R. *Angew. Chem. Int. Ed.* **2003**, *42*, 4375.

MESOPOROUS CARBONS OBTAINED FROM POLYSTYRENE SULFONIC ACID-BASED ORGANIC SALTS BY TEMPLATE CARBONIZATION METHOD

Conchi O. Ania and Teresa J. Bandosz

Department of Chemistry
City College of New York, City University of New York
138th Street at Convent Avenue
New York, NY 10031

Introduction

Recent developments in technology require porous carbons with tailorable pore sizes, specific shapes of pores, and large surface areas. The preparation of mesoporous carbons with uniform mesopores, large surface areas and large pore volumes carbons have attracted widespread attention due to their relevance for applications in emergent areas such as energy storage as double layer capacitors[1], catalytic supports in fuel cells electrodes[2], adsorbents of bulky molecules form liquid phase[3], etc. Although numerous novel approaches to design a pore structure can be found in the literature [4], only a few of them allow for full control of porosity. Nevertheless, the template carbonization has been proven to be an excellent method for obtaining carbons with large surface areas, high porosity and controlled narrow pore size distributions in the mesopore range[4, 5].

Generally in the approach of template carbonization, the preparation of materials involves the synthesis of the mesostructured silica (the template), functionalization of the silica and impregnation of the template with the carbon precursor (polysaccharides, polymers, etc), polymerization of the precursor, carbonization and elimination of the template. Thus, mesoporous carbons are obtained as inverse replicas of the template. MSU-X silicas (X refers to the type of surfactant) are used as templates owing to their 3-D wormhole porous framework[6].

A polystyrene-based polymer (poly-(styrene sulfonic acid co maleic acid)- sodium salt) is used as a carbon precursor in this research. Prior to carbonization, in order to increase surface heterogeneity, the precursor chemistry is modified by cation exchange with catalytically active metals (i.e., copper, nickel, cobalt). An important aspect of the preparation procedure is alteration the surface properties by changing the contents of the metals. Thus, besides tailoring the porosity, the surface chemistry of the synthesized carbon can also be designed according to the desired application. For comparison, carbon is also prepared from sucrose.

The objective of this research is to study the effects of the template porosity and the type of metals in the carbon precursors on the surface features of the template derived carbons. Moreover, the flexibility of the "tailoring" process is also evaluated.

Experimental

Synthesis of mesoporous silica. The template is synthesised in a two-step pathway using tetraethyl orthosilicate as the silica source and non-ionic surfactants following the procedure described by Boissiere et al.[7]). As a surfactant, non ionic poly(ethylene oxide) - PEO- surfactant Tergitol 15-S-N was selected.

Briefly, the silica source is added under stirring to the solution of a nonionic surfactant and the pH is adjusted at around 2 with HCl. The solution is kept in a closed vessel for 18 h without stirring at room temperature. Then a small amount of NaF is added to promote silica condensation. The mixture is aged for 3 days at two temperatures, 30 and 60 ºC. The white precipitate obtained is filtrated, dried and calcined at 600 ºC to eliminate the excess of the surfactant. The samples will be referred to in the text as T30 and T60, respectively.

Carbon template. Sucrose and a polystyrene-based polymer (poly-(styrene sulfonic acid co maleic acid)- sodium salt) are used as carbon precursors in the template carbonization method. For the sucrose synthesis, organic phase was introduced into the silica channels by liquids impregnation of a sucrose solution according to the process described by Ryoo et al.[8]. Briefly, the silica pores are impregnated with an aqueous solution of sucrose and sulfuric acid. After drying at 160ºC, the sucrose/silica composite is again impregnated with a sucrose solution and heated at 800ºC in an inert atmosphere. After two impregnation cycles, the amount of carbon deposited in the template represents 36 wt.% . The sample is denoted as the template silica followed by SUC (T30-SUC or T60-SUC).

In the case of polystyrene-based carbons, the silica is coated with an aqueous solution containing 16% of the organic salt, until the incipient wetness was achieved. The impregnated sample was cured in air for 16 hours at 120 ºC, and then carbonized under nitrogen at 800 ºC for 40 min. In some cases, the precursor chemistry was modified by incorporation of catalytically active metals. Previous to carbonization, cation-exchange was done using $Cu(NO_3)_2$, $Co(NO_3)_2$, and $Ni(NO_3)_2$) for 24 hours, and the samples were heated at 120 °C to evaporate the water. After removal the silica matrix using hydrofluoric acid (48%) at room temperature a Soxhlet washing with distilled water was performed to remove an excess of water-soluble inorganic salts (sodium and excess of transition metal salts). The carbons are designated as the template silica followed by PS, PS-Co, PS-Ni and PS-Cu.

Characterization Methods. Nitrogen adsorption isotherms were measured using an ASAP 2010 (Micromeritics) at -196 ºC. Before the experiment the samples were heated at 120 °C and outgassed at this temperature under high vacuum for 24 h. The BET specific surface area, total pore volume and pore size distributions were evaluated from the nitrogen adsorption data. The pore size distributions and total pore volumes, V_t were calculated using density functional theory (DFT)[9]. A subdivision of microporosity was made: narrow microporosity (pore diameter < 0.7 nm), and medium-sized microporosity (0.7<pore diameter<2 nm).

Thermal analysis was carried out using a TA Instrument thermal analyzer. The instrument settings were as follows: heating rate 10 ºC min^{-1} and a nitrogen atmosphere with 100 mL min^{-1} flow rate. For each measurement about 25 mg of a ground sample was used.

Results and Discussion

Figure 1 shows the nitrogen adsorption isotherms of the silica templates obtained with Tergitol at 30 and 60 ºC. It is clearly seen that the temperature of the synthesis plays an important role in the final structure of the template. The isotherm for T60 sample exhibits a typical type IV isotherm shape with a hysteresis loop and pronounced capillary condensation step, suggesting the presence of mesopores. In contrast, T30 presents a type I isotherm with no hystereis loop, indicating a pore size distribution dominated by micropores. The BET surfaces areas showed a decrease with an increase in hydrothermal temperature from 1014 to 980 m[2]g[-1] for T30 and T60, respectively.

The analysis of PSD indicates that the sample obtained at 30ºC has a unimodal distribution of pores whereas for T60 the bimodal distribution is revealed. The maxima on the PSDs are at 3.7 nm for T60, and at 2.7 nm for T30. The results obtained are in good agreement with those reported by Alvarez et al.[10].
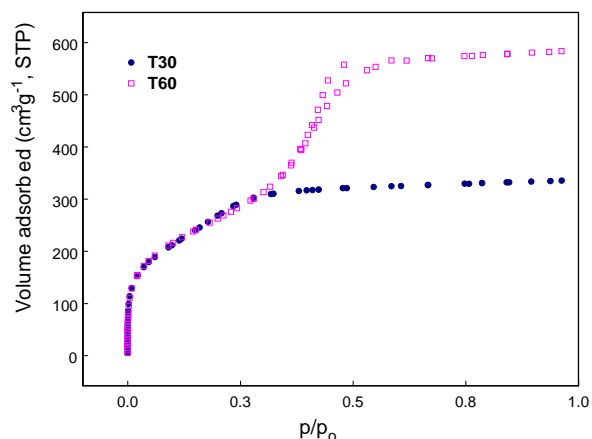
Figure 1. Nitrogen adsorption isotherms of the silica templates obtained at different temperatures.

It is important to use carbon precursor with a high carbon yield (atomic ratio of carbon after / before pyrolysis 40–50%) to limit the shrinkage induced by densification and preserve the overall shape of the structure. Despite the fact that sucrose does not present a high carbon yield (25%), it was selected for this study as it is water soluble and thus easy to handle. In the case of the polystyrene salts, the yield after carbonization represents approximately 40%, although it decreases significantly after water and acid washing due to the elimination of water-soluble salts, sulfates and oxides. Nevertheless, this precursor allows the possibility of incorporation of metals in the carbonaceous matrix of the templated carbon.

In addition, by controlling the amount of the carbon precursor infiltrating the silica porosity (various impregnation –carbonization cycles or incipient wetness), carbons with one or two pore systems (unimodal or bimodal) might be expected.

Application of a polystyrene-based salt as a carbon precursor led to a strong alteration of the silica template. The replicated carbon presented a large mesopore system, as indicated by the hystereis loop and capillary condensation step in the nitrogen adsorption data. Moreover, the creation of complementary mesoporosity with a wide pore size distribution was noticed. This behavior has been attributed in the literature to the water vapor released during the carbonization process (due to the use of a liquid carbon precursor) that could hydrolyzed the poorly hydrothermally stable silica network[11]. On the contrary, when a sucrose solution was used as precursor, the formation of complementary mesopores in the templated carbon was not observed. This corroborates the hypothesis suggested by Fuertes et al., about the coalescence of unfilled silica pores when silica walls are removed (thus, the sizes of the mesopores increases remarkably)[5]. The absence of complementary mesopores in the case of sucrose template is a consequence of the use of a two impregnation step procedure, providing a better impregnation of the silica pores. In the case of sucrose impregnation, the mesoporous structure of the silica is quite a faithful replica of the one corresponding to the original silica, with a shift in the maximum on the PSD towards wider mesopores (i.e., 3.2 nm); in addition, microporosity is developed during the carbonization, leading to a microporous material of the high surface area and well-developed mesoporosity.

Figure 2 shows the effect of the presence of metallic cations on the carbon precursor in the final structure of the templated carbons. The structural parameters are collected in Table 1. The incorporation of metals in the carbonaceous structure also leads to a strong alteration of the ordered porous structure of the silica.

Table 1. Structural Parameters of the Templated Carbons (S - m^2/g; V- cm^3/g)

Sample	S_{BET}	V_t	V_{nmic}	V_{mic}	V_{mes}
T30	1042	0.487	0.013	0.201	0.256
PS	1737	1.021	0.146	0.368	0.288
T30 PS	997	1.866	0	0.083	1.754
T30 PS Ni	959	2.339	0.060	0.071	2.171
T30 PS Cu	907	2.540	0.002	0.071	2.426
T30 PS Co	820	1.132	0.033	0.085	0.989
T30	1042	0.487	0.013	0.201	0.256

It is noteworthy that adsorbents obtained from nickel and copper salts have larger surface areas and higher volumes of mesopores. For the nickel and copper containing samples, the similarities in the pore size distributions exist, especially for the complementary mesopores. The narrow mesopore size distribution of the original silica is not obtained in the case of copper and nickel-containing samples, as it is obtained in the case of the sample impregnated with the sodium form of the material. In contrast, a wide mesopore PSD with a maximum at 20 nm is revealed.
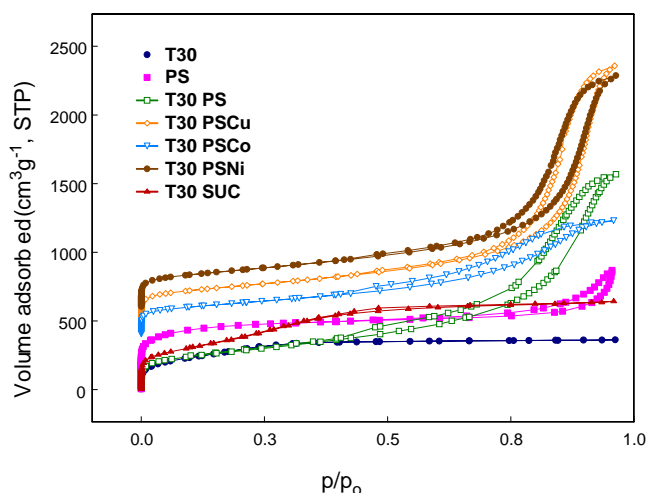
Figure 2. Nitrogen adsorption isotherms of the templated carbons obtained from the T30 silica precursors (isotherms for PS-Co, PS-Cu and PS-Ni are vertically shifted 400, 500 and 600 $cm^3 g^{-1}$ for clarity).

A remarkable difference in porosity is noticed for the cobalt-containing sample, as the enlargement of the complementary mesopores is sharply reduced (maximum at 9.3 nm), along with the BET surface area.

These differences in the porosity might be related to the uniformity of metal dispersion achieved in the carbon precursor, as it is well known that this factor is extremely important for the formation of novel carbon entities on various supports, and to the forces that arise from the decomposition of the carbon precursor during the carbonization process. In the case of carbonization of polystyrene based salts the significant expansion of the volume of the carbon precursor was noticed with the formation of foam like structure. As pyrolysis occurs in a confined space (the silica structure), these expansion forces (from gases released during carbonization) might result in a partial expansion of the silica structure, and hence in formation of additional porosity. At the same time, the active surface of carbon is exposed to various gases reacting with metal, thus resulting in expansion of the graphene layers. A

similar behavior was also observed when carbonization was carried out on the metal-containing precursors directly[12].

Conclusions

The results of this study show the feasibility of the template carbonization method in the process of preparation of mesoporous carbons from polystyrene sulfonic acid-based organic salts with a tailorable surface chemistry. Large BET surface areas and mesopores volumes are attained, although the presence of reactive gases during the carbonization results in expansion of the graphene layers, and thus in wide mesopore size distributions of the templated carbons. This effect was less remarkable in the case of the cobalt-containing carbon, which is likely due to different chemistry involved during the carbonization process.

Acknowledgment

References

(1) Yoon, A., , Lee J., Hyeon, T., Oh, S.M., J. *Electrochem. Soc.* **2000**, 147, 2507.
(2) Joo, S.H., Choi, S.J., Oh, I., Kwak, J., Liu. Z., Teresaki, O., Ryoo, R., *Nature*, **2001**, 412, 169
(3) Han, S., K Sohn, T Hyeon, Chem. Mater. 12 (2000) 3337.
(4) Kyotani, T., *Carbon*, **2000**, 38, 269.
(5) Fuertes, A.B., *Micro Meso Mater.* **2004**, 67, 273.
(6) Bagshaw, S.A., Pouzet, E., Pinnavaia, T.J., *Science*, **1995**, 269, 1242.
(7) Boissiere C., Larbot, A., van der Lee, A., Kooyman, P.J., Prouzet, E., *Chem Mater.*, **2000**, 12, 2902.
(8) Ryoo, R., Joo, S.H., S. Jun, *J. Phys. Chem. B*, **1999**, 103, 7743.
(9) Olivier, J., *Carbon* **1998**, 36, 1469.
(10) Alvarez, S., Fuertes, A.B., *Carbon* **2004**, 42, 423.
(11) Parmentier, J., Vix-Guterl, C., Gibot, P., Reda, M., Ilescu, M., Werckmann J., Patarin, J., *Micro. Meso. Mater.* **2003**, 62, 87.
(12) Hines, D.H, Bagreev, A., Bandosz, T.J., *Langmuir*, **2004**, 20, 3388-97.

NOVEL POROUS CARBON NANOFIBERS HAVING RADIALLY ORIENTED NANO-SIZED TUNNELS

Seongyop Lim, Seong-Hwa Hong, Seong-Ho Yoon, and Isao Mochida

Institute for Materials Chemistry and Engineering,
Kyushu University,
Kasuga, Fukuoka, 816-8580 Japan

Introduction

Several carbon materials have been reported to have predominantly pores in the mesopore size range. These include some exotic materials prepared in a manner similar to the lost wax process. In such processes, a material that contains a removable moiety, of some desired size, is polymerized so as to incorporate the moiety into a solid product. The moiety is then, removed by a second process, leaving a porous solid having pores that are similar in size to the original moiety. For example, for thermally labile moieties, the solid polymer product is heated to high temperature to remove a thermally unstable moiety. Alternatively, a mixed inorganic-organic polymer is burned to leave pores similar in size to the organic portion that is burned. In some cases, the product is further treated with a reagent that dissolves the moiety, or its decomposition products, out of the solid. The resultant porous solid can have a very narrow pore size distribution in the mesopore range, however, the preparation of such materials is very expensive and time consuming.

Recently, the present authors found that carbon nanofibers (CNF) consist of assemblages of smaller sub-structural units or carbon nanorods by comprehensive observations using SEM, TEM, STM, and XRD. Bulk properties of CNFs were also found to be governed by the carbon nanorods and their assembly[1-4].

In this paper, novel mesoporous and fibrous nano-carbons were prepared through two steps: the careful preparation of CNFs having graphitic layers substantially perpendicular or angled to the fiber axis, and then selectively drilling nano-sized tunnels within them by means of catalyzed gasification reactions from the outside of the fiber into the center of the fiber in a substantially transverse fashion using carefully selected nano-sized catalysts under specific reaction conditions, which we call 'nano-drilling'.

Experimental

Catalyst for synthesis of CNFs. A herringbone CNF was synthesized from ethylene over a copper-nickel catalyst (Cu-Ni (2/8 w/w)). The carbonate precursors (Fe and Cu-Ni) were precipitated from aqueous solution of their corresponding nitrates by addition of ammonium bicarbonate in prescribed amounts. These were converted into the corresponding metals or alloys through calcination and reduction as described elsewhere[5].

Synthesis of CNFs. The apparatus used for the preparation of CNF throughout this study has been previously described[2,3]. Powdered catalysts in an alumina boat were treated in a 10% H_2/He mixture for 1 ~ 2 h at a prescribed reaction temperature in a conventional horizontal furnace, before introduction of the reactant gases such as a CO/H_2 mixture or a C_2H_4/H_2 mixture, where the gas flow to the reactor was precisely controlled by mass flow controllers.

Nano-drilling. A Ni precursor as a 'nano-drilling' catalyst was dispersed on the herringbone nanofiber prepared by the incipient wetness with aqueous solution of nickel nitrate (Ni: nanofiber = 5: 100 w/w) and then drying the composition at 150oC in a vacuum oven for 2 h. The nanofiber with nickel component as prepared above (0.5 g) was heat-treated at 300 ~ 900oC in hydrogen or air.

**Analysis.** The structure of CNF was examined using SEM (scanning electron microscope; JSM-6320F, JEOL) and HR-TEM (high resolution transmission electron microscope; JEM-2010F, JEOL). Nitrogen sorption isotherms of carbon were measured with Sorptomatic 1990 adsorption analyzer (FISONS Instruments) at liquid nitrogen temperature. All samples were degassed at 150oC for 2 h prior to the measurements. The specific surface area was calculated in the relative pressure interval of 0.05 – 0.35 using BET (Brunauer-Emmett-Teller) method.
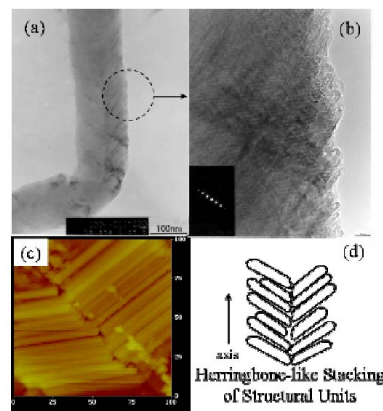
Figure 1. Surface structure of herringbone CNFs: TEM (a, b), STM (c), and illustration of the assembly of nanorods (d).

Results and Discussion

As-prepared herringbone CNFs were found to be composed of carbon nano-rods. After graphitization at 2800oC, the herringbone structure became clear under TEM, the surface edges being closed with concentric loop-ends as shown Fig. 1. Under STM, the herringbone structure was formed by a pair of rod assemblies aligned at angles relative to the fiber axis, with overall fiber diameters of about 130 nm. Some defects or pores appear to be naturally formed at the bridge of V-shape connection between rod assemblies.
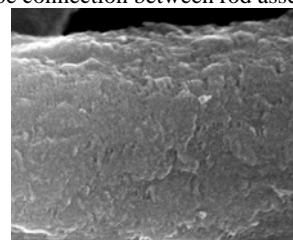
Figure 2. SEM image: the porous surface of nano-drilled CNF.

Hydrogenative gasification of herringbone CNF by using a Ni catalyst and hydrogen produced a porous and fibrous carbon as shown in Fig. 2. TEM images showed that pores with 5 ~ 30 nm diameters were formed along the graphene alignment (a herringbone texture) with no structural change of intact parts like nano-sized channels as shown in Fig. 3. From the nitrogen sorption isotherm, the majority of these pores were found to be distinctly mesoporous, comparing to as-prepared CNFs or KOH-activated CNFs[4] as shown in Fig. 4.

To create the desired pore size distribution and pore volumes, selective catalytic reactions are used such that nano-tunnels are created within the structures of the CNFs. The catalysts may be envisioned as drilling nano-tunnels within the CNF structures through the most reactive regions of the CNFs. These nano-tunnels constitute the mesopore system that is observed by BET measurements and TEM. Though not wanting to be confined to a particular theory, these reactive regions appear to be located at the ends of the nano-

rods and within the interiors of the nano-rods. The reactivity of the walls of the nanorods is believed to be much less than the ends of the nanorods. Thus, reactions (and tunnel formation) proceeds from the exterior of the CNF surface into the central regions of the fibers along the linear axis of the nano-rods and perpendicular to the major fiber axis. Typically, more than one nano-rod reacts with the reactive gas and catalyst to produce nano-tunnels with diameters in the mesopore range. These nano-tunnels have a very narrow distribution of tunnel diameters and this size is particularly useful for selective adsorption, chromatography and electrochemical applications.

There are several methods that may be used to create the nano-tunnels. All of these methods consist of a catalyzed reaction in which the catalyst is a very small nano-size particle that can be envisioned as drilling nano-tunnels into the nano-fibers. The entry points of these nano-tunnels are the exposed ends of nano-rods located on the exterior surfaces of the nano-fibers. Catalysts deposited on these exterior surfaces then react with and remove reactive carbon moieties by gasification reactions and the nanocatalysts drill deeper and deeper into the interior of the carbon nano-fiber, creating nano-tunnels in a radial distribution within the fiber as they proceed.

The deposition of the nano-particle catalysts on the exterior of the nano-rods prior to the gasification reaction is particularly critical. The preferred catalyst sizes are in the range of 2-50nm as smaller sizes create unwanted micropores and larger sizes create macro pores. If a large portion of macro pores are created, excessive amounts of the nano-fibers are consumed by the gasification reaction, with a subsequent unwanted loss in valuable product.

This study proposes not only a new methodology of preparation of mesoporous carbons without a template, but also proves the structural characteristics of CNFs depending on the structural units.

References
1. Lim, S., Yoon, S-H., Mochida, I., Chi, J-H., J. Phys. Chem. B 2004, 108 (5): p. 1533 –6.
2. Yoon, S-H., Lim, S., Hong, S-H., Mochida, I., An, B., Yokogawa, K., Carbon 2004, 42 (15): p. 3087-3095.
3. Yoon, S-H., Lim, S., Hong, S-H., Whitehurst, D. D., Mochida, I., An, B., Yokogawa, K., Carbon 2004, submitted.
4. Yoon, S-H., Lim, S., Song, Y., Ota, Y., Qiao, W., Tanaka, A., Mochida, I., Carbon 2004, 42 (8-9): p. 1723-1729.
5. Sinfelt, J. H., Carter, J. L., Yates, D. J. C., J. Catal. 1972, 24: p. 283-296.
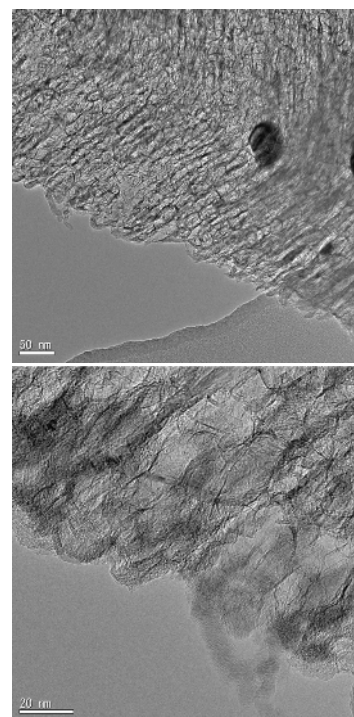
Figure 3. TEM of nano-drilled herringbone CNF showing radial mesopores.
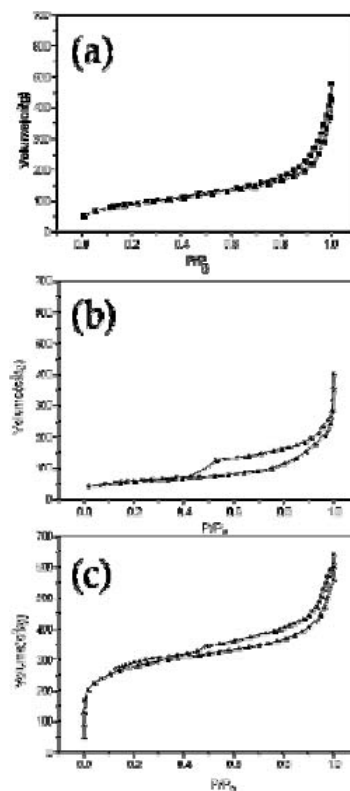
Figure 4. Nitrogen sorption isotherms of herringbone CNFs as prepared (a), as activated by using hydrogen and nickel (b), and as activated by KOH (c).

MESOCARBON NANOBEADS SYNTHESIZED FROM A LYOTROPIC LIQUID CRYSTAL

Aihui Yan, Nancy Yang, Robert H. Hurt

Engineering Division
Brown University
182 Hope Street
Providence, RI 02912

Introduction

Several structures have been observed in existing carbon nanoparticles and microbeads. Soots and carbon blacks, which are nanophase materials, show a concentric "onion" structure in which the graphene basal layers are parallel to the outer surface, leading to their chemical inertness in composites[1]. An alternative structure with accessible and active graphene edge sites[2] is observed in mesocarbon microbeads (MCMBs), which find applications in the manufacture of high-density and high-strength carbons[3], separators and electrodes for fuel cells[4], packings for high performance liquid chromatography (HPLC)[5] and ion exchangers. MCMBs are supra-micron-sized powders; to date the synthesis of nanophase mesocarbon spheres has not to our knowledge been demonstrated.

Our goal was to synthesize a new type of nano-scale carbon particles with high-concentration exposed graphene layers on the surface, by carbonizing a micron-scale mist of low concentration lyotropic liquid crystal solution. We refer to the product as "mesocarbon nanobeads" ("meso" means derived from a "mesophase", or liquid crystals, and "nano" means less than 100 nm in size). Here we synthesize them and characterize them by heat treatment, SEM, HRTEM and XRD.

Experimental

12 wt% indanthrone disulfonate (**Figure 1**) aqueous solution was diluted to 0.5 wt% with deionized water before use. 0.1 wt% and 0.01 wt% indanthrone disulfonate aqueous solutions were also made and exploited in our study for comparison.
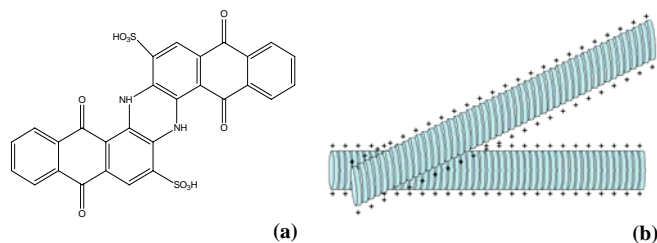
Figure 1. (a) Indanthrone disulfonate, a water soluble carbon precursor. (b) Molecular disks of indanthrone disulfonate assemble into massive π–stack rod-like aggregates, about 1.5 nm in diameter and about 300 nm in length, in aqueous solution when the concentration is higher than ~4 wt%.

Carbonization. An indanthrone disulfonate aqueous solution (e. g., 0.5 wt%) was transformed to fine droplets in an ultrasonic nebulizer. The mist was carried by N$_2$ (flow rate: 5 L/min) into a 750 mm quartz tube (I. D. = 24.7 mm) that had been kept at 700 °C, followed by a continuous ~3-second drying and heating process. Finally, the products were carried out of the quartz tube and collected by a Nucleopore® filter with pore size of 1 μm; while waste passed through a waste treatment device and went into the vacuum.
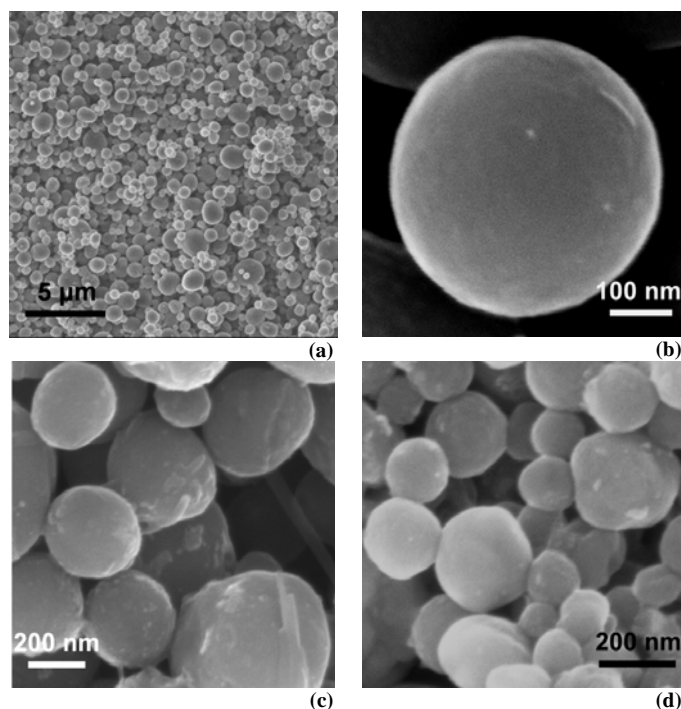
Heat Treatment. The products from 0.5 wt% indanthrone disulfonate solution were studied by post heat treatment in two ways. (1) They were dispersed and heated at 900 °C for 60 min in UHP (ultrahigh purity) N$_2$ (flow rate: 0.53 L/min). (2) They were heated to 1500 °C and 2400 °C, and kept at the corresponding temperature for 5 seconds in a transient heat treatment device.

Characterization Methods. Scanning Electron Microscopy (SEM) was conducted on LEO 1530 VP (LEO Electron Microscopy Inc.), using 5 kV voltages below 10^{-5} bar. High-resolution transmission electron microscopy (HRTEM) was carried out at Sandia National Laboratories. X-ray Diffraction (XRD) was performed on Diffraktometer D5000 (Siemens Inc.).

Results and Discussion

The products synthesized from 0.5 wt% precursor solution were spherical particles with diameter of 0.2 – 2 μm, as shown in **Figure 2**(a) and **2**(b). It is observed that not only the size but also the morphologies of the particles depend on the concentration of the precursor solution. The particle diameter decreased to the range of 130 nm – 1 μm when 0.1 wt% precursor solution was used instead; and went further down to the range of 80 – 500 nm, as shown in **Figure 2**(d), when 0.01 wt% precursor solution was used. On the other hand, the morphologies of the products turned from nearly spherical to diversely polygonal as the concentration of the precursor solution decreased. Some rod-like structures with diameter around 25 nm were observed on the surface of the products from 0.1 wt% precursor solution, as shown in **Figure 2**(c), implying that as the particle size decreased, the morphologies of liquid crystal aggregates formed in drying precursor droplets began to have an influence on the morphologies of as-prepared carbon particles. TEM images of the products from 0.01 wt% precursor solution exhibited that there were high concentration of exposed graphene layers on the surface of those nanobeads.

Figure 2. (a,b) SEM images of the products from 0.5 wt% indanthrone disulfonate solution. (c) SEM image of the products from 0.1 wt% indanthrone disulfonate solution. (d) SEM image of the products from 0.01 wt% indanthrone disulfonate solution.

A possible formation mechanism based on "surface anchoring" is shown in **Figure 3**. Fine droplets from the precursor solution were

heated and dried. As the concentration increased, separate indanthrone disulfonate disks in those liquid droplets aggregated into rod-like structure through π–stacking. The parallel alignment of those rod-like aggregates at surface made liquid crystal disks normal to the interface between the droplets and the exterior[2]. After carbonization, mesocarbon nanobeads with high concentration of exposed graphene layers were obtained.
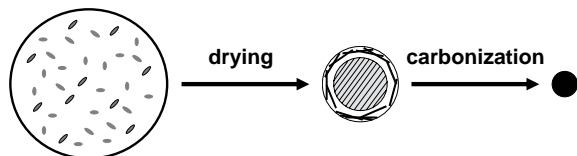

Figure 3. Possible assembly mechanism of mesocarbon nanobeads.

Mesocarbon nanobeads from 0.5 wt% precursor solution were dispersed and heated at 900 ^{o}C for 60 min in UHP N_2 (flow rate: 0.53 L/min). SEM image in **Figure 4** implied that as-prepared nanobeads were not completely carbonized at 700 ^{o}C in the quartz tube, because after 60-min post heat treatment a new structure formed on their surfaces, which appeared to pass their liquid phase.
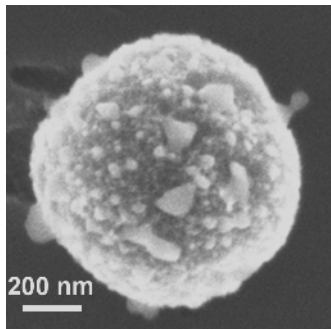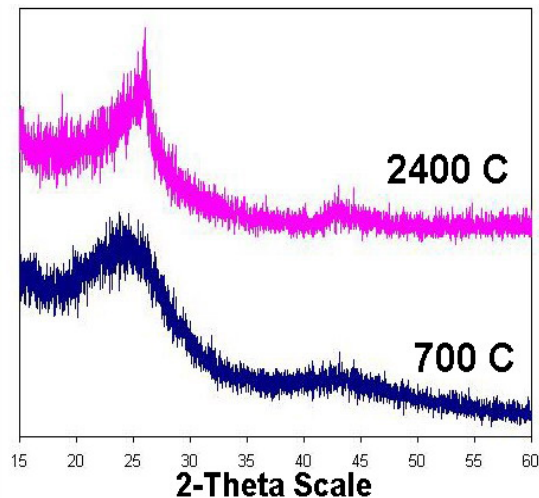

Figure 4. SEM image of the products from 0.5 wt% indanthrone disulfonate solution after post heat treatment at 900 ^{o}C for 60 min in N_2.

After heat treatment at 1500 ^{o}C and 2400 ^{o}C, respectively, the products from 0.5 wt% precursor solution did not show obvious self-sinterability bulkily. However, the formation of a "bridge" between two neighboring nanobeads has been observed in both cases (**Figure 5**), which is consistent with accessible edge sites on the surface as the HRTEM images imply.

| (a) | (b) |
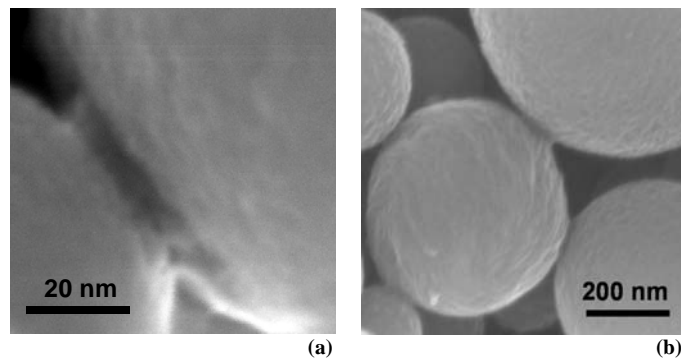
Figure 5. SEM images of the products from 0.5 wt% indanthrone disulfonate solution after transient heat treatment: (a) heated up to 1500 ^{o}C; (b) heated up to 2400 ^{o}C.

XRD results (**Figure 6**) of the products from 0.5 wt% precursor solution also indicated somewhat difference in structure between before and after heat treatment at 2400 ^{o}C for 5 seconds. Before heat treatment, the FWHM (Full Width Half Maximum) of 002 diffraction (around 24.3^o) is about 5°; while after heat treatment, the FWHM of that diffraction (shift to around 26.2^o) decreased to 2.5^o. The decrease of FWHM after heat treatment means that the products became a little more ordered in the bulk.

Figure 6. XRD profiles of the products from 0.5 wt% indanthrone disulfonate solution before and after transient heat treatment.

Conclusions

Carbon spheres with high concentration of graphene edge sites and from 2 μm to ~100 nm in size were fabricated from different indanthrone disulfonate aqueous solutions with the concentration of 0.01 – 0.5 wt% at 700 ^{o}C in N_2. The particle size can be varied systematically by varying the concentration of the precursor solution. HRTEM images show that in many surface regions of those nanobeads gaphene layers are perpendicular to the surface. After rapid heat treatment at 1500 ^{o}C and 2400 ^{o}C, respectively, a new bridge-like structure formed between two neighboring nanobeads. As a result, this type of carbon spheres may be promising in a series of applications, for example, fillers for the manufacture of particle/matrix structures through sintering due to their small size (comparable to MCMBs) and active surface (comparable to carbon blacks and soots). In addition, they may act as a substitute for carbon black where active surfaces are useful. Further study is underway on their structure, properties, and applications.

References
(1) (a) Park, S.-J.; Kim, J.-S. *J. Colloid Interface Sci.*, **2000**, *232*, 311-316. (b) Park, S.-J.; Kim, J.-S. *Carbon*, **2001**, *39*(13), 2011-2016.
(2) Brooks, J. D.; Taylor G. H. *Carbon*, **1965**, *3*(2), 185-186.
(3) Wang, Y.-G.; Korai, Y.; Mochida, I. *Carbon*, **1999**, *37*(7), 1049-1057.
(4) Endo, M.; Kim, C.; Nishimura, K.; Fujino, T.; Miyashita, K. *Carbon*, **2000**, *38*(2), 189.
(5) (a) Yokono, T.; Nakahara, M.; Makino, K.; Sanada, Y. *J. Mater. Sci. Lett.*, **1988**, *7*(8), 864-866. (b) Yokono, T.; Nakahara, M.; Sanada, Y. *Tanso*, **1988**, *134*, 188-190.

MESOPHASE STABILIZATION AT LOW TEMPERATURES AND ELEVATED OXYGEN PRESSURES

Bahram Fathollahi, Brent Jones, Pau C. Chau, and Jack. L. White

Chemical Engineering Group
University of California, San Diego
9500 Gilman Dr..
La Jolla, Ca, 92093-0411

Introduction

The oxidation of mesophase pitch is a crucial step in stabilizing flow-induced microstructures after fiber spinning or mesophase injected composites[1]. Oxidation by air or oxygen at 200 to 300 °C is standard practice for stabilization of as-spun mesophase filaments[1]. The oxidation process involves diffusion of oxygen with simultaneous reactions at various sites on the mesophase molecules. There are a large number of possible chemical reactions between oxygen and mesophase pitch; most such reactions begin at or above 150°C[2,3,4,5,6]. This paper reports results from oxidation at temperatures as low as 130°C and oxygen pressure up to 0.7MPa. The retention of the as-spun and as-extruded mesophase microstructure is used as the criterion to measure the depth of stabilization. Furthermore, FTIR is used to characterize the changes in functional groups under different oxidation temperatures and pressures.

Experimental

The experimental method was developed in a study of the stabilization of an alkylbenene-based mesophase pitch produced by Mitsubishi Oil [11]. The naphthalene-based ARA24R pitch by Mitsubishi Gas-Chemical is the subject of the present investigation. Mesophase rods were extruded and thick filaments spun to obtain the fine fibrous microstructures. Specimens were oxidized at pressures up to 100 psia and at temperatures in the range of 270 down to 130°C, then carbonized to 1150°C to "develop" the stabilized region of the cross sections. A sufficiently oxidized rim retains the fine as-spun microstructure, but less oxidized mesophase melts or coarsens sharply in microstructure, and can be blown from the interior of the rod or filament by pyrolysis gases.

Results and Discussion

The strong effect of modest oxygen pressure in enhancing the oxidation mass gain (OMG) of mesophase particles or filaments at 170 °C is shown in **Figure. 1**. The filaments and particle OMG curves display similar patterns. The small, but consistently higher, increments in OMG for filaments appear to reflect their larger effective surface area. Furthermore, there is only a marginal increase in OMG of the filaments as the oxygen pressure is increased from 0.38 to 0.7 MPa. To obtain an OMG of 0.07, usually sufficient to ensure stabilization, the application of 0.38MPa reduced the exposure time by nearly 10x.

The depths of microstructural stabilization, for extruded rods oxidized at 170 °C at conditions of ambient and 0.7Mpa pressure is illustrated in **Figure 2**. The boundaries between stabilized and coarsened microstructures are clear and consistent, and the depths of stabilization are readily measured by microscope reticle. The depths of stabilization for various conditions of temperatures and pressures are summarized in **Figure 3**. Striking features of these plots are (1) the sharply limited growth of the stabilized rim at room pressure and
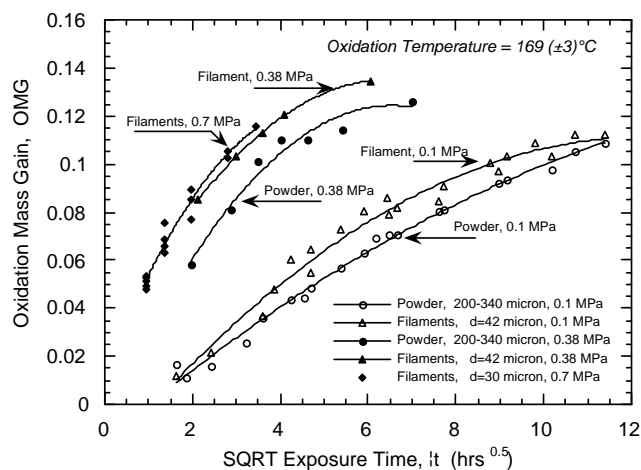
Figure 1.. The effect of oxygen pressure on oxidation mass gains of sieved mesophase particles and spun filaments at 170 °C.

| Oxygen pressure:	0.1MPa	0.7MPa
Exposure time:	46.5 h	49.1 h
Stabilized depth:	13.6 (±1.4) µm	48.5 (±7.1) µm
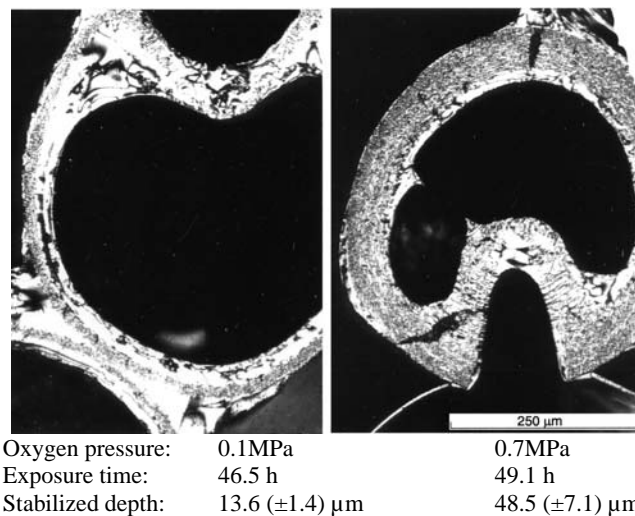
Figure 2. The effect of oxygen pressure on extruded mesophase rods oxidized at 170°C, after carbonization to 1150°C.

high temperature, e.g. at 270°C, and (2) the increasing tilt of the growth curves at lower oxidation temperatures. At the lower temperatures, there is a delay time before oxidation makes its effect apparent in terms of a stabilized layer

The results at 270 °C are representative of higher temperature stabilization: an initial high rate of stabilization to a depth of about 7 µm after which no further growth is perceptible. At 220 °C, the stabilization rises steadily with time. At the lower 170 and 150 °C, the stabilization depth increases very slowly initially, but given time, the stabilization can extend beyond 25 µm, or better than what can be achieved at 220 °C.

For oxidation temperatures under 220 °C, elevating the oxygen pressure to 0.7 MPa was effective in increasing the stabilization depth. The 220 °C curve at 0.1 MPa is duplicated in Figure 3b for comparison. The increase in stabilization depth can be significant, to as much as 80 µm at the lower temperatures, if processing time is not a constraint. At lower oxidation temperatures (170 °C and below), there is a lag period before a measurable stabilization depth appears even at the higher pressure. By prolonging the exposure time,

oxidation at lower temperatures is capable of achieving depth of stabilization greater than those attained at higher temperatures. Thus oxidation at lower temperatures, enabled by relatively modest levels of pressure, offers a means of avoiding the effects of over-oxidation at the surface of a mesophase body or filament.
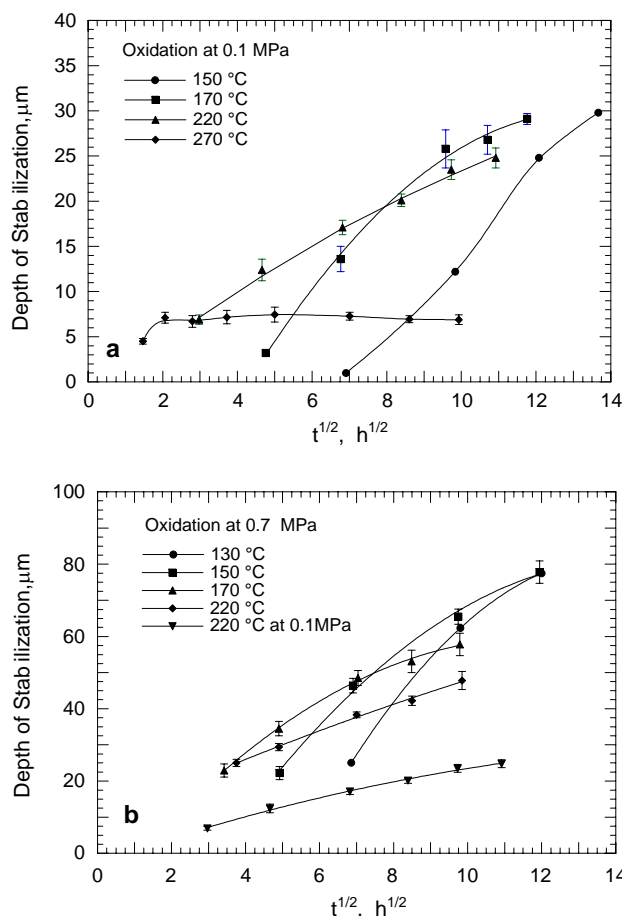
Figure 3. Stabilization depths for extruded rods as a function of exposure time: (a) 0.1 MPa, and (b) 0.7MPa. In (b) results for 0.1 MPa and 220 °C are included to demonstrate the effect of pressure

References
1. Mochida I, Toshima H, Korai Y, Hino T. Oxygen distribution in the mesophase pitch fiber after oxidative stabilization, J. Mate. Sci. **1989**, 24, 389-94.
2. Drbohlav J, Stevenson WTK. The oxidation stabilization and carbonization of a synthetic mesophase pitch, part I: The oxidatative stabilization process, Carbon **1995**, 33, 693-711.
3. Miura K, Nakagawa H, Hashimoto K. Examination of the oxidative stabilization reaction of the pitch-based carbon fiber through continuous measurement of oxygen chemisorption and gas formation rate, Carbon **1995**, 33, 275-82.
4. Lavin JG. Chemical reactions in the stabilization of mesophase pitch-based carbon fiber, Carbon **1992**, 30, 351-7.
5. Singer LS, Mitchell S. Diffusion of oxygen into pitch, Carbon 1997;35:599-604.
6. Fathollahi B, Jones B, Chau PC, White JL. Mesophase stabilization at low temperatures, **2005**, 43, 143-151.

EFFECT OF INDIVIDUAL METAL AND METAL MIXTURE ADDITIVES ON THE ACTIVATION AND PORE STRUCTURE OF PITCH-BASED FIBERS

Yulia V. Basova and Dan D. Edie

Center for Advanced Engineering Fibers and Films
Clemson University, Clemson, SC 29634-0910, USA

Introduction

Critical parameters for controlling pore size distribution in activated carbon include: precursor selection, precursor modification and activation conditions. An efficient method for controlling pore structure, extensively studied over the past decade, involves distributing individual transition metal additives in the carbon matrix and then activating the mixture with steam or carbon dioxide. During activation, the transition-metal particles are effective agents/catalysts for pore formation. The catalytic activity is related to the nature of the metal precursor employed. The catalytic activity of bimetallic particles should depend strongly on the phase behavior and the composition of the particles. If these can be understood and documented during the preparation process, metal mixtures may provide additional flexibility in controlling the formation of porosity and, subsequently, the adsorption and catalytic properties of the resulting activated carbon fibers (ACFs).

The aim of this work is to review the pathways by which metal-containing ACFs are formed and to show the effect of different metal precursors on the final properties of pitch-based ACFs. These properties include particle size and distribution, specific surface area, pore size and distribution -- properties which are useful in selecting ACF to adsorbing specific chemicals, for catalysis or for other applications where a defined surface structure is required.

Here, the production parameters are summarized for ACFs containing silver, cobalt and palladium as individual metals or as metal mixtures.

Experimental

Materials. The isotropic pitch precursors with softening points (S. P.) of 230, 245 and 253°C used in this study were supplied by Chungnam National University, Korea. Metal precursors (AgNO$_3$, Co(NO$_3$)$_2$·6H$_2$O, cobalt (II) acetylacetonate, Co(acac)$_2$, and palladium (II) acetylacetonate, Pd(acac)$_2$) were supplied by Alfa Aesar Company, USA.

Preparation of activated carbon fibers. The experimental setup is described in detail in a previous publication[1]. The metal-containing salts were ground into a powder and sifted using ATM Sonic Sifter. The Ag-Co, Co-Pd and Ag-Pd mixtures were prepared by grinding and sifting individual salts separately. The smallest fraction of salt/salt mixture particles (size ≤38μm) were mixed into molten pitch using an intensive mixer heated to a temperature approximately 10°C lower than the softening point of the pitch, yielding isotropic pitch precursors that contained 1.0 wt% metal or metal mixture in a weight ratio of 0.5:0.5 %. The pure and metal-containing pitches were then melt spun into multi-filament fiber tows using a batch extrusion system. The diameters of the fibers spun from the unmixed and metal/metal mixture-containing pitches ranged from approximately 15 to 20 microns. As-spun fibers were stabilized in air using a conventional oven. The stabilized fibers were carbonized at 1000°C in helium using a Raytec Thermalert® 1V Astro programmable furnace. Finally, the carbonized fiber samples were activated at 900°C in pure CO$_2$ at atmospheric pressure using a temperature-controlled Lindberg tube furnace.

Characterization Methods. The phase composition and crystallinity of Ag, Co and Pd-containing compounds during ACF preparation were determined by x-ray diffraction (XRD) using a Scintag 2000 XDS θ/θ powder diffractometer. EDX was performed using an Hitachi 3500 SEM to determine the uniformity of the composition. An Hitachi FE SEM 4700 was used to determine the size and dispersion of the metal/metal containing particles and to observe the surface morphology and surface pore size of both the outer surface and the cross section of selected fibers. The surface properties of the ACFs were determined from nitrogen adsorption-desorption isotherms obtained at -196ºC using a Micromeritics ASAP 2020 surface analyzer.

Results and Discussion

Individual metal (Ag, Co, Pd)-containing fibers. The notations in all tables and plots (KU, KAn, KCa, KCn and KPa) indicate that Korean isotropic pitch (K) was either unmixed, (U), or mixed with AgNO$_3$, (An), Co(acac)$_2$, (Ca), Co(NO$_3$)$_2$, (Cn), or Pd(acac)$_2$, (Pa), respectively.

As was described in our earlier publications[2,3], the behavior of individual transition metal ions in molten pitch, as well as the properties and size of metal-containing particles are closely related to the chemistry of the pitch and the nature of metal precursor. The observed differences[3] strongly affect the activation process and surface properties of the resulting ACFs. **Figure 1** shows nitrogen adsorption isotherms for selected ACFs (BO 62-70%.). The nitrogen adsorption isotherm for KAn gradually increased with increasing relative pressure, a tendency observed in highly activated carbons and attributed to the presence of large micropores and small mesopores. The adsorption isotherm for KPa had a sharp knee at low relative pressures and a slight hysteresis, behavior that is characteristic of microporous carbon with pore-size distribution extending to the mesopore range. Micropores and mesopores were detected in both KAn and KPa ACFs. Mesopores are generated by the Ag and Pd particles as they tunnel through the fiber core during activation. The widths of the micropores and mesopores in the Ag-containing fibers were as large as 200 Å. In the case of the Pd-containing fibers, pore widths varied from several Å to about 500 Å.
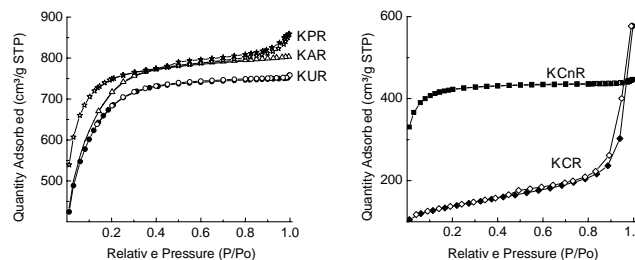

Figure 1. Nitrogen adsorption isotherms.

The pore network of the KCa fibers contained much larger pores, similar to that observed in meso-/macroporous materials. KCn fibers had a pore size distribution similar to that of a microporous material. Pore size distribution curves for ACFs formed from Ag and Co nitrate (KA and KCn) were nearly identical, indicating that these two types of fibers prepared from nitrate salts had very similar pore structures, and these differed dramatically from the pore structure for the KCa ACFs. This clearly indicates that a different mechanism controls the interaction between metal precursor and pitch during fiber processing and the formation of pore structure in the two Co-containing samples.

Metal mixture (Ag/Co, Co/Pd, Ag/Pd) - containing fibers. Notations KAC, KCP and KAP indicate that Korean isotropic pitch (K) was mixed with a mixture of AgNO$_3$ and Co(acac)$_2$, Co(acac)$_2$ and Pd(acac)$_2$, AgNO$_3$ and Pd(acac)$_2$, respectively.

Ag/Co (KAC) fibers. The metal-containing particles formed from this mixture were irregular in shape and size. The chemical composition of the particles also varied. The larger particles contained mainly Co, Co oxide and carbide, whereas the smaller particles contained mostly Ag. However, some particles contained both metal compounds **(Figure 2)**. Activation and nitrogen adsorption results for the KAC ACFs indicated that activation rates for these fibers were intermediate between those for the KAn and the KCa fibers. However, the pore size distribution (PSD) plot for the KAC ACFs demonstrates the individual effect of the two metals **(Figure 2)**. Small pores as well as large macropores developed with increasing activation time. At high degrees of burnoff the KAC ACFs had high specific surface areas and significantly higher pore volumes, properties that are characteristic of both KAn and KCa ACFs.
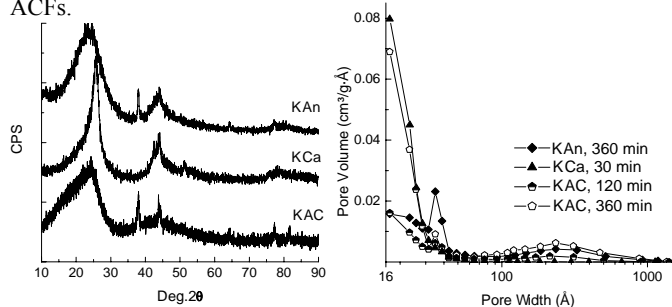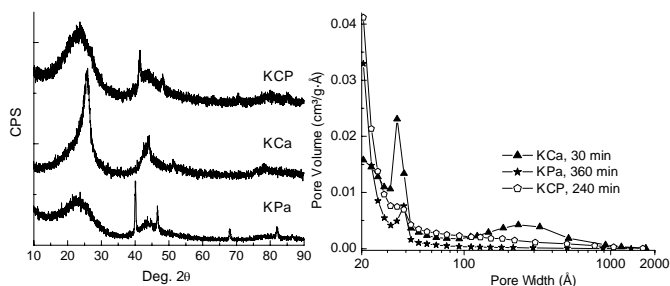

Figure 2. XRD patterns of carbonized (left panel), PSD plot for activated Ag-, Co- and Ag/Co-containing fibers (right panel).

Co/Pd (KCP) fibers. SEM observation of numerous surfaces and cross sections of carbonized Co/Pd-containing fibers showed that the particles were evenly distributed and more uniform in size. X-ray analyses of the Co/Pd mixture prior to spinning and the as-spun fibers did not show any clear peaks attributable to metallic (or elemental) Co and Pd. However, the XRD pattern for the carbonized fibers, when compared with the XRD patterns of fibers containing individual metals, contained peaks which were characteristic of a Co/Pd alloy. The result obtained from EDX analyses showed that the composition of these metal particles consisted of Co:Pd in a 1:1 atomic % ratio. It is noteworthy that the alloy was also formed below the melting temperature for Co and Pd metals. However, some small particles appear to be pure Pd. Activation and surface analyses results for Co/Pd-containing ACFs showed that activation rates for these fibers were also intermediate between those for the individual metal-containing ACFs, *i.e.*: the surface area increased dramatically with activation time, while the average pore size was comparable to that of Co-containing ACFs at a lower degree of activation and it decreased with activation time. Like the Ag/Co ACFs, the Co/Pd-containing ACFs exhibited extremely high pore volumes at high degrees of activation. A comparison of the surface morphology and the PDS plot **(Figure 3)** for Co/Pd fibers with those for fibers containing individual metals indicates that fibers formed from both Co- and Pd-containing salts do not bear features attributable to either salt. The results suggest that combining the two salts creates an additive effect.

Ag/Pd (KAP) fibers. The SEM observation of these fibers established that the addition of silver to palladium significantly decreased particle size and improved particle distribution. XRD patterns of mixture and as-spun fibers **(Figure 4)** display a clear peak attributable to crystalline silver, while the Pd peak is not pronounced. By comparison, the XRD pattern of carbonized Ag/Pd fibers, when compared to the XRD patterns of carbonized fibers containing these same two individual metals, shows that carbonization and activation processes favors the formation of nearly perfect spherical Ag/Pd

alloy particles, with diameters less than 50nm. However, a few particles have diameters greater than 100mn. EDX analysis supported the XRD results and indicated that the particles were an alloy, formed well below the melting point, with a composition of approximately 1:1 Ag:Pd (wt%). PSD curves **(Figure 4)** exhibit a more pronounced peak at 39 Å than that detected for the Pd-containing sample, even at a higher burnoff. An additional peak appears between 60 and 70 Å, and this peak is not observed for the fibers containing the individual metals. These peculiarities are most likely attributable to the formation of the Ag/Pd alloy during the heat treatment, and they illustrate the synergistic effect of combining these two metals.

Figure 3. XRD patterns of carbonized (left panel), PSD plot for activated Pd-, Co- and Co/Pd-containing fibers (right panel).
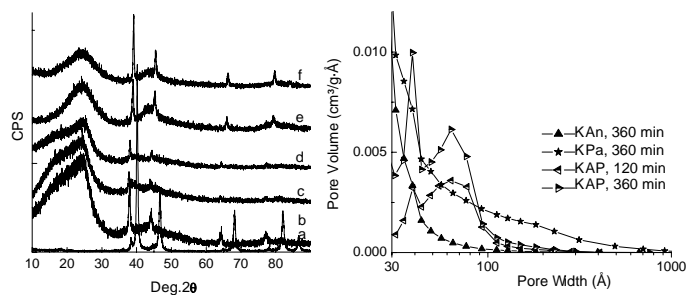
Figure 4. XRD patterns for: a-Pd black, b-Ag-pitch mixture, c-Ag/Pd-pitch mixture, d-KAP as-spun fibers, e-KAP carbonized fibers, f-KAP ACFs (left panel) and pore size distribution plot for activated Ag-, Pd- and Ag/Pd-containing fibers (right panel).

Conclusions

Silver and cobalt additives in the form of nitrate salts primarily enlarge the micropores and generate small mesopores with a narrow range of sizes. The cobalt additive as an acetylacetonate salt catalyzes the activation process, creating large mesopores and macropores. The palladium additive gives rise to the formation of both small micropores and larger mesopores. Mixing of two different metal additives affects both the particle size and the pore structure of the final activated fibers. Combining two different metals can result in any of the following: an individual metal contribution, an additive or a synergistic effect.

References
(1) Lee, Y. S.; Basova, Y. V.; Edie, D.D.; Reid, L.K.; Newcombe, S.R.; and Ryu S.K., *Carbon*, **2003**, *41* (13), 2573.
(2) Basova, Y. V.; Edie, D.D.; Lee, Y. S.; Reid, L.K.; and Ryu S.K., *Carbon*, **2004**, *42* (3), 485.
(3) Basova, Y. V.; and Edie, D.D., *Carbon*, **2004**, *42* (12-133), 2748.

SOFT X-RAY SPECTROMICROSCOPY STUDY OF CARBONACEOUS MATERIALS: CHARACTERIZATION OF THEIR CHEMICAL HETEROGENEITIES IN SUB-MICROMETER SCALE.

Tae Hyun Yoon[1], Karim Benzerara[1], Sungwoo Ahn[2], Richard G. Luthy[2], Tolek Tyliszczak[3] and Gordon E. Brown, Jr[1,4].

[1]Surface & Aqueous Geochemistry Group,
Department of Geological & Environmental Sciences, Stanford
University, Stanford, CA 94305-2115
[2]Department of Civil & Environmental Engineering, Stanford
University, Stanford, CA 94305-4020
[3]Chemical Sciences Division, Lawrence Berkeley National
Laboratory, 1 Cyclotron Rd., Berkeley, CA 94720
[4]Stanford Synchrotron Radiation Laboratory, SLAC, MS 69, 2575
Sand Hill Road, Menlo Park, CA 94025

Introduction

Carbonaceous materials have been the subject of various research areas including organic geochemistry, environmental and material sciences, due to their ubiquitous presence in our environment (e.g., air-borne particulate matter from diesel fuel combustion and various type of coals as energy sources) and wide industrial applications (e.g., adsorbents for water and gas purification processes and reinforcing component in composite materials).

One of the important environmental issues related to these carbonaceous materials is their ability to sorb non-polar organic pollutants, such as PCBs (polychlorinated biphenyls) and PAHs (polycyclic aromatic hydrocarbons) in sediment[1]. Partitioning to aqueous phase and bioavailability of these pollutants were typically predicted by simple model based on equilibrium partitioning approach with organic matter partitioning (OMP) parameters. However, this simple OMP modeling approach often overpredicts the concentrations of PAHs and PCBs in aqueous phase[2,3], probably due to the heterogeneity of carbonaceous materials. Recently, new modeling paradigms considering the heterogeneity of these carbonaceous materials have been suggested, which describe the sorption properties of carbonaceous materials in sediments by linear or non-linear combination of multiple phases with different sorption properties, such as soot carbon and amorphous organic carbons[4,5]. However, despite the importance of understanding heterogeneities in carbonaceous materials, there have been only a few spectroscopic and/or microscopic studies performed to prove this assumption yet, mainly due to the lack of appropriate tool to probe their chemical heterogeneity in sub-micron scale. Our knowledge on their chemical heterogeneity in sub-micron scales is thus very limited.

Synchrotron-based soft x-ray spectromicroscopy (i.e., scanning transmission x-ray microscopy (STXM) and near edge x-ray absorption fine structure (NEXAFS)) is an ideal tool to address questions on chemical heterogeneity of carbonaceous materials at sub-micron scales. STXM is one of the few methods capable of characterizing particles > 30 nm in diameter in the presence of water and/or under atmospheric conditions and NEXAFS spectra combined with STXM imaging can provide sub-100nm scale chemical information on various environmental and biological samples[6-10].

Here, we present a synchrotron-based soft x-ray spectromicroscopy characterization of carbonaceous materials (i.e., coke and activated carbon) and show the capability of this novel spectromicroscopic tool to identify local chemical heterogeneity of carbonaceous materials.

Experimental

Sample preparation. Two different types of carbonaceous materials were tested with soft x-ray spectromicroscopy in this study. Coke was obtained from Ispat Inland Inc. (East Chicago, IL) and activated carbon (MRX 10x30) was purchased from Calgon Carbon Corporation (Pittsburgh, PA). These raw materials were finely grounded and prepared for STXM experiment as follows. Aqueous suspensions of these powdered carbonaceous materials were prepared in DI water (~0.5 g/L) and approximately 1 μl of each suspension was dropped on 100 nm-thick Si_3N_4 membranes (Silson Ltd.), which were then air-dried before STXM observations.

STXM experiments. STXM studies were performed at ALS branch line 11.0.2.2 with the synchrotron storage ring operating at an energy of 1.9 GeV and 200-400 mA stored current. Energy calibrations were made using the well-resolved C 3p Rydberg peak at 294.96 eV of gaseous CO_2. The detector was a photomultiplier tube with a phosphor scintillator. The STXM sample chamber is He-filled to minimize attenuation of the soft x-rays. Normalization and background correction of the NEXAFS spectra were performed by dividing each spectrum by a second spectrum (I_0) taken at a location on the sample in which the element of interest is absent. AXis2000 software (ver2.1p)[11] was used to align image stacks and extract NEXAFS spectra from image stack measurements.

Results and Discussion

Soft X-ray Spectromicroscopic Study on Coke particles. A STXM image collected on finely grounded coke powders is shown in **Figure 1(A)**. A STXM image stack was also collected for the same area over the C K-edge energy range (E = 280~310 eV). **Figure 1(B)** and **1(C)** shows two STXM images from this image stack, obtained from the same sample region at two different energies corresponding to different functional groups, such as aromatic (**B**: E=285.7 eV) and ketonic/phenolic group (**C**: E=286.7 eV). Carbon K-edge NEXAFS spectra extracted from different areas of image stack (see **Figure 1(A)**, indicated by red lines with annotations, **a**, **b**, **c**, **d**, **e**, **f**, and **g**) were also presented in **Figure 1(D)**.
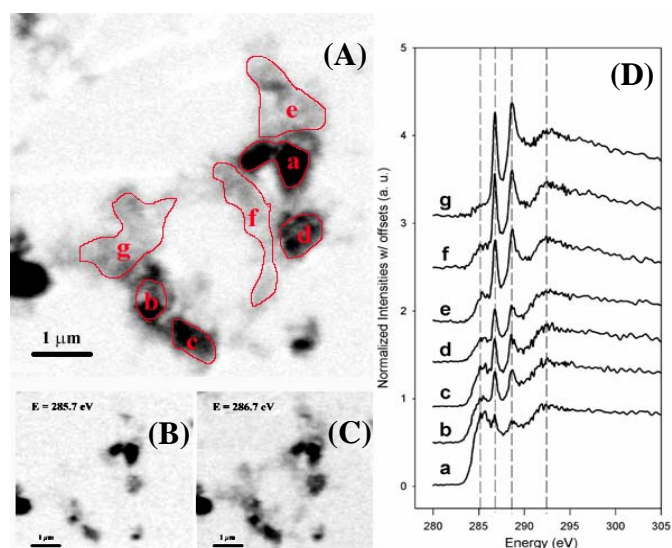
Figure 1. STXM images of Coke particles measured at (A) E = 286.9 eV (B) E = 285.7 eV (energy corresponds to 1s-π* transition of C=C bond in aromatic group) (C) E = 286.7 eV (energy corresponds to 1s-π* transition of ketone C=O or phenolic Ar-OH bond), and (D) C K-edge NEXAFS spectra collected from different areas of image (A) indicated by **a**, **b**, **c**, **d**, **e**, **f**, and **g**

As can be seen from **Figures 1(B) and (C)**, STXM images collected at different energies can be used to map chemical heterogeneities in this carbonaceous material. The image collected at E = 285.7 eV, which is near the peak positions of the 1s-π* transition of C=C bonds in aromatic group[9,10] (**Fig. 1(B)**) shows several dark spots, indicating that the aromatic group is only dominating in this regions of the mapped area. As the incident x-ray energy is increased to the energy corresponds to 1s-π* transition of ketone C=O or phenolic Ar-OH bond[9,10] (286.7eV, see **Figure 1(C)**), the rest of the coke particles become apparent in the mapped area. These gray areas, which are visible **Figure 1(C)** but not apparent in **Figure 1(B),** most likely contain significant amount of ketonic and/or phenolic functional groups with minor aromaticities.

Further characterization of chemical heterogeneities in this coke powder sample can be done through the C K-edge NEXAFS spectral analysis (**Figure 1(D)**). In addition to the two major chemical moieties assigned above (i.e., aromatic and ketone/phenolic groups), Carbon K-edge NEXAFS spectra in **Figure 1(D)** clearly showed one additional major peak located at 288.7 eV, which can be assigned to 1s-π* transition of carboxylic C=O bond[9,10]. Wide variation of the chemical moiety distributions was also confirmed by NEXAFS spectra in this mapped area. The NEXAFS spectrum from region **a** showed spectral features dominated by aromatic moieties, while the spectral features of regions **b**, **c** and **d** indicate the presence of mixtures of aromatic, ketone/phenolic and carboxylic functional groups in this regions. In contrast to these areas visible at an incident x-ray energy of 285.7 eV, regions **e**, **f**, and **g**, which were not apparent in **Figure 1(B)** but became visible in **Figure 1(C)**, showed spectral features dominated by ketone/phenolic and carboxylic functional groups with only minor contribution from aromatic functional groups.

Soft X-ray Spectromicroscopic Study on Activated Carbon particles. STXM images and NEXAFS spectra collected on a finely grounded activated carbon powder are shown in **Figure 2**. Similar experimental methods used for coke sample were applied to collect STXM images and carbon K-edge NEXAFS spectra. As can be seen from **Figures 2(B) and (C)**, STXM images collected at an energy of 285.1 eV, which corresponds to aromatic group, show only few small dark spots, indicating that regions dominated by aromatic groups represent only a small portion of the mapped area (see **Figures 2(B)**). As the incident x-ray energy is increased to the absorption energy of ketone C=O or phenolic Ar-OH bonds (286.7eV, see **Figure 2(C)**), the rest of the activated carbon particles becomes apparent in the mapped area. NEXAFS spectra shown in **Figure 2(D)** also indicate the presence of carboxyl groups in these activated carbon particles (peak located at 288.7eV). However, the chemical heterogeneity in activated carbon is much less distinct compared to that of coke powders shown in **Figure 1**. Compared to the micrometer sized aromatic-rich domains widely distributed in coke powder sample, aromatic-rich regions in activated carbon powder were found only in a few location and displayed a diameter less than a few hundreds nanometer, probably due to much higher specific surface area and extensive surface modification during activation process (SSA_{coke} = 3.2 m^2/g, SSA_{AC} = 1032 m^2/g)[12].

Conclusions

We have demonstrated direct observations of sub-micrometer scale chemical heterogeneities present in carbonaceous materials using a novel synchrotron-based x-ray spectromicroscopy method. Various chemical moieties (i.e., aromatic, ketonic/phenolic and carboxylic functional groups) were found in these carbonaceous materials and they display a heterogeneous distribution at a micron or sub-micrometer scales. These observations of chemical heterogeneities support recent new modeling paradigm considering carbonaceous materials as a mixture of multiple phase components.
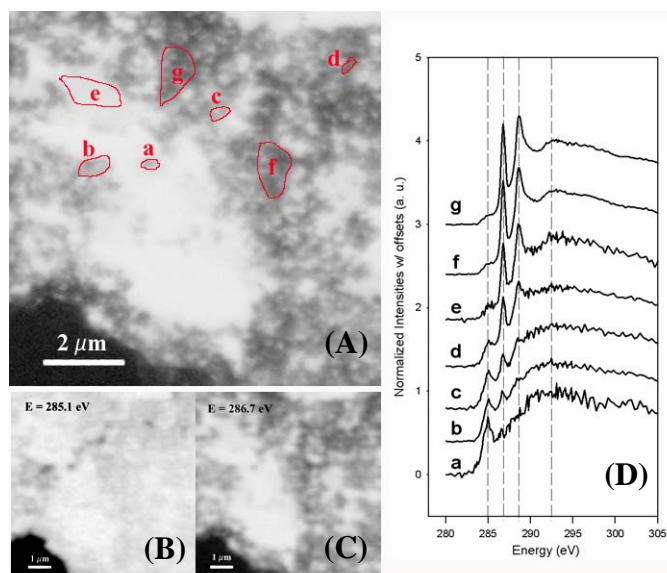
Figure 2. STXM image of activated carbon particle measured at (A) E = 286.8 eV (B) E = 285.1 eV (energy corresponds to 1s-π* transition of C=C bond in aromatic group) (C) E = 286.7 eV (energy corresponds to 1s-π* transition of ketone C=O or phenolic Ar-OH bond), and (D) C K-edge NEXAFS spectra collected from different areas of image (A) indicated by **a**, **b**, **c**, **d**, **e**, **f**, and **g.** Big dark spot located at the bottom left region of STXM images are due to uncrushed big particle. In this region, most of the x-ray was absorbed and NEXAFS analysis of this region is impossible.

References
(1) Luthy, R. G.;Aiken, G. R.;Brusseau, M. L.;Cunnimgham, S. D.;Gschwend, P. M.;Pignatello, J. J.;Reinhard, M.; Traina, S. J.; Weber, W. J. Jr.;Westall, J.C. *Environ. Sci. Technol.* **1997**, *31,3341*.
(2) McGroddy, S. E.;Farrington, J. W. *Environ. Sci. Technol.* **1995**, *29, 1542.*
(3) McGroddy, S. E.;Farrington, J. W.; Gschwend, P. M. *Environ. Sci. Technol.* **1996**, *30, 172.*
(4) Allen-King, R. M.;Grathwohl, P.;Ball, W.P. *Adv. Water Resour.* **2002**, *25, 985.*
(5) Accardi-Dey, A.; Gschwend, P. M. *Environ. Sci. Technol.* **2003**, *37, 99.*
(6) Yoon, T. H.; Johnson, S. B.; Benzerara, K.; Doyle, C. S.; Tyliszczak, T.; Shuh, D. K.; Brown, G. E. Jr. *Langmuir*, **2004** In press.
(7) Myneni, S. C. B. *Rev. Mineral. Geochem.* **2001,** *49*, 485-579.
(8) Hitchcock, A. P. *J. Synchrotron Rad.* **2001,** *8*, 66-71.
(9) Braun, A.;Shah, N;Huggins, F. E.;Huffman, G. P.;Wirick, S.;Jacobsen, C.; Kelly, K.; Sarofim, A. F. *Fuel* **2004**, *83, 997.*
(10)Braun, A.; Huggins, F. E.; Shah, N;Chen, Y.; Wirick, S.;Mun, S. B.;Jacobsen, C.; Huffman, G. P *Carbon* **2004**, In press.
(11)Hitchcock, A. P. *http://unicorn.mcmaster.ca/aXis2000.html*.
(12)McLeod, P.B; Van Den Heuvel-Greve, M. J; Allen-King, R. M.; Luoma, S. N; Luthy R. G. *Environ. Sci. Technol.* **2004**, *38, 4549*.

KINETIC MONTE CARLO SIMULATIONS OF SOOT PARTICLE AGGREGATION

Michael Balthasar,[a] Markus Kraft,[b] and Michael Frenklach[c]

[a]CFD and Combustion, VOLVO Technology, Göteborg, Sweden,

[b]Department of Chemical Engineering, University of Cambridge, UK,

[c]Department of Mechanical Engineering, University of California at Berkeley, and Environmental Energy Technologies Division, Lawrence Berkeley National Laboratory, Berkeley, CA 94720, USA

Figure 1. Illustration of the aggregate-aggregate collision algorithm.

Introduction

Soot particles formed in flames and practical combustion devices can be described as fractal-like aggregates comprised of spheroidal primary particles. The size of primary particles is known to exceed that of particles incepted from the gas phase. It is therefore often argued that particle aggregation is preceded by a period of coalescent growth.[1]

It has been argued that transition from coalescent to aggregate growth is a result of simultaneous coagulation and surface growth.[2] Mitchell and Frenklach[3,4] investigated the mechanism of transition from coalescent to aggregate growth by calculating trajectories of individual collector particles using a dynamic Monte-Carlo method, where collector particles allowed to grow through collisions with the surrounding monodispersed candidate particles and simultaneous surface growth. These authors concluded that the morphology of aggregating particles is intimately related to both the surface deposition and particle nucleation rates.

Extending this study, Balthasar and Frenklach[5] conducted similar simulations using a realistic size distribution for selecting candidate particles. The simulation results provided further support to the notion that particle nucleation and the presence of small particles influence the morphology of primary particles and the location of transition.

In the both studies, however, aggregate-aggregate formation was not taken into account. While the aggregation kinetics was recently modeled using a method of moments,[6] the morphology of the forming aggregates could not be examined with this approach.

In the present study, we extend the Monte-Carlo method to enable numerical simulations of the entire particle ensemble with aggregate-aggregate collisions included. The new approach is applied to the formation of soot particles in laminar premixed flames.

Method

The dynamics of a soot particle ensemble was modeled by the Smoluchowski master equations with additional source terms included for nucleation and surface reactions. The latter terms along with the gas-phase chemistry were described using the kinetic model of Appel et al.[7]

The geometric structure of each particle was considered explicitly. The incepting particles were assumed to be spherical. A detailed physical model[4] of aggregate-aggregate collisions was employed, treating individual constituent particles as hard spheres upon collision. Surface growth was modeled as a uniform increase in the diameters of constituent particles comprising the aggregates.

The population balance was solved by an efficient stochastic algorithm, which is built on the concept of majorant kernels.[8,9] The aggregate-aggregate collisions were treated following Mitchell and Frenklach,[3,4] as illustrated in **Figure 1**.
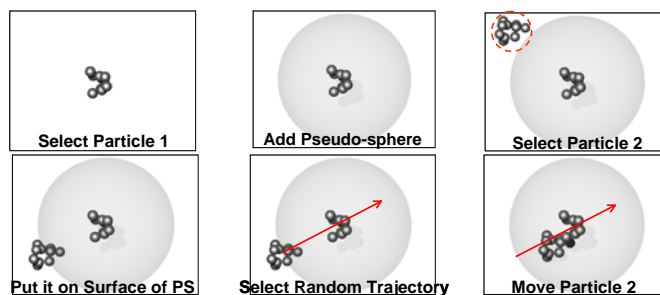
Results and Discussion

Stochastic Model Validation. To validate the numerical implementation, the model was tested for coalescent coagulation. A monodispersed size distribution of spherical particles was used at outset and the temperature was kept constant. The results of the stochastic simulations were compared to the solution of the master equations obtained with a deterministic ODE solver. A close agreement between the two was obtained.

Testing Aggregation Only. Aggregation phenomena and aggregate properties formed by collision of mono-dispersed particles have been investigated extensively in the past (see, e.g., Ref. [10]). Hence, as the next test of the model, we performed numerical simulations, using the present model, of aggregation of mono-dispersed particles. The resulting fractal dimension of $D_f = 1.9$ compares well with the literature report of 1.91 ± 0.03[11]. The resulting particles are shown in Figure 2.
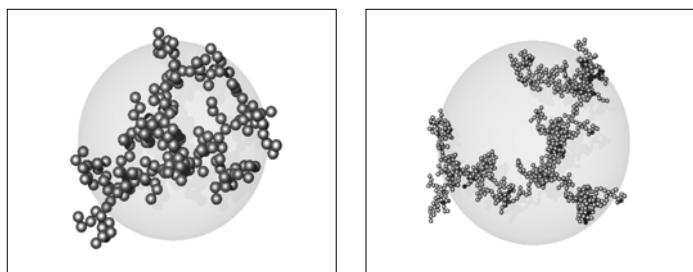

Figure 2. Three-dimensional rendering of sample particles produced in the aggregation-only numerical simulations.

Application Test Cases. In the first of this series of test cases, we started with nucleation without surface reactions for the first interval. In the second interval, for reaction times greater than 0.5 ms, nucleation decreased and surface growth increased linearly. This case was constructed mainly to generate large particles (in terms of particle volume) within a small simulation time and to test the Monte-Carlo sampling of particle properties: radius of gyration, R_g, surface area, S, and volume, V. After a coagulation event, surface area and volume were calculated directly by adding the surface areas and volumes of the two colliding particles. After each surface reaction step, the Monte-Carlo sampling was used to calculate R_g, S, and V of each particle.

The next test we constructed aimed at closely mirroring soot formation processes in a premixed flame but on a shorter time scale. In the beginning of the simulation, a strong peak in nucleation was constructed with a surface growth being small but non-zero. Shortly

after nucleation started decreasing, surface growth increased and peaked. Surface growth then decreased again and at the end only coagulation was active. Number densities and volume fraction computed for this case are shown in **Figure 3**. It can be seen that evolutions of these two variables closely resemble those usually found in a premixed flame. The mean collision diameter and shape descriptor d obtained from the simulated distributions were very similar to those found in the simulations using the method-of-moments aggregate model.[6]
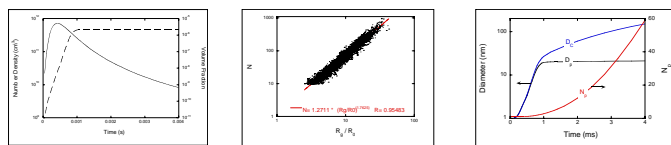

Figure 3. Numerical results; left panel: N and f_v; middle panel: number of primary particles versus radius of gyration; right panel: primary particle diameter d_p, aggregate diameter d_c and number of primary particles per aggregate N_p.

Figure 4 shows an example of a soot aggregate generated in these tests. It can be seen that the primary particles comprising the aggregates appear to be spheres of similar sizes. The two-dimensional projection of the particle shown in the right-hand panel compares well to typical transmission electron microscopy (TEM) images of soot aggregates.
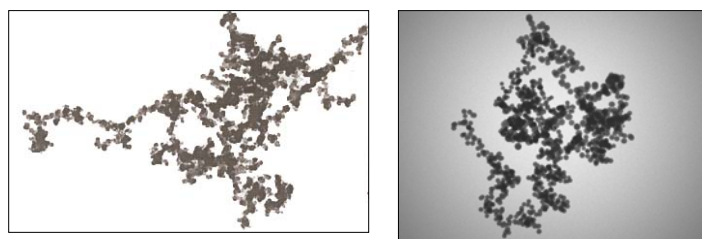

Figure 4. TEM image of a soot aggregate (left), and two-dimensional TEM-style projection (right) of a sample particle generated in the numerical simulations.

Finally, we performed numerical simulations with the present model for the condition of a 10-bar laminar premixed ethylene-air flame, at C/O = 0.673.[7,12] **Figures 5** and **6** below present the results obtained.
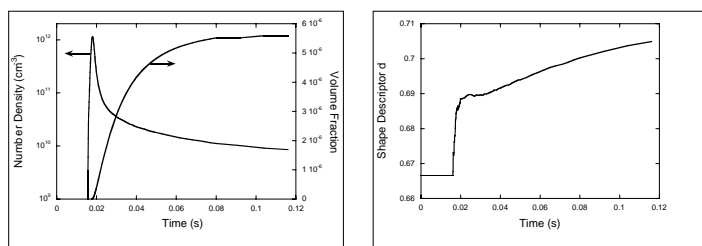
Figure 5. Number density, volume fraction, and shape descriptor as a function of time for a 10-bar laminar premixed ethylene-air flame at C/O=0.673.[7,12]
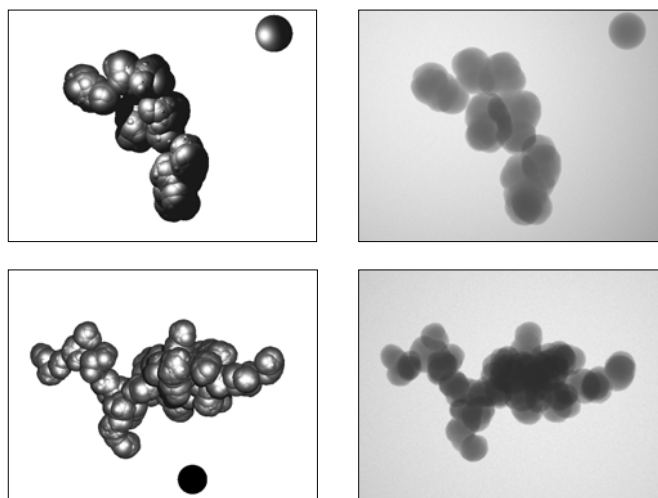
Figure 6. Three-dimensional renderings (left panels) and two-dimensional TEM-style projections (right panels) of sample particles taken from the simulation of the 10=bar premixed laminar ethyelene-air flame.

Summary

A stochastic algorithm was used to simulate the population balance of soot particles in laminar premixed flames of hydrocarbon fuels. The size and shape of the particles was determined by means of a ballistic particle-particle algorithm that simulates the particle collisions. Two-dimensional TEM-style projections of sample particles generated in these numerical simulations show features similar to the typical TEM images of soot particle collected in experimental flame studies.

References
(1) Haynes, B. S.; Wagner, H. G. *Prog. Energy Combust. Sci.* **1981**, *7*, 229.
(2) Wersborg, B. L.; Howard, J. B.; Williams, G. C. *Proc. Combust. Inst.* **1973**, *14*, 929.
(3) Mitchell, P.; Frenklach, M. *Proc. Combust. Inst.* **1998**, *27*, 1507.
(4) Mitchell, P.; Frenklach, M. *Phys. Rev. E* **2003**, *67*, 061407.
(5) Balthasar, M.; Frenklach, M. *Proc. Combust. Inst.* **2004**, *30*, in press.
(6) Balthasar, M.; Frenklach, M. *Combust. Flame* **2005**, accepted for publication.
(7) Appel, J.; Bockhorn, H.; Frenklach, M. *Combust. Flame* **2000**, *121*, 122.
(8) Eibeck, A.; Wagner, W. *SIAM J. Sci. Res.* **2000**, *22*, 802.
(9) Goodson, M.; Kraft, M. *J. Comput. Phys.* **2002**, *183*, 210.
(10) Jullien, R.; Botet, R. *Aggregation and Fractal Aggregates*; World Scientific: Singapore, 1987.
(11) Jullien, R. *J. Phys. A* **1984**, *17*, L771.
(12) Jander, H. **1992**, Personal communication.

COMPARING HALOGENATION OF SWNTs, SWNT MODELS, AND SIMPLE ALKENES

Donna J. Nelson[1], Christopher N. Brammer[1], Ruibo Li[1], and E. Ann Nalley[2]

(1) Department of Chemistry, University of Oklahoma, Norman, OK 73019, Fax: 405-325-6111, djnelson@ou.edu,
(2) Physical Sciences Department, Cameron University

Chemical modification and solubilization of SWNTs represents an emerging area in research on nanotube based materials. Chemical modification of these nanotubes can serve not only to increase their solubility but also to affect their properties and therefore their applications. Studying them and characterizing their reactivity toward various chemical reactants provides an exciting challenge for chemists today.

Results of addition reactions to SWNTs are now clouded by a number of obstacles, typical of a young field. (1) The manufacture of SWNTs did not produce well-defined molecules as was produced with fullerenes. (2) The situation was further complicated by the fact that methods used to purify the SWNTs involved the use of harsh chemical reagent to remove impurities such as amorphous carbon, metallic catalysts and other impurities. This also changed the nature of the SWNTs, because the reagents attached to the SWNTs themselves. (3) Many reactions enhanced the separation of the bundled nanotubes, but this could only be effected through functionalization.

Both of these needs (separation and functionalization) have plagued earlier attempts to carry out chemical reactions with individual SWNTs. Although a number of reactions with SWNTs have been studied, many of them involved only reactions at the ends of the tubes with the oxidative functional groups. In some cases, the presence of these functionalities can interfere with or consume the addition reagent, and given the extent of oxidation, the interference might not have permitted reliable results in subsequent addition reactions. Reactions with the sidewalls were further complicated by the fact that it was not possible to obtain pure single-unit SWNTs; thus reactions at the side walls were most likely performed on the outsides of bundles.

Because of the above problems, even simple SWNT halogenation reactions haven't yet been standardized. This is partially because the exact structure and/or bonding of the SWNTs undergoing reaction has not been fully understood and/or known. Recently Resasco and co-workers perfected a metal catalyzed CO reduction process which produces purified SWNTs, with well defined morphology, including length, diameter, and stereochemistry. These SWNTs provide a unique opportunity to study SWNT reactivity and to further characterize the double bonds in terms of their aromatic/alkene character. We report the comparison of these halogenations of SWNTS versus halogenation of selected model compounds and versus halogenation of selected alkenes in order to increase the understanding of these SWNT reactions and C=C bonds constituting the SWNTs themselves.

A NEW SYNTHETIC METHOD FOR NANOPOROUS GRAPHITE-DERIVED CARBON-SILICA COMPOSITES

Y. -H. Chu,[1] Z. -M. Wang, [1, 2]* M. Yamagishi,[2]
H. Kanoh,[3] T. Hirotsu[2]

[1] PRESTO, Japan Science and Technology Agency
[2] Applied Interfacial Chemistry RG,
Research Institute for Environmental Management Technology,
National Institute of Advanced Industrial Science and Technology,
2217-14 Hayashi-cho, Takamatsu-shi, Kagawa 761-0395, Japan
[3] Department of Chemistry, Faculty of Science, Chiba University,
Yayoi 1-33, Inage-ku, Chiba, Japan

Introduction

Nanoporous composites of thin hydrophobic carbon layers and nanosized metal oxide particles are ideal materials applicable to specific adsorption and high-performance catalysis under moisture condition. Our group has reported that nanoporous C/SiO_2 composite can be synthesized from graphite oxide (GO) by using a soft chemical method.[1, 2] The obtained novel porous nanocomposite of carbon and silica has a high surface area greater than 1000 m^2/g and presents medium hydrophilicity falling between the typical activated carbon and hydrophilic silica particles.

However, the present method requires a large amount of organic silicon sources and long hydrolyzing time. A mechanochemical method, on the other hand, is a simple but very effective means recently applied to the solid state ion-exchange of zeolites and also intercalation chemistry of layered materials.[3, 4] For improvement of the method of synthesis, the subject of this work is to apply the mechanochemical method to introduce a controlled amount of organic silicon species into the interlayer spaces of GO pre-expanded by a long-chain surfactant. We found that this method is very effective for obtaining a regular tetraethoxylsilane(TEOS)-intercalated GO structure and the final composites with very high surface areas. Some new findings regarding the intercalation structure of silicon species after introduction and the resulting silica structure in the final nanoporous composites were also obtained.

Experimental

Material Synthesis. GO was synthesized from natural graphite by Staudenmier's method.[5] Chemical analysis and thermal gravimetry result give the chemical formula of GO to be $C_8O_{4.8}H_{1.4}$ (oxygen content was from subtraction of carbon and hydrogen). The cation exchange capacity (CEC) of the prepared GO was determined to be 4.92 meq-$[H^+] \cdot g^{-1}$, being 4 to 5 fold that of montmorillonite (0.8 to 1 meq·g^{-1}).

GO sample pre-expanded by hexadecyltrimethyl ammonium ions was prepared by the following reported method.[2] GO was first dispersed in a 0.05 N NaOH solution by ultrasonic treatment, after which 600 ml of 1.8 mM hexadecyltrimethyl ammonium (C_{16}TMA) bromide aq. was added dropwise. After filtration with an aspirator and sufficient washing with distilled water, the surfactant-intercalated GO precipitate (denoted GOC_{16}) was collected and dried in air at 333 K overnight. The surfactant intercalation amount was determined to be 1.48 mmol·(g-GOC_{16})$^{-1}$ or 4.86 mmol·(g-GO-C)$^{-1}$, being equivalent to 55 % of the total ion exchange sites.
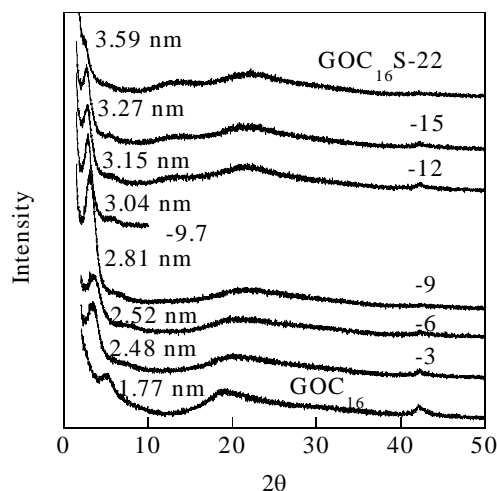
For intercalation of TEOS, the required GOC_{16} was placed into an agate mortar and determined volume of TEOS was accurately added. The solid and TEOS were mechanically mixed quickly to obtain GOC_{16}S-n where n stands for the mole ratio of TEOS over the total amount of exchangeable ion sites in GO and the final products

(denoted GOC_{16}S-n-823) were obtained by carbonization at 823 K. GOC_{16}T-n and GOC_{16}T-n-823 were synthesized at n = 0.5, 1.0, 3.0, 6.0, 9.0, 9.7, 12, 15, and 22.
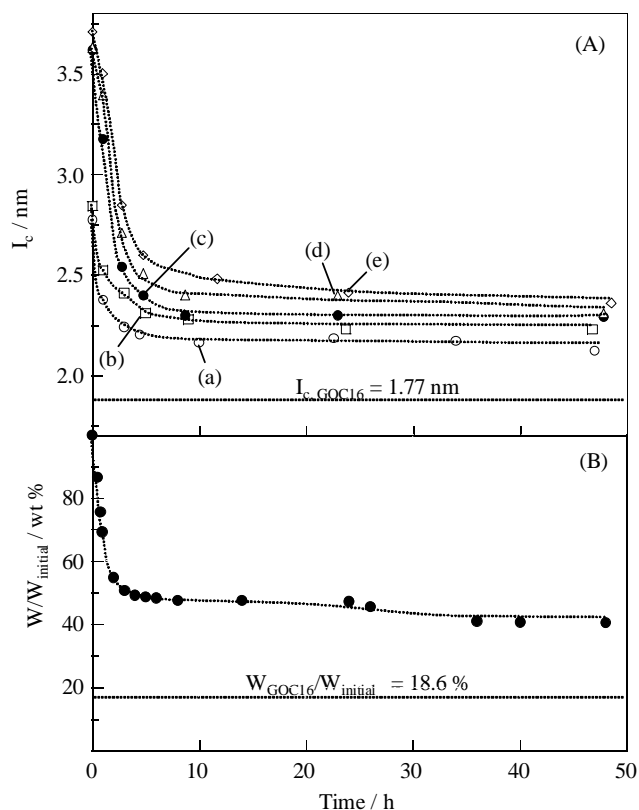
Characterization Method. X-ray diffraction patterns (XRD) of samples were measured by a Rigaku 1200 or 2100 system using Cu K_α radiation (λ = 0.15418 nm) in the 2θ range of 1.5 to 50° at the operating tube voltage and current of 40 kV and 30 mA. Data were collected at a scanning speed of 2°·min^{-1} and a sampling angle interval of 0.02°. The weight loss changes of GOC_{16}S-n in air at 303 K and the silicon contents in GOC_{16}S-n-823 were determined by a MacScience-made TG/DTA 2000-type apparatus. Diffuse reflectance infrared Fourier transform (DRIFT) spectra were measured by a Nicolet NEXUS 470-type FT-IR spectrometer under a continuous flow of nitrogen gas of 99.999 % purity from 256 scans at a resolution of 2 cm^{-1}. Nitrogen adsorption isotherms were measured at 77 K by a commercial volumetric apparatus (Belsorp 18A, Belsorp Co. or Autosorp-1, Quantachrome Co.). Samples were calcined at 823 K for 2 h under vacuum before adsorption. The microscopic features of samples were observed by a JEOL-made JSM 6330F type field-emission scanning electron microscope (FE-SEM) at an accelerating electron voltage of 2 kV.

Results and Discussion

Figure 1 shows XRD patterns of GOC_{16} and GOC_{16}S-n. GOC_{16} has a diffraction peak at 2θ = 2.49 that corresponds to an I_c value (1.77 nm) greater than two fold that of GO (I_c = 0.831 nm). Using conventional approach, further treatment of GOC_{16} by excess amount of TEOS leads to complete disappearance of the ordered structure.[1] However, as shown in Figure 1, samples after TEOS intercalation by mechanochemical method present clear peaks with expanded interlayer distances at n < 22. While I_c values and silicon contents of samples gradually increase with the increase of added TEOS amount, the diffraction peak becomes broader and finally disappears at a n value more than 22. Approximated calculation using surfactant molecular size implies that surfactant molecules in GOC_{16} exist in GO layers in a titled angle which gradually becomes greater with the increase of the TEOS intercalation amount (or n values). Surfactant molecules are completely vertical to the GO layers when I_c = 2.81 nm. Thus, a greater amount of TEOS intercalation at a high n value weakens interlayer attraction of GO, easily inducing the layer delamination.

Figure 1. XRD patterns of GOC_{16} and GOC_{16}S-n samples.

the subtraction of $V_{0, 0.95}$ and $V_{0, meso}$. All samples have mesopores with an average pore radius around 2 nm. GOC_{16} and $GOC_{16}S$-n-823 with n < 6 almost have only mesoporosities, indicating the importance of the house-of-card structure of carbon layers in the formation of porosities. On the other hand, $GOC_{16}S$-n-823 samples with n ≥ 6 exhibit high porosities with a specific surface area around 1000 m^2/g, indicating contribution of the interstitial spaces between silica nanosized particles to the total porosities.
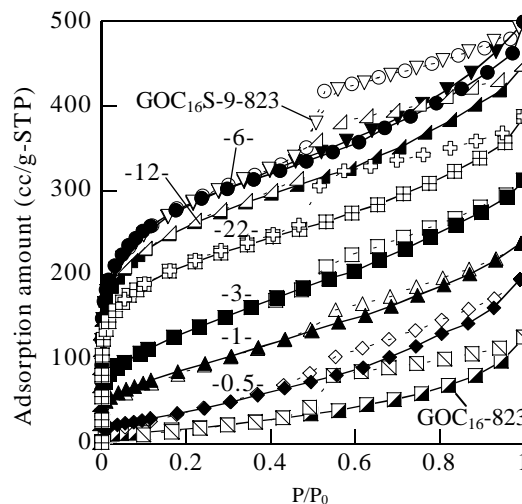
Figure 3. N_2 adsorption isotherms at 77 K on GOC_{16}-823 and $GOC_{16}S$-n-823. Filled and unfilled symbols represent the adsorption and desorption branches, respectively.

Table 1. Porosities of $GOC_{16}S$-n-823.

n	A_{BET} (m^2/g)	$V_{0,0.95}$ (ml/g)	$V_{0,meso}$ (ml/g)	$V_{0,micro}$ (ml/g)	$R_{p, meso}$ nm
0	60	0.17	0.22	~0	2.1
0.5	155	0.27	0.32	~0	2.1
1	314	0.34	0.33	0.01	2.1
3	460	0.45	0.41	0.04	2.0
6	1030	0.73	0.48	0.25	1.9
9	1040	0.70	0.50	0.20	2.1
12	945	0.65	0.46	0.19	2.0
22	780	0.55	0.40	0.15	2.0

Conclusions

Mechanochemical method is a simple but very effective way to intercalate a controlled amount of TEOS into interlayers of surfactant-pre-expanded GO, by which highly nanoporous carbon-silica composite can be obtained.

References
(1) Wang, Z. –M.; Hoshinoo, K.; Xue, M.; Kanoh, H.; Ooi, K. *Chem. Commun.* **2002**, 1696-1697.
(2) Wang, Z. –M.; Hoshinoo, K.; Shishibori, K.; Kanoh, H.; Ooi, K. *Chem. Mater.* **2003**, 15, 2926-2935.
(3) Karge, H. G. *Stud. Surf. Sci. Catal.* **1997**, 105, 2043.
(4) Yariv, S.; Lapides, I.; Michaelian, K. H.; Lahav, N. *J. Thermal Anal. Calorimetry* **1999**, 56, 865.
(5) Staudenmaier, L. Ber Deutsche Chem. Ges., 1989,31,1481.

Figure 2. (A) Time course of I_c values from XRD measurements of $GOC_{16}S$-n samples at n = (a) 1, (b) 3, (c) 6, (d) 9, and (e) 12, and (B) the weight ratio change of $GOC_{16}S$-6 measured by a TG balance in air at RT.

Figure 2 shows the changes of I_c values and weight changes of $GOC_{16}S$-n samples with the time exposed to air immediately after TEOS intercalation. I_c values and the weight ratios of the samples gradually decrease with the exposure time and almost become constant after 9 hours. The constant I_c values and the constant weight ratio are still higher than that of GOC_{16} and that of W_{GOC16}/$W_{initial}$, respectively, indicating simultaneous evaporation of TEOS molecules during formation of stable silica structure in GO layers. DRIFT spectra confirmed the formation of silica structure and a condensed silica network structure for samples at a higher n value. Morphologies of thicker stacking plates were observed for the $GOC_{16}S$-6 sample. The FE-SEM image of the sample after carbonization exhibits a clear curved layered structure, indicative of formation of a uniform composite between carbon layers and silica particles by using mechanochemical intercalation method.

Figure 3 shows the N_2 adsorption isotherms on GOC_{16}-823 and $GOC_{16}S$-n-823 samples at 77 K. All N_2 adsorption isotherms present the shape typical of type IV or a mixed shape of types I and IV. N_2 adsorption increases with the increase of added TEOS amount, reaching a maximum at n = 6 and 9, however, decreasing slightly at n > 9. These N_2 adsorption isotherms exhibit the evident adsorption hysteresis which is closed at P/P_0 = 0.45, characteristic of mesoporosity. There is also a sharp uprising at P/P_0 < 0.1 in N_2 adsorption isotherms of $GOC_{16}S$-n-823 at n > 3, manifesting the formation of microporosities in these samples. **Table 1** shows the pore parameters of the samples where A_{BET} and $V_{0, 0.95}$ are calculated from BET equation and adsorption amount at P/P_0 = 0.95, respectively, $V_{0, meso}$ and $R_{P, meso}$ from BJH method, and $V_{0, micro}$ from

DEVELOPMENT AND FORMATION MECHANISM OF MESOPOROUS CARBONS FROM MESOPHASE PITCH USING MOVABLE TEMPLATE

WM Qiao, Y Song, SY Lim, SH Hong, SH Yoon*, I Mochida

Institute of Materials Chemistry and Engineering
Kyushu University, Fukuoka 816-8580, Japan

Introduction

Mesoporous AC or ACF are expected in many applications such as catalyst supports, adsorption of large molecules, chromatography separation, desulfurization for clean energy, electrodes for batteries and fuel cells (1-5). Three methods are effective to introduce mesopores in activated carbons: catalytic gasification, carbonization of polymer aerogel through sol-gel process and templating with silica, zeolite and related inorganic materials in which precursors with isotropic textures are generally used. Synthetic mesophase pitch showed high graphitic properties, high carbonization yield, special structures composed of domains and micro-domains, is recognized a unique anisotropic precursor to develop carbon materials with high performance (6). Although alkali activation such as KOH and NaOH provided a large surface area, ascribed to micropores developed in anisotropic precursors such as needle coke (7) and mesophase pitch, it resulted into a sharp decrease of orderly graphitic structures, even their destruction and severe reactor corrosion. Template method appears to be expected to induce controlled pores in anisotropic structures by careful choosing template (8).

In the present study, nanosized silica and $Fe(NO_3)_3$ were added in synthetic mesophase pitch (MP) and its pyridine soluble part (PS), and the obtained mixture was simple stabilization, carbonization and removals of silica and iron by KOH solution and dilute HCl to be expected to synthesize mesoporous carbons with anisotropic structure, respectively. The properties of prepared mesoporous carbon derived from mesopase pitch were investigated using nitrogen adsorption at low temperature, XRD, SEM and TEM.

Experimental

Preparation of mesoeporous carbons (MCs). (a) Without $Fe(NO_3)_3$ addition: Mesophase pitch (MP) or its soluble part in pyridine (PS) was mixed with SiO_2 in pyridine in which the ratio of MP or PS to silica varied from 2:2.5, 2:5 and 2:10 (wt/wt), solvent was removed through rotating evaporation apparatus to obtain the mixture, then it was oxidatively stabilized and carbonized to obtain carbonized mesoporous carbon/silica composite, and finally, the composite was washed using KOH solution to get mesoporous carbon (MC); (b) With $Fe(NO_3)_3$ addition: $Fe(NO_3)_3$ (5-20%, base: silica) was adsorbed on the surface of SiO_2 in pyridine, then poured the solution into MP or PS pyridine solution for uniform mixing, and solvent was removed through rotating evaporation apparatus to obtain the mixture, then it was oxidatively stabilized and carbonized to obtain carbonized mesoporous carbon/silica composite, and finally, the composite was washed using KOH solution and dilute HCl to prepare MC.

Characterization of mesoeporous carbons (MCs). Surface area of MCs was calculated by BET equation according to nitrogen adsorption isotherm in the relative pressure range of 0.05-0.35. Pore size distribution of MCs was analyzed by using BJH method. The structural feature was characterized by using X-ray diffractometer (Rigaku, CuKα target). Morphologies of MCs were observed by using HR-TEM and FE-SEM.

Results

Figure 1 showed nitrogen adsorption isotherm of mesoporous carbon-PS5. The adsorption isotherm was Type IV, exhibiting a marked hysteresis loop, which belongs to typical mesoporous carbons. **Figure 2** showed BJH pore distribution of mesoporous carbon-PS5. PS5 showed a broad mesopore distribution between 2nm and 50nm. The surface areas and pore volumes of mesoporous carbons were summarized in **Table 1**.
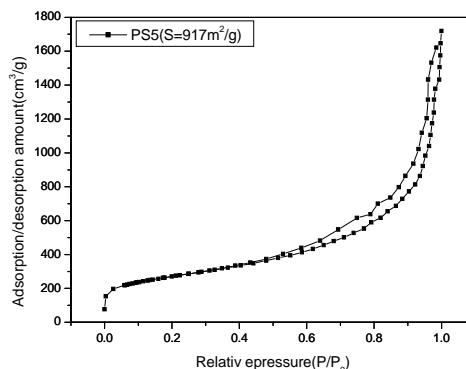

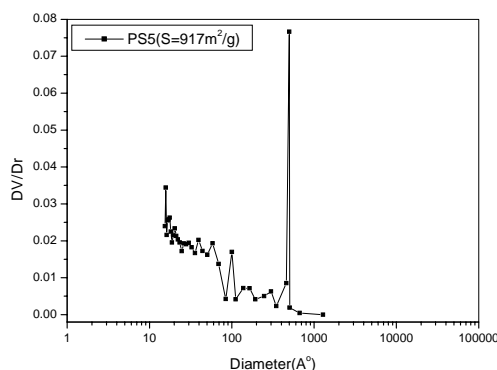**Figure 1.** N_2 adsorption isotherm of mesoporous carbon-PS5.

Figure 2. BJH pore distribution of mesoporous carbon-PS5.

Direct carbonization resulted in a low surface area and pore volume ($127m^2/g$ and 0.187ml/g, respectively) based on the possible separation of silica from pitch during the process. With the increase of stabilization time, total yield of MC increased and surface area and pore volume were markedly improved, up to $369m^2/g$ and 0.578ml/g, respectively. Silica additive amount had influential on the properties of MCs. Suitable additive amount resulted in the maximum surface area and pore volume. The addition of iron nitrate into MP series appeared to not improve surface area.

Compared with mesophase pitch (MP), its pyridine part (PS) precursor without the addition of iron nitrate permitted to obtain twice large surface area and pore volume, $608m^2/g$ and 0.914ml/g, respectively. Its average pore diameter and mesopore ratio were about 6nm and 95%, respectively. The addition of iron salt increased the surface area and pore volume and enlarged average pore diameter and mesopore ratio. The additive amount of 5% resulted in the maximum surface area, pore volume, mesopore ratio and average pore diameter ($917m^2/g$, 2.031ml/g, 99.5% and 8.86nm, respectively). The addition increased mesopores varied from 3nm to 7nm as observed in their pore size distributions, too.

The sharp peak of (002) reflections from XRD profiles indicated that MCs remained relatively developed graphite structures and MP-series showed high crystalline than PS-series, originated from precursors. The resultant mesopores whose diameters varied from

2nm to 50nm were directly observed by using SEM and TEM, in which mesoporous channels were observed. Domains and microdomains composing mesopores, mesoeporous channels were observed under high magnification.

Table 1. Preparation conditions and properties of mesoporous carbons (MP and PS series)

Sample	Ratio of mixture MP(or PS):SiO$_2$:Fe(NO$_3$)$_3$	Stabilization conditions	Yield wt%	S$_{BET}$ m^2/g	Pore volume ml/g	Mesopore ratio %	D nm
MP0-1	2g : 5g : 0%	no	78.1	127	0.187	97.8	5.89
MP0-2	2g : 5g : 0%	300°C for 1h	80.5	247	0.458	95.7	7.42
MP0-3	2g : 5g : 0%	300°C for 5h	82.0	369	0.557	98.5	6.04
MP0-4	2g : 2.5g : 0%	300°C for 5h	82.1	304	0.563	99.7	7.41
MP0-5	2g : 10g: 0%	300°C for 5h	82.2	275	0.376	94.7	5.47
MP5	2g : 5g : 5%	300°C for 5h	78.2	254	0.377	92.1	5.94
MP10	2g : 5g : 10%	300°C for 5h	76.0	359	0.643	92.7	7.16
MP20	2g : 5g : 20%	300°C for 5h	74.3	275	0.445	93.6	6.47
PS0	2g : 5g : 0%	300°C for 5h	70.3	608	0.914	95.2	6.01
PS5	2g : 5g : 5%	300°C for 5h	68.5	917	2.031	99.5	8.86
PS10	2g : 5g : 10%	300°C for 5h	66.4	877	1.567	97.4	7.15
PS20	2g : 5g : 20%	300°C for 5h	64.2	888	1.708	99.6	7.69

*Carbonization: 750°C for 1h with a heating rate of 5°C/min; D=4*Pore Vol/S$_{BET}$; yield base: pitch;
base for additive of Fe(NO$_3$)$_3$: SiO$_2$; pore volume: calculated at P/P0 of 0.98; SBET: calculated during P/P0 range from 0.05 to 0.35.

Discussion

Enough stabilization is important to obtain mesoporous carbons with high surface area because the process ensures good coating of pitch on the surface of silica particles. So, the resultant product should inherit the surface morphologies of silica. When silica is removed, mesoprous carbons should show similar surface characteristics, including area and pore size distribution. Iron salt addition increased mesopores from 3nm to 7nm from the pore size distributions of mesoporous carbons-MP5, 10, 20, 30 series, mainly attributed to the removal of metal particles and slightly decreased mesopore ratio, ascribed to the increase of micropore volume based on the effect CO$_2$ activation from the reaction between carbon and iron oxide from the decomposition of iron nitrate during stabilization. Particles of metal iron mostly distributed in carbon change in this span after carbonization. So, the removal of iron using acid-washing provides these mesopores.

Uniform mixing is always important to obtain good coating of pitch on the surfaces of silica to exhibit high surface area with highly developed mesoprous carbons. Without the addition of iron salt, PS precursor provided a much higher surface area and larger pore volume than MP after carbonization, 369 and 608m^2/g, respectively. It is obvious that PS can be more uniformly mixed with silica in pyridine solution than MP. Another factor that is responsible for higher surface area is the conversion of closed pores into open ones. During the carbonization of PS, there is the formation of a lot of closed pores (mainly mesopores whose diameters varied from 2 to 5nm) around silica particles because of the evolution of small molecules and the arrangement of microdomains composed of stacking of cluster units (every unit consists of 3-5 graphitic layers). After the removal of silica, closed mesopores are converted into open ones to provide higher surface area and larger pore volume and give networked mesopore channels as observed by using SEM and TEM photographs. The microdomain whose dimension is about5nm appears round morphology.

The addition of iron nitrate or iron oxide remarkably improved the surface area and pore volume of mesoporous carbons derived from PS, up to 880-920m^2/g and 1.5-2.0ml/g, respectively. On the one hand, evolved CO$_2$ reacted with carbon wall to provide some micropores. On the other hand, more importantly, the removal of iron particles not only provides mesopores whose diameters are similar to the dimension of those particles but also converts closed pores formed around iron particles into open pores, too. It should be noted that the resultant mesoporous carbons (MCs) remains high graphitic structures derived from mesophase pitch.

Conclusion

In the present study, mesoporeous carbons high surface area (300-900m^2/g) and pore volume (0.5-2ml/g) were firstly prepared successfully from mesophase pitch by through movable template process without further activation. The removal of nanosized silica not only provided mesopores having a surface area about 300 and pore size distribution varied from 25 to 50nm, but also converted closed pores produced during the carbonization of mesophase pitch into open ones, giving mesopores having a surface area about 300 and pore size distribution varied from 2 to 10nm derived from the arrangement of microdomains. Iron addition resulted in a markedly improvement of surface area (about 300m^2/g) based on three mechanisms: template effect, pore conversion effect and CO$_2$ activation. The study provided a simple and practical method to develop or synthesize mesoporous carbons with high yield from anisotropic precursors.

References

1.   Kyotani, T., *Carbon*, **2000**, 38, 269-86.
2.   Tamai, H, Kakii, T., Hirota, Y., Kumamoto, T, Yasuda, H., *Chem. Mater.*, **1996**, 8, 454-62.
3.   Han, S., Sohn, K., Hyeon, T., *Chem. Mater.*, **2000**, 12, 3337-41.
4.   Knox, J.H., Ross, P., *Adv. Chromatogr*, **1997**, 37, 73-162.
5.   Lee, J., Han, S,, Hyeon, T., *J. Mater. Chem.*, **2004**, 14, 478-86.
6.   Mochida, I., Korai Y., Ku C-H., Watanabe F., Sakai Y., *Carbon*, **2000,** 38, 305-28.
7.   Mitani, S., Lee, S., Yoon, S.H., Korai, Y., Mochida, I., *J. Power Sources*, **2004**, 133, 298-301.
8.   Li, Z., Jaroniec, M., *Carbon*, **2001**, 39, 2077-82.